AFRPL TR-84-057

AD:

Final Report
for the period
October 1980 to
June 1984

Solar Rocket Component Study

February 1985

Author:
J. M. Shoji

Rockwell International
Rocketdyne Division
6633 Canoga Avenue
Canoga Park, CA 91304

RI/RD84-180
F04611-80-C-0039

AD-A154 186

Approved for Public Release

Distribution unlimited. The AFRPL Technical Services Office has reviewed this report, and it is releasable to the National Technical Information Service, where it will be available to the general public, including foreign nationals.

DTIC FILE COPY

DTIC
ELECTE
MAY 24 1985
S D
A

prepared for the: **Air Force Rocket Propulsion Laboratory**

Air Force Space Technology Center
Space Division, Air Force Systems Command
Edwards Air Force Base,
California 93523-5000

NOTICE

When U.S. Government drawings, specifications, or other data are used for any purpose other than a definitely related government procurement operation, the government thereby incurs no responsibility nor any obligation whatsoever, and the fact that the government may have formulated, furnished, or in any way supplied the said drawings, specifications, or other data, is not to be regarded by implication or otherwise, or conveying any rights or permission to manufacture, use, or sell any patented invention that may in any way be related thereto.

FOREWORD

This is the Solar Rocket Component Study and was submitted by Rocketdyne Division of Rockwell International, 6633 Canoga Avenue, Canoga Park CA 91304 under Air Force Rocket Propulsion Laboratory (AFRPL) contract No. F04611-80-C-0039. AFRPL project manager was Curt Selph.

This technical report has been reviewed and is approved for publication and distribution in accordance with the distribution statement on the cover and on the DD Form 1473.

CURTIS C. SELPH
Project Manager

GERALD D. NORDLEY, Maj, USAF
Chief, Advanced Propulsion Branch

FOR THE DIRECTOR

CLARK W. HAWK
Chief, Liquid Rocket Division

UNCLASSIFIED

SECURITY CLASSIFICATION OF THIS PAGE

REPORT DOCUMENTATION PAGE

1a. REPORT SECURITY CLASSIFICATION Unclassified	1b. RESTRICTIVE MARKINGS
2a. SECURITY CLASSIFICATION AUTHORITY	3. DISTRIBUTION/AVAILABILITY OF REPORT Approved for public release. Distribution unlimited
2b. DECLASSIFICATION/DOWNGRADING SCHEDULE	
4. PERFORMING ORGANIZATION REPORT NUMBER(S) RI/RD84-180	5. MONITORING ORGANIZATION REPORT NUMBER(S) AFRPL-TR-84-057
6a. NAME OF PERFORMING ORGANIZATION Rocketdyne Division Rockwell International 6b. OFFICE SYMBOL (If applicable)	7a. NAME OF MONITORING ORGANIZATION Air Force Rocket Propulsion Laboratory
6c. ADDRESS (City, State and ZIP Code) 6633 Canoga Ave Canoga Park, CA 91304	7b. ADDRESS (City, State and ZIP Code) AFRPL/LKCS Edwards AFB, CA 93523-5000
8a. NAME OF FUNDING/SPONSORING ORGANIZATION Air Force Rocket Propulsion Lab 8b. OFFICE SYMBOL (If applicable)	9. PROCUREMENT INSTRUMENT IDENTIFICATION NUMBER F04611-80-C-0039
8c. ADDRESS (City, State and ZIP Code) Edwards AFB, CA Lancaster, CA 93523	10. SOURCE OF FUNDING NOS. PROGRAM ELEMENT NO. 62302F; PROJECT NO. 5730; TASK NO. 05; WORK UNIT NO. IF
11. TITLE (Include Security Classification) SOLAR ROCKET COMPONENT STUDY (U)	
12. PERSONAL AUTHOR(S) Shoji, James M.	
13a. TYPE OF REPORT Final 13b. TIME COVERED FROM 80/10 TO 84/06	14. DATE OF REPORT (Yr., Mo., Day) 85/2 15. PAGE COUNT 296
16. SUPPLEMENTARY NOTATION *	

17. COSATI CODES		
FIELD	GROUP	SUB. GR.
21	08	

18. SUBJECT TERMS (Continue on reverse if necessary and identify by block number)
Solar Thermal Propulsion, Absorber/Thruster Design, Solar Window, Solar Absorber, Rhenium Fabrication, Window Heat Transfer, Thruster Performance, Hydrogen Performance, Absorber/Thruster, Heat Transfer

19. ABSTRACT (Continue on reverse if necessary and identify by block number)

A program was conducted to identify the most promising solar-thermal rocket thruster concept and to design, fabricate, and deliver to the Air Force Rocket Propulsion Laboratory, a demonstrator absorber/thruster based on the selected concept for subsequent ground test evaluation.

A concept assessment, in which windowless and windowed designs involving both direct and indirect propellant heating, resulted in the selection of the windowless heat exchanger cavity configuration. The selection considered the criteria of achievable specific impulse, thrust achievable, durability, complexity, technical risk, and relative cost.

Based on the concept selected, a ground test demonstration absorber/thruster was designed. Supporting detailed thermal, stress, and performance analyses were conducted together with evaluations of critical materials and fabrication processes. The projected performance of the demonstrator absorber/thruster was a specific impulse of 7930 N sec/kg (807 lbf sec/lbm), with a thrust of 3.69 N (0.83 lbf).

Fabrication and assembly were completed and the thruster satisfactorily leak-checked. The absorber coil was fabricated from rhenium tubing produced by the chemical vapor deposition process. The thruster nozzle was also rhenium made by the same process. Radiation shielding and insulation minimized heat losses. ... Figures 2 ... 4

20. DISTRIBUTION/AVAILABILITY OF ABSTRACT UNCLASSIFIED/UNLIMITED ☒ SAME AS RPT ☐ DTIC USERS ☐	21. ABSTRACT SECURITY CLASSIFICATION
22a. NAME OF RESPONSIBLE INDIVIDUAL Seigh, Curtis	22b. TELEPHONE NUMBER (Include Area Code) (805) [illegible] 22c. OFFICE SYMBOL LKCS

DD FORM 1473, 83 APR EDITION OF 1 JAN 73 IS OBSOLETE.

UNCLASSIFIED

SECURITY CLASSIFICATION OF THIS PAGE

20. (Continued)

A system safety analysis performed resulted in recommendations for initial testing to minimize risk.

Recommendations are presented for continued technology required to realize the full potential of solar thermal propulsion.

Accession For
NTIS GRA&I
DTIC TAB
Unannounced
Justification
By
Distribution/
Availability Codes
Avail and/or
Dist Special
A-1

CONTENTS

Introduction and Summary 1

Introduction 1

Program Summary 3

Phase I, Concept Assessment 10

Incident Solar Radiation Distribution 11

Windowless Heat Exchanger Cavity Concept 14

Windowed Heat Exchanger Cavity Concept 38

Windowed Particulate Absorbtion Concept 56

Windowed Vortex Flow Concept Evaluation 76

Rotating Bed Concept 80

Additional Advanced Absorber/Thruster Concepts 101

Materials and Fabrication Assessment 107

Concept Comparison and Selection 111

Phase II, Absorber/Thruster Design 121

Configuration Definition 121

Design Layout and Detailed Design 130

Thermal Analysis 143

Stress Analysis 171

Materials and Fabrication Processes 177

Performance Analysis 186

Phase III, Fabrication 205

Component Fabrication 206

Absorber Coil Subassembly 233

Absorber/Thruster/Backplate Subassembly 243

Final Assembly 250

Phase IV, System Safety 254

Analysis 254

Conclusions 262

Conclusions and Recommendations 265

Continued Technology Investigations 265

Initial Test Recommendations 265

Appendix A

Windowless Absorber/Thruster Efficiency Calculational Method 269

Appendix B

Delivered Specific Impulse and Thrust Analysis Method 273

Appendix C

Vacuum Chamber Window Specifications 275

Appendix D

Thermocouple Error 278

References 283

ILLUSTRATIONS

1. Inflatable Cone/Paraboloid Collector 1
2. Phase I Primary Concepts Evaluated 4
3. Windowless Heat Exchanger Cavity Solar Rocket Thruster 6
4. Final Hardware Assembly 8
5. Solar Concentration Ratio and Cumulative Energy Fraction Distribution at Focal Plane 12
6. Solar Flux Distribution at Focal Plane 13
7. Windowless Heat Exchanger Cavity 14
8. Candidate Windowless Cavity Absorber Configurations 16
9. Windowless Heat Exchanger Cavity Absorber Total Efficiency for Different Absorber Configurations 17
10. Windowless Heat Exchanger Cavity Absorber Total Efficiency for Different Absorber Configurations 18
11. Windowless Heat Exchanger Cavity Absorber Total Efficiency for Different Absorber Configurations 19
12. Windowless Heat Exchanger Cavity Absorber Surface Area for Different Absorber Configurations 22
13. Windowless Heat Exchanger Cavity Absorber Efficiency Variation with Surface Area 23
14. Coiled Tube Windowless Heat Exchanger Cavity Tube Temperature . . . 26
15. Coiled Tube Windowless Heat Exchanger Cavity Static Pressure . . . 27
16. Delivered Specific Impulse for Open-ended Cylinder and Sphere/Horn/Disc Absorber Configurations 30
17. Delivered Thrust for Open-ended Cylinder and Sphere/Horn/Disc Absorber Configurations 31
18. Delivered Specific Impulse for the Open-ended Cylinder Absorber Configuration 32
19. Deliver Thrust for the Open-ended Cylinder Absorber Configuration . 33
20. Delivered Specific Impulse Variation with Hydrogen Temperature for an Open-ended Cylinder 34
21. Thrust Variation with Hydrogen Temperature for an Open-anded Cylinder 35
22. Stress Rupture Life Variation with Temperature for Rhenium 37
23. 12-inch Diameter Absorber/Thruster 39
24. 18-inch Diameter Absorber/Thruster 40
25. Windowed Heat Exchanger Cavity Absorber 41
26. Cavity L/D Influence 42

27. Window Configuration Comparison 43
28. Absorber/Thruster Window Thermal Model Nodal Network 45
29. Sapphire Absorber/Thruster Window Maximum Temperatures for Various Cooling Side Heat Transfer Coefficients 46
30. Quartz Absorber/Thruster Window Maximum Temperatures as a Function of the Absorptivity Coefficients 47
31. Quartz Window Temperature Profile of Cavity Chamber 49
32. Window (Quartz) Temperature Distribution for Window Heat Exchanger Cavity with 30.48 cm (12 inch) Diameter and 85% IR Reflectivity . . 50
33. Windowed Heat Exchanger Cavity Absorber - Porous Liner Incident Heat 51
34. Absorber Efficiency Comparison of the Windowless and Windowed Heat Exchanger Cavity Absorbers 53
35. Delivered Specific Impulse Comparison 54
36. Delivered Thrust Comparison 55
37. Windowed Molecular or Particulate Concept 56
38. Theoretical Vacuum Specific Impulse Variation 57
39. Percent Solar Radiation Absorption Variation with Particle Density and Particle Size 59
40. Percent Solar Radiation Absorption Variation with Particle Density at 0.2 μm Particle Radius 60
41. Axial Propellant Temperature Distribution (70% Absorption) for Particulate Absorption Concept 61
42. Transient Particulate/Molecular Absorption Thermal Model 62
43. Carbon Extinction Coefficient 64
44. Carbon Mass Fraction Requirements 66
45. Particulate Absorption Injection Approaches 67
46. Propellant Temperature Distribution of 6 m (2.362 inch) Absorbing Length 68
47. Comparison of Particulate Absorption H_2/C Injection Techniques . . 69
48. Quartz Window Temperature Profile of Discharged Seed Chamber . . . 70
49. Inflatable Cone/Paraboloid Collector 71
50. Inviscid, Gas Only, Plume Study 72
51. Viscous, Gas Only, Plume Study 73
52. Delivered Specific Impulse for the Particulate Absorption Absorber/Thruster 74
53. Delivered Thrust for the Particulate Absorption Absorber/Thruster 75
54. Windowed Vortex Flow Concept 77

55. Probabilty of Carbon Particle Loss Under Steady State Vortex Flow 78
56. Rotating Bed Concept Retained Seed 80
57. Rotating Bed Drive Approaches 81
58. Window Configuration Comparison 83
59. Window (Quartz) Temperature Distribution for Rotating Bed Concept with 30.48 cm (12 inch) Diameter Disc and 85% IR Reflectivity . . . 84
60. Window (Quartz) Temperature Distribution for Rotating Bed Concept -- 30.48 cm (12 inch) Diameter Double Pane (Inner Window) with 85% Reflectivity 85
61. Window (Quartz) Temperature Distribution for Rotating Bed Concept -- Hemispherical Window with 85% IR Reflectivity and 20% Window Coolant 86
62. Rotating Bed Concept Solar Radiation Absorption 89
63. Rotating Bed Speed Requirements 91
64. In-Bed Pressure Gradient 92
65. Tube Dimensions for Rotating Bed Thruster 93
66. Temperature Distribution for Rotating Bed Thruster 95
67. Thruster Coolant Pressure Distribution for Rotating Bed Thruster . . 96
68. Delivered Specific Impulse for the Rotating Bed Absorber/Thruster 97
69. Delivered Thrust for Rotating Bed Absorber/Thruster 98
70. Rotating Bed Absorption Concept 99
71. Rotating Bed Absorption Concept Schematic 100
72. Rotating Bed Foil Bearing Approach 103
73. Reduced IR Radiation View Factor Configurations 104
74. Aerowindow/Absorption Concept. 105
75. Solar Thermal Rocket Concept Performance Comparison 114
76. Delivered Specific Impulse Comparison 115
77. Windowless Heat Exchanger Cavity Absorber/Thruster 119
78. Coversion to Windowed Heat Exchanger Cavity with Porous Liner . . . 119
79. Conversion to Windowed Absorber/Thruster with Stationary Porous Cylinder 120
80. Thruster Orientation 122
81. Omnium-G Focal Plane Heat Flux Distribution 124
82. Omnium-G Focal Plane Power Distribution 125
83. Absorber Efficiency versus Geometry 127
84. Test Hardware Absorber Efficiency Trends 128

85. Test Hardware Absorber Geometery and Size 129
86. Solar Absorber/Thruster Experimental Layout 131
87. Modified Absorber/Thruster Design Layout 132
88. Final Absorber/Thruster Design Layout 133
89. Hydraulic Circuit Schematic 135
90. Solar Absorber/Thruster Assembly (Side View) 137
91. Solar Absorber/Thruster Assembly (End View) 138
92. Solar Absorber/Thruster Assembly 140
93. Thermal Analysis Regions 144
94. Results from Regen Computer Output for Absorber/Chamber with L/D = 2.5 and Tube of 0.254 cm (0.1 inch) ID 146
95. Temperature Distribution for Five-Tube Absorber Design 147
96. Heat Balance on Quartz Window 148
97. Absorber/Thruster Window Thermal Model Nodal Network 149
98. Quartz Window Thermal Model 149
99. Window Temperature Variation with IR Coating Reflectivity [$h_{c_{GN_2}}$ = 0.0000581 kCal/cm^{2}sec K (0.000826 Btu/inch^{2}sec F)] . . . 151
100. Typical Absorber/Window Temperature Distribution 152
101. Quartz Window Temperature Distribution with 30.48 cm (12 inches) Diameter and 85% IR Reflectivity 154
102. Quartz Window Temperature Distribution with 30.48 cm (12 inches) Diameter and 85% Reflectivity 155
103. Absorber Intermediate Radiation Shield Thermal Analysis Results . . 157
104. Influence of Number of Intermediate Radiation Shields on Heat Transferred to Regenerative-Cooled Shield 158
105. Radiation Shield Cooling Approaches 160
106. Absorber Shield Thermal Analysis Results 162
107. Thermal Schematic of Absorber Forward End 163
108. Typical Results of Nozzle Joint Temperature Distribution 166
109. Heat Distribution at the End Closure Cavity 167
110. Cooling Passages Design for Cavity Chamber Closeout Plate 168

111. Overall Heat-Distribution in Absorber/Chamber 169
112. Overall Temperatures and Pressures 170
113. Stress Analysis Regions 171
114. Rhenium Tube Finite Element Model and Analytical Results 172
115. Solar Absorber/Thruster Radiation Shield Shell 174
116. Radiation Shield Back Plate Factors of Safety 174
117. Nozzle Finite Element Model and Analytical Results 175
118. Absorber/Thruster Materials 178
119. Absorber Tooling 179
120. Absorber Mandrel With Plug Installed 179
121. First Tube Coiling Attempt 181
122. Rhenium Tube Joint Approaches 181
123. Welded Sleeve 182
124. Graphite Vapor Pressure Variation With Temperature 184
125. Theoretical Specific Impulse Variation With Area Ratio for Hydrogen at 2778 K (5000 R) 187
126. Simplified JANNAF Procedure 188
127. Thruster Performance Losses 189
128. Delivered Specific Impulse Variation With Final Hydrogen Temperature 190
129. Hydrogen Flowrate Variation With Final Hydrogen Temperature . . . 191
130. Thrust Variation With Final Hydrogen Temperature 192
131. Diffuser/Ejector Design 194
132. Parameter Variations With Final Hydrogen Temperature 196
133. Absorber/Thruster Propellant Temperatures and Pressures 202
134. Instrumentation 202
135. Overall Ground Test Solar Rocket Conf guration 204
136. Simplified Fabrication and Assembly Sequence 205
137. Final Absorber/Thruster Design Layout 206
138. Rhenium Hardware Assembly Flow Chart 209
139. Typical Rhenium Tube Pit Defects 210
140. Representative Loosely Deposted Material Rhenium Tube Regions 211
141. Typical Nodules and Depression in Rhenium Tubing 212
142. Rhenium Tube Weld Investigation A 217
143. Rhenium Tube Weld Investigation B 218

144. Absorber Stainless Steel Mockup No. 1 220
145. Graphite Case 221
146. Split Graphite Baseplate and Nut 223
147. Graphite Nut Installation in Graphite Case 224
148. Vacuum Chamber Outer Shell 225
149. Absorber Radiation Shield Assembly 227
150. Rhenium Thruster 230
151. Rhenium Thruster (Backside) 230
152. Nominal Rhenium Thruster Design and As-Deposited Configuration 231
153. Peak Strain Summary for Rhenium Thruster 232
154. Rhenium Tube/Sleeve Assembly 234
155. Coiled Rhenium Tube Assembly 237
156. Rhenium Tube-to-Header Plate Design Configuration 238
157. Rhenium Thruster Assembly 239
158. Pressure/Temperature Test Configuration 240
159. Pressure/Temperature Furnace Assembly 241
160. Probe/Thermocouple Test Furnace Assembly 242
161. Thruster/Backplate Assembly 244
162. Thruster/Ring Brazing Tooling 245
163. Absorber/Backplate Jumper Line Assembly 246
164. Coiled Absorber/Backplate Assembly 247
165. Coiled Absorber/Backplate Assembly Absorber Inlet and Thruster . . 248
166. Backplate Assembly - View Looking Forward 249
167. Solar Rocket Assembly Fixture 251
168. Solar Thermal Rocket Assembly (Viewed From Absorber Cavity End) . . 252
169. Solar Thermal Rocket Assembly (Viewed From Thruster End) 253
A-1. Windowless Heat Exchanger Cavity Absorber Performance Parameters . . 270
A-2. Cavity to Opening Shape Factors 271
D-1. Temperature Distribution at the End Enclosure Cavity 280
D-2. Thrust Wall Thermocouple Error with Thruster Radiation Shield . . . 281

TABLES

1. Cavity Heat Transfer Analysis Summary 25
2. Rotating Bed Concept Window Cooling Analysis Summary 87
3. Window Material Properties 108
4. Phase I, General Conclusions 112
5. Technology Unknowns 113
6. Absorber/Thruster Comparison 117
7. Absorber/Thruster Rating 118
8. Omnium-G Reflector 124
9. Solar Rocket Drawings 139
10. Results of Coil-Tube Flow at Different Configurations 145
11. Properties of Aluminum Oxide Radiation Insulation 161
12. Solar Rocket Weight Breakdown 176
13. Solar Thruster Rhenium Tests 182
14. Diffuser/Ejector Analysis Results 193
15. Absorber/Thruster Nominal Performance Summary 201
16. Solar Rocket Assembly Parts List 207
17. Rhenium Tube Minimum Wall Thickness Data 213
18. Rhenium Tube Minimum Wall Thickness Range Characterization 215
19. Absorber Fabrication Sequence 235
20. Preliminary Hazard List 255
21. Preliminary Hazard Analysis 256

C-1. Vacuum Chamber Window Specifications 276
C-2. Vacuum Chamber Window IR Coating Specifications 277

INTRODUCTION AND SUMMARY

INTRODUCTION

A previous study funded by the Air Force Rocket Propulsion Laboratory (AFRPL) (Ref. 1) investigated solar thermal propulsion concepts for space missions requiring high performance. In the solar thermal rocket concept, a single propellant is heated by concentrated solar radiation and exhausted through a nozzle to produce thrust. A typical system concept with its large solar concentrators is shown in Fig. 1.

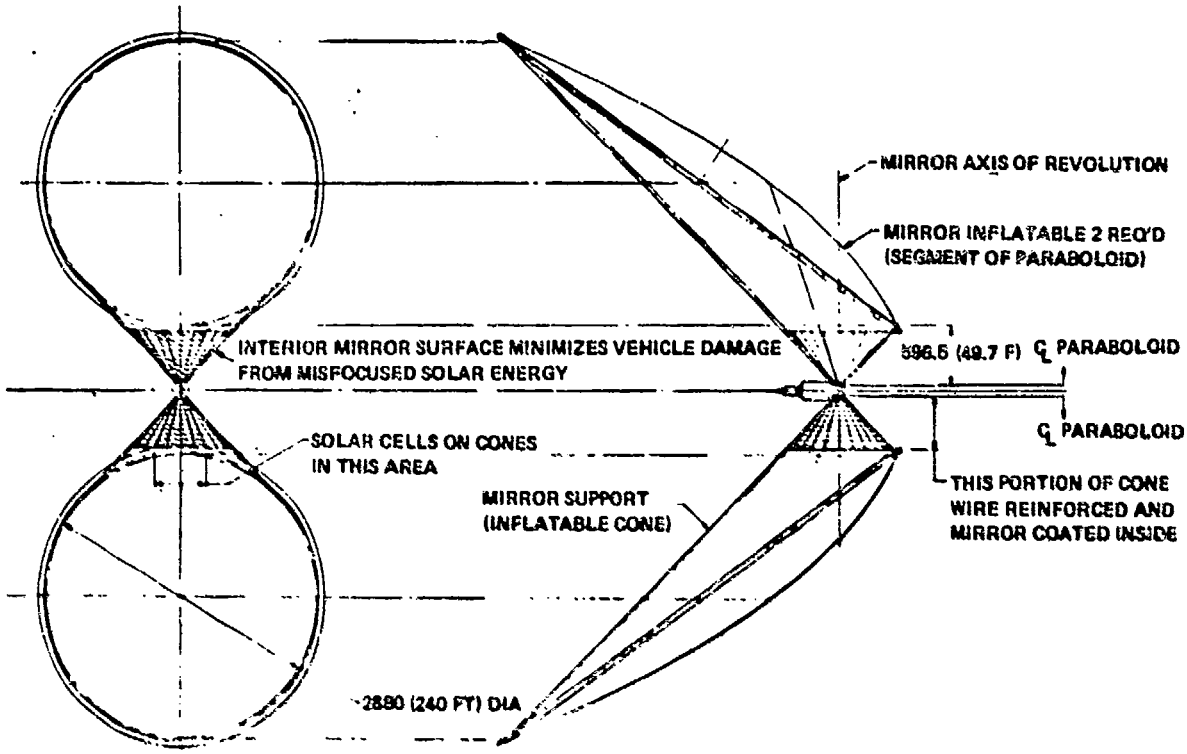

Figure 1. Inflatable Cone/Paraboloid Collector

The reference study defined system concepts which showed significant advantage over typical chemical-powered systems in terms of higher specific impulse and over electric propulsion systems in terms of greater thrust capability, which reduces mission duration. Hydrogen was established as the most desirable propellant. A critical technology area defined from the reference study was the solar-thermal rocket thruster.

The objective of this current program was to identify the most promising solar-thermal rocket absorber/thruster concept, and to design, fabricate and deliver to AFRPL a small thruster based on the selected concept for subsequent ground testing.

The program was conducted in four phases.

Phase I: Concept Assessment

Phase I provided the basis for selection of the most promising absorber/thruster approach and consisted of conceptual description and analysis of various types of solar thermal rocket thrusters within the context of a nominal primary propulsion system. Based on the previous study (Ref. 1), a pair of off-axis collector dishes on opposite sides of the absorber/thruster was assumed (Fig. 1) with side entry of the two opposed beams into the absorber. A projected collector dish area normal to the sun equivalent to 30.48 m (100 foot) diameter was assumed with a reflectivity of 0.85. Mass flow was varied to produce specific impulse values from 800 seconds to the maximum value achievable with the concentrator described above and the particular absorber/thruster concept. The output of this phase was the selection of the most promising concept within the content of high performance, durability, and technological feasibility.

Phase II: Design

Phase II consisted of detailed design of an absorber/thruster assembly based on the most promising concept identified in Phase I and suitable for ground testing. The output of Phase II was a set of drawings and specifications to enable the subsequent fabrication of a subscale ground test article for proof-of-principle demonstration. The absorber/thruster design incorporated a single-beam entry aperature and was scaled to the power and flux distribution characteristics of the "Omnium-G" 6-m-diameter solar concentrator which was planned for future testing at AFRPL.

Phase III: Fabrication

Phase III consisted of fabrication of the test article according to the drawings and specifications developed in Phase II and the delivery of the test article to AFRPL for inspection and acceptance.

Phase IV: System Safety

Phase IV consisted of a preliminary analysis of system safety for the test article design. The analysis was performed during the conduct of the hardware design and fabrication and was based on sound, practical engineering judgment, experience, and test data. The objective of this analysis was to minimize unintentional catastrophic failure of the hardware and physical harm to personnel.

PROGRAM SUMMARY

The Phase I concept assessment evaluated seven concepts (five primary and two secondary) which included both windowless and windowed designs involving both direct and indirect propellant heating. The five primary concepts evaluated are illustrated in Fig. 2.

With the windowless heat exchanger cavity concept, the solar energy is absorbed at the surface of a pressure vessel wall and transmitted through the wall by conduction to the hydrogen working fluid on the high-pressure side.

In the windowed heat exchanger cavity concept, a physical window is provided to transmit the solar energy while containing the hydrogen gas pressure. The hydrogen flows into the chamber through a porous liner which is heated by the solar flux entering through the window.

In the windowed molecular or particulate absorption concept, the solar flux is absorbed volumetrically into the working fluid through the addition of opaque seedants. The seedant is injected into the working fluid and exhausted with it.

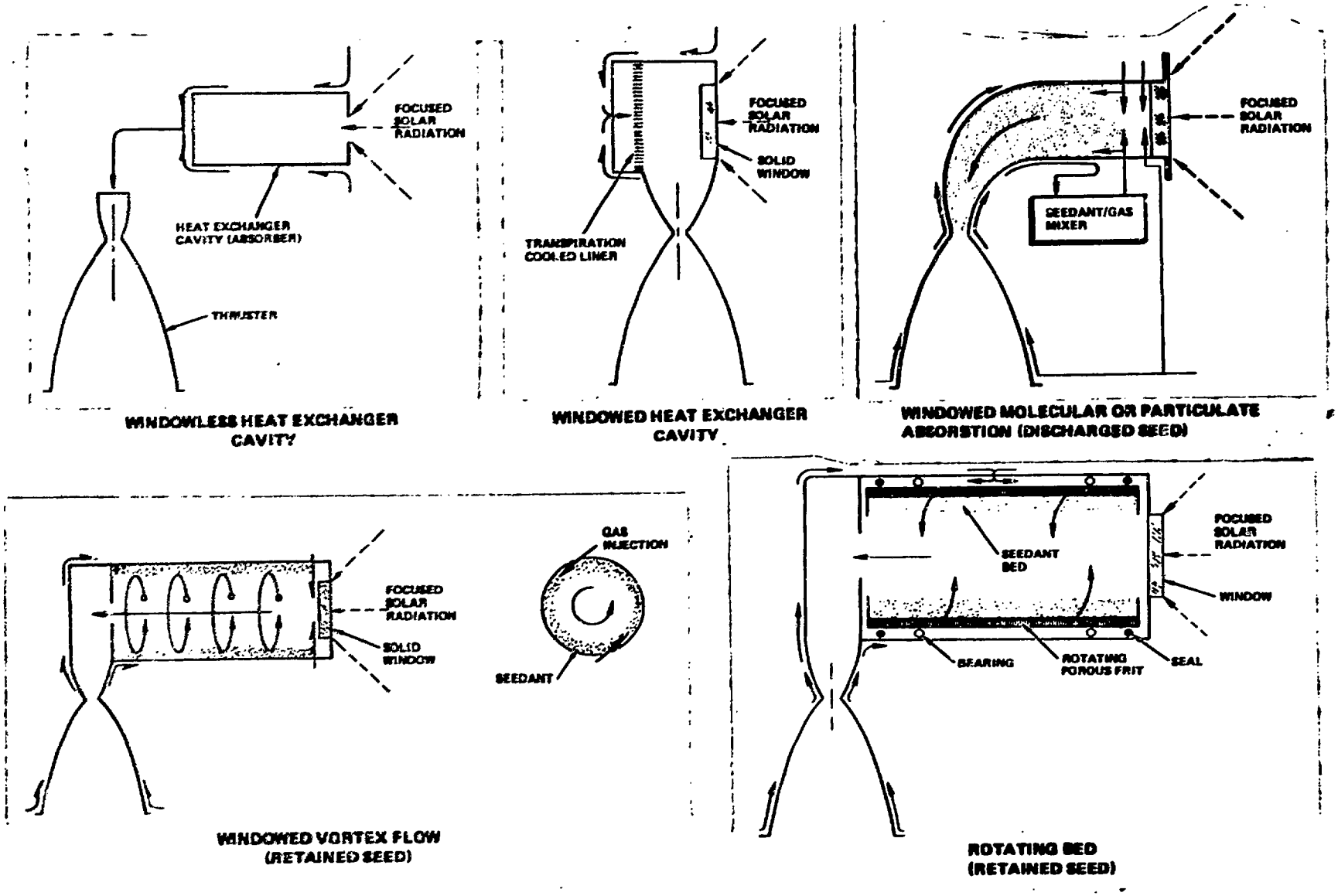

Figure 2. Phase I Primary Concepts Evaluated

The windowed vortex flow and the rotating bed concepts utilize seedants with vortexing or mechanical means to eliminate the exhausting of significant amounts of seedant. Discharge of seedant is undesirable from considerations of performance loss and contamination of concentrator optics.

Based on the data resulting from the concept evaluations, a comparative rating was established considering the criteria of:

- Specific impulse achievable
- Thrust achievable
- Durability
- Complexity
- Technical risk
- Relative cost

The highest overall rating was achieved by the windowless heat exchanger cavity concept. This concept, while not the highest in achievable specific impulse, rated superior in terms of minimum complexity, technical risk, and cost. The windowless heat exchanger cavity concept was selected for design and fabrication.

Phase II design effort established the basic configuration definition including the orientation of the absorber/thruster to the solar flux, the Omnium-G solar concentrator characteristics and the size and geometry of the absorber. Design layout and refinement through 12 individual configuration, provided the final configuration from which the detailed component drawings were prepared. The design effort was supported with detailed thermal, stress and performance analyses, and an evaluation of critical materials and processes, to ensure the fabricability of the design.

The design of the solar rocket ground test thruster (Fig. 3) features a heat exchanger cavity formed by coiled rhenium tubing to which the rhenium thruster nozzle is attached. The unit is surrounded by radiation shields and insulation to minimize the heat losses. This assemby is enclosed by a regenerative cooled vacuum chamber which also serves as the final radiation shield.

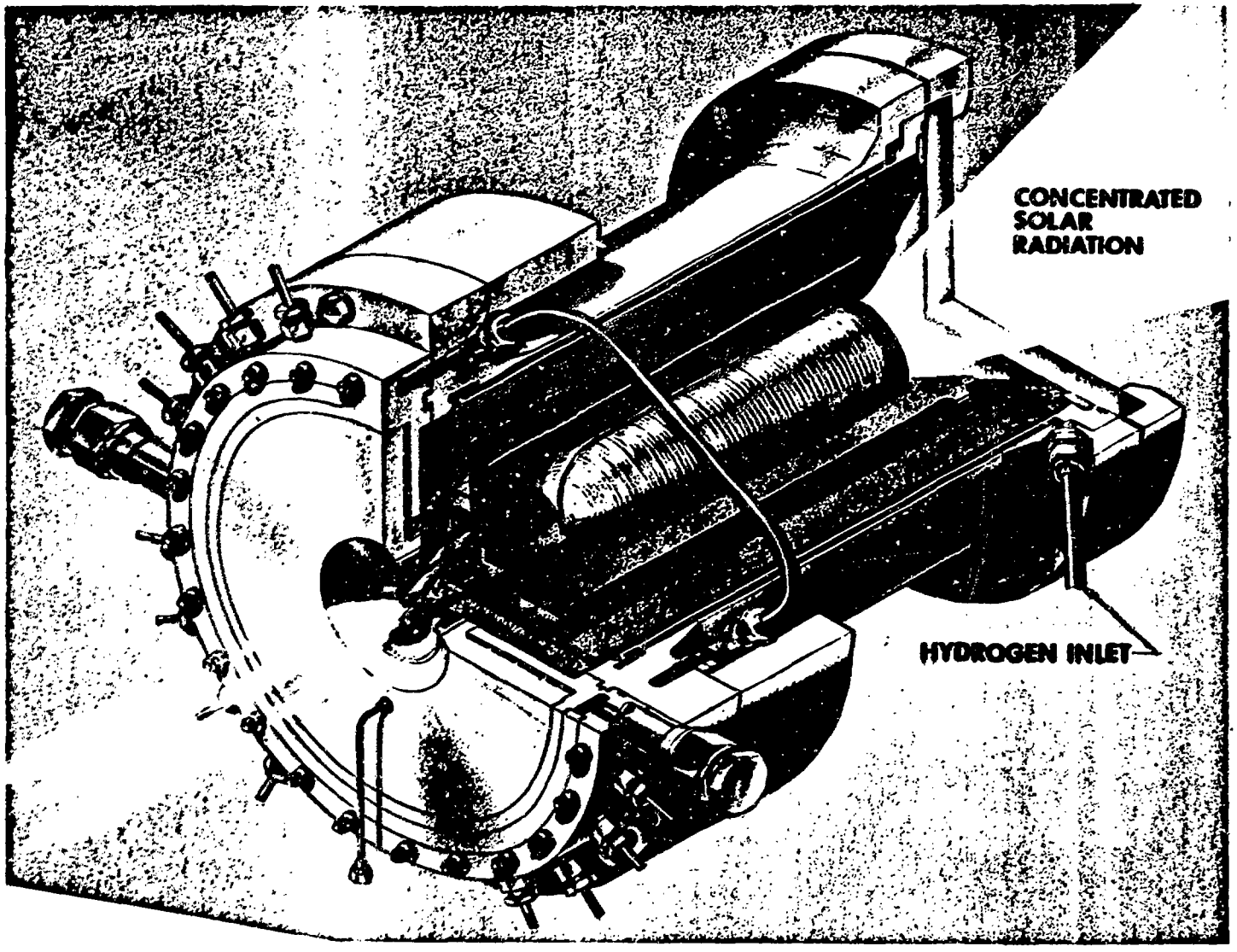

LC379-805A

Figure 3. Windowless Heat Exchanger Cavity Solar Rocket Thruster (Ground Test Article)

The solar flux enters the absorber through a quartz window. The window is required for ground testing to provide a vacuum even though a windowless concept was selected. Since rhenium oxidizes at fairly low temperatures, testing in an earth environment requires that the rhenium be contained in an inert or an evacuated environment (vacuum) which requires that the assembly have a transparent window. Therefore, the window was considered a test equipment item. The design provides for minimizing thermal strains and utilizes established technology to maintain fabricability.

The projected performance and operating characteristics of the solar rocket thruster (test article) are summarized below:

Absorber:

Efficiency	76.9%
Hydrogen flow	0.000467 kg/sec (0.00103 lb/sec)
Hydrogen temperature (maximum)	2722 K (4900 R)

Thruster:

Chamber pressure	34.5 N/cm^2 (50 psia)
Hydrogen flow	0.000467 kg/sec (0.00103 lb/sec)
Hydrogen temperature	2705 K (4870 R)
Nozzle expansion area ratio	20:1 (80% length)
Delivered specific impulse	7929.7 N sec/kg (808.6 lbf sec/lbm)
Thrust	3.69 N (0.83 lbf)

As indicated, the projected specific impulse exceeded the program goal of 7845.4 N sec/kg (800 lbf sec/lbm).

Fabrication of the solar rocket thruster components, installation of instrumentation and final assembly were accomplished in Phase III. Final leak checks performed indicated minimal leakage and the assembly was packaged and delivered to AFRPL. The final assembly is shown in Fig. 4.

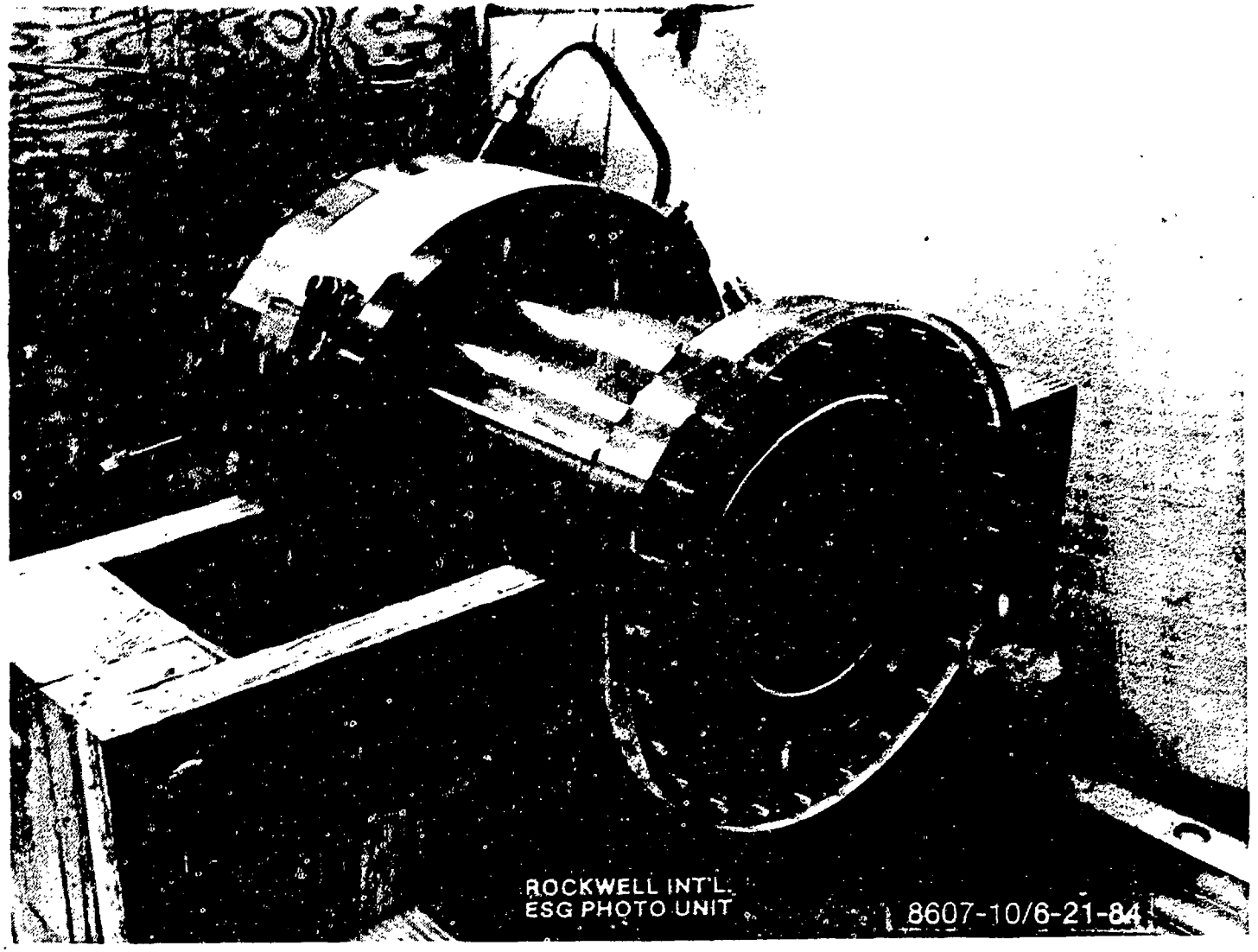

Figure 4. Final Hardware Assembly

The Phase IV System Safety Analysis was completed and is included in this report.

Acknowledgements

This report documents the results of the Solar Rocket Component Study (Contract F04611-80-C-0039).

The Solar Thermal Propulsion Concept study and fabrication and delivery of the ground-test hardware clearly represents a step forward in advanced technology of high-performance propulsion concepts. The AFRPL Project Manager was Curtis Selph and the Rocketdyne Program Managers involved during the program included Hal Diem, Don Fulton, Paul Coffman, and Paul Buergin. The final report was written with the help of the unique organizational and writing talents of Mr. Diem.

The analysis, evaluation, and fabrication performed in this program required expertise in solving unique problems in heat transfer, material and processes, structures and design. The challenges in these areas were aptly met with technical ingenuity by Dennis Lim (Heat Transfer), Charles (Chip) Moss, Jerry Lin, and Al Pard (Material and Processes), Randy Beer (Stress), and Irving Kaith (Design). Primarily through the dedicated efforts of A. Pard and I. Kaith, the ground-test hardware fabrication was successfully completed.

PHASE I, CONCEPT ASSESSMENT

Phase I consisted of the conceptual description and analysis of various types of solar thermal absorber/thruster concepts within the context of a nominal primary propulsion system for a space vehicle. The essential interface characteristics between the thruster and the rest of the system were largely defined by the concentrator mirrors. Previous studies (Ref. 1) indicated system advantages of a pair of off-axis paraboloidal dishes on opposite sides of the thruster. This approach was assumed for the study. As specified in the SOW, a projected area normal to the sun equivalent to a 30.48 m (100 foot) disc was used. A concentrator reflectivity of 0.85 was also assumed. Hydrogen was defined as the propellant with selected seedants added as necessary for solar absorption, depending upon the absorber/thruster concept. A specific impulse goal equal to or greater than 800 seconds and a life of 1000 hours of thrusting were assumed as specified in the SOW.

The Phase I studies were initiated with an analysis of the incident solar radiation distribution based in the solar concentrator mirrors defined above. Utilizing these data, the following primary absorber/thruster concepts were evaluated and included both windowed and windowless concepts involving both direct and indirect propellant heating:

Windowless Heat Exchanger Cavity
Windowed Heat Exchanger Cavity
Windowed Particulate/Molecular Absorbtion (Discharged Seed)
Windowed Vortex Flow (Retained Seed)
Rotating Bed (Retained Seed)

In addition to these primary concepts, three other more complex concepts were briefly studied.

To support the concept evaluations, preliminary absorber/thruster materials and fabrication assessments were conducted.

Utilizing the results of the evaluations listed above, the Phase I concept comparison and selection was completed based on selection criteria established.

INCIDENT SOLAR RADIATION DISTRIBUTION

From the solar concentration distributions of the previous solar rocket program (Ref. 1), at 1/8-degree surface angular error, the distribution for a collector efficiency of 0.85 was established and is presented in Fig. 5 as a function of the radius ratio (focal plane radius divided by the concentrator radius). A peak concentration ratio of 12,850 was obtained. An integration of the concentration ratio curve enabled the determination of the fraction of accumulated energy shown in Fig. 5. As shown, a radius ratio of approximately 0.0063 is required to receive 50% of the incident solar radiation. A radius ratio of 0.0127 is required to receive 90% of the incident solar radiation.

Using the solar constant and a 100-foot diameter solar collector, the concentration ratio versus radius ratio curve was translated into an incident solar heat flux versus radius curve presented in Fig. 6. A peak heat flux of 1740.5 watts/cm^2 (10.65 Btu/in.^{2}second) resulted. The total integrated incident heat input was 834.1 Kw or 790.7 Btu/second. These results were used in the analysis of candidate absorber/thruster concepts which follow.

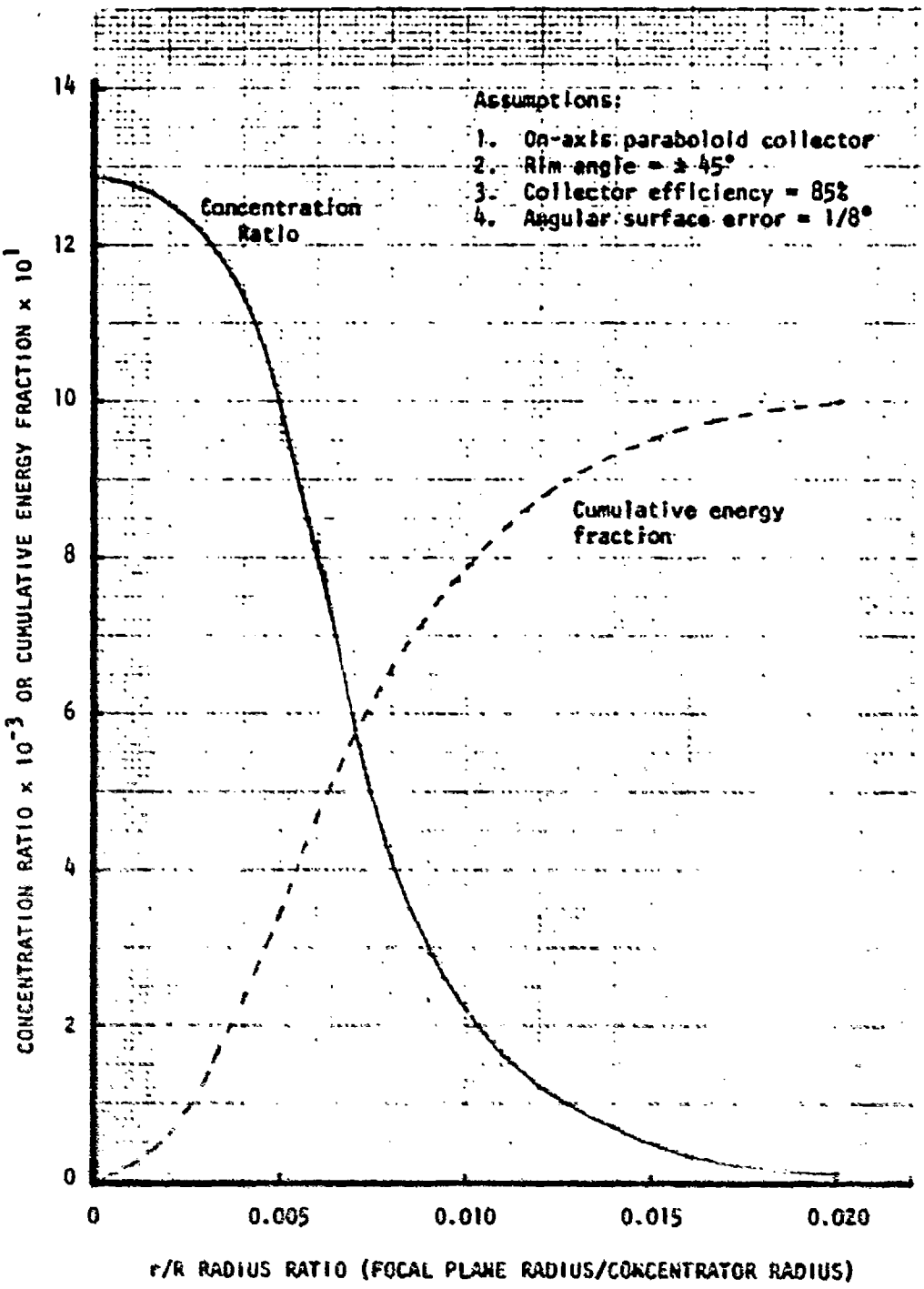

Figure 5. Solar Concentration Ratio and Cumulative Energy Fraction Distribution at Focal Plane

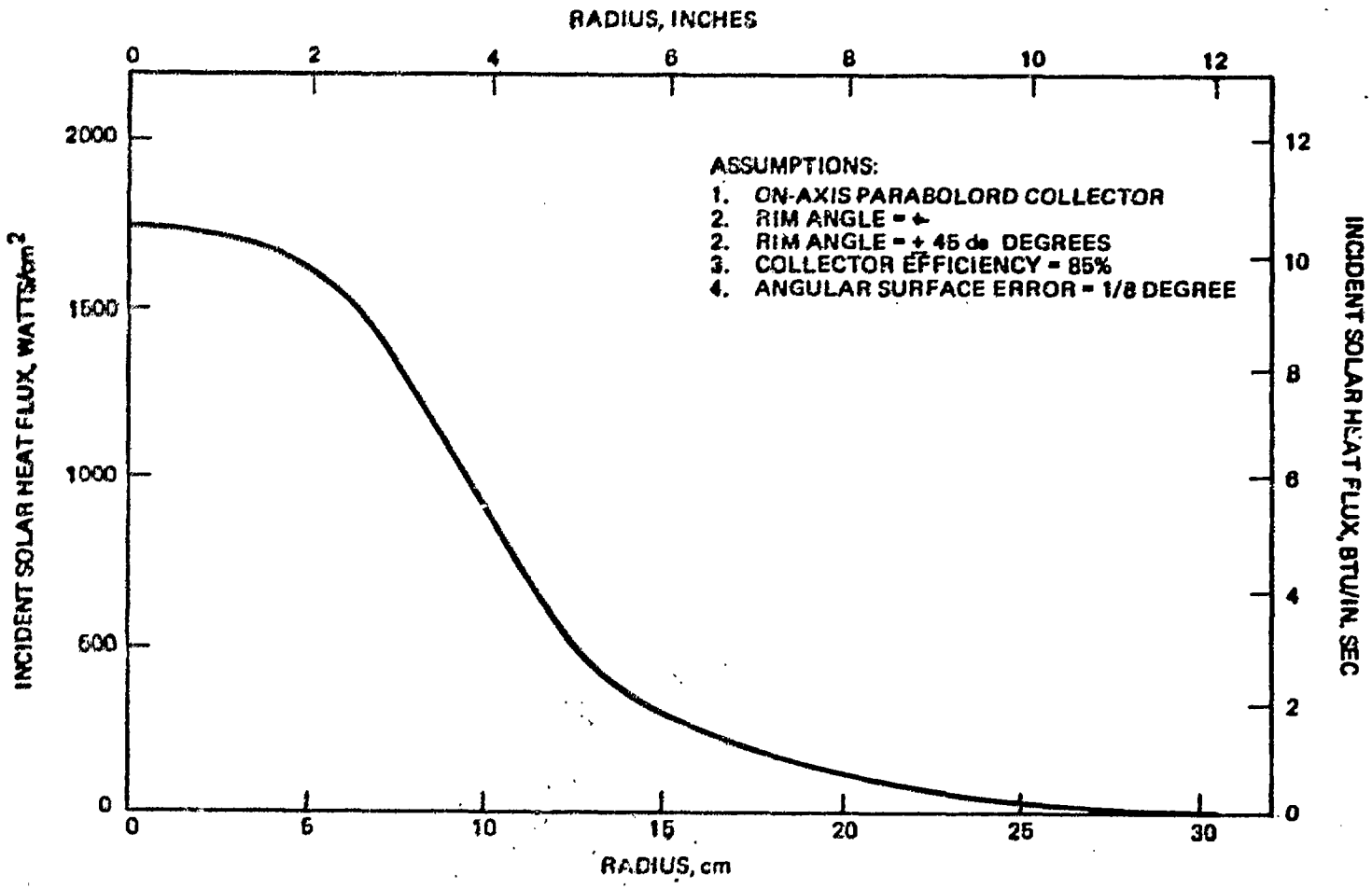

Figure 6. Solar Flux Distribution at Focal Plane

WINDOWLESS HEAT EXCHANGER CAVITY CONCEPT

The overall performance of the windowless heat exchanger absorber/thruster concept, illustrated in Fig. 7, is the result of a combination of absorber cavity performance (radiation intercepted and cavity efficiency) and the thruster efficiency. The thruster performance is only a function of the nozzle contour and the nozzle area ratio once the thrust chamber pressure and the final propellant (hydrogen) temperature are known. However, the performance of the absorber cavity is primarily dependent on the size and configuration of the cavity and its effectiveness in reducing re-radiation losses.

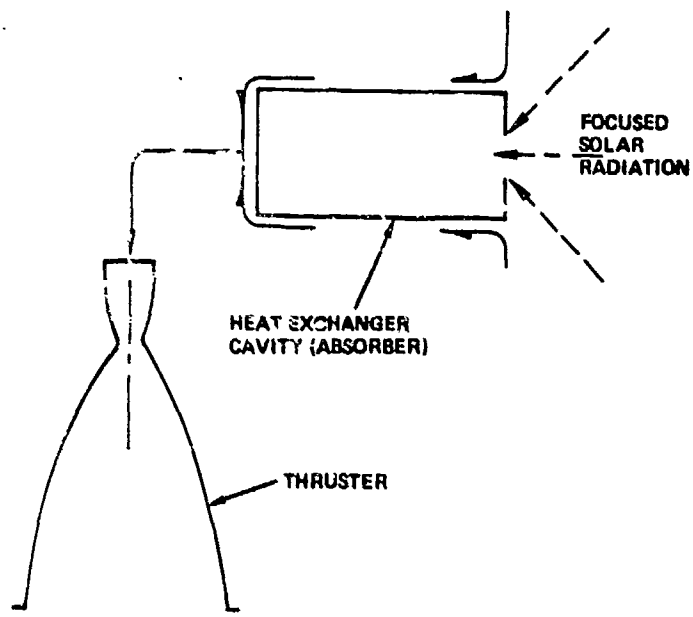

Figure 7. Windowless Heat Exchanger Cavity

Absorber Cavity Performance

Six windowless heat exchanger cavity configurations were evaluated in this study and are illustrated in Fig. 8. These configurations were chosen to encompass both simple and complex configurations. Complex geometric cavity configurations may yield the highest cavity efficiencies but may result in fabrication difficulty especially with the high temperature materials available for fabrication. Simple geometric cavity configurations offer easier fabrication but generally lower cavity efficiencies.

Using the method of analysis presented in Appendix A, the evaluation of the six windowless heat exchanger cavity configurations was conducted assuming the following surface conditions:

Internal wall emissivity:	0.3
Internal wall temperature:	1667 K(3000 R)
External wall emissivity:	0.05
External wall temperature:	533 K(960 R)

These parameters were assumed to provide an overall absorber efficiency for each configuration performance comparison. Although the internal and external wall temperatures will, in reality, vary dependent on the internal surface area, cooling approach, and cooling circuit, this initial screening analysis with representative fixed temperature values was performed to determine which cavity configuration offered the highest efficiency potential. Detailed thermal analyses were performed once the preferred cavity configuration was selected. The total absorber efficiency for each configuration was determined for various aperture area-to-internal surface area ratios (A_2/A_1), basic absorber diameters, and length-to-aperture radius ratios (β). For the spherical absorber, the length, L, is the diameter of the sphere. For absorber configurations consisting of a cavity and a disc, the heat absorbed by each section was combined to obtain the total absorber efficiency.

The calculated total absorber efficiencies for the six absorber configurations are presented in Fig. 9 through 11 for three different absorber diameters. For a majority of the configurations, an aperture area-to-internal surface area ratio (A_2/A_1) of 0.10 was assumed as a representative value in the

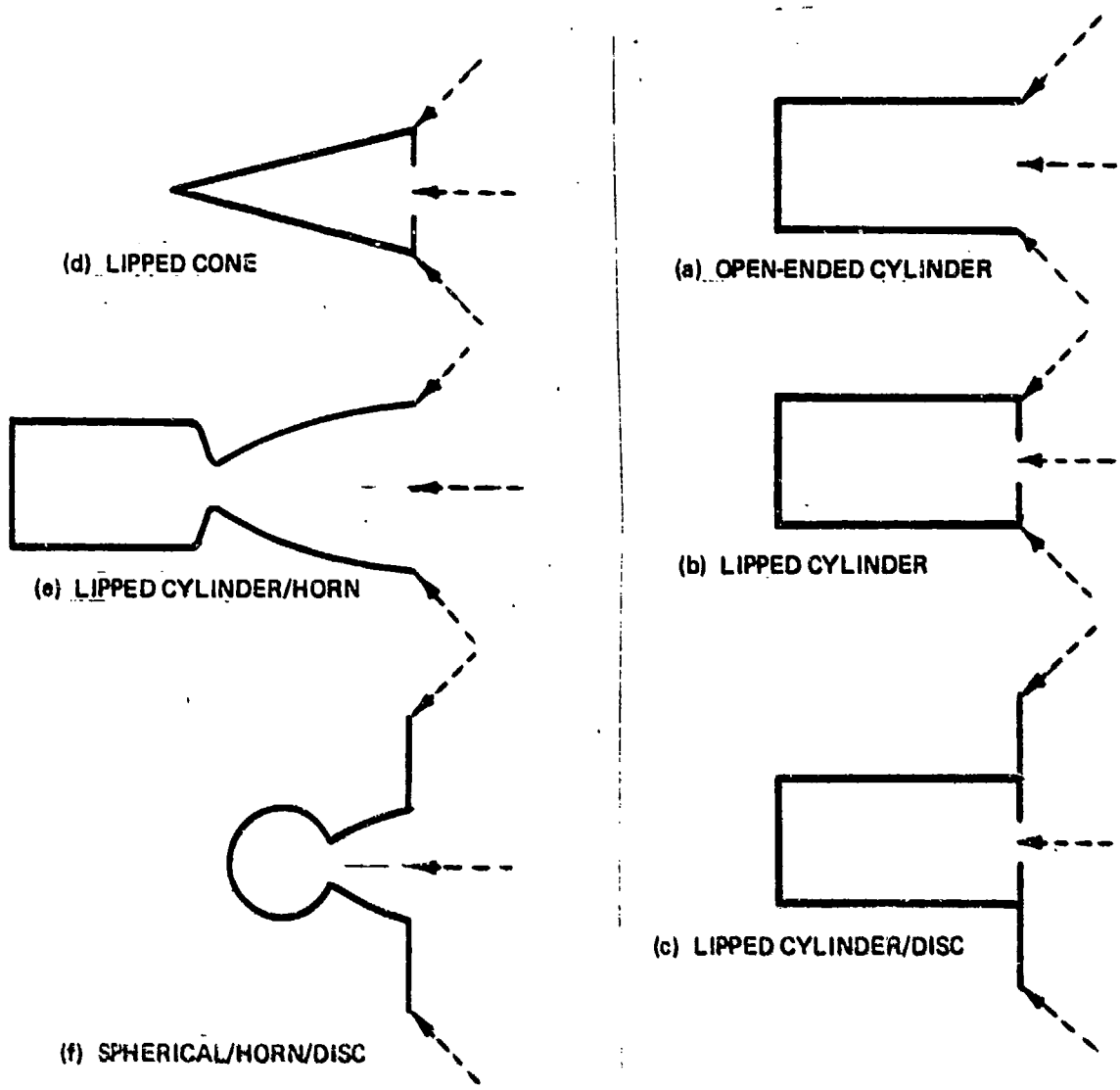

Figure 8. Candidate Windowless Cavity Absorber Configurations

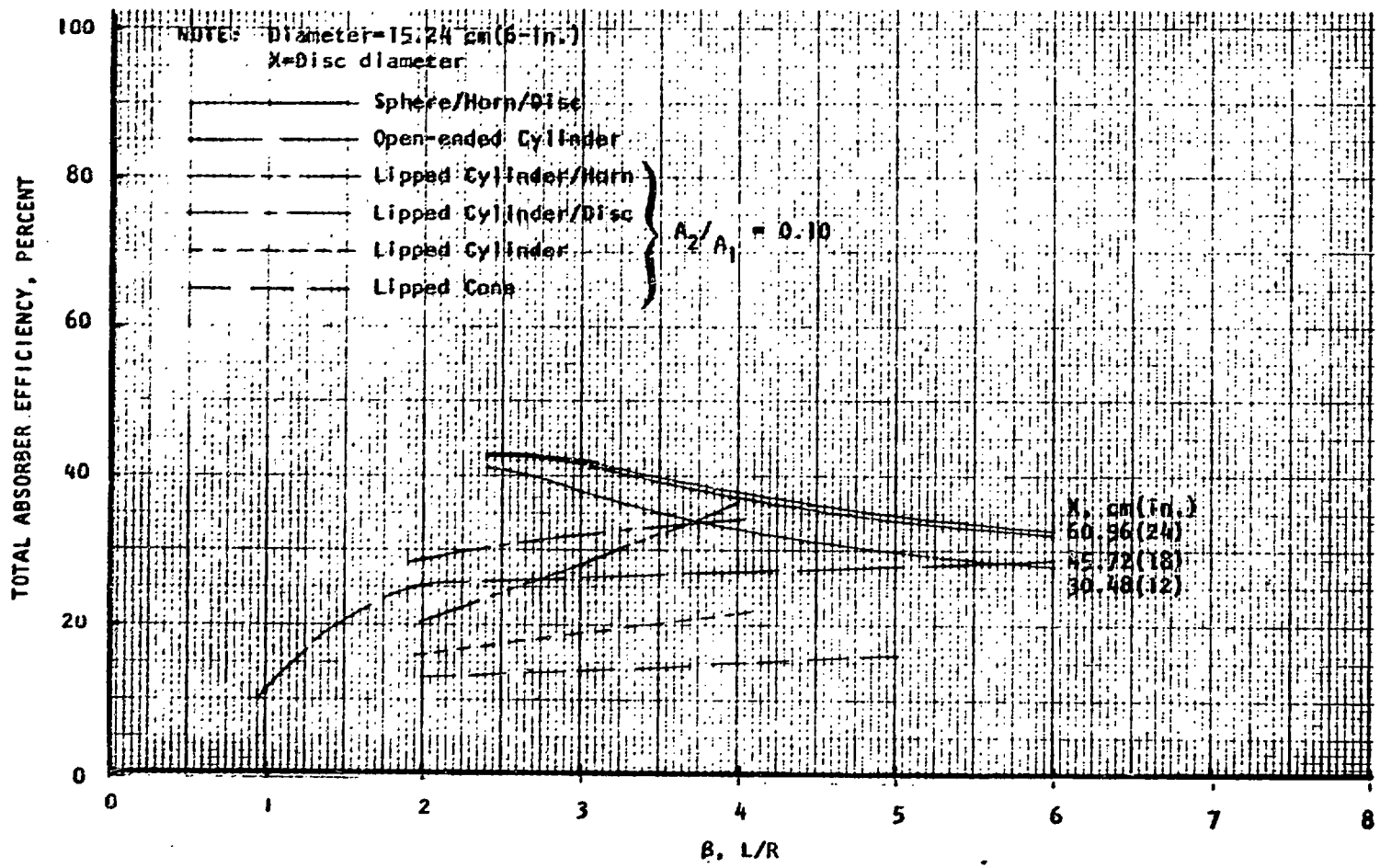

Figure 9. Windowless Heat Exchanger Cavity Absorber Total Efficiency for Different Absorber Configurations (Diameter = 15.24 cm or 6 inches)

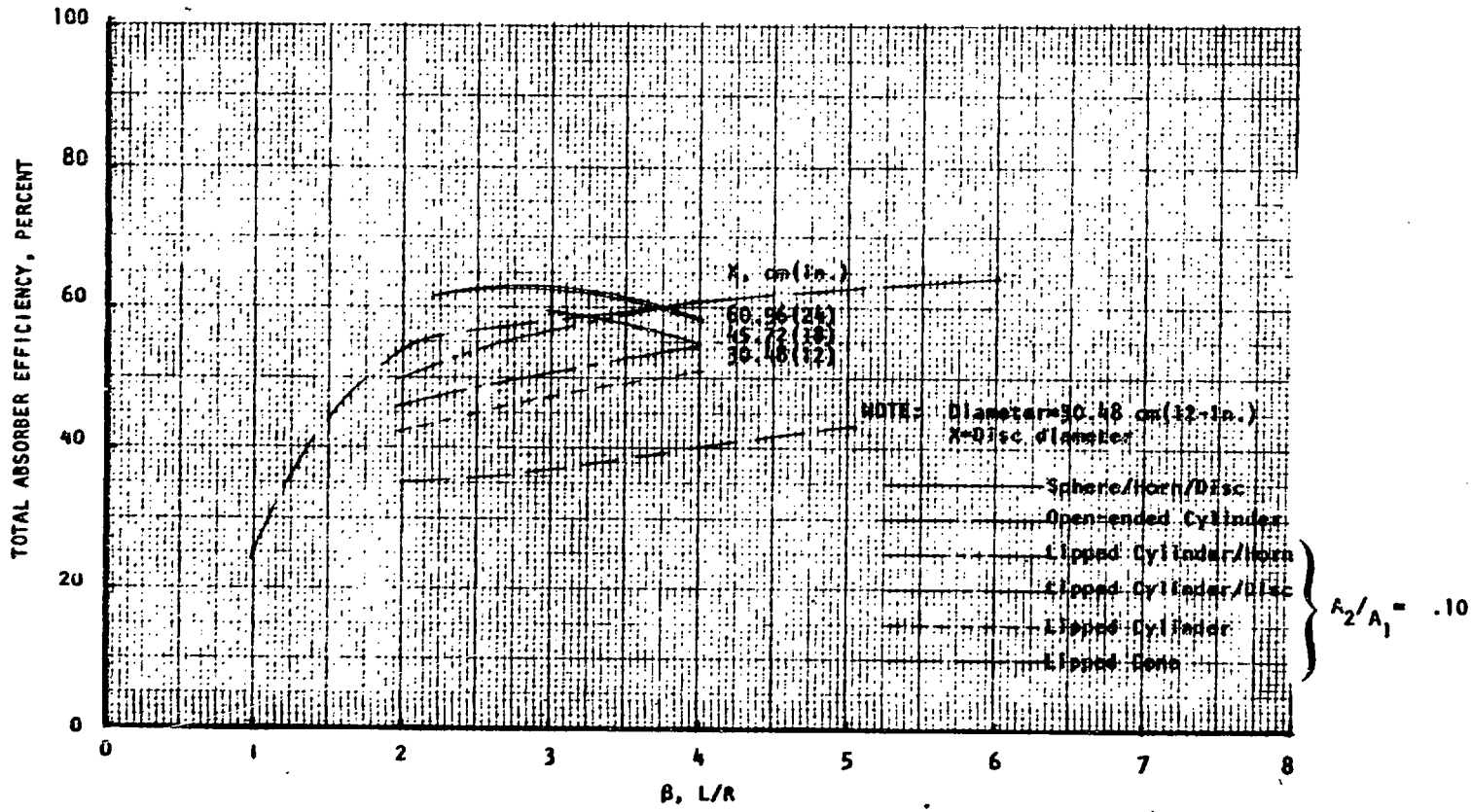

Figure 10. Windowless Heat Exchanger Cavity Absorber Total Efficiency for Different Absorber Configurations (Diameter = 30.48 cm or 12 inches)

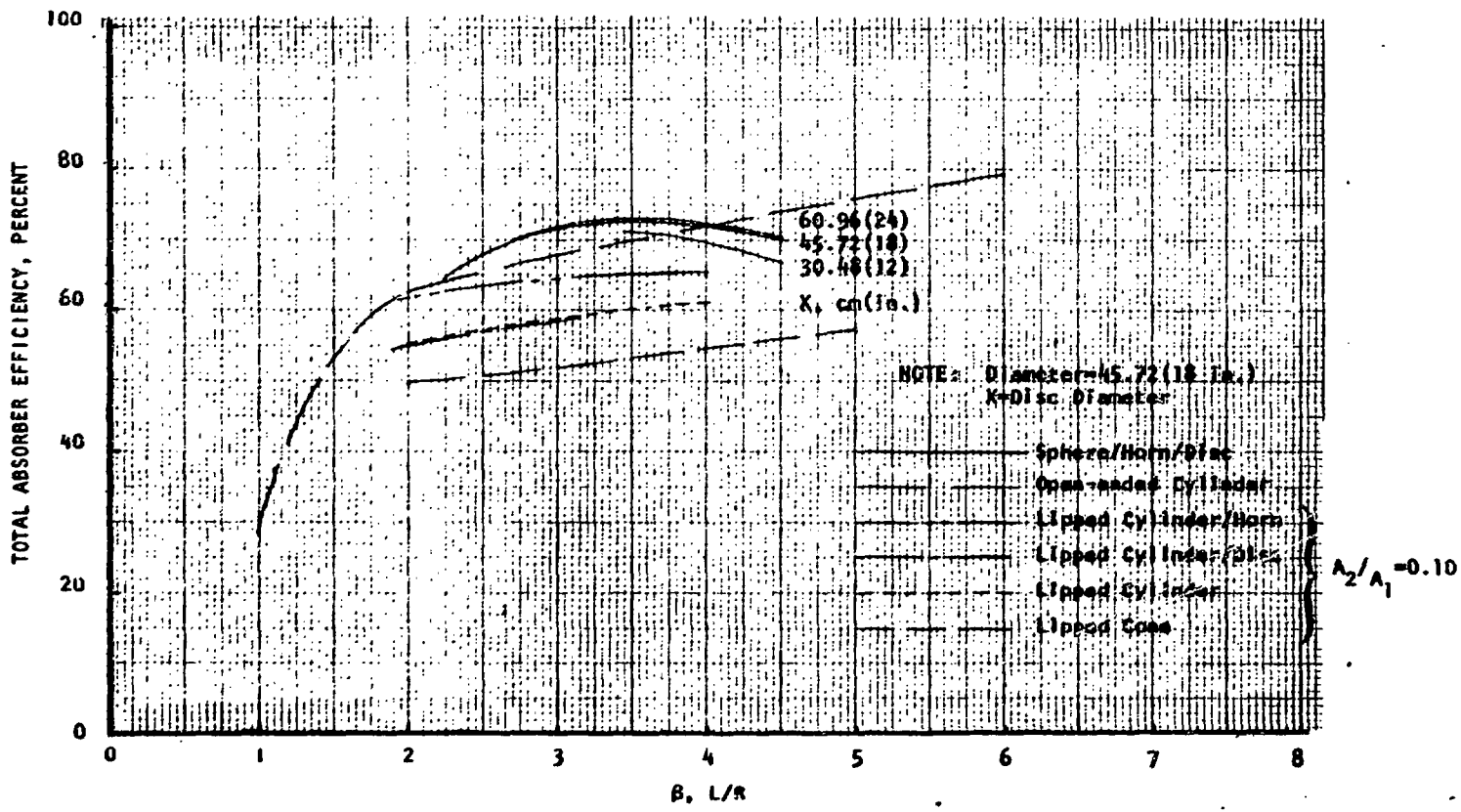

Figure 11. Windowless Heat Exchanger Cavity Absorber Total Efficiency for Different Absorber Configurations (Diameter = 45.72 cm or 18 inches)

data presented. As shown in Fig. 9 through 11, the sphere/horn/disc absorber configuration generally achieved the highest total efficiencies. For the 15.24 cm (6-inch) basic absorber diameter (not including disc), the lipped cylinder/disc achieved the second highest efficiency with the lipped cylinder/horn configuration third and the open-ended cylinder a close fourth. The lipped cone absorber configuration resulted in the lowest efficiency of the six configurations.

As the basic absorber diameter was increased, the total efficiencies of all absorber configurations increased and the open-ended cylinder configuration achieved the second highest total absorber efficiency with the lipped cylinder/horn a close third. Although the disc can intercept more of the incoming solar radiation, it has a high view factor and therefore poor efficiency. In fact, adding a horn to the lipped cylinder at larger absorber diameters resulted in higher total efficiencies than adding a disc.

The efficiency of the disc portion of the absorber configurations incorporating a disc is limited by the surface emissivity. A high emissivity will increase the the efficiency of the disc portion and therefore will increase the total absorber efficiency. For this comparative analysis, a surface emissivity of 0.3 was assumed for the cavity interior and the disc. The open-ended cylinder intercepts more radiation than the lipped cylinder configurations and results in a higher total absorber efficiency. Also the larger basic absorber diameters tend to intercept more radiation and as a result achieve higher total efficiencies.

Total absorber efficiencies exceeding 70% were achieved with the 45.72 cm (18-inch) sphere/horn/disc and with the open-ended cylinder. At this basic absorber diameter, the sphere/horn/disc configuration achieved a maximum of 4% higher efficiency than the open-ended cylinder configuration. The simple geometric configuration of the open-ended cylinder is, however, attractive compared to the more complex configuration of the sphere/horn/disc absorber.

As the cavity length-to-aperture radius ratio (B) is increased for the sphere/horn/disc for a fixed sphere diameter, the aperture is being reduced and, therefore, the amount of radiation intercepted by the sphere/horn portion decreases but the radiation intercepted by the disc portion increases. The

efficiency of the disc portion of this absorber configuration is less than that of the sphere/horn portion. Therefore, as ß is increased, the heat absorbed by the respective portions of the sphere/horn/disc absorber results in an optimum total efficiency. The net result for the 30.48 cm (12-inch) and 45.72 cm (18-inch) diameter sphere was that a maximum total absorber efficiency occurred at a ß of 3.0 and 3.6, respectively. However the total efficiency variation with ß was relatively flat near the maximum efficiency value.

For the open-ended cylinder absorber configuration, a larger ß for a fixed absorber diameter resulted in a lower cavity view factor and as a result the total efficiency increased with increase in ß.

For the windowless absorber/thruster concept, a 5% lower total absorber efficiency (65% instead of 70%) can result in a 7% lower thrust if the final propellant temperature is fixed at 2778 K (5000 R) by reducing the propellant flowrate or a 3.5% lower specific impulse and thrust if the propellant flowrate is fixed.

Since the absorber/thruster concept can require a high-density expensive wall material due to the high temperatures involved, another important consideration is the amount of material required for each absorber configuration. The absorber surface area required to achieve a certain total efficiency would provide an indication of this trend and was determined as shown in Fig. 12 and 13 for the sphere/horn/disc and the open-ended cylinder absorber configurations. A lower surface area is desirable up to a point. If the absorber surface area is reduced to a condition in which the average cavity heat flux presents a cooling problem, the surface area is too low.

As shown in Fig. 12 and 13 (30.48 cm or 12-inch basic diameter), the lipped cone absorber configuration resulted in the lowest surface area but also resulted in the lowest total absorber efficiency. The surface area of the lipped cylinder configurations was approximately the same as the open-ended cylinder; however the open-ended cylinder achieved slightly higher absorber efficiencies. The sphere/horn/disc absorber configuration with a 30.48 cm (12-inch) disc obtained essentially the same surface area and efficiency as the open-ended cylinder. For the sphere/horn/disc absorber configuration, increased total absorber efficiency was achieved with increased disc diameter;

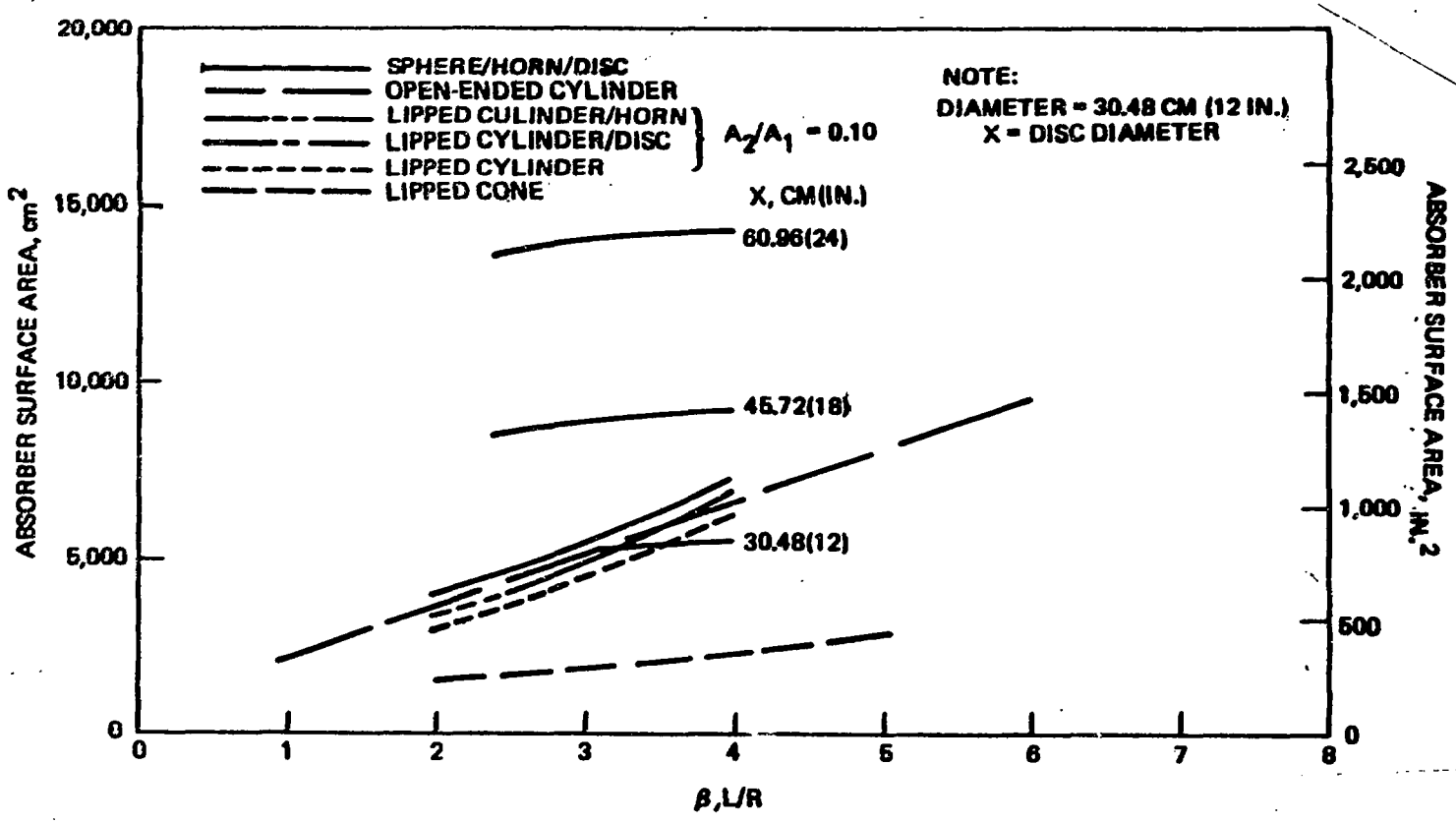

Figure 12. Windowless Heat Exchanger Cavity Absorber Surface Area for Different Absorber Configurations (Diameter = 30.48 cm or 12 inches)

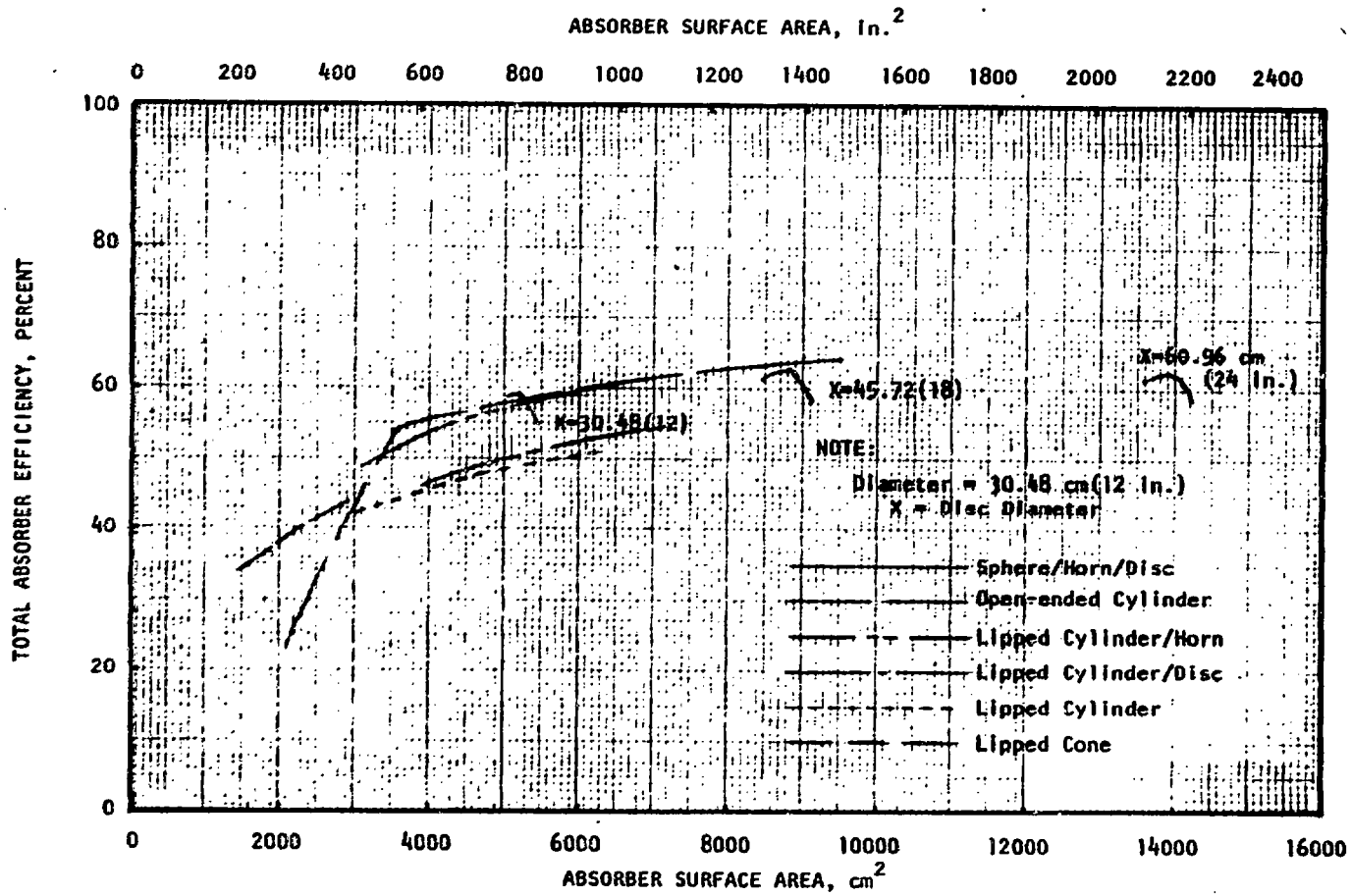

Figure 13. Windowless Heat Exchanger Cavity Absorber Efficiency Variation with Surface Area (Diameter = 30.48 cm or 12 inches)

however, as shown in Fig. 13 a significant surface area increase was required (approximately a 70% surface area increase for a 3% efficiency improvement). This is primarily due to the low efficiency of the annular disc configuration.

Based on the above analyses and considerations of total efficiency, surface area and fabrication ease, the sphere/horn/disc and open-ended cylinder were judged the most promising windowless heat exchanger cavity absorber/thruster concepts and were carried into the following heat transfer and performance analysis. The larger diameter configurations achieved higher efficiencies, therefore the analyses were continued on the 30.48 cm (12-inch) and the 45.72 cm (18-inch) assemblies.

Cavity Heat Transfer

Detailed heat transfer analysis of two open-ended cylindrical cavity absorber configurations were performed to evaluate cooling feasibility (wall temperature and hydrogen pressure drops). The two absorber configurations (Table 1) represent two different sizes (30.48 cm/12-inch diameter and 45.72 cm/18-inch diameter. The large diameter absorber achieved a higher absorber efficiency (71.8% compared to 60.8%) and a 0.24% higher delivered specific impulse and an 18.34% higher thrust.

The tube wall and hydrogen bulk temperature distributions for a coiled tube configuration are shown in Fig. 14 for the 30.48 cm/12-inch diameter absorber. For a hydrogen temperature of approximately 2778 K (5000 R), the radiation side tube wall temperature was approximately 83 K (150 F) higher than the fluid temperature. The absorber hydrogen pressure drop for the 246.4 cm (97-inch) tube coil was 24N/cm^2(34.8 psi) as shown in Fig. 15. For 45.72 cm (18-inch) diameter absorber configuration, the tube wall temperature was 50 K (90 F) higher than the hydrogen exit temperature and the hydrogen pressure drop was 27.6N/cm^2(40 psi). The lower temperature differential (T_{wall} T_{bulk}) of the larger diameter absorber was due to the lower average heat flux (larger absorber surface area).

This heat transfer analysis indicated that if the maximum tube wall temperature was limited to 2778 K (5000 R), hydrogen temperatures of 2694 K (4850 R) to 2728 K (4910 R) can be achieved with hydrogen absorber pressure drops of only 24N/cm^2(35 psi).

TABLE 1. CAVITY HEAT TRANSFER ANALYSIS SUMMARY

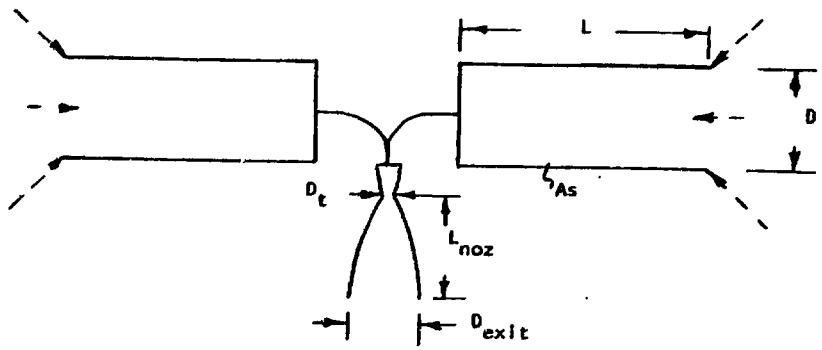

ε=100
90% length

DESIGN	L, cm (in.)	D, cm (in.)	A_s, cm^2 ($in.^2$)	$(q/A)_{avg}$, watts/cm^2 (BTU/in.^{2} sec)	$\dot{m}_{H_2}$, K_g/sec (lb/sec)	$\eta_{absorber}$	$I_{s\,del}$, Nsec/Kg ($\frac{lb_f sec}{lbm}$)	F, N (lb_f)	Number of Tubes	D_t, cm (in.)	L_{noz}, cm (in.)	D_{exit} cm (in.)	
1	60.96 (24)	30.48 (12)	6567.1 (1017.9)	77.20 (0.4724)	0.0104 (0.0229)	0.6082	8543.8 (871.22)	177.26 (39.85)	100	2.008 (0.791)	30.58 (12.04)	20.08 (7.91)	
2	91.44 (36)	45.72 (18)	14775.4 (2290.2)	40.51 (0.2479)	0.0123 (0.0270)	0.718	8564.3 (873.31)	209.78 (47.16)	150	2.182 (0.859)	33.25 (13.09)	21.82 (8.59)	

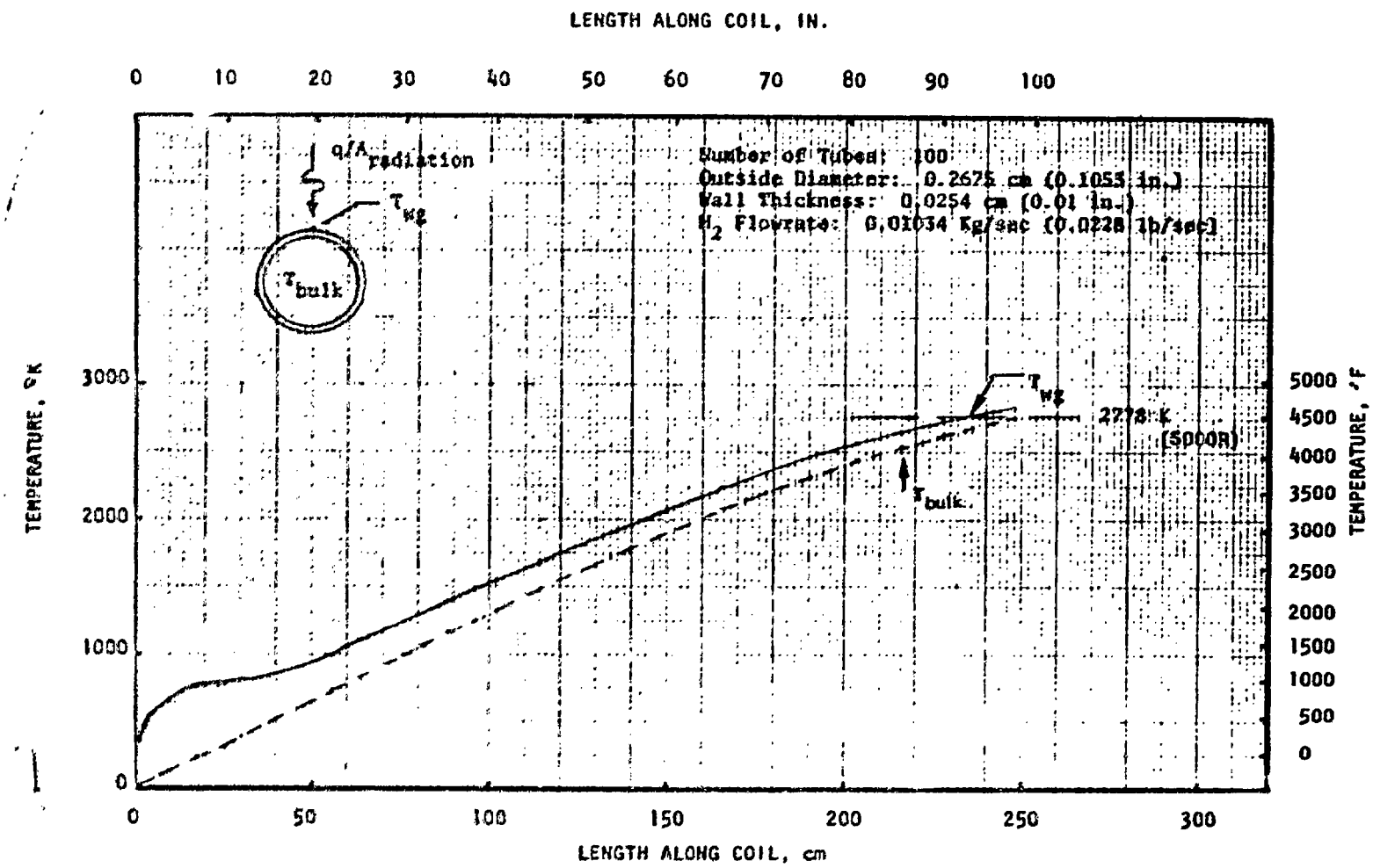

Figure 14. Coiled Tube Windowless Heat Exchanger Cavity Tube Temperature (Diameter = 30.48 cm or 12 inches)

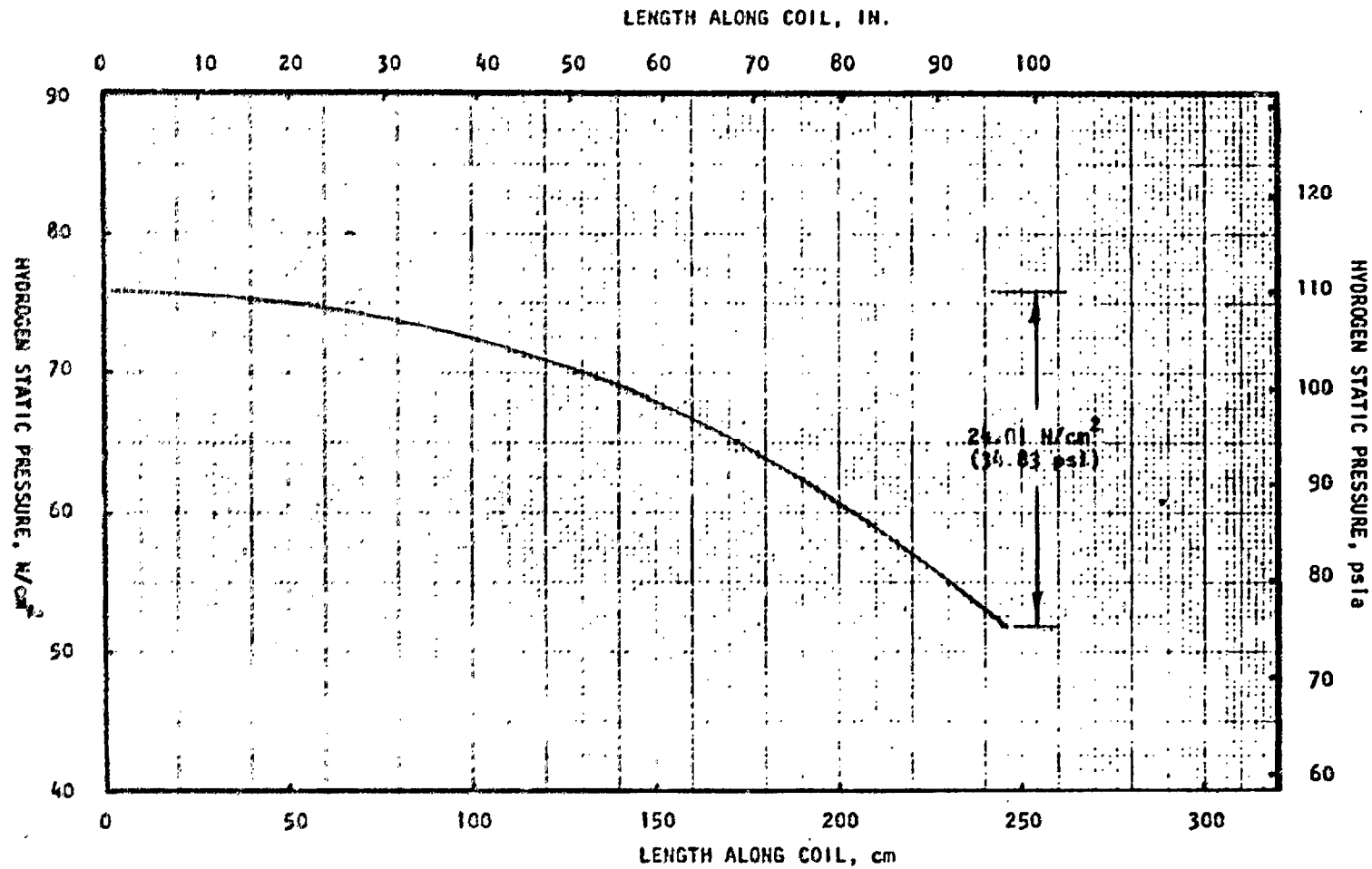

Figure 15. Coiled Tube Windowless Heat Exchanger Cavity Static Pressure (Diameter = 30.48 cm or 12 inches)

Thruster Performance

The thruster performance was determined utilizing the simplified JANNAF procedure (Ref. 2) and included the nozzle geometric or two-dimensional loss, the boundary layer loss, and the reaction kinetic loss. The nozzle geometric loss (two-dimensional loss) is associated with nonaxial flow uniformity at the nozzle exit plane. The boundary layer loss accounts for the viscous loss and boundary layer heat loss encountered in cooling. The reaction kinetic loss results from changes in pressure and temperature as the high temperature gas expands through the nozzle and the lag in gas composition in responding the associated change in equilibrium.

The delivered specific impulse (Fig. 16 and 17) were computed for a 30.48 cm (12-inch) diameter open-ended cylinder and a sphere/horn/disc absorber for the following design conditions:

T_{H_2} = 2778 K (5000 R)

P_c = 34.47 N/cm^2 (50 psia)

ε = 100-to-1

As discussed in the Materials and Fabrication section, the upper temperature limit for available materials is approximately 2778 K (5000 R) and, therefore, this value was selected for this concept evaluation. In Ref. 1, the influence of chamber pressure (Pc) was investigated and indicated that the theoretical specific impulse increase from 50 to 100 psi chamber pressure was not significant and, therefore, to reduce the impact of system pressure, a value of 50 psi was chosen.

The thruster performance analysis for the two absorber configurations was performed for a fixed final hydrogen temperature of 2778 K (5000 R) to achieve the maximum thruster performance within wall material temperature limitations. As shown previously, varying β resulted in a varying absorber efficiency that changed the heat absorbed. To maintain the same final hydrogen temperature, the hydrogen flowrate was varied. This flowrate variation resulted to a varying thruster size, thrust, and specific impulse.

As shown in Fig. 16, delivered specific impulses exceeding 8530 N sec/k (870 lbf sec/lb) were achieved. The delivered specific impulse of the open-ended cylinder and the sphere/horn/disc absorber were approximately the same for cavity length-to-aperture ratios (ß) greater than two. The thrust of these windowless absorber/thrusters is presented in Fig. 17. With two absorbers on one thruster, a thrust level of approximately 178 N (40 lbf) was obtained.

Although the performance potential of the two concepts was comparable, the open-ended cylinder concept was judged the more attractive candidate based on fabrication considerations and was selected for further analysis.

For the open-ended cylinder absorber/thruster configuration, the delivered specific impulse and thrust variation with ß (L/R) and the cylinder diameter were determined for a final hydrogen temperature of 2778 K (5000 R), a chamber pressure of 34.47 N/cm^2 (50 psia), and a nozzle area ratio of 100-to-1. As shown in Fig. 18 and 19, the delivered specific impulse and thrust increased rapidly with increase in ß until a ß of approximately 2, then leveled off. As the cylinder diameter was increased, the amount of heat absorbed increased and for a fixed final hydrogen temperature the thrust increased (Fig. 19). The increase thrust reduced the boundary layer and reaction kinetic loss and the delivered specific impulse increased approximately 1.6 percent.

The influence of the final hydrogen temperature on the delivered specific impulse and thrust for the open-ended cylinder absorber/thruster configuration are presented in Fig. 20 and 21 for a chamber pressure of 34.47 N/cm^2 (50 psia) and a nozzle area ratio of 100-to-1. As expected, as the final hydrogen temperature was increased from 1667 K (3000 R) to 2778 K (5000 R), the delivered specific impulse increased approximately 30% and the thrust decreased approximately the same amount. From the relationship,

$$I_s \propto \sqrt{\frac{T}{M}}$$

The delivered specific impulse will increase as the gas temperature is increased. In addition, as the hydrogen dissociates at the higher temperatures, the accompanying decrease in molecular weight adds to the rate of specific impulse increase with temperature.

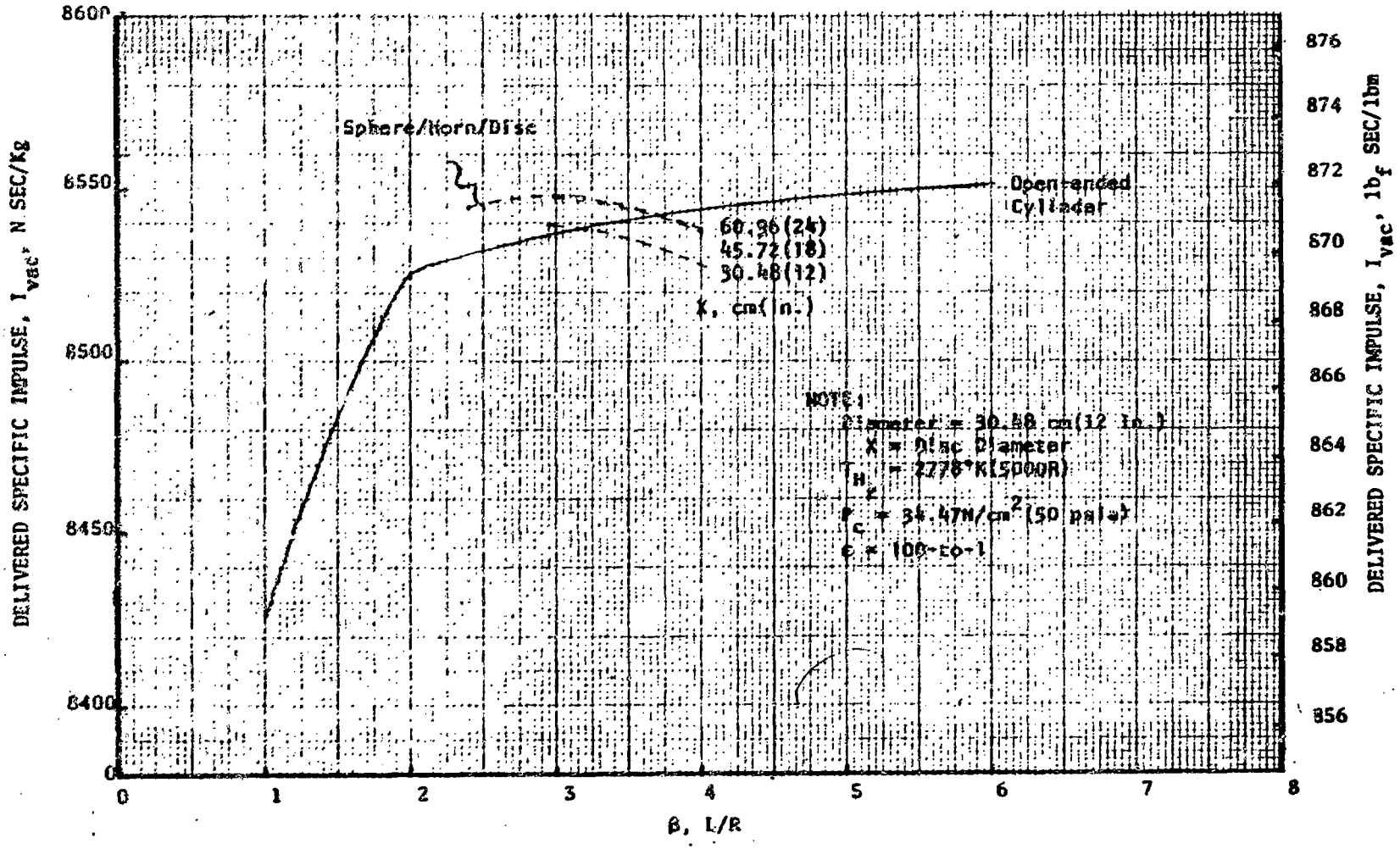

Figure 16. Delivered Specific Impulse for Open-ended Cylinder and Sphere/Horn/Disc Absorber Configurations (Diameter = 30.48 cm or 12 inches)

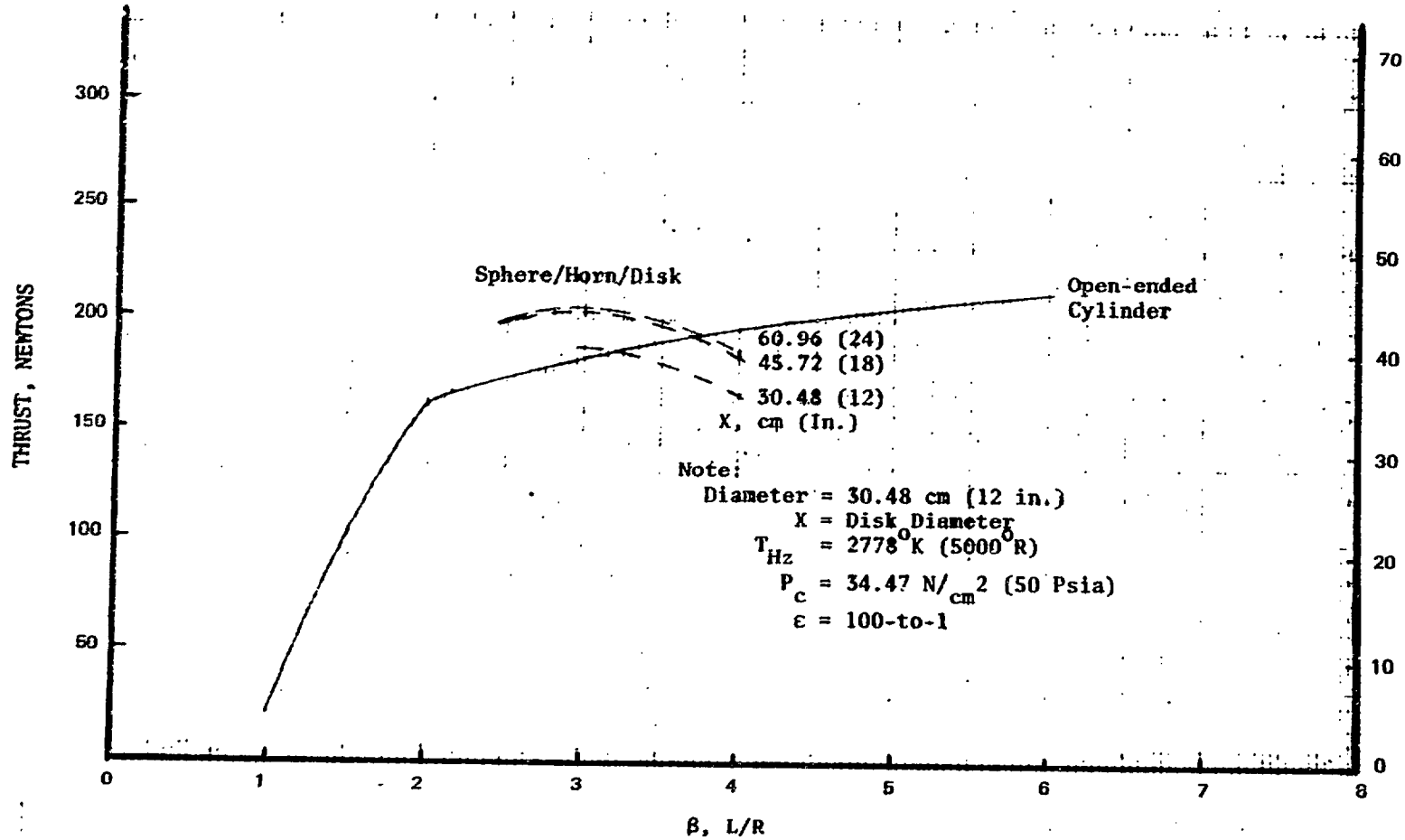

Figure 17. Delivered Thrust for Open-ended Cylinder and Sphere/Horn/Disc Absorber Configurations (Diameter = 30.48 cm or 12 inches)

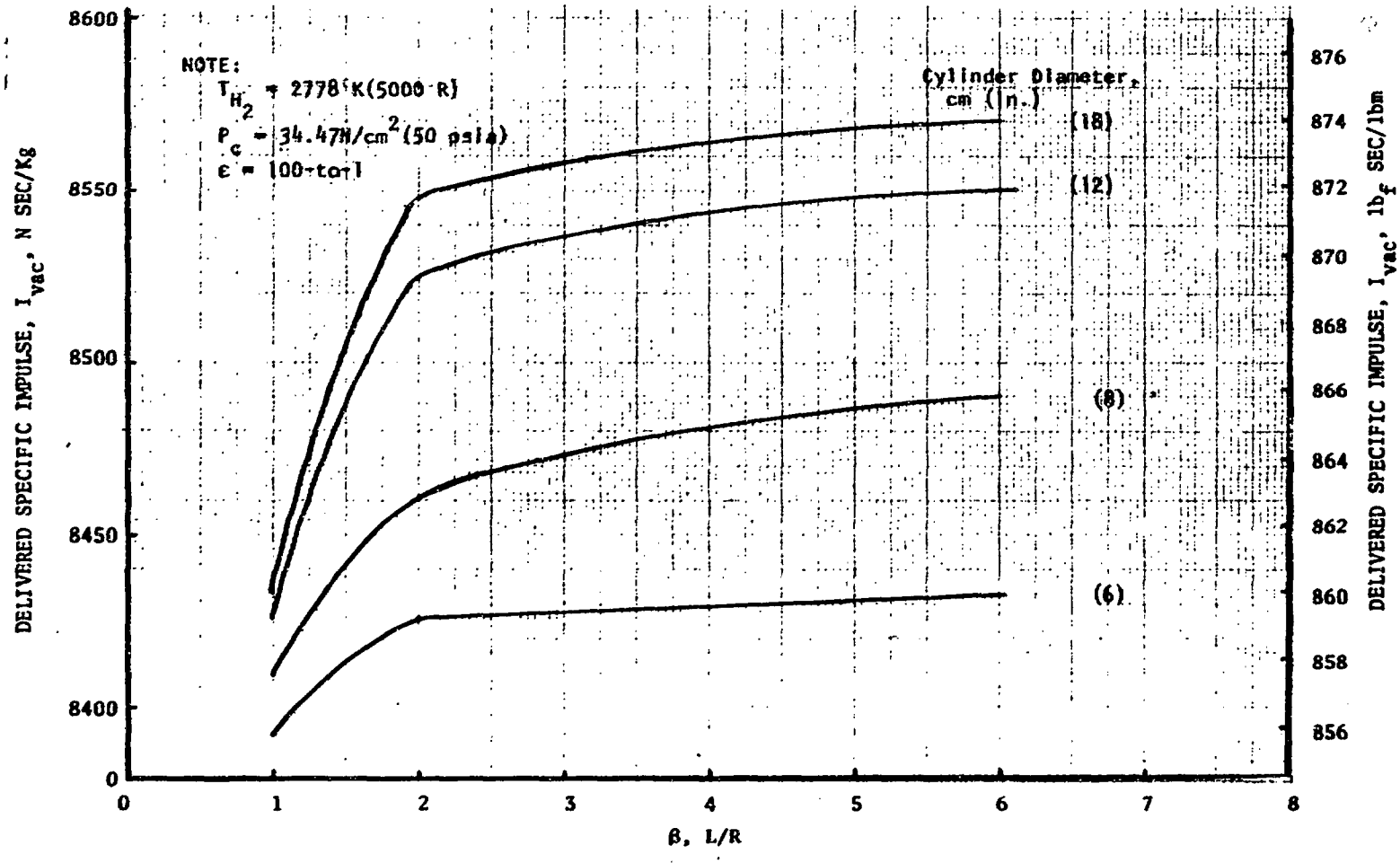

Figure 18. Delivered Specific Impulse for the Open-ended Cylinder Absorber Configuration

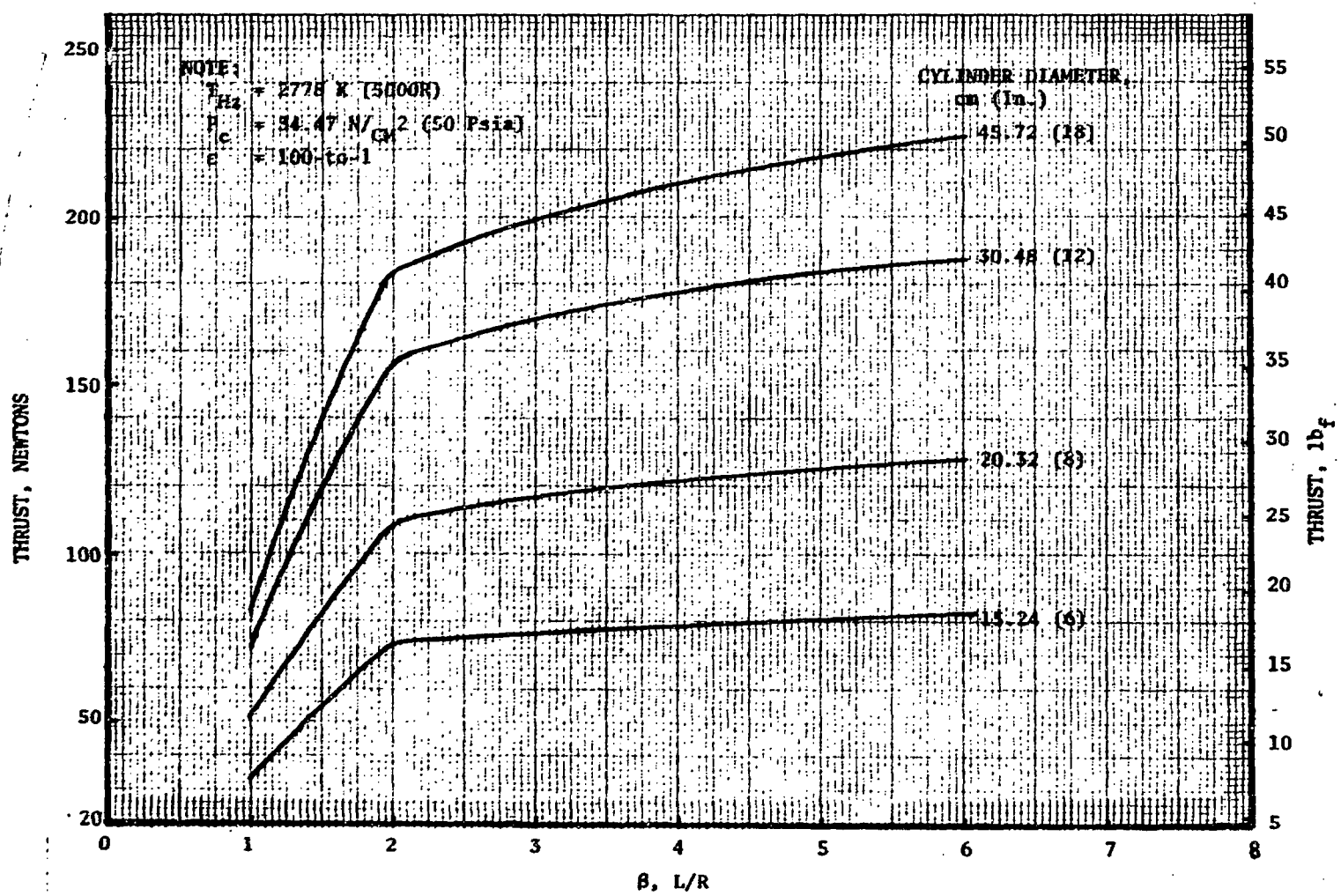

Figure 19. Deliver Thrust for the Open-ended Cylinder Absorber Configuration

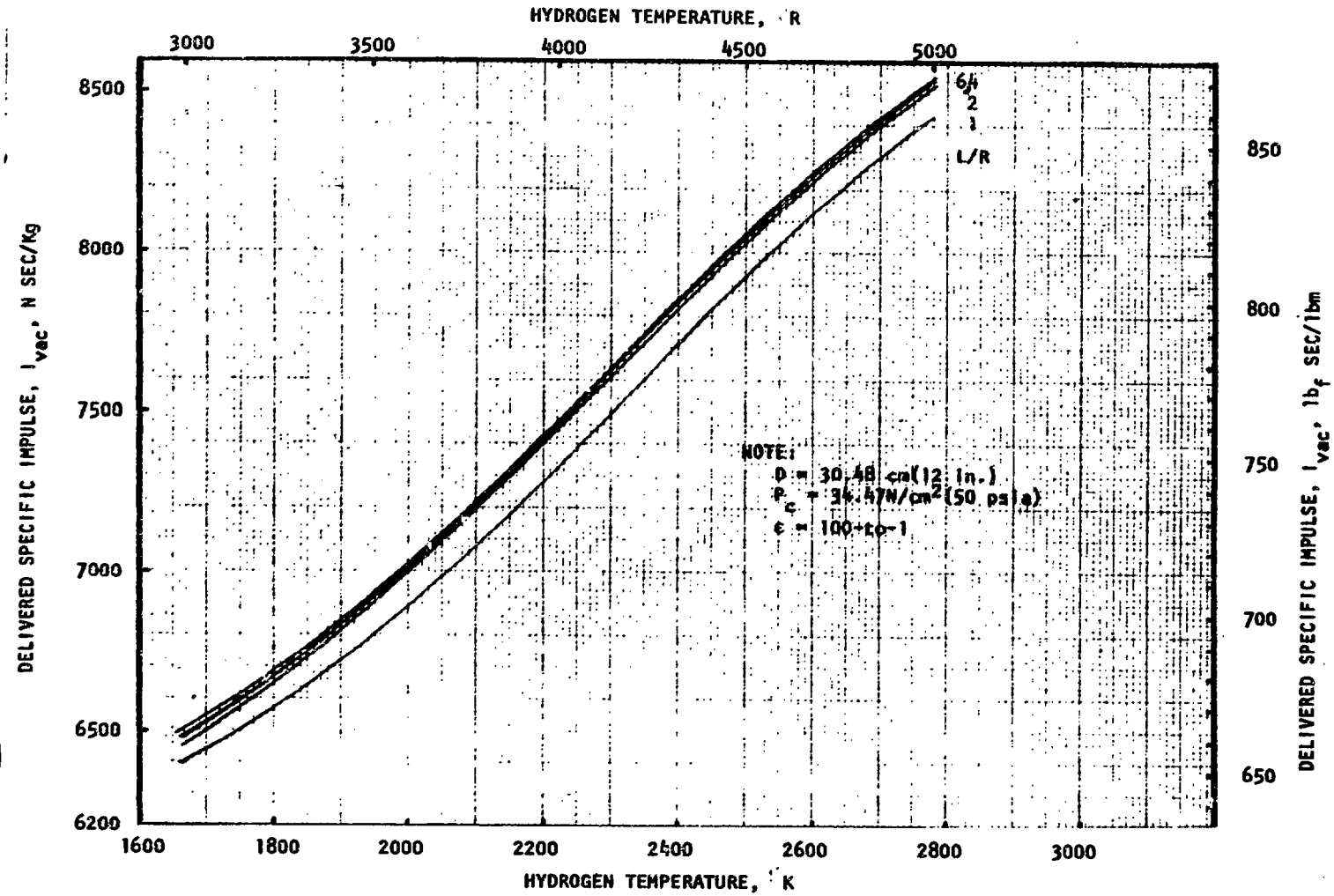

Figure 20. Delivered Specific Impulse Variation with Hydrogen Temperature for an Open-ended Cylinder (Diameter = 30.48 cm or 12 inches)

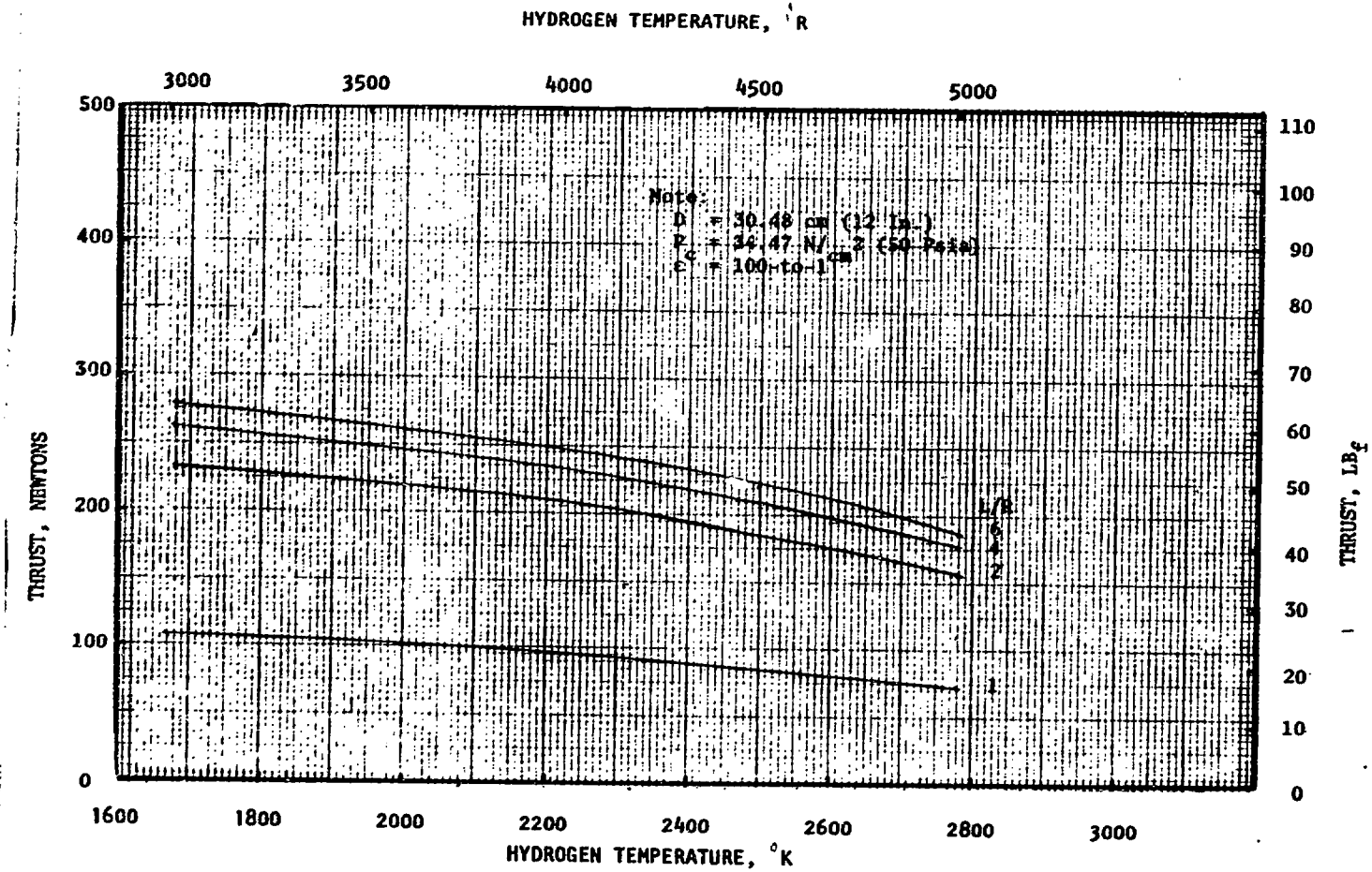

Figure 21. Thrust Variation with Hydrogen Temperature for an Open-ended Cylinder (Diameter = 30.48 cm or 12 inches)

From the relationship,

$$F \propto \Delta Q \sqrt{\frac{M}{T}}$$

The engine thrust will decrease with increase in temperature and the corresponding decrease in molecular weight (Fig. 21). The cavity length-to-aperture ratio (S or L/R) did not significantly influence the delivered specific impulse but the thrust increased with S.

Cavity Absorber Life

Based on tube material evaluation (presented in the Materials and Fabrication Assessment), rhenium was determined to be the most promising tube material. Considering the creep rupture strength of rhenium, the variation of the time to rupture with temperature was determined for two tube sizes and two internal tube pressures (34.5 N/cm^2 (50 psi) and 68.9 N/cm^2 (100 psi). As shown in Fig. 22, absorber life values in the range of 200 to 500 hours were achieved near the maximum wall temperature limit of 2777.8 K (5000 R).

Concept Evaluation Summary

The results of the windowless heat exchanger cavity absorber/thruster concept evaluation are summarized as follows:

• Absorber Performance	>60% efficiency (open-ended cylinder or sphere/horn/disc)
• Delivered Specific Impulse	Up to 7926.6 N sec/kg (870 lbf sec/lbm) (ϵ = 100)
• Thrust	89 to 222 N (20 to 50 lbf)
• Cooling	Feasible [$T_{wall} \leq$2777.6 K (5000 R)] with 24.1 N/cm^2 (35 psi) pressure drop using coiled tube approach
• Limitation	$TH_2 \leq$2727.6 K (4910 R) (material temperature limit) [limits I_{sp}]
• Other Features	No seedant No window No moving parts No leakage No performance loss due to window cooling

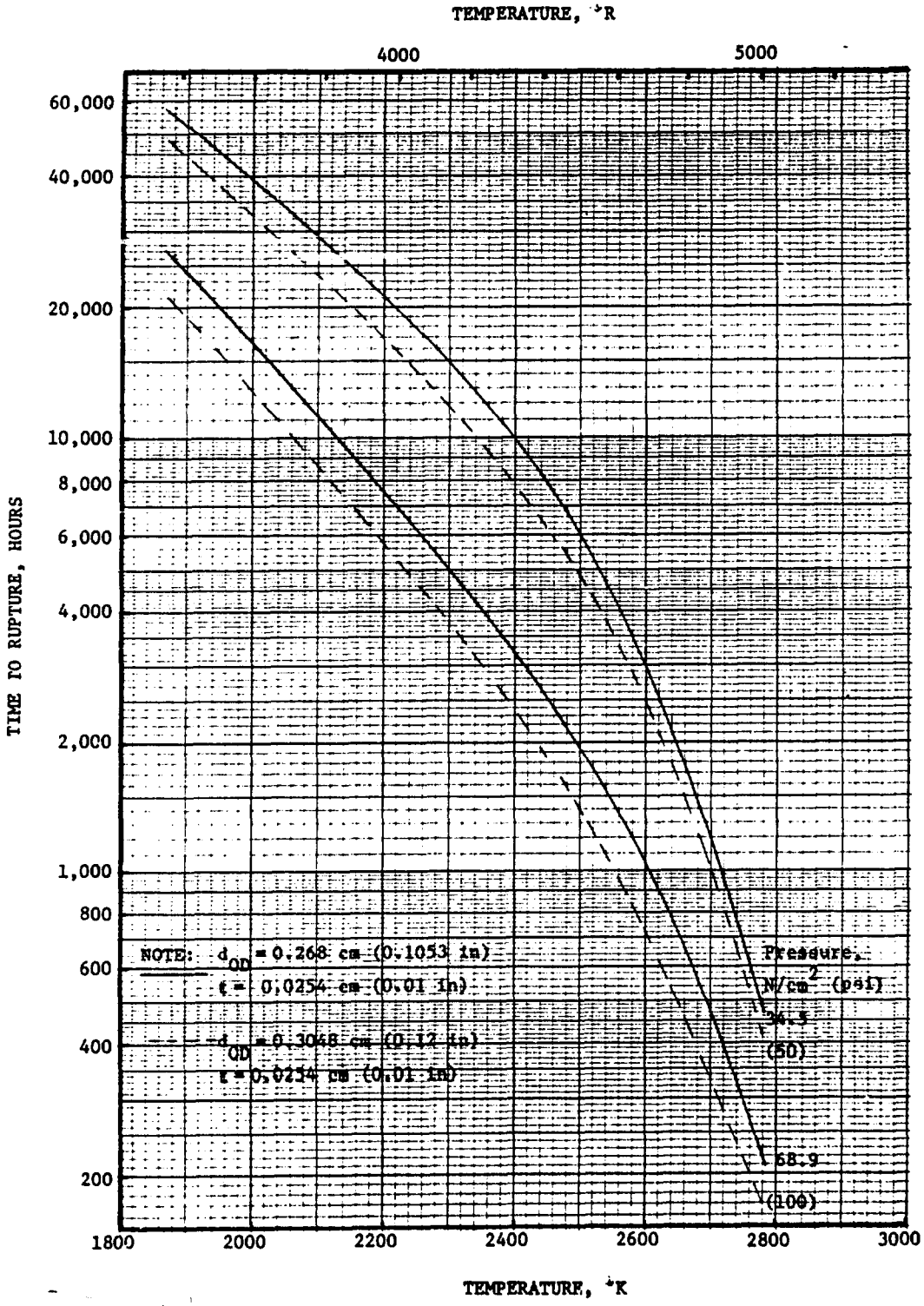

Figure 22. Stress Rupture Life Variation with Temperature for Rhenium

Absorber/Thruster Conceptual Design

Based on the open-ended cylindrical absorber/thruster thermal analysis, conceptual designs for the 30.48 cm (12-inch) diameter absorber configuration and the 45.72 cm (18-inch) diameter absorber configuration were prepared. As shown in Fig. 23 and 24, both these absorber designs incorporated a multitube coil (rhenium tubes). Only one of the two identical absorbers for each absorber/thruster configuration is shown. The 30.48 cm (12-inch) diameter absorber had a brazed rhenium disc for the cylinder bottom whereas the 45.72 cm (18-inch) diameter absorber incorporated a hemispherical configuration with a smaller disc which was cooled prior to the main coils. Both designs had a carbon block housing with a coiled tube discharge to permit thermal growth.

WINDOWED HEAT EXCHANGER CAVITY CONCEPT

The overall performance characteristics of the windowed heat exchanger cavity absorber/thruster concepts were determined similarly to that of the windowless absorber/thruster concepts. The influence of the absorber window was determined and included in the absorber analysis.

Configuration Definition

The propellant heating principle of the windowed heat exchanger concept is similar to that of the windowless heat exchanger concept. However, in the windowed version (Fig. 25) the heated porous liner is only subjected to a modest pressure differential, therefore the high temperature material strength characteristics required will be reduced. Incorporation of the window, however, adds other problems such as window cooling and energy loss through the window.

Evaluation of the absorber configuration of the windowed concept considered two absorbers with one thruster as the specified configuration. Two basic absorber configurations were considered as shown in Fig. 25. Configuration A incorporates a plate between the two porous liners which would add strength to the porous liner subassembly and could be contoured to provide a certain amount of flow control. However, the plate would tend to absorb and reflect

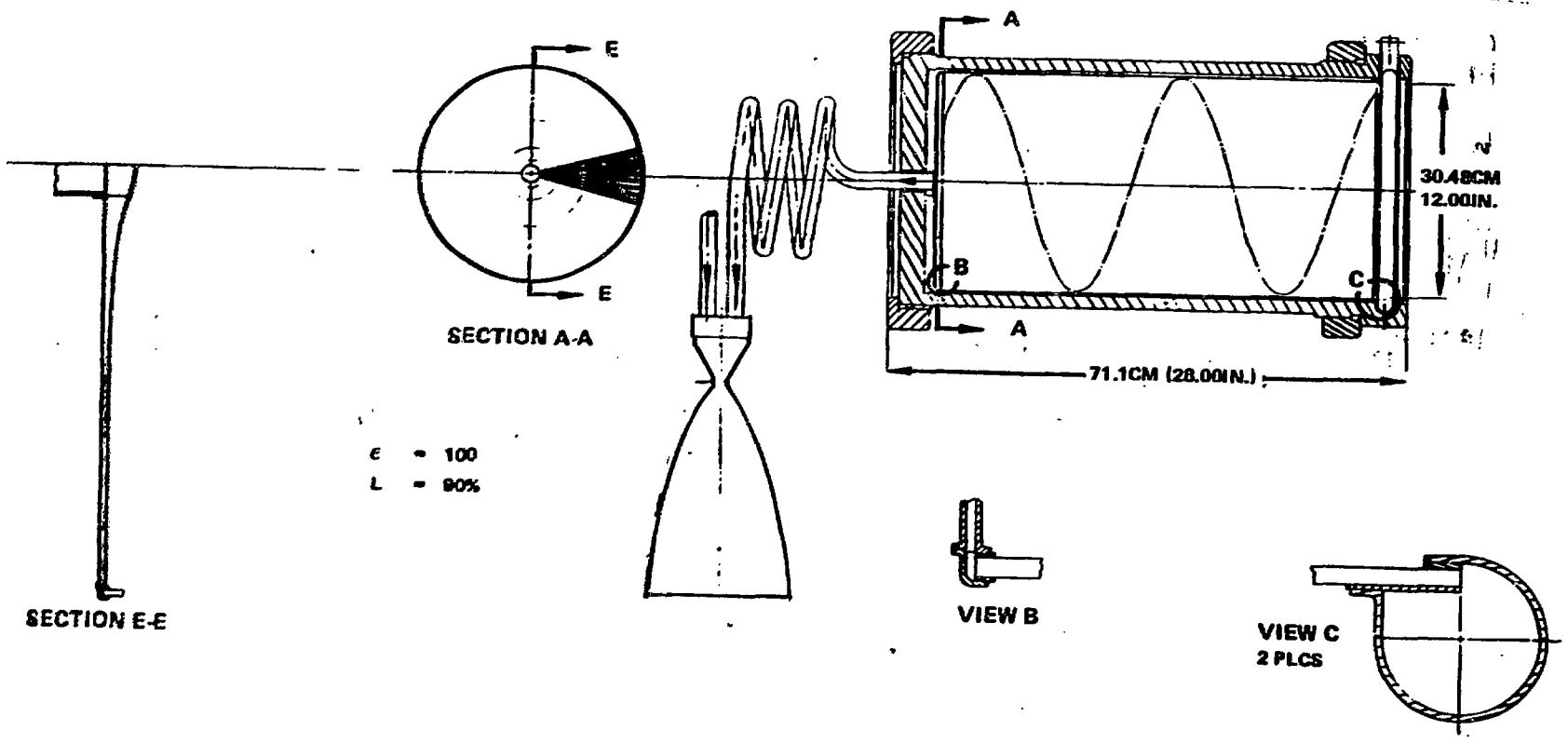

Figure 23. 12-inch Diameter Absorber/Thruster

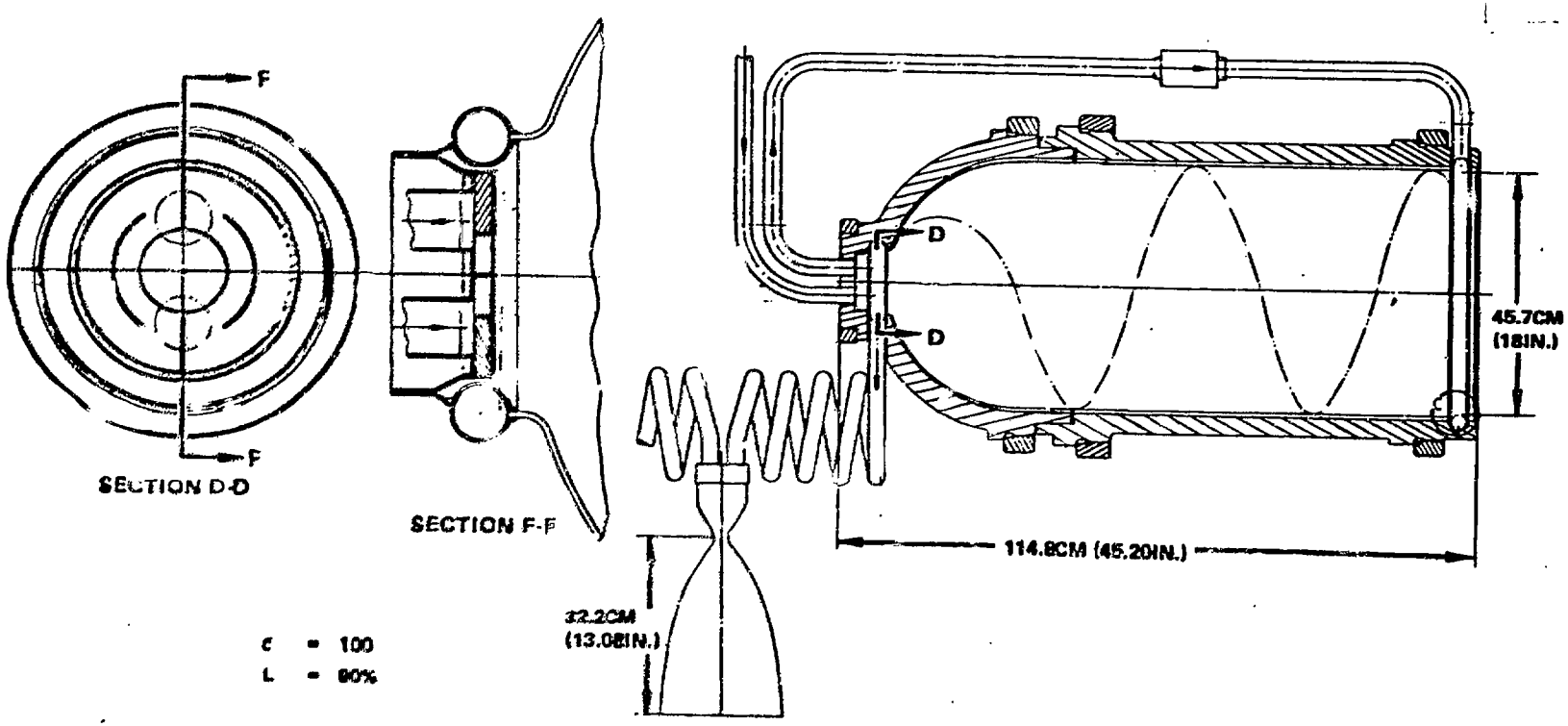

Figure 24. 18-inch Diameter Absorber/Thruster

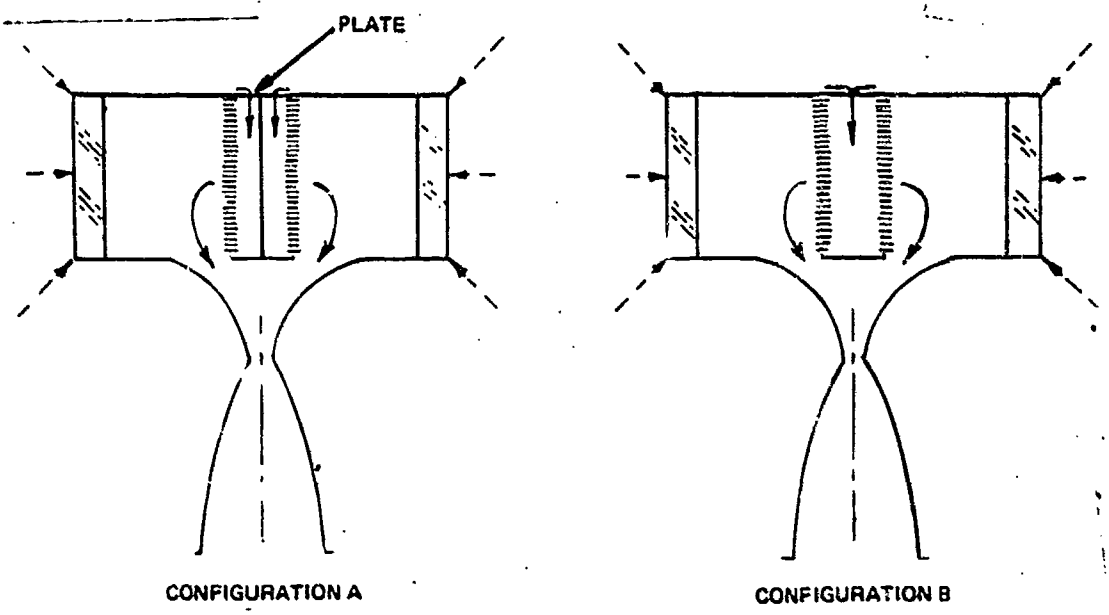

Figure 25. Windowed Heat Exchanger Cavity Absorber

radiation which penetrates the liner. The plate is removed in configuration B and the porous liner can be placed so that radiation passing through one liner is received and absorbed by the backside of the other. This absorber configuration is simpler and would improve absorber efficiency.

The porous liner can consist of a random mesh-type structure or a defined passage liner (holes). To enable quantitative analysis, a defined passage liner was chosen for analysis.

Another absorber geometry varisble evaluated was the distance between the window and the porous liner (Fig. 26). If this distance-to-window diameter ratio (L/D) is greater than one, the majority of the incoming solar radiation will be absorbed by the absorber walls and not by the porous liner. For the majority of the incoming radiation to be absorbed by the porous liner the L/D ratio should be between 0.5 and 1.0. For preliminary analysis, a L/D of 1.0 was analyzed.

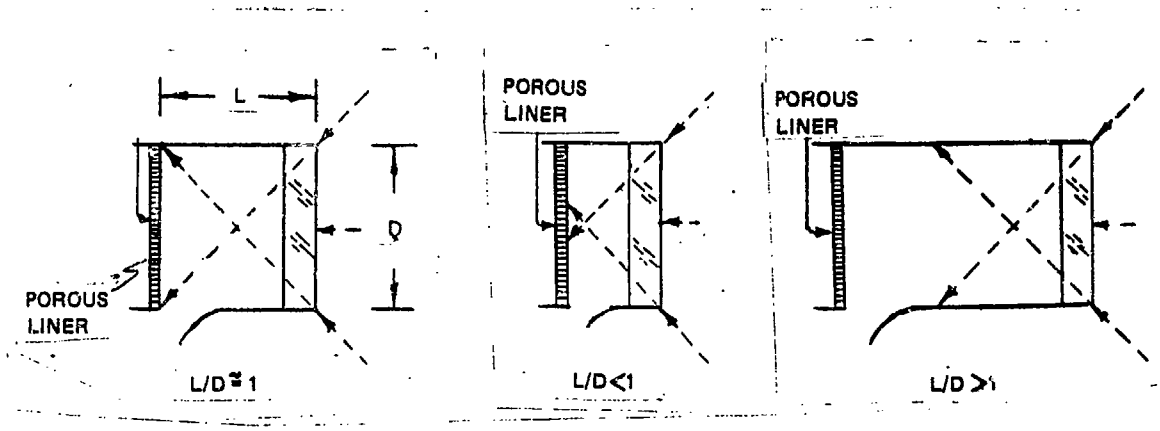

Figure 26. Cavity L/D Influence

Window Analysis

A variety of window design configurations is possible; three representative configurations are presented in Fig. 27 along with their respective advantages and disadvantages. The single pane configuration provides the simplest approach but incurs an absorber/thruster performance loss due to the required cooling. In addition, cooling can be difficult at high levels of reradiation. The double pane configuration provides additional convective cooling for the second window which absorbs the majority of the IR radiation; however, this approach is a more complex design in terms of fabrication, cooling, and sealing. Also due to engine start loads, the window thickness must be the same as that of the single pane configuration.

The hemispherical window configuration is an unique approach providing an ideal pressure vessel shape toward the high pressure side. A thinner window thickness results, which reduced the solar and IR absorption and the thermal gradient. This window configuration, as in all configurations, results in a performance loss due to cooling and is a complex window configuration in terms of fabrication, mounting and sealing.

Based on a window material evaluation (presented in the Materials and Fabrication Assessment), sapphire and quartz were the most promising window materials. Therefore thermal analysis of these two materials were performed. For a representative window diameter of 20.32 cm (8 inch), the thickness for the respective window materials was calculated using the relationship.

$$t = 1.05\ r\sqrt{\frac{Fp}{M}}$$

WINDOW CONFIGURATION	ADVANTAGES	DISADVANTAGES
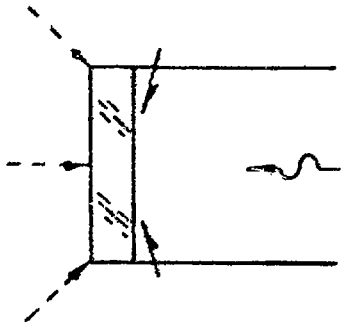 Single Pane	• Simple Approach	• Performance loss due to cooling • Cooling difficulty at high Reradiation levels
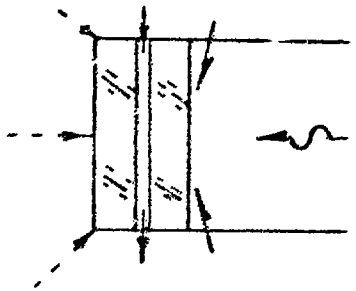 Double Pane	• Second window absorbs most of IR radiation • Second window receives additional cooling (convective)	• More complex configuration (fabrication, cooling, and sealing) • No window thickness reduction (engine start loads)
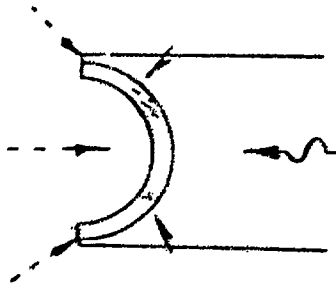 Hemispherical	• Thinner window (Reduced solar and IR absorption) • Reduced thermal gradient	• Complex window configuration (Fabrication mounting and sealing) • Performance loss due to cooling.

Figure 27. Window Configuration Comparison

where

t = window thickness

r = radius

F = safety factor

p = pressure

M = modulus of rupture

A chamber pressure of 34.5 N/cm^2 (50 psia) and a safety factor of 4 were used to result in an 0.635 cm (0.25 inch) thickness for the sapphire and 1.524 cm (0.60 inch) for the quartz window. Therefore, although the absorption coefficient for quartz is a factor of 10 lower, the thicker window and lower allowable temperature will tend to reduce its low absorption coefficient advantage.

Analysis of the solar rocket absorber/thruster window involves the following heat transfer mechanisms: (1) radiation heating from the solar collector with reflective losses from the window outer surface, (2) reradiation heating from the absorber, (3) forced convection cooling along the window inner surface, and (4) two-dimensional conduction within the window. In addition to the heat flow mechanisms stated, the effect of reflectivity (ρ) on the incident solar radiation was incorporated such that the incident solar flux was modified to:

$$\text{Incident:} \quad q_i = Q_s A (1 - \rho)$$

The thermal model (Fig. 28) consists of 60 nodes, accounts for these influences and computes window temperatures for a specified window material, diameter, thickness, and cooling condition. The heat transfer surface areas, node volumes, conductances and incident heat absorbed by each node are internally computed by the program based on the input window diameter and thickness. Material properties and incident heat flux are provied in tabular form to be utilized by the model. In addition to the window temperatures, the program calculates the net transmissive flux, Q_τ, passing through the window available for the absorber.

Assuming a coolant velocity of approximately 15.24 m/sec (50 ft/sec) parallel to the window surface, a coolant-side film coefficient of 0.00581 cal/cm^2 sec K (0.00003268 $Btu/in.^2$ sec F) was calculated to be a representative value.

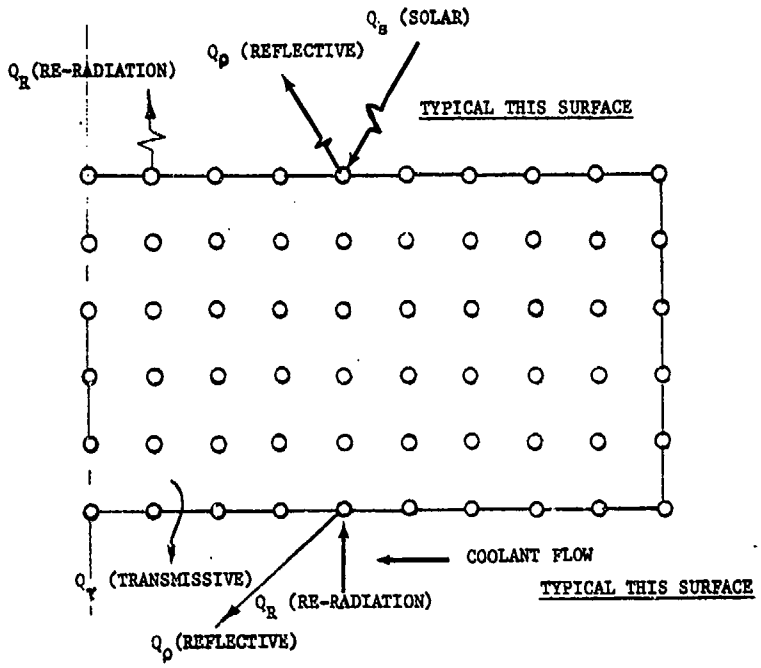

Figure 28. Absorber/Thruster Window Thermal Model Nodal Network

The results of the thermal anlaysis for the sapphire window using the thermal model described are presented in Fig. 29. To achieve satisfactory window temperatures with a sapphire window, a coolant-side film coefficient approximately an order of magnitude higher than the representative value would be required. This would be difficult, if not impossible, to achieve.

For quartz, only the absorption coefficient versus wave length at room temperature was available from the vendors contacted. Therefore the thermal analysis was performed for a range of average absorption coefficients using the calculated coolant-side film coefficient. As shown in Fig. 30, if the room temperature absorption coefficient of 0.0081 per cm (0.0032 per inch) does not significantly increase with temperature and the coolant-side film coefficient can be maintained, the quartz window can be easily cooled with maximum temperatures below 589 K (600 F). However, typically, the absorption coefficient increases slightly with temperature and for a gas cooling jet, the film coefficient will decay with the distance away from the injection point.

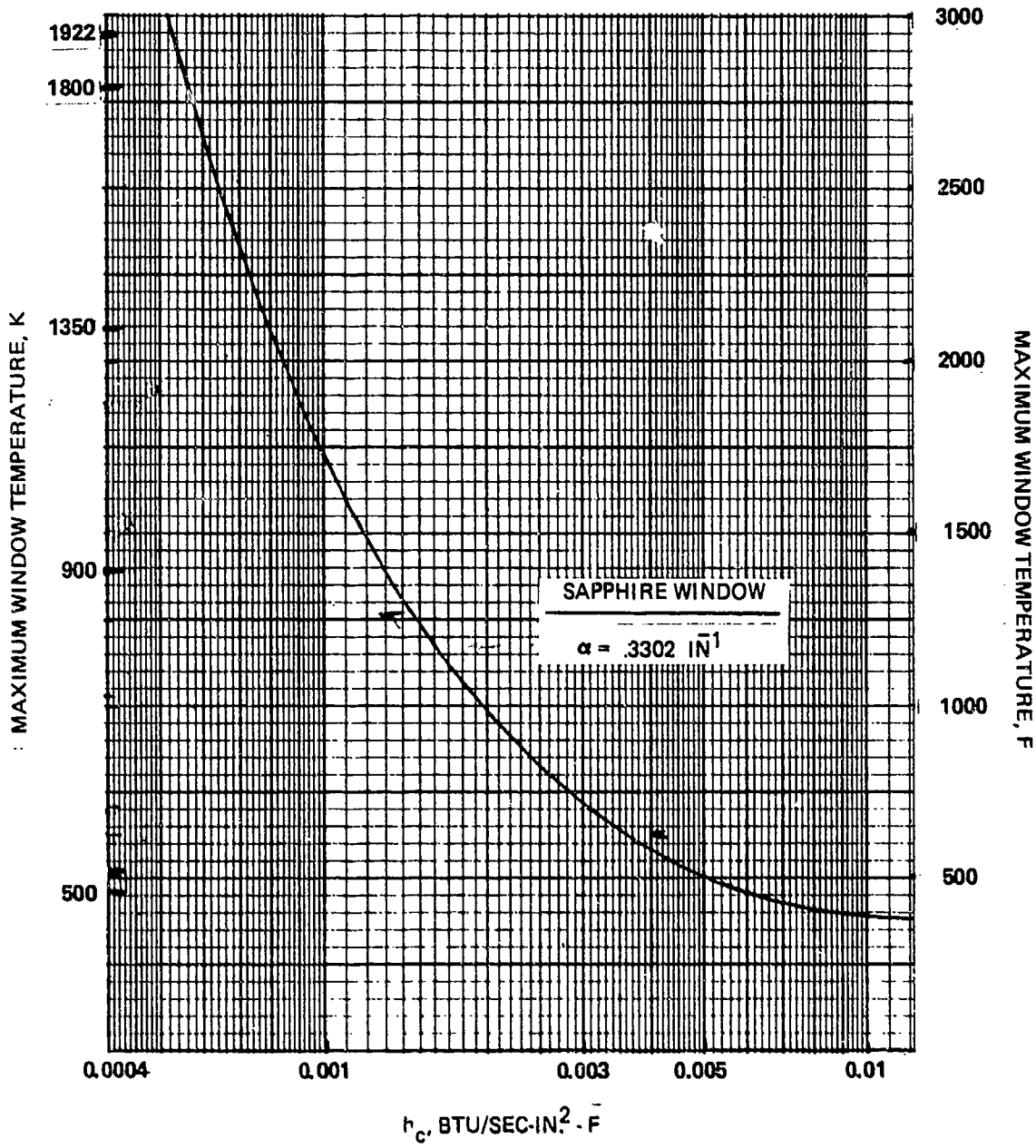

Figure 29. Sapphire Absorber/Thruster Window Maximum Temperatures for Various Cooling Side Heat Transfer Coefficients

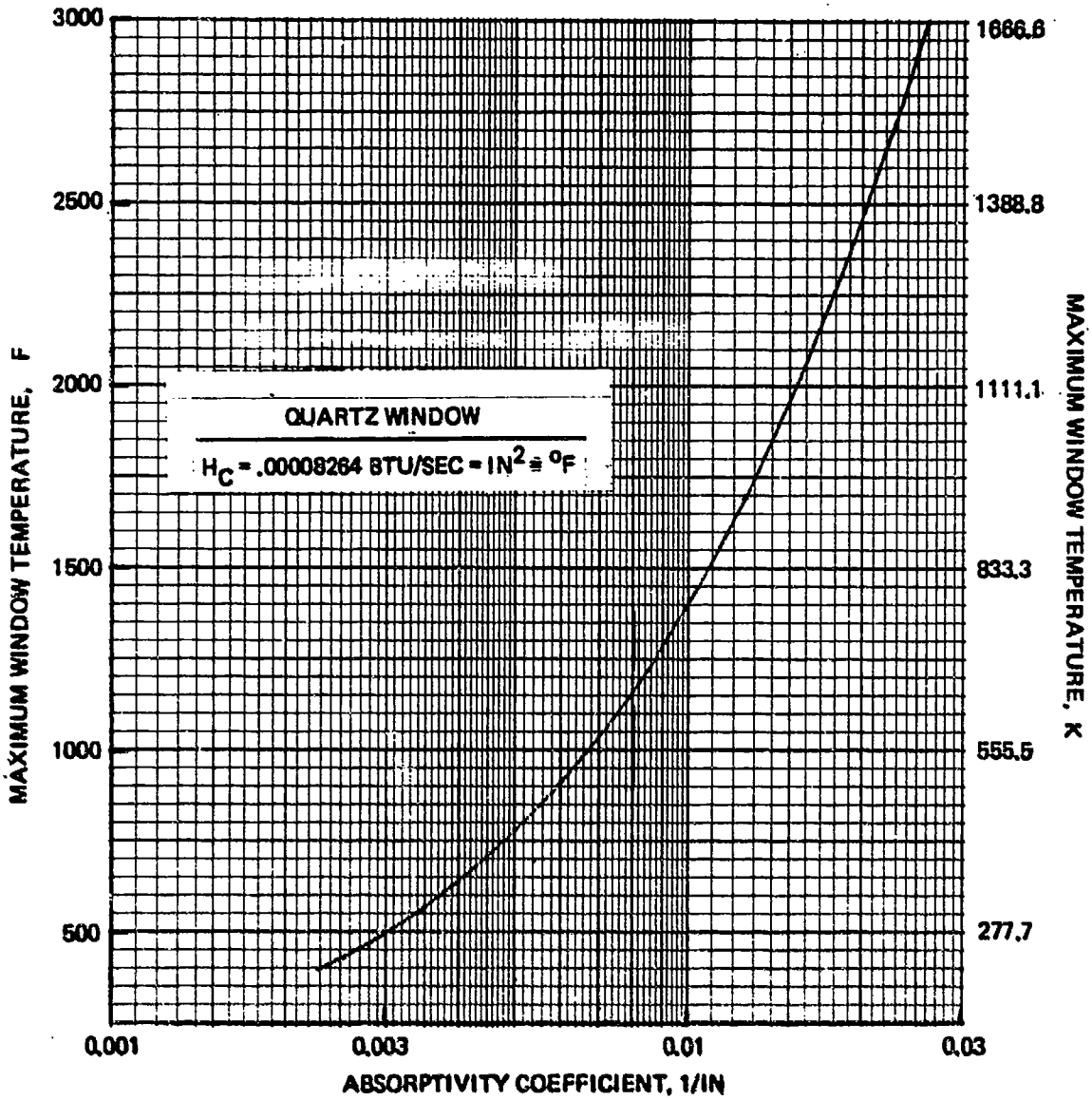

Figure 30. Quartz Absorber/Thruster Window Maximum Temperatures as a Function of the Absorptivity Coefficients

Calculations assuming a discrete number of angled hydrogen cooling jets impinging on the window have indicated that representative coolant-side film coefficients of 0.07 cal/cm^2 sec K (0.0001 Btu/in.^{2} sec C) are possible.

To minimize window cooling requirements and to minimize absorber reradiation losses, the influence of an infrared (IR) reflective coating on the inside surface of the quartz window (flat disc) was evaluated. An effective IR coating would reduce the reradiated heat absorbed by the window and reduce the IR radiation lost through the window. As discussed later, an IR coating reflectivity of 85% was projected using indium tin oxide but more recent vendor contact by AFRPL personnel has indicated an unaccounted for absorption in the visible wavelength range and the transition wavelength region between transmission and reflection. Therefore, other coating materials need to be investigated.

As shown in Fig. 31 due to the low radiation source temperature, the windowed heat exchanger cavity absorber (L/D = 1.0) resulted in a maximum window temperature below the allowable quartz temperature limit even without an IR reflectivity coating. Higher cavity surface temperatures may present a problem, however, and dictate the use of an IR reflective coating.

The detailed window temperature distribution for the 30.48 cm (12 inch) diameter windowed heat exchanger cavity concept is shown in Fig. 32 for a quartz window (2.286 cm or 0.9 inch thickness) with 85% IR reflectivity on the internal window surface. The resulting window temperatures are satisfactory for quartz. As expected, the center of the window on the solar radiation incident side was the highest temperature point and the internal edge first exposed to the hydrogen coolant was the coolest point.

Absorber Cavity Performance

As discussed previously, the amount of radiation incident on the porous liner of the windowed heat exchanger cavity absorber is dependent on the absorber length-to-diameter ratio (L/D). As shown in Fig. 33, the ratio of heat incident on the porous liner-to-the total heat fell below 50% for L/D greater than 1.12. Therefore, to obtain maximum benefit of the porous liner, the L/D should be 1.0 or less.

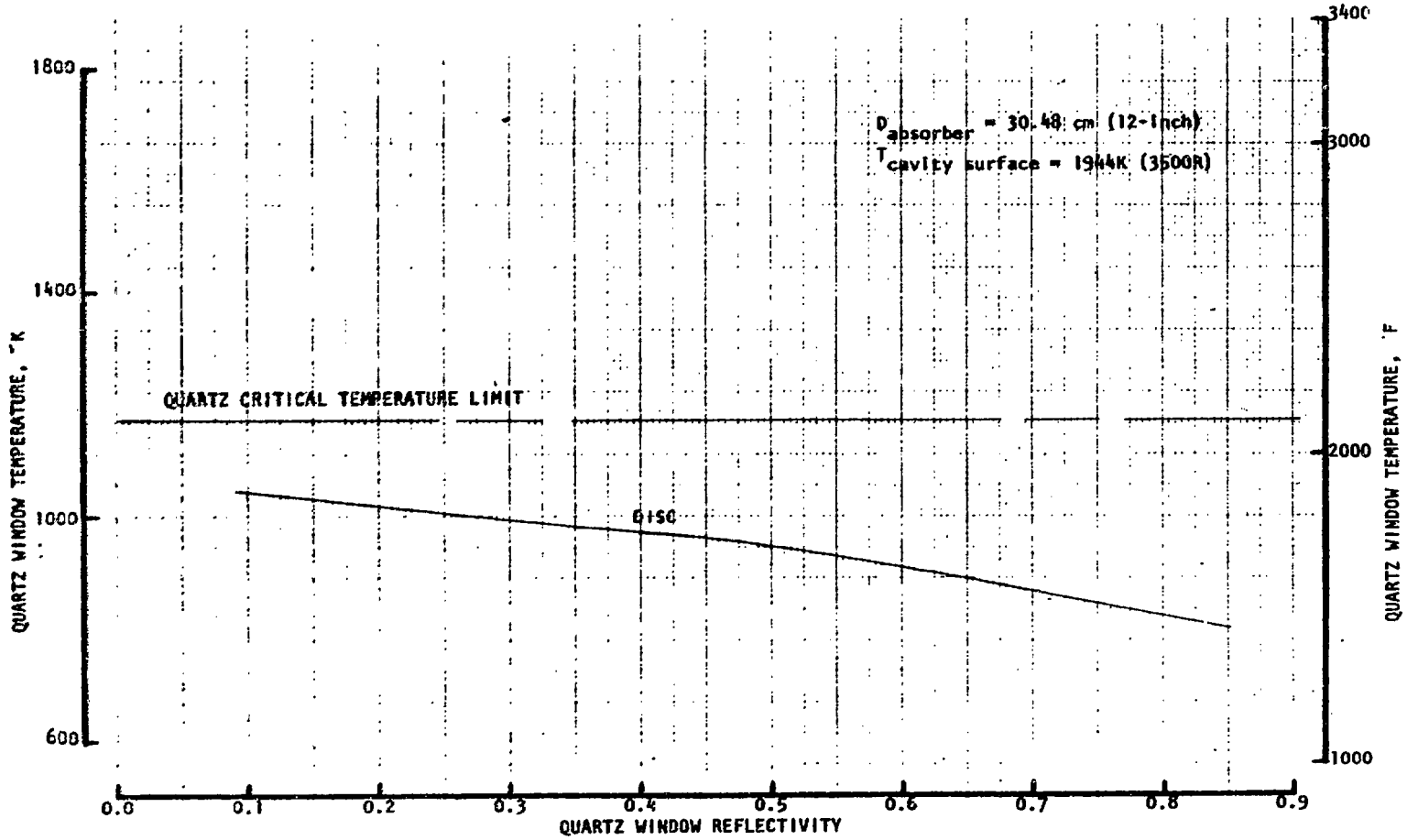

Figure 31. Quartz Window Temperature Profile of Cavity Chamber

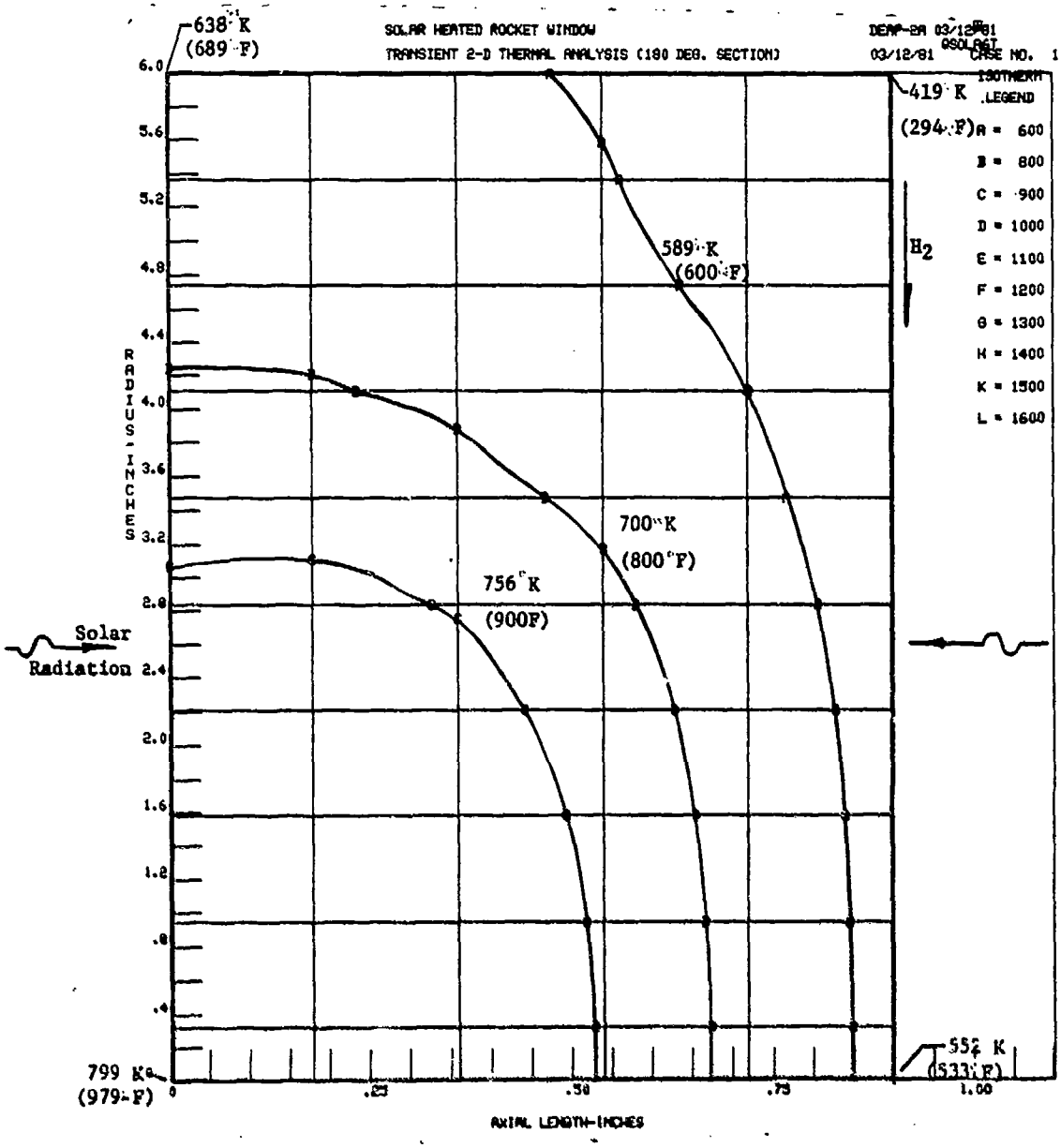

Figure 32. Window (Quartz) Temperature Distribution for Window Heat Exchanger Cavity With 30.48 cm (12 inch) Diameter and 85% IR Reflectivity

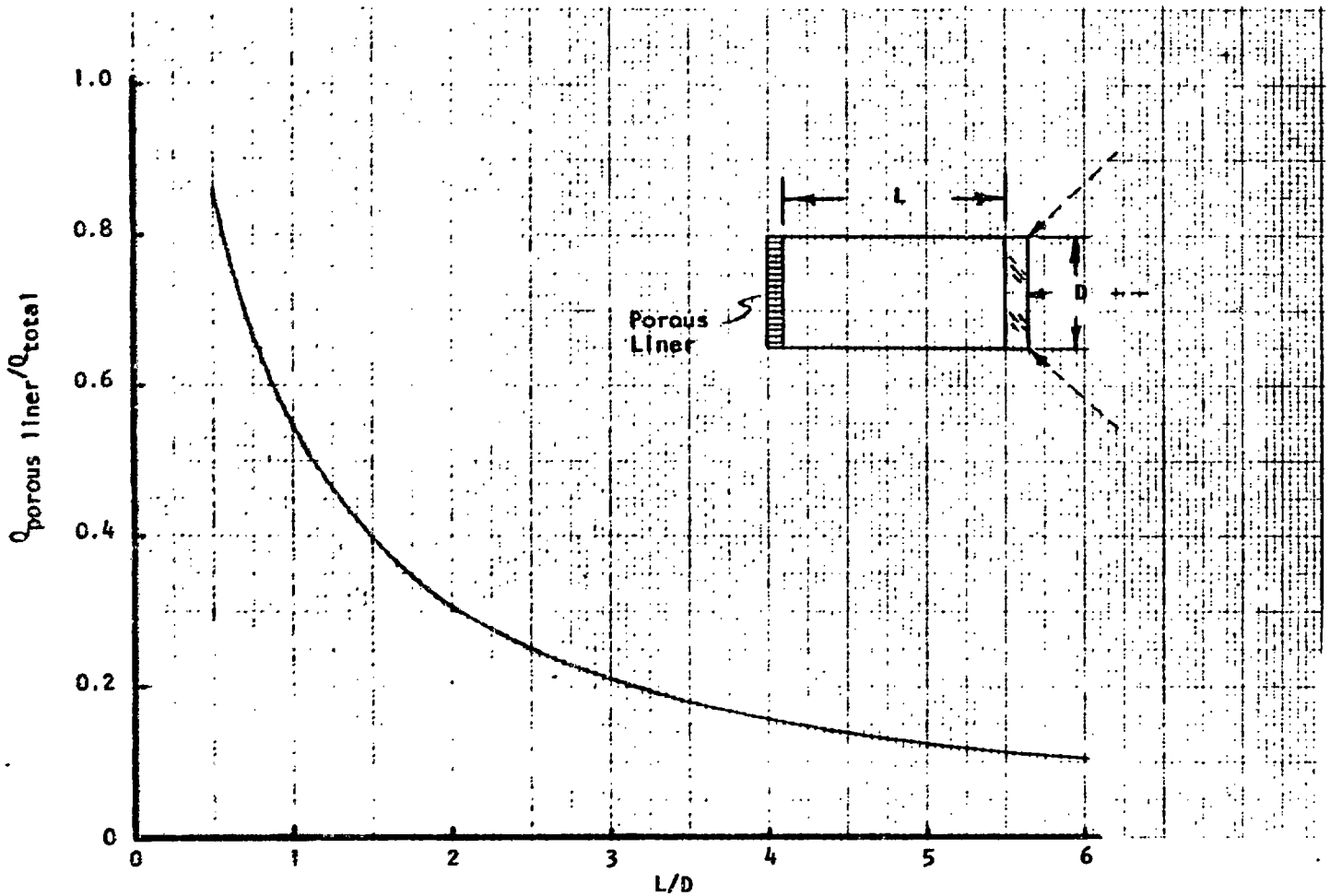

Figure 33. Windowed Heat Exchanger Cavity Absorber - Porous Liner Incident Heat

The absorber efficiency for the windowed heat exchanger cavity absorber configuration was calculated and compared to the windowless configuration for a range of L/D. As shown in Fig. 34, the windowed heat exchanger cavity achieved higher absorber efficiencies for all L/Ds. This improved absorber performance is due to the reduced cavity reradiation loss as the result of the window. An IR reflective coating (85% reflectivity) on the inside surface of the window was assumed. Achieving a solar reflectivity of zero would increase the absorber efficiency by approximately 5%.

Thruster Performance

A comparison of the resulting thruster performance (delivered specific impulse and thrust) for the windowless and windowed heat exchanger cavity configurations is presented in Fig. 35 and 36 as a function of the final hydrogen temperature. Thruster performance for the windowed configuration is shown with and without window cooling.

The specific impulse of the windowless and the windowed configuration with no window cooling was very similar. However, adding the window coolant to the windowed configuration (10% fuel flow), which lowered the effective propellant temperature, reduced the performance by approximately 250 N sec/kg (25.5 lbf sec/lbm). This concept achieved a higher thrust capability than the previous windowless heat exchanger cavity concept.

Concept Evaluation Summary

The results of the windowed heat exchanger cavity absorber/thruster concept evaluation are summarized as follows:

• Window Cooling	Single pane quartz with angled cooling jets for 2777 K (5000 R) H_2 temperature
• Absorber efficiency	$\geq$65%
• Delivered specific impulse	Up to 8336 N sec/kg (850 lbf) sec/lbf
• Thrust	200 to 289 N (45 to 65 lbf)
• Absorber cooling	Similar to windowless concept
• Limitation	Porous liner material temperature limit ($T_{H_2 AVG} \leq$ 2667 K (4800 R)
• Other features	Highest thrust concept no moving parts

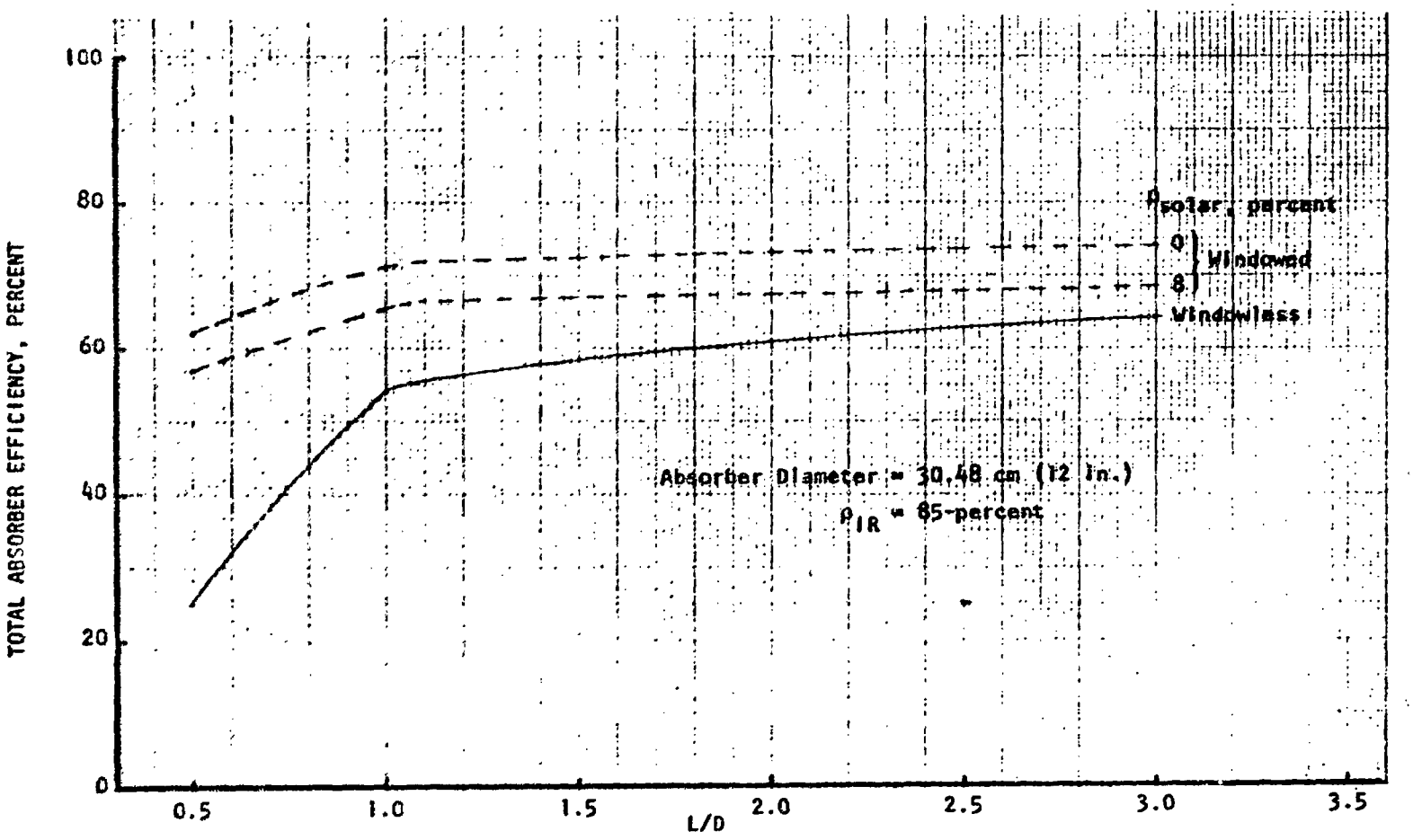

Figure 34. Absorber Efficiency Comparison of the Windowless and Windowed Heat Exchanger Cavity Absorbers

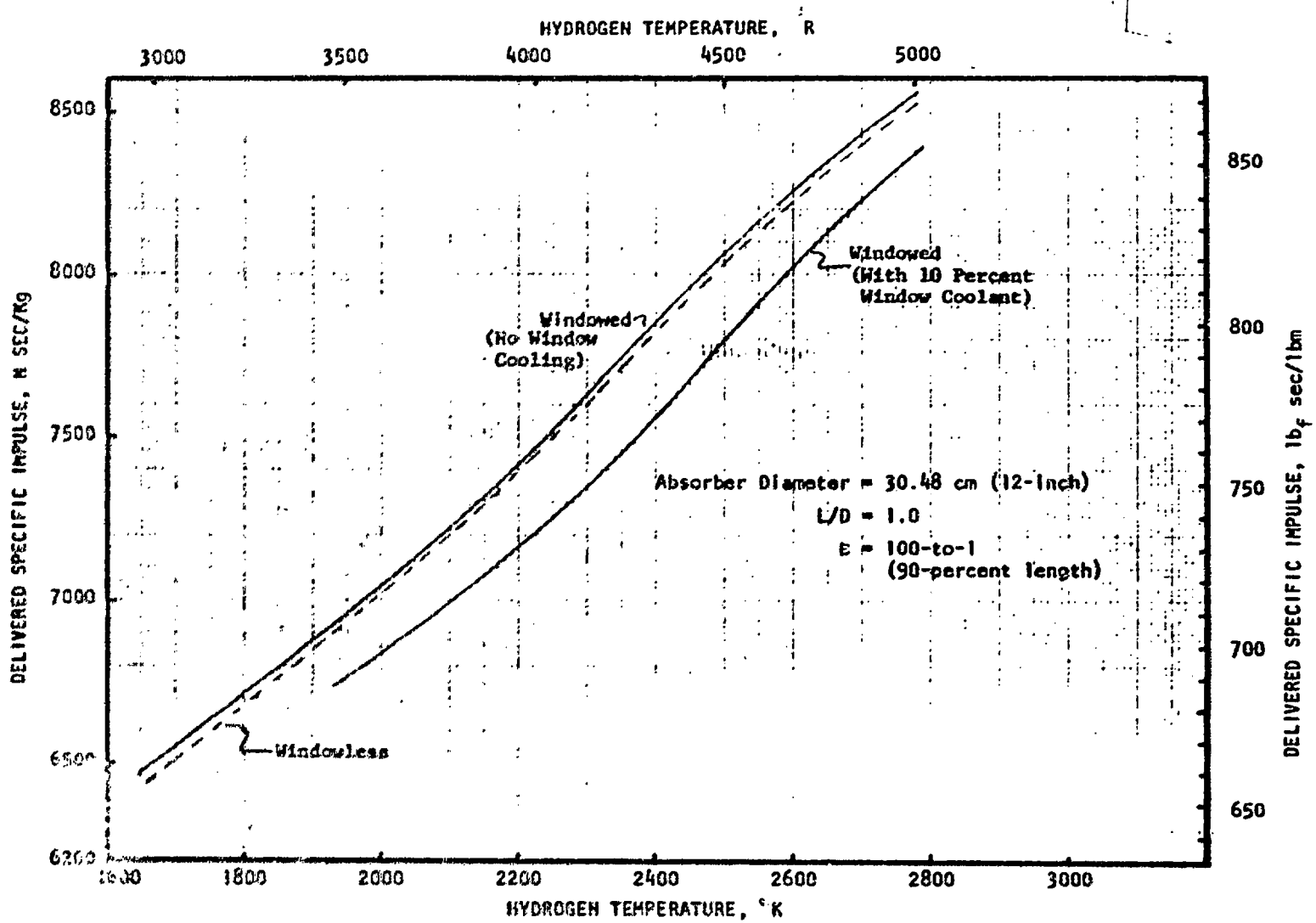

Figure 35. Delivered Specific Impulse Comparison

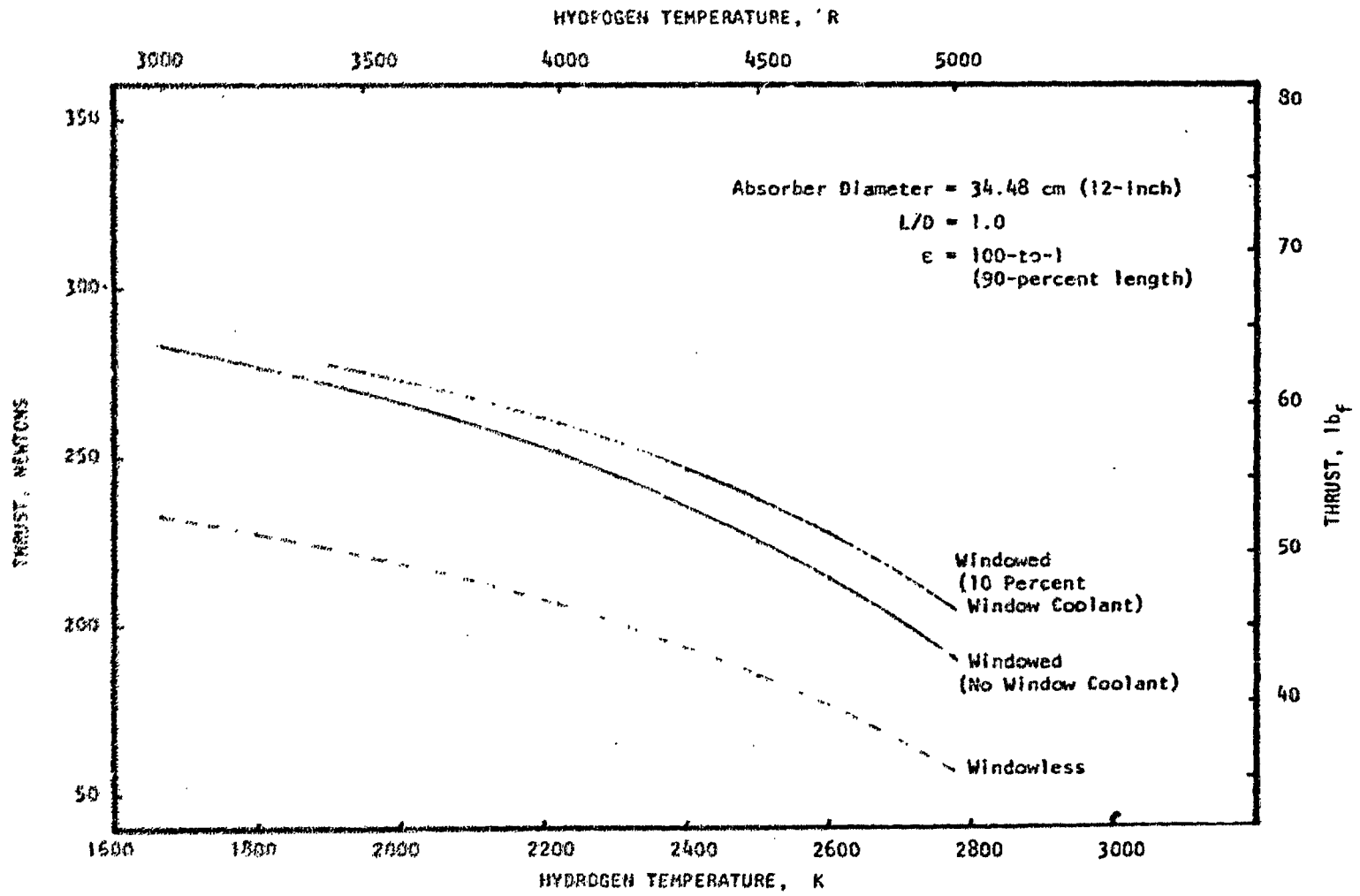

Figure 36. Delivered Thrust Comparison

WINDOWED PARTICULATE ABSORPTION CONCEPT (DISCHARGED SEED)

The overall performance characteristics of the windowed particular/molecular absorption concept (Fig. 37) were dependent on: (1) the attainable propellant temperature, (2) the specific impulse, and (3) window temperature. In evaluating the feasibility of this concept, the magnitude of the achievable propellant temperature is the primary parameter to be determined. The final gas temperature is achieved through heat transfer from the particle to the gas. In order to attain the desired high temperature level, the total incoming heat flux and the particle selection are both critical.

Absorption Media Selection

The particle selection is dependent upon its emissivity, melting point temperature, and the density. The carbon particle which has the highest emissivity and lowest density, was selected as a baseline particle although other particles were evaluated. The influence of carbon concentration on specific impulse at various gas/particle mixtures is shown in Fig. 38.

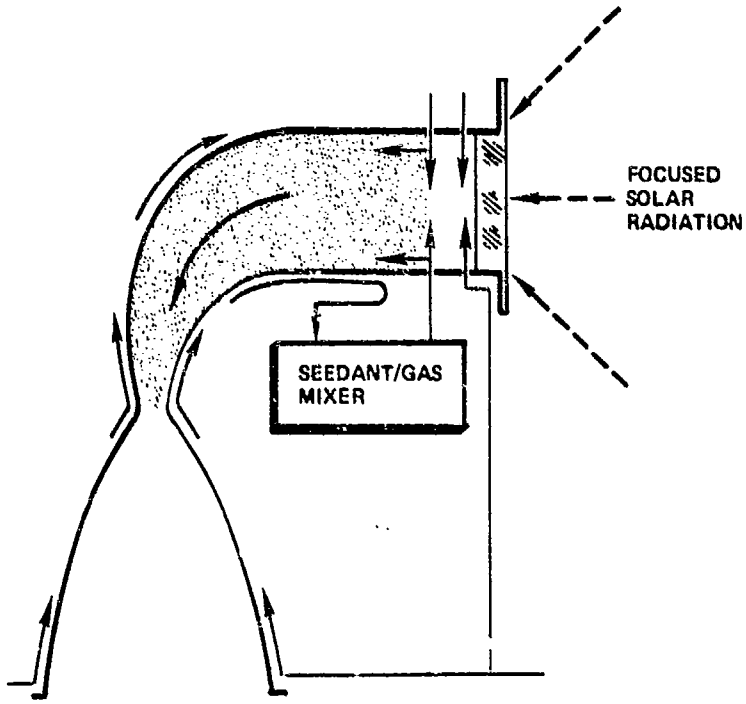

Figure 37. Windowed Molecular or Particulate Concept (Discharged Seed)

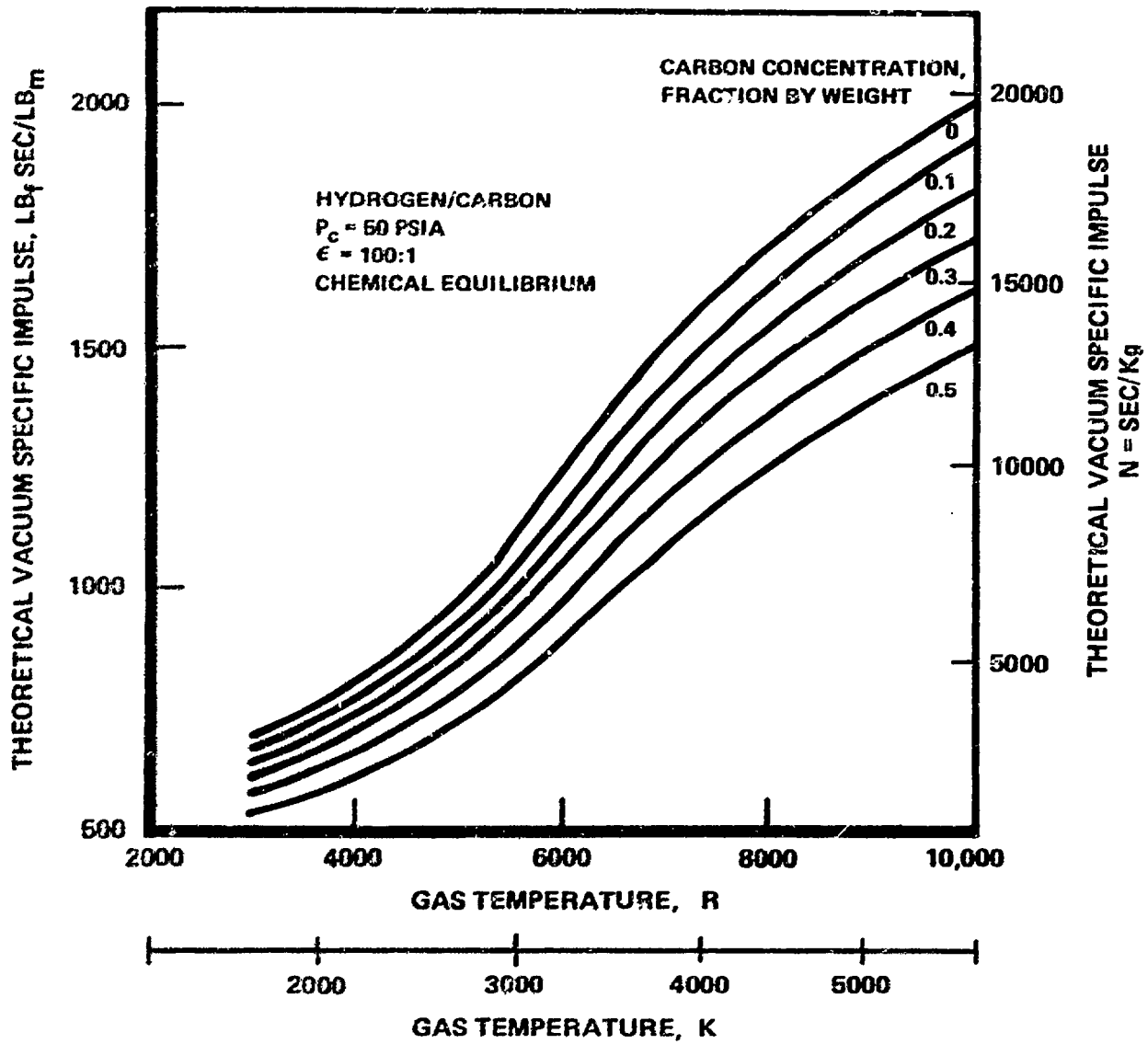

Figure 38. Theoretical Vacuum Specific Impulse Variation

The influence of particle density and particle radius on percent heat absorbed for a given particle mass fraction is presented in Fig. 39. The higher density particles resulted in significantly lower heat absorption. In addition, for the discharged seed absorber/thruster concept, the higher density particles will tend to reduce the delivered specific impulse due to a higher effective molecular weight. The influence of particle radiation scattering on total particulate absorptivity is illustrated in Fig. 39. The absorptivity for a given particle concentration decreased for small particle sizes due to scattering.

The percent heat absorption for four candidate particles (carbon, hafnium carbide, tantalum carbide, and tungsten) are shown in Fig. 40 for a 0.2 μm particle radius (near optimum). The advantage of carbon particles is clearly shown with the other particles resulting in approximately 1/6 the heat absorption.

Another important consideration is the temperature at which significant reaction occurs with hydrogen or the reaction rate of the hydrogen/particle mixture. Carbon will tend to react with hydrogen at lower temperatures than with the other particles.

For the particulate absorption concept (discharged seed), carbon particles would be the obvious choice if the particle/gas mixture could be heated to 3333 to 3889 K (6000 to 7000 R) in approximately 40 milliseconds without significant reaction. For the additional concept analysis, carbon was selected as the particle material.

In addition to the particle material, size, concentration, and thruster geometry, the propellant flowrate is another critical issue in determining the particle and propellant temperature profile along the thruster. Since the time increment during which the particles and propellant are exposed to the radiation field depends on the total flowrate, a higher flowrate causes both the particle and propellant to flow faster and reduces the exposure time in radiation field. As shown in Fig. 41, the total mass flowrate of 0.00238 Kg/sec (0.00525 lbm/sec) results in 778 K (1400 F); higher temperature than the mass flowrate of 0.00556 Kg/sec (0.01226 lbm/sec) for a 7.48 cm (3.14 inch) chamber length.

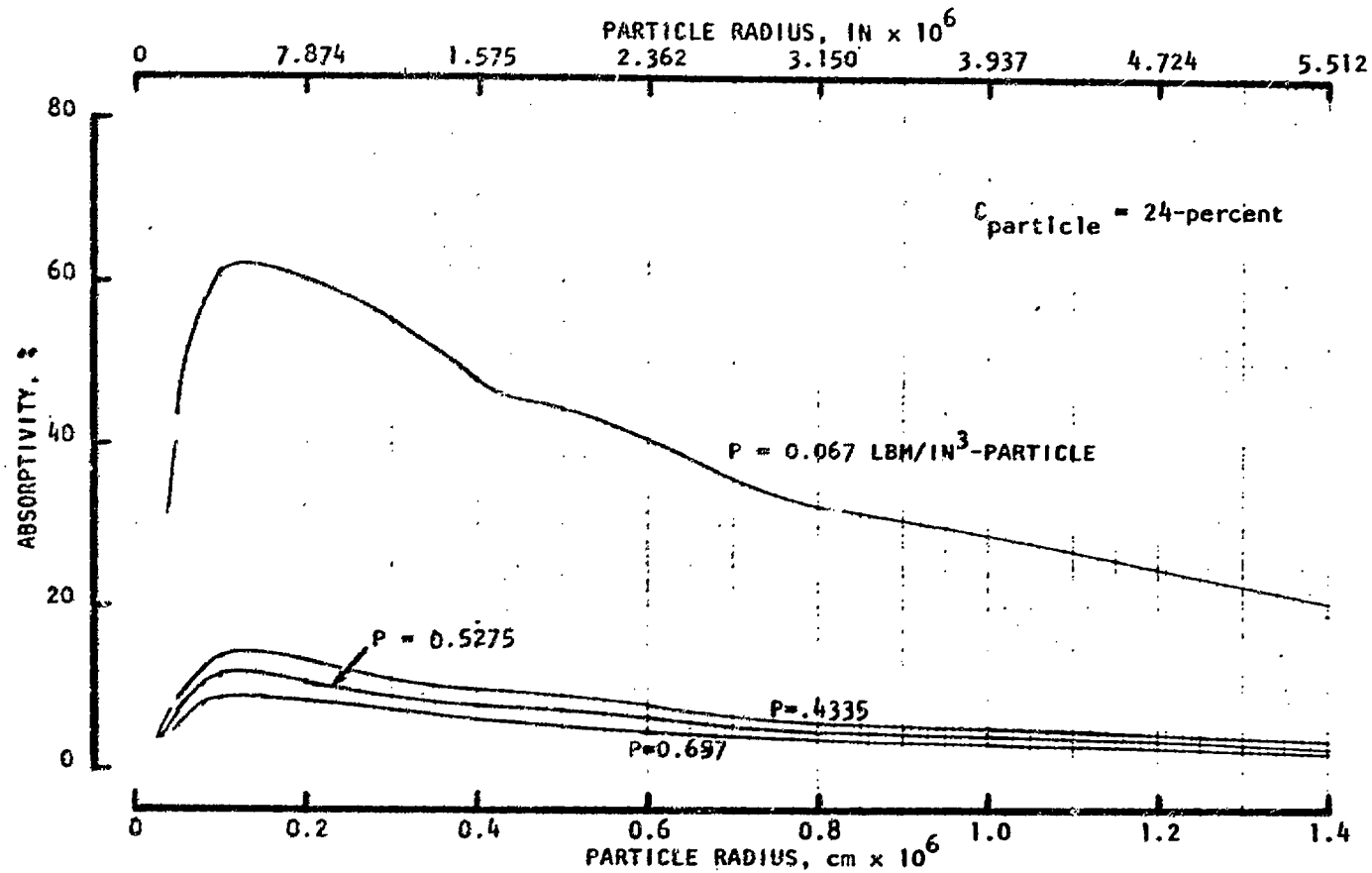

Figure 39. Percent Solar Radiation Absorption Variation With Particle Density and Particle Size

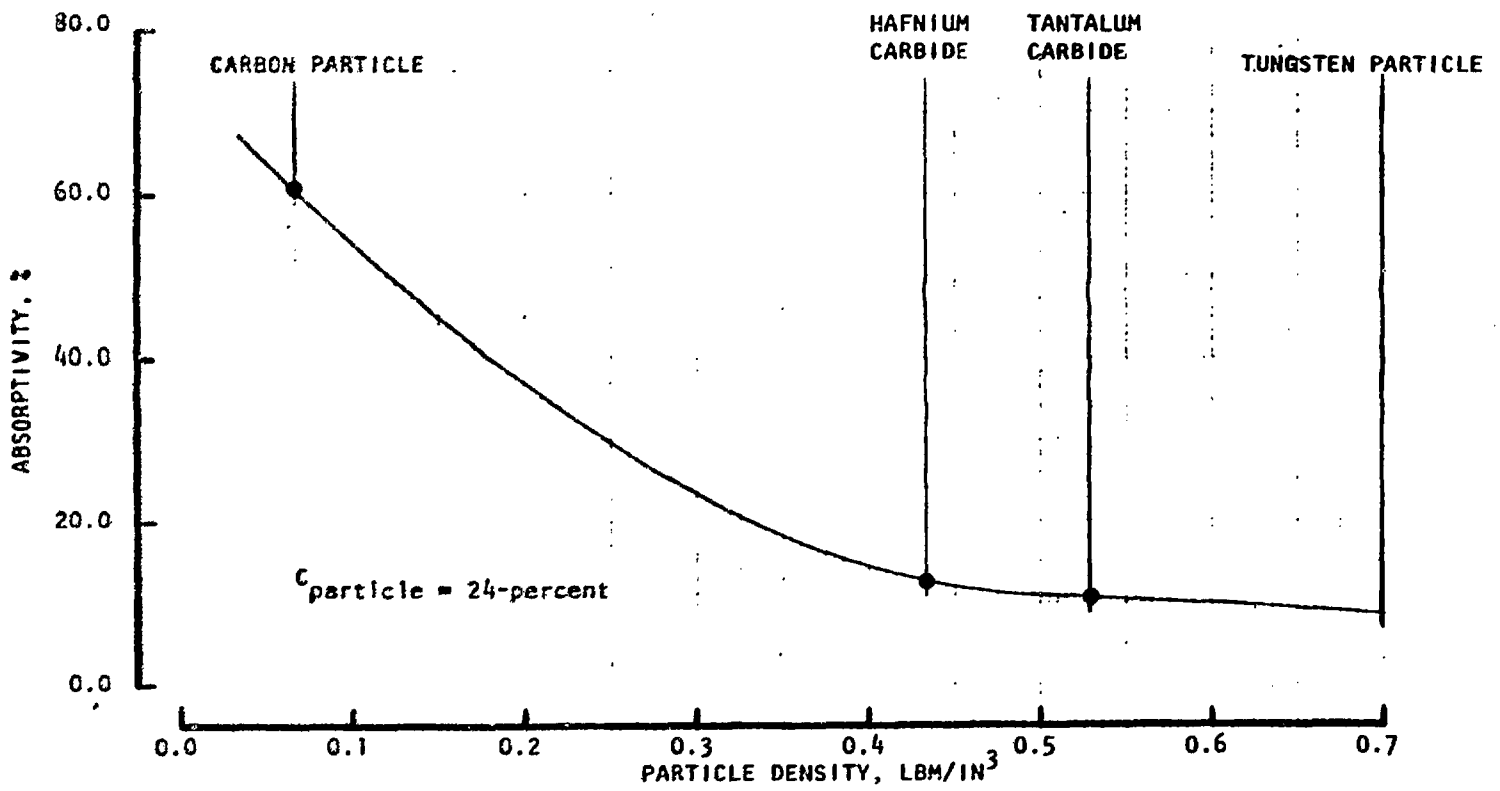

Figure 40. Percent Solar Radiation Absorption Variation With Particle Density at 0.2 μm Particle Radius

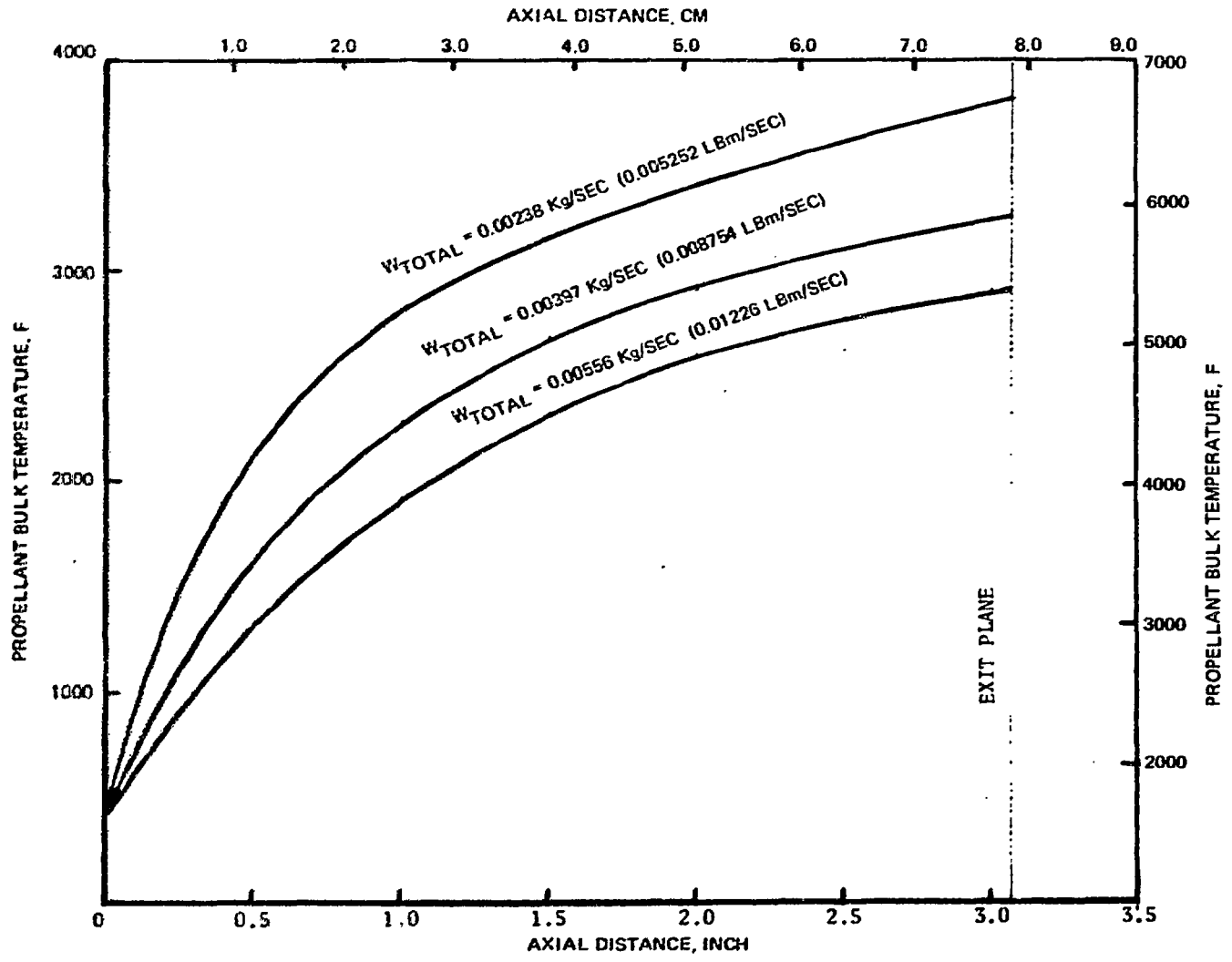

Figure 41. Axial Propellant Temperature Distribution (70% Absorption) for Particulate Absorption Concept

Absorption Analysis

The complex transient flow, solar radiation absorption, and heating problem was analyzed using a disc model (Fig. 42) which simulates one slice of propellant and absorbing media. The seedant and the main propellant (H_2) are lumped into two thermal modes. As the disc flows from near the window to the thruster throat, the seedant absorbs solar radiation and the seedant, in turn, radiates heat to the wall and the cooled window and also conducts heat to the hydrogen. The heated hydrogen transfers heat to the absorber wall through convection. The model performs this complex transient heat balance as the disc flows toward the thruster throat. The decay in incoming solar radiation and the decreased reradiation to the window as the disc moves away from the window are also modeled.

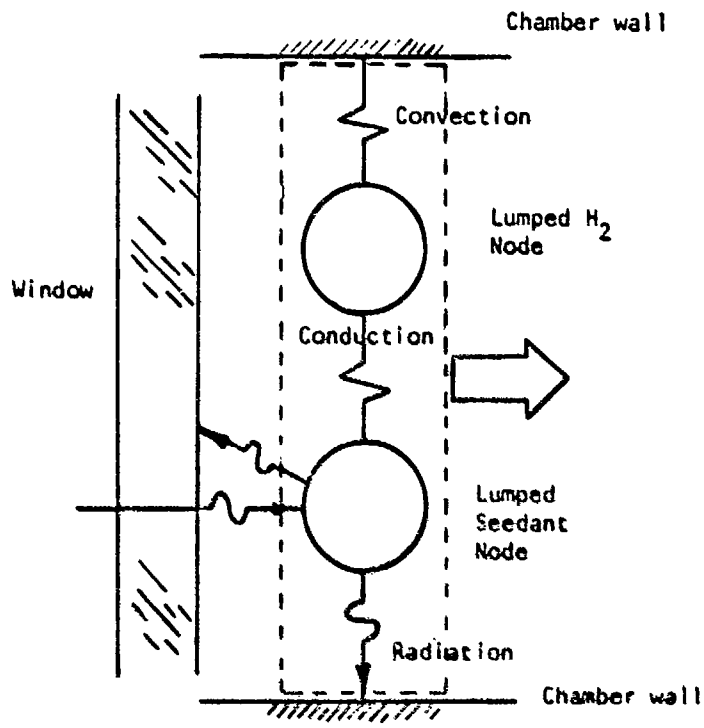

Figure 42. Transient Particulate/Molecular Absorption Thermal Model

The evaluation of the windowed particulate absorption concept indicated that a high-carbon concentration was favorable to achieve efficient solar radiation absorption. Because of this tendency, the local reradiation within each

incremental slice of the particle/gas media is primarily from adjacent particles that are close to the same temperature. Therefore, the particle-to-particle radiation heat transfer rate is small compared to the total heat transfer rate. The incorporation of the particle-to-particle radiation may result in a more rapid initial rise in hydrogen temperature than that shown in Fig. 41, but the final gas temperature (total heat) would essentially be the same.

As discussed previously, the influence of optical scattering caused by the particle was considered in this model.

Analyses were performed to evaluate the influences of carbon mass fraction, particle size and absorption chamber size to define the concept feasibility and its design configuration.

Carbon Particle Mass Fraction. The carbon particle mass fraction is one of the critical issues in evaluating the potential of particulate/molecular absorption absorber/thruster concept. A high carbon mass fraction provides high propellant temperatures required to increase specific impulse but tends to decrease specific impulse due to the higher molecular weight carbon added.

In evaluating the mass fraction of the carbon particle, certain mechanisms have to be determined: (1) the total length of the absorber zone, (2) the radius of the absorption chamber, (3) the fraction of the total absorbed radiation heat, and (4) the carbon particle size. Generally, the minimum carbon particle size is selected to minimize the reradiation heat loss and maximize the heat dissipation to the main propellant. Due to the resonance phenomena of the Mie scattering, the minimum carbon particle size is confined at about 0.2 μm radius. Once the minimum particle size is determined, the carbon particle concentration can be computed for various particle sizes using the relationship below without having the resonance vibration condition:

$$N = \frac{-\ln\left(1 - \frac{Qi}{Qo}\right)}{\left(L\right)\left(\frac{\varepsilon}{N}\right)}$$

where N = particle concentration

L = total absorber length

Qi = total absorbed radiation heat

Qo = total incoming radiation heat

$\frac{\epsilon}{N}$ = extinction coefficient per particle

The extinction coefficient per particle for carbon, which is determined experimentally, is presented in generalized form in Fig. 43. As shown, the ratio of extinction coefficient per particle to the particle radius is much larger at the small particle radius and this indicates that the temperature of the particle is higher at the smaller particle size.

The carbon particle mass fraction can be incorporated with the particle concentration as:

$$C_c = \frac{(N)\left(\frac{4}{3}\pi R^3\right)(\rho_1)}{[1-(N)\left(\frac{4}{3}\pi R^3\right)]\,\rho_2}$$

where R = particle radius

ρ_1 = carbon graphite density

ρ_2 = propellant density

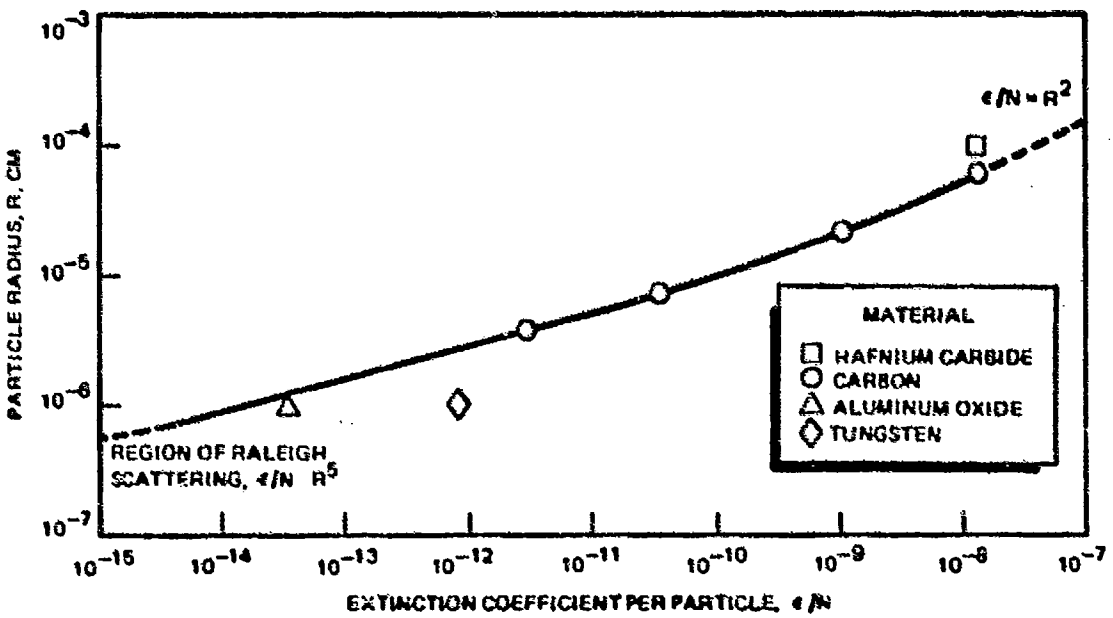

Figure 43. Carbon Extinction Coefficient

Figure 44 presents the carbon mass fraction as a function of carbon particle radius, with the percentage of total radiation heat absorbed as a parameter for a 10 cm (3.94 inch) absorption length. The curves show that as the particle radius increases, the carbon mass fraction increases for a same equivalent absorbed heat. For a selected particle radius, the curves also indicate that a higher mass fraction is required in order to absorb more of the incoming solar radiation. Therefore to achieve 70% or greater heat absorption by the carbon particles, carbon mass fractions exceeding 40% are required.

Particulate Injection Methods. Two approaches for particulate injection were evaluated and are illustrated in Fig. 45. Approach (a) provides for hydrogen window cooling and injects the particle/gas mixture just downstream from the window. Approach (b) provides the same window cooling, incorporates a second hydrogen injection station just downstream of the window and injects the particle/gas mixture approximately 2 inches downstream from the window. Approach (b) results in lower reradiation losses due to a reduced cavity view factor and therefore, improved absorber and thruster performance. The resulting axial temperature profiles for the particle/gas mixture of approach (b) are presented in Fig. 46 for three representative total flowrates for a carbon mass fraction of 24% and a 30.48 cm (12 inch) absorber diameter. The final propellant temperature as a function of the propellant mass flowrate is shown in Fig. 47.

Window Cooling. Analysis of window cooling similar to that discussed earlier for the heat exchanger cavity absorber was performed for the particulate/molecular absorption concept. As shown in Fig. 48, evaluation of the double pane and hemispherical window configurations for the particulate absorption concept indicated significant reductions in maximum window temperatures. The thinner hemispherical window resulted in the lowest window temperature of 927.8 K (1210 F), which is satisfactory for quartz. This was accomplished with an 85% IR reflectivity.

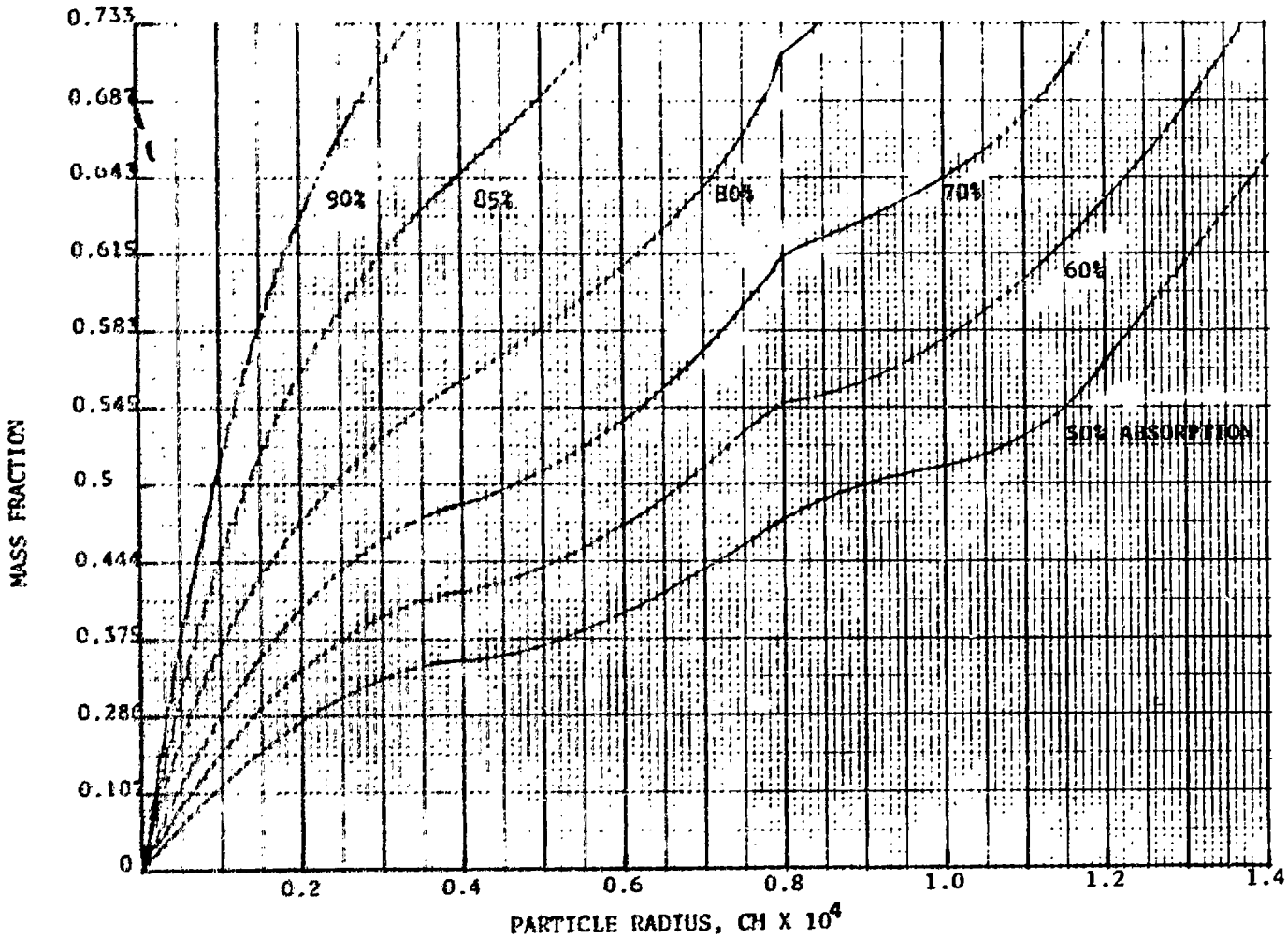

Figure 44. Carbon Mass Fraction Requirements (Absorption Length = 10 cm)

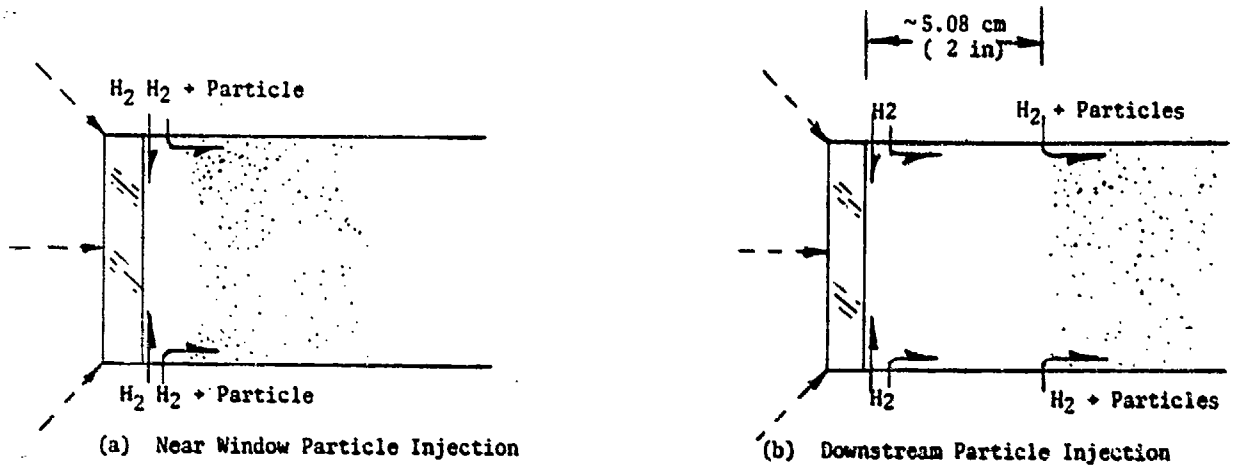

Figure 45. Particulate Absorption Injection Approaches

Seedant Deposition on the Solar Collectors. For solar collectors of the configuration shown in Fig. 49 (Ref. 1) which are inflated, the deposition of seed on the collectors would not be critical since the conical portion from the absorber to the collector is an internally mirrored surface to produce a light funnel. Therefore, external seed deposition would not appreciably influence the collector operation for the collector/engine position illustrated. If the collectors are turned 90 degrees with respect to the engine line of thrust, the transparent portions of the inflated cone may be subject to carbon deposition.

For a rigid collector configuration (not inflated), the edge of the collector surface would be approximately on a 45-degree line out from the absorber. As shown by the general inviscid and viscous nozzle plumes (Fig. 50 and 51), the plume without a hydrogen nozzle exit shroud gas would impinge on the collector. Therefore, if the condensed seed particles are on the order of one micron, the particles would behave like the gas and impinge and deposit on the collectors.

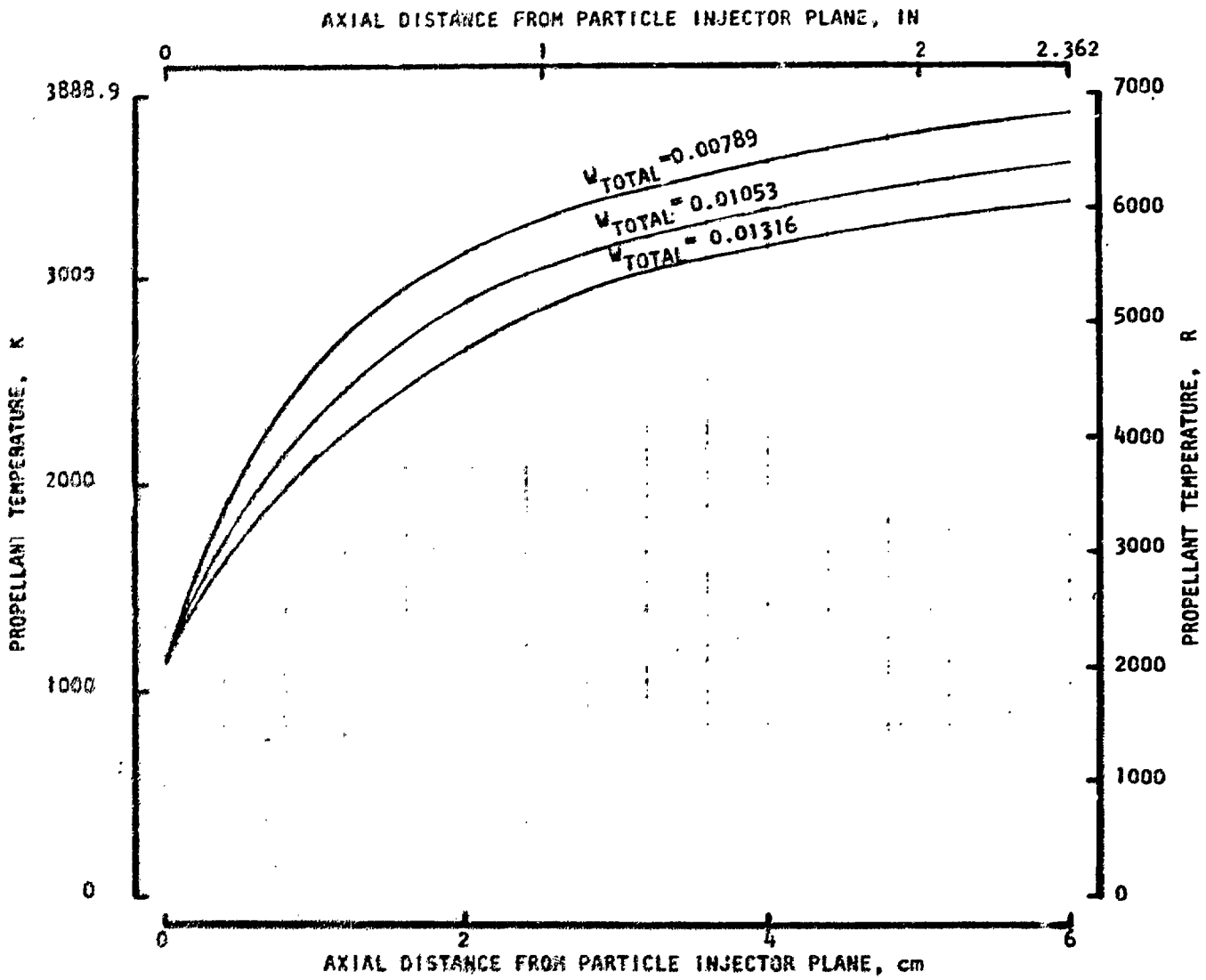

Figure 46. Propellant Temperature Distribution of 6 cm (2.362 inch) Absorbing Length

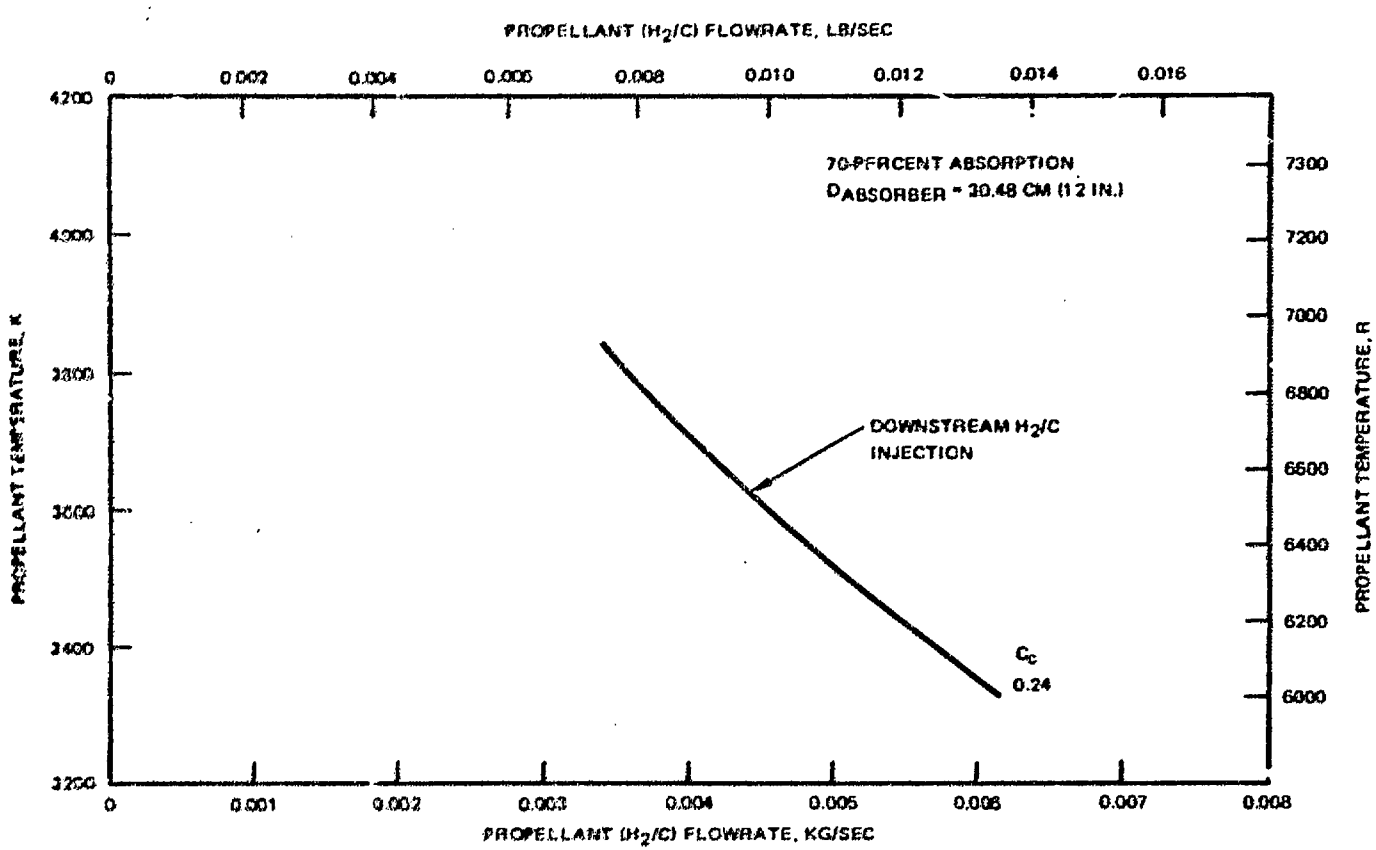

Figure 47. Propellant Temperature Variation with Propellant Flowrate for the Particulate Absorption Concept

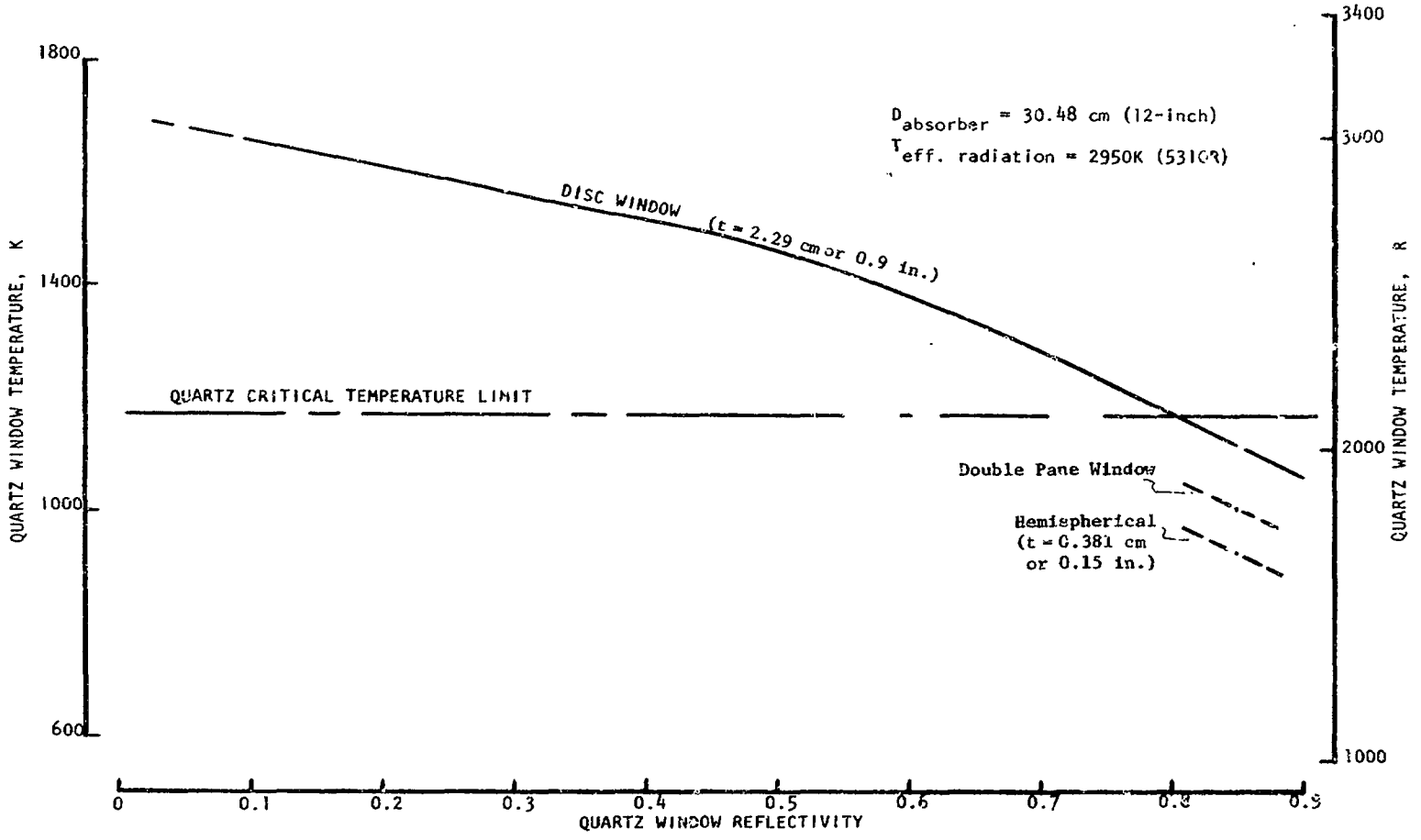

Figure 48. Quartz Window Temperature Profile of Discharged Seed Chamber

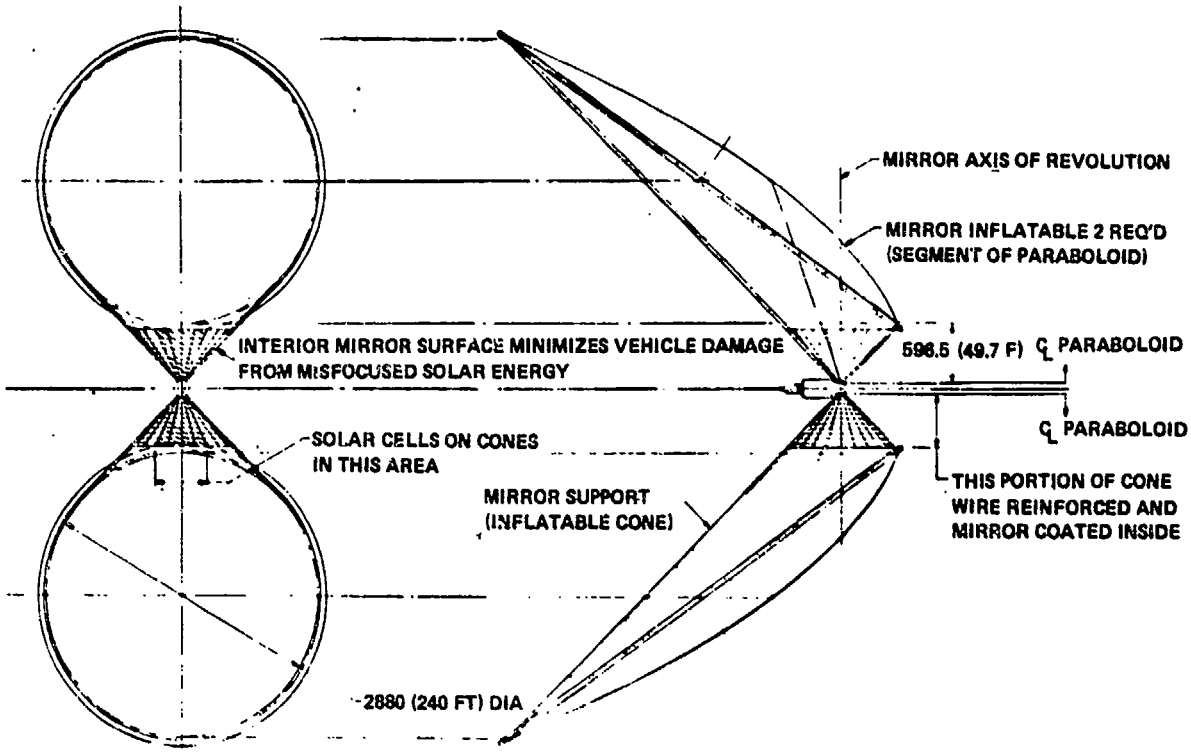

Figure 49. Inflatable Cone/Paraboloid Collector

Analysis of carbon particle trajectory and the influence of a clean, pure hydrogen nozzle exit shroud gas was attempted but computer program difficulties prevented completion. However, qualitatively the core flow (contains particles) and the shroud gas (pure hydrogen) will eventually mix and most likely particle deposition, although less, will occur with the rigid solar collector configuration.

Thruster Performance

The delivered specific impulse (Fig. 52) and thrust (Fig. 53) for the particulate absorption concept were determined as a function of the propellant temperature for various amounts of hydrogen shroud gas. The shroud gas performance loss was computed assuming this gas was injected at the nozzle exit with a total temperature of 2777.8 K (5000 R). The delivered specific impulse was significantly higher than the previous two concepts even with the shroud gas loss due to the higher effective propellant temperatures achievable.

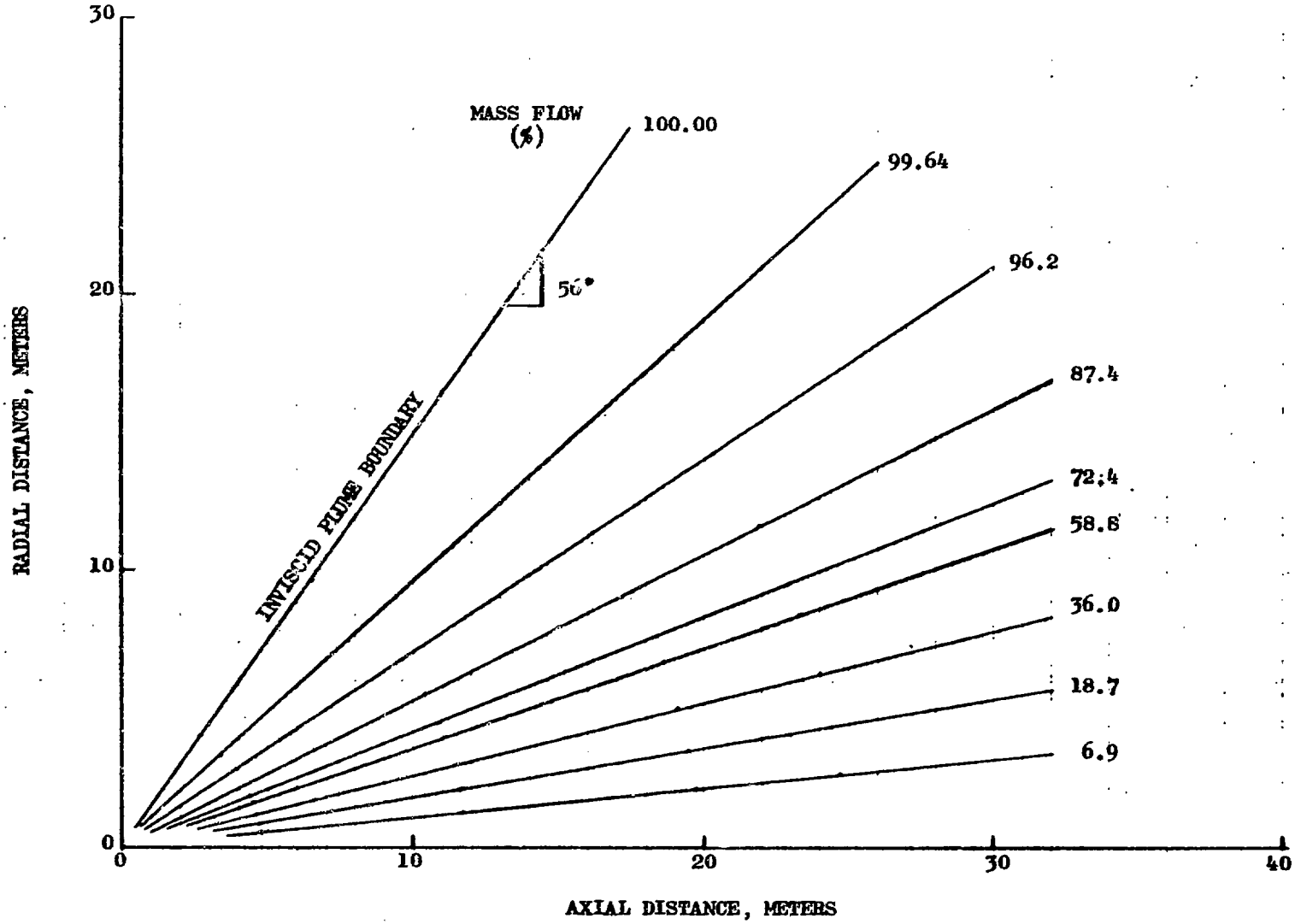

Figure 50. Inviscid, Gas Only, Plume Study

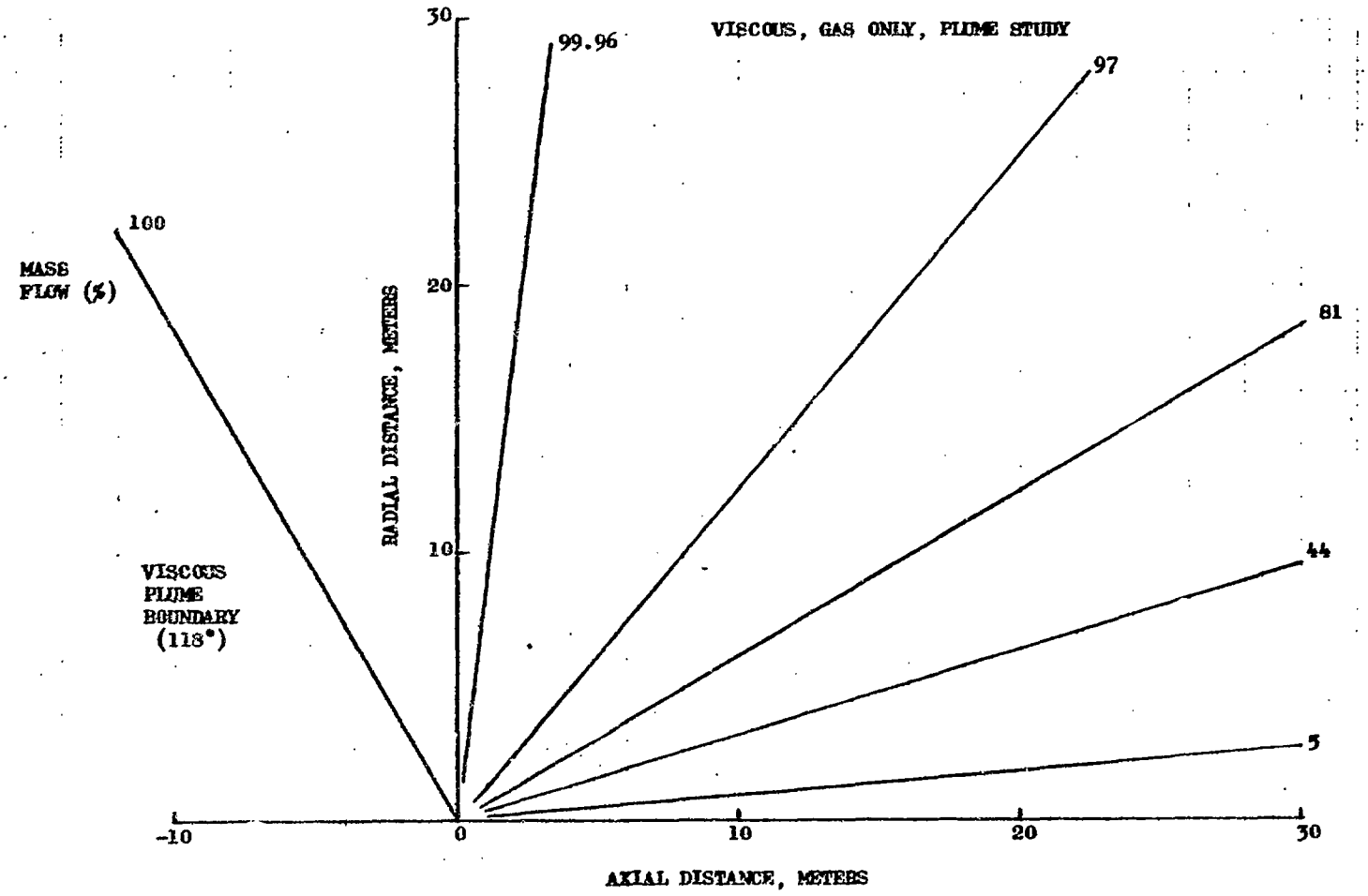

Figure 51. Viscous Gas Only, Plume Study

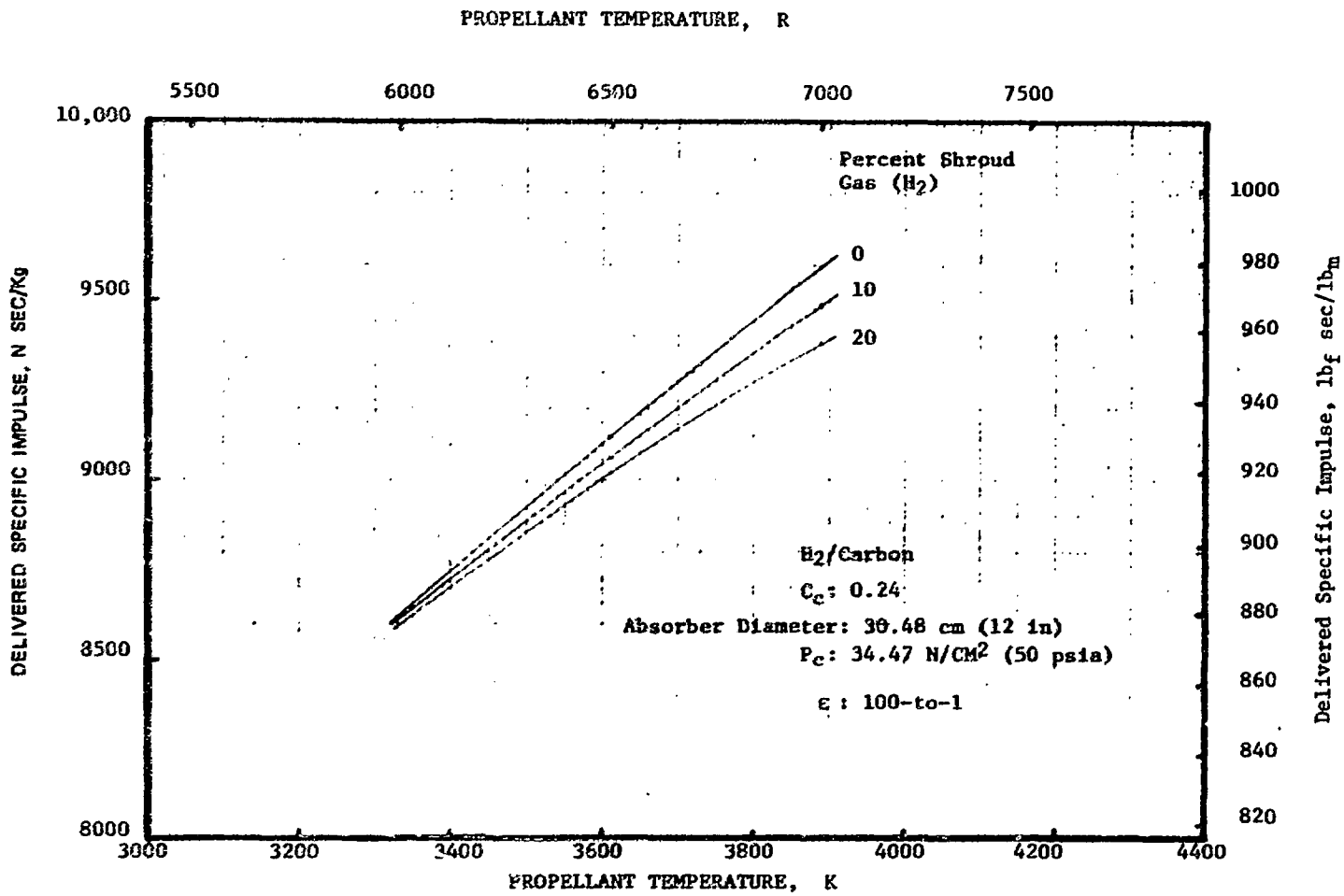

Figure 52. Delivered Specific Impulse for the Particulate Absorption Absorber/Thruster

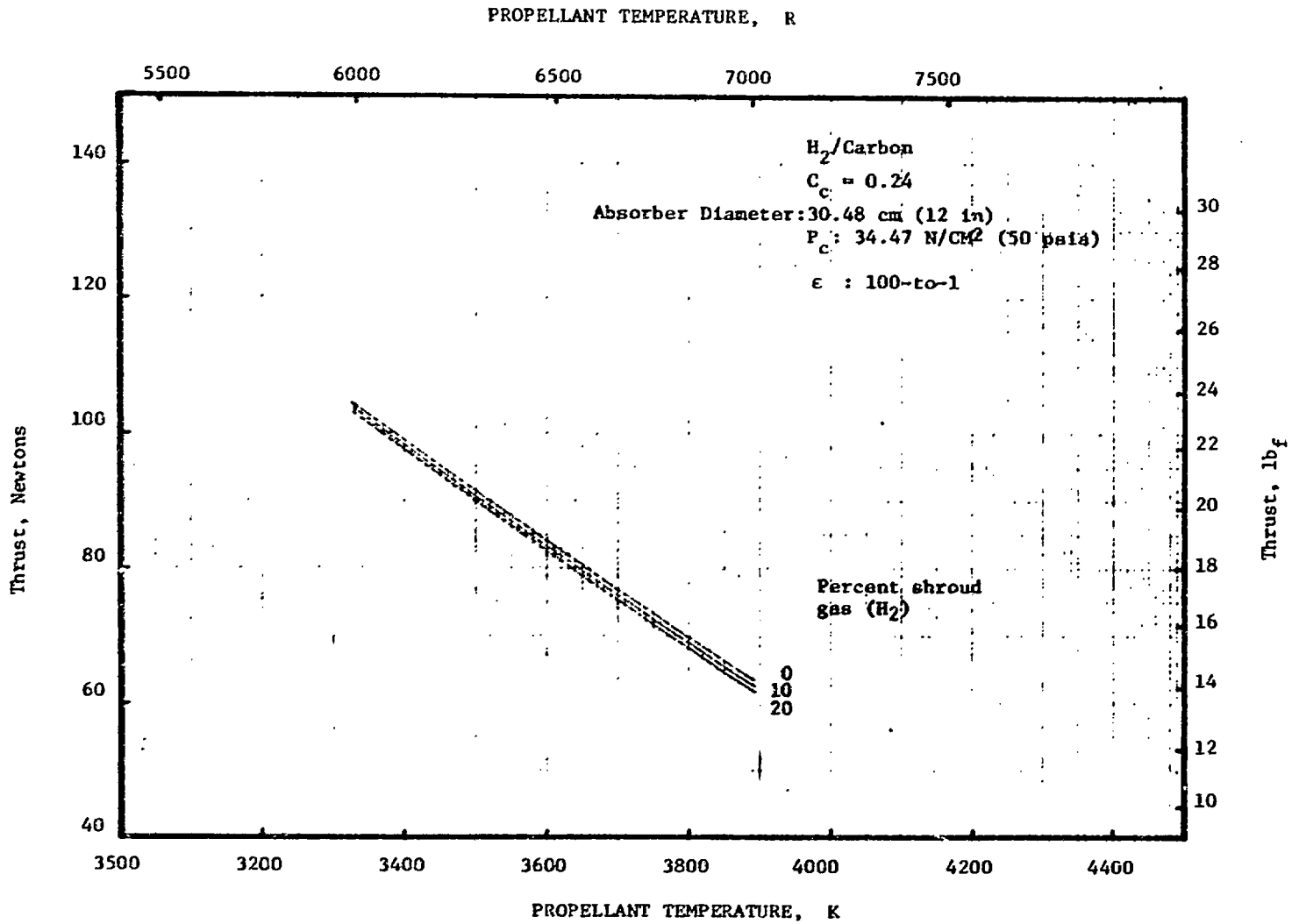

Figure 53. Delivered Thrust for the Particulate Absorption Absorber/Thruster

Concept Evaluation Summary

The results of the windowed particulate/molecular absorption concept evaluation are summarized as follows:

• Window cooling	Marginal with single pane quartz with IR reflective coating and angled cooling jets
	Lowest temperature with hemispherical window
• Seedant	Carbon particles (highest I_s potential with minimum concentration)
• Absorber Efficiency	70% direct solar radiation absorption + heat exchange and minimum IR radiation loss
• Delivered Specific Impulse	Up to 9494 N sec/Kg (968 lbf sec/lbm)
• Thrust	Approximately 62.3 N (14 lbf) at 3889 K (7000 R) (with 10% shroud coolant)
• Absorber/Thruster Cooling	Regenerative cooling using rhenium tubes ($T_{WG_{MAX}} \cong 2644$ K (4300 F)
• Limitation	Rapid heating of carbon particles without significant reaction (~40 milliseconds)
• Other features	No moving parts

WINDOWED VORTEX FLOW CONCEPT EVALUATION (RETAINED SEED)

The evaluation of the Windowed Vortex Flow concept, illustrated in Fig. 54, concentrated on analysis of the vortex flow to establish the design parameters. The basic approach to the analysis was to apply the theory and experimental data which have been well established in conjunction with cyclone separators, while noting that the requirement of the small particle size, 0.5μm for carryover (or escape), and the significant heatup of the gas phase do not permit direct extension of a present separator design practice. Preliminary analysis was made based on the existing model and the assumption of isothermal gas phase in the chamber and was refined by accounting for the change of vortex structure associated with density reduction. The model was structured to determine the performance in terms of size-graded separation probability allowing parametric variation of inputing key design parameters, such as length, diameter of the chamber, size and number of inlets, and diameter of gas phase exhaust port.

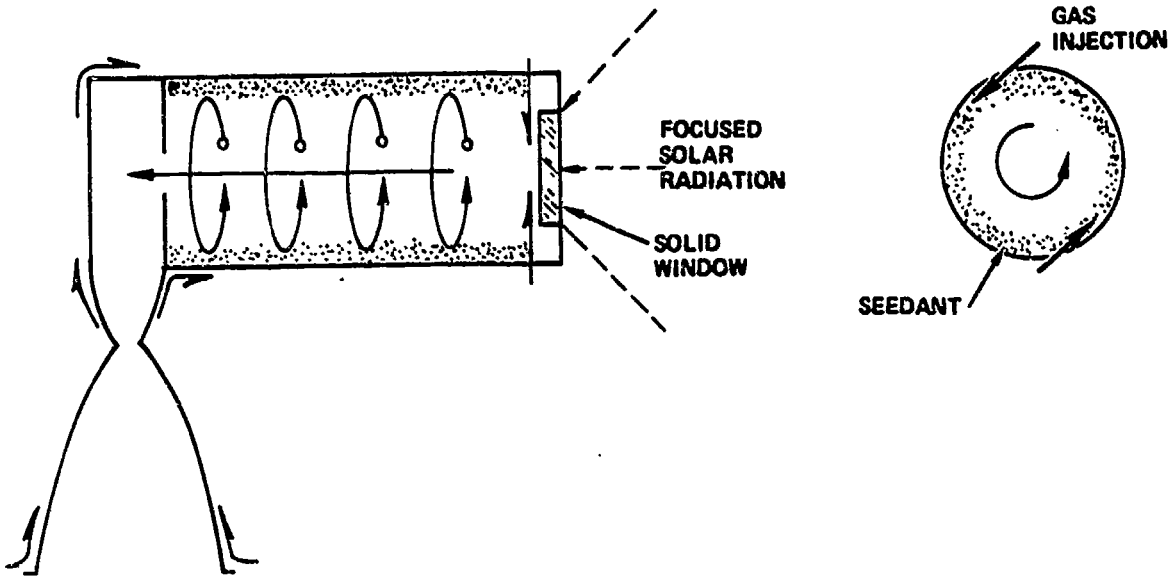

Figure 54. Windowed Vortex Flow Concept (Retained Seed)

The vortex chamber configuration evaluated in the parametric study (illustrated in Fig. 55) included variation of chamber diameter (inside) from 20.32 cm (8 inches) to 40.64 cm (16 inches) and effective chamber length from 40.64 cm (16 inches) to 91.44 cm (36 inches). The chamber exit (to thruster) size was selected at 4.32 cm (1.7 inch) diameter to induce a maximum rotational velocity at the vortex core at approximately 1.52 cm (0.6 inch) radial position from the axis of symmetry which approximately corresponds to the equilibrium position for 0.5μm diameter particle size with 50% chance of retention.

Two tangential inlets to the vortex chamber (0.64 by 5.08 cm or 0.25 by 2-inch slot) were considered. The results of this parametric study indicated substantial loss of carbon particles in the submicron size range and only a minor difference of the retention capability for chamber design variations considered. A typical analysis result is presented in Fig. 55. This design study limited the vortex chamber flow pressure drop to approximately 0.17 N/cm^2 (0.25 psid). For the smaller carbon particle size (approximately 0.5 μm diameter) desired for efficient radiation absorption, approximately 30% of the particles would escape the vortex chamber.

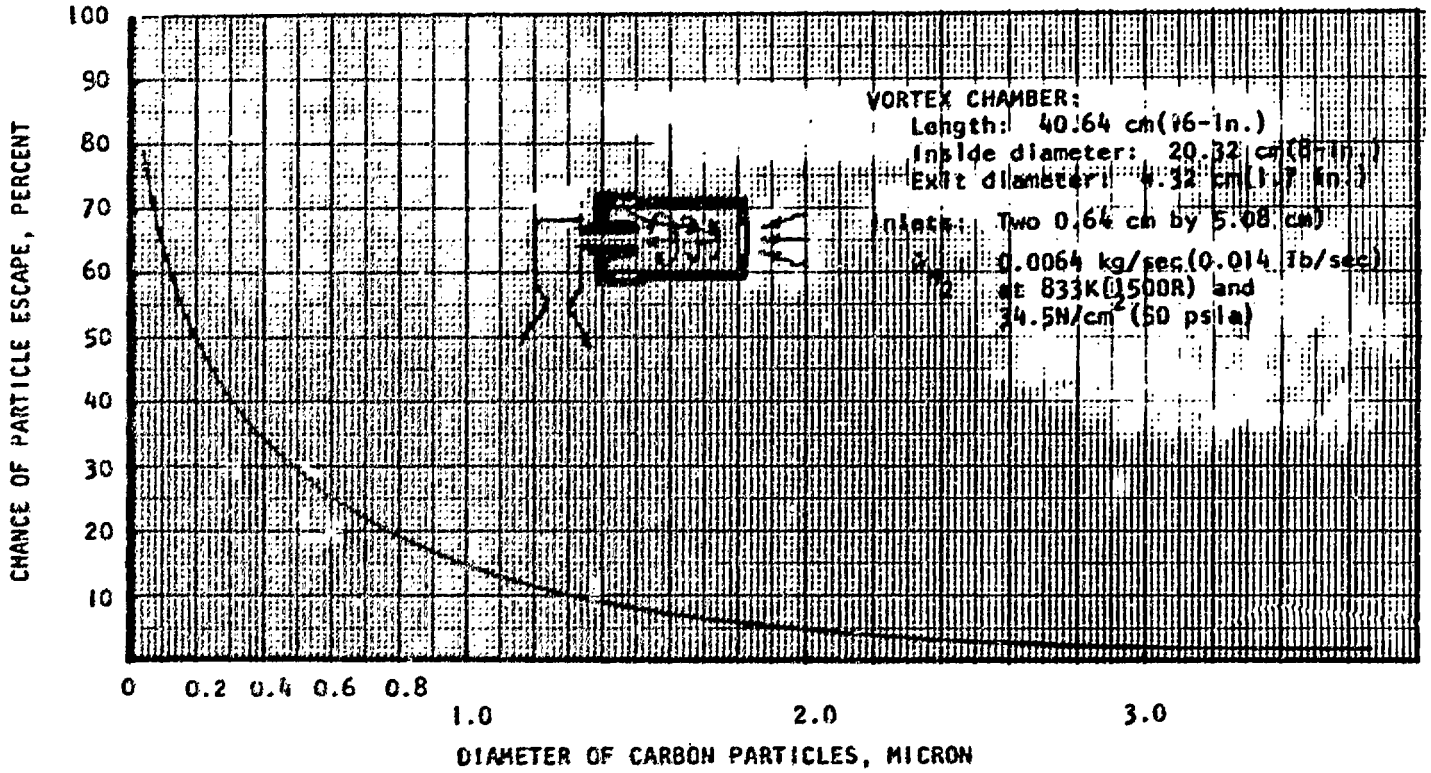

Figure 55. Probability of Carbon Particle Loss Under Steady State Vortex Flow

The carbon seedant retention capability of the vortex flow concept was evaluated further by considering two additional cases of reduced diameter of the vortex chamber exit. With the inlets and overall chamber size unchanged for practical consideration, the chamber exit size is the only parameter that can change the rotational velocity at the vortex core.

The computation, assumed isothermal gas phase (at 833 K, 1500 R), and was made for exit diameters of 0.5- and 1-inch, which represented a significant reduction from 1.7-inch considered previously. Two significant points resulted from analysis:

1. The peak velocity at the vortex core, bounded by free vortex region and the forced vortex region (or, solid body-like rotation), showed only small increase in either case (the momentum of the rotating gas at the core region suffers further dissipation due to a steeper forced vortex region rendering effectively little change to the velocity for narrower vortex core diameter)
2. As a result, seedant retention capability showed insignificant improvement, thus still representing nearly 30% cumulative loss of the submicroscopic particles.

It was concluded that the vortex flow concept is inherently limited for the present application and no further analysis was conducted.

In addition, from a practical application standpoint, the vortex flow concept lacks an effective means for preventing massive seedant escape during the start and shutdown transients of the absorber chamber. This difficulty can be best overcome by a rotating fluidized bed concept in which the high pressure gas (unheated) provides the energy to turn the absorber cylinder and the seedant constituting the bed material is kept within the absorber during the transients by discharging the gas to ambient, bypassing the absorber section. This approach was evaluated as the rotating bed concept presented in the following section.

ROTATING BED CONCEPT (RETAINED SEED)

The evaluation of the rotating bed concept, illustrated in Fig. 56, considered the following areas: drive method, window cooling, seedant and bed behavior, thruster thermal conditions and overall concept performance. In addition, a conceptual design was completed.

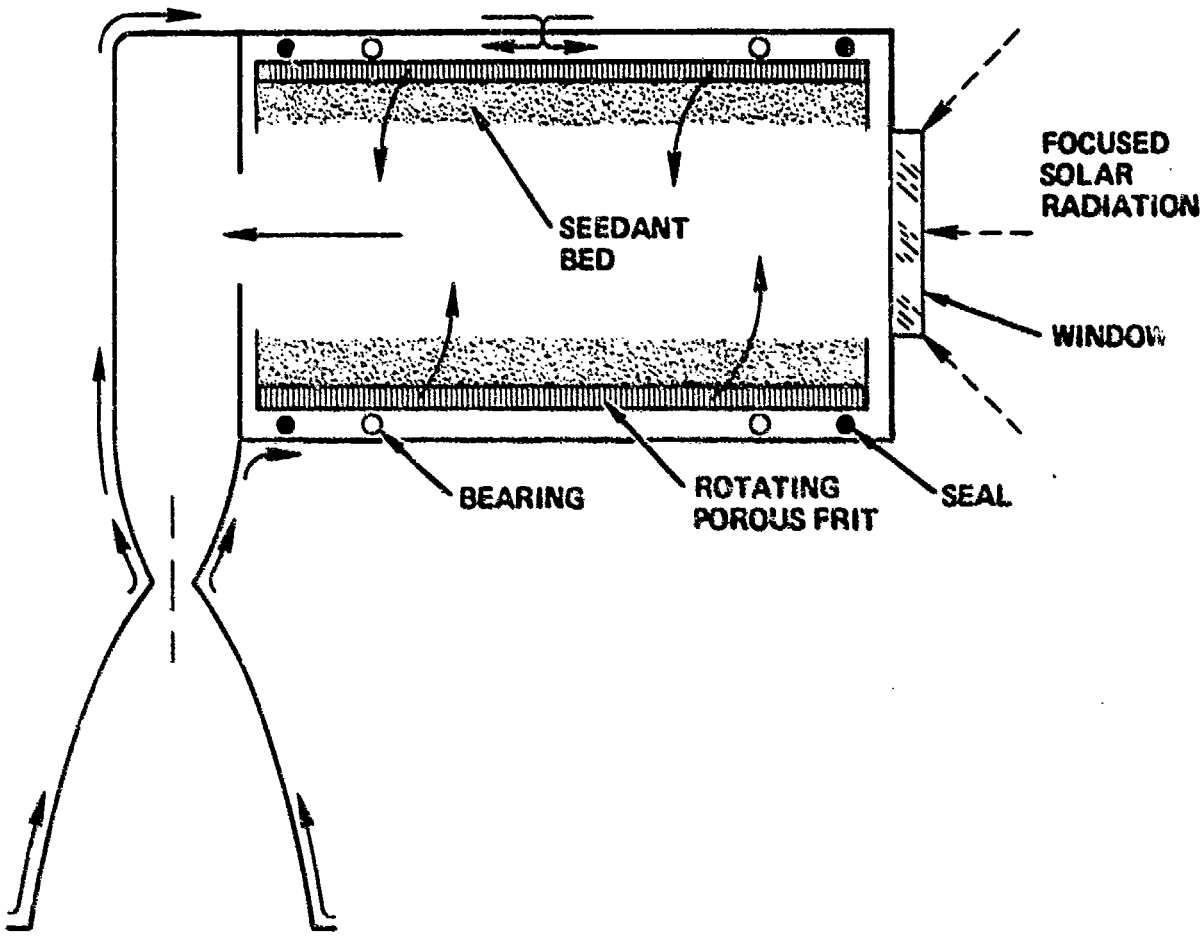

Figure 56. Rotating Bed Concept Retained Seed

Rotating Bed Drive

Three candidate rotating bed drive approaches evaluated are presented in Fig. 57 along with respective advantages and disadvantages of each approach. The first approach incorporates a turbine drive which utilizes the available

		ADVANTAGES	DISADVANTAGES
Turbine	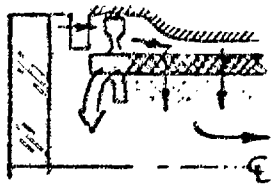	• Simple Approach • Utilizes Available H_2 Flow	• Slow Start • Higher H_2 Inlet Pressure • Response of Speed Control (Electronic Sensor with Turbine Bypass)
Electric Motor	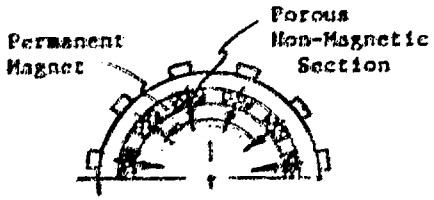	• Rapid Startup • Lower H_2 Inlet Pressure • Electronic Speed Control	• Requires External Power Supply • Difficulty of Uniform Porous Cylinder Flow Distribution • High Temperature Magnetic Components
Gear Driven	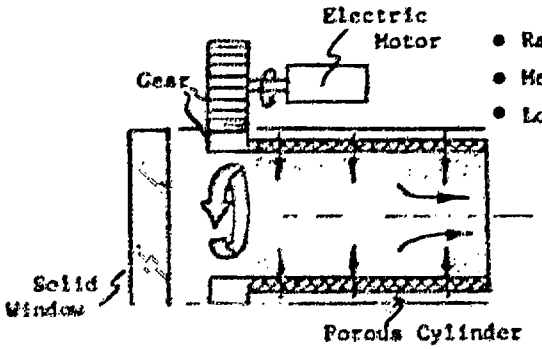	• Rapid Startup • Mechanical Speed Control • Lower H_2 Inlet Pressure	• Gear Life Limits • Sealing of Gears • Requires External Power Supply

Figure 37. Rotating Bed Drive Approaches

heated hydrogen flow. This approach is simple but may result in a relatively slow engine start and speed control response. The speed control is maintained by bypassing hydrogen flow away from the turbine and directly to the porous cylinder. Due to the turbine pressure ratio, a higher inlet hydrogen pressure will be required with this approach.

In the second drive approach, the porous cylinder becomes the rotor of an electric motor through the incorporation of permanent magnets. This approach provides a rapid start with electronic speed control and would reduce the inlet hydrogen pressure. However it does require an external power supply and due to the incorporation of the magnets within the porous cylinder, the flow uniformity through the cylinder would be questionable. Also unlike conventional electric motors, the magnets will be subjected to the 835 K (1500 F) temperature environment.

The third drive approach was a geared mechanical drive utilizing an external electric motor. The problems envisioned with this approach were the gear life and sealing of the gears from the absorber.

From this qualitative evaluation of the three drive approaches, the hydrogen turbine approach was selected for further evaluation.

Window Cooling

Window cooling analyses were performed for the rotating bed concept using the three candidate window configurations as shown in Fig. 58. Results of the analysis are shown in Fig. 59 through 61. The hemispherical and double pane window configurations resulted in approximately the same maximum window temperatures but as shown in Table 2, the hemispherical configuration achieved significantly lower axial temperature differentials which would reduce thermal strains. The resulting window temperatures for this window concept were marginal. Even increasing the window coolant to 20% of the total hydrogen flow resulted in a marginal cooled condition with maximum temperatures of 1168 K (1643 F). However the analysis approach used was somewhat conservative in

WINDOW CONFIGURATION	ADVANTAGES	DISADVANTAGES
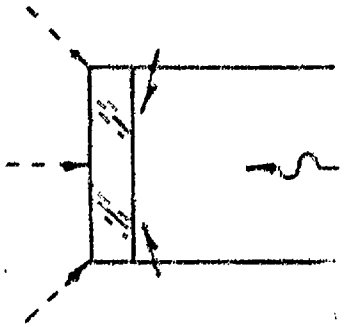 Single Pane	• Simple Approach	• Performance loss due to cooling • Cooling difficulty at high Reradiation levels
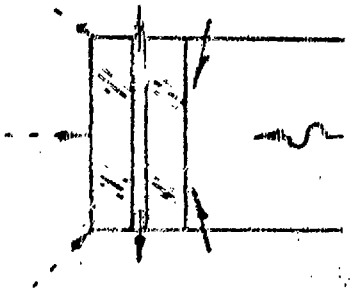 Double Pane	• Second window absorbs most of IR radiation • Second window receives additional cooling (convective)	• More complex configuration (fabrication, cooling, and sealing) • No window thickness reduction (engine start loads)
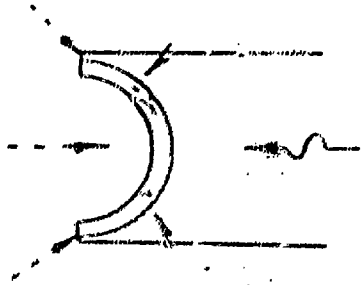 Hemispherical	• Thinner window (Reduced solar and IR absorption) • Reduced thermal gradient	• Complex window configuration (Fabrication mounting and sealing) • Performance loss due to cooling.

Figure 58. Window Configuration Comparison

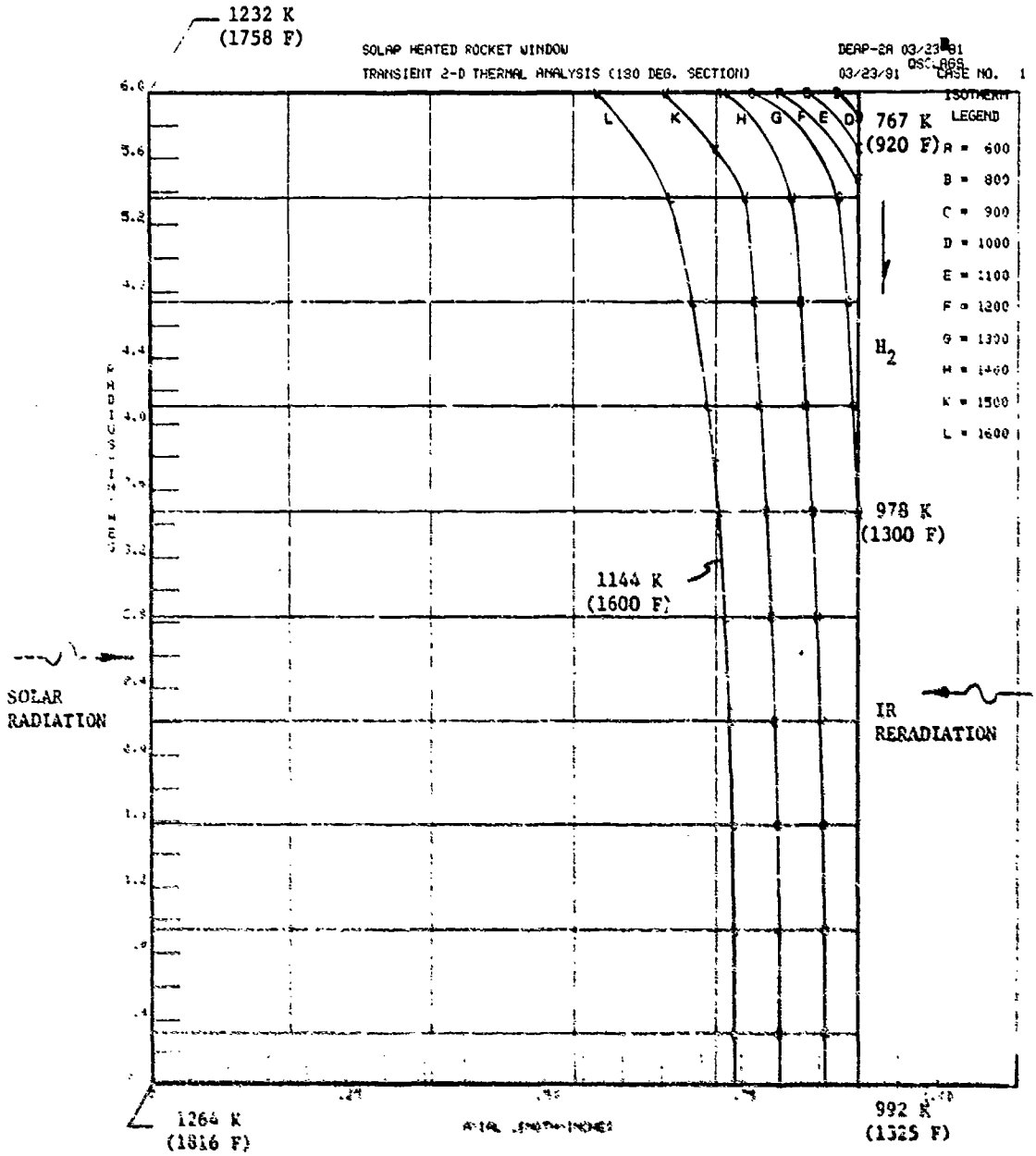

Figure 59. Window (Quartz) Temperature Distribution for Rotating Bed Concept With 30.48 cm (12 in.) Diameter Disc and 85% IR Reflectivity

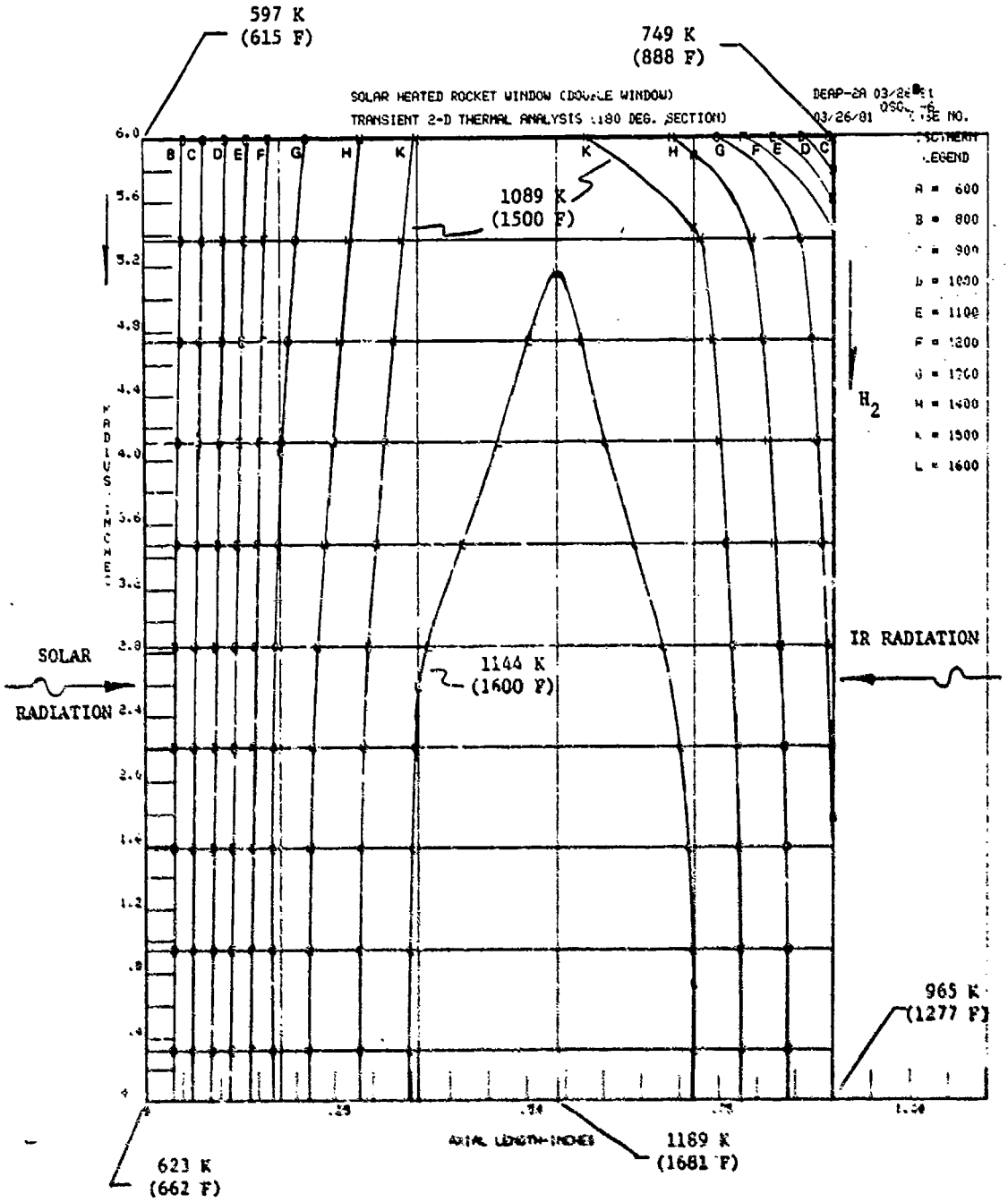

Figure 60. Window (Quartz) Temperature Distribution for Rotating Bed Concept -- 30.48 cm (12 in.) Diameter Double Pane (Inner Window) With 85% Reflectivity

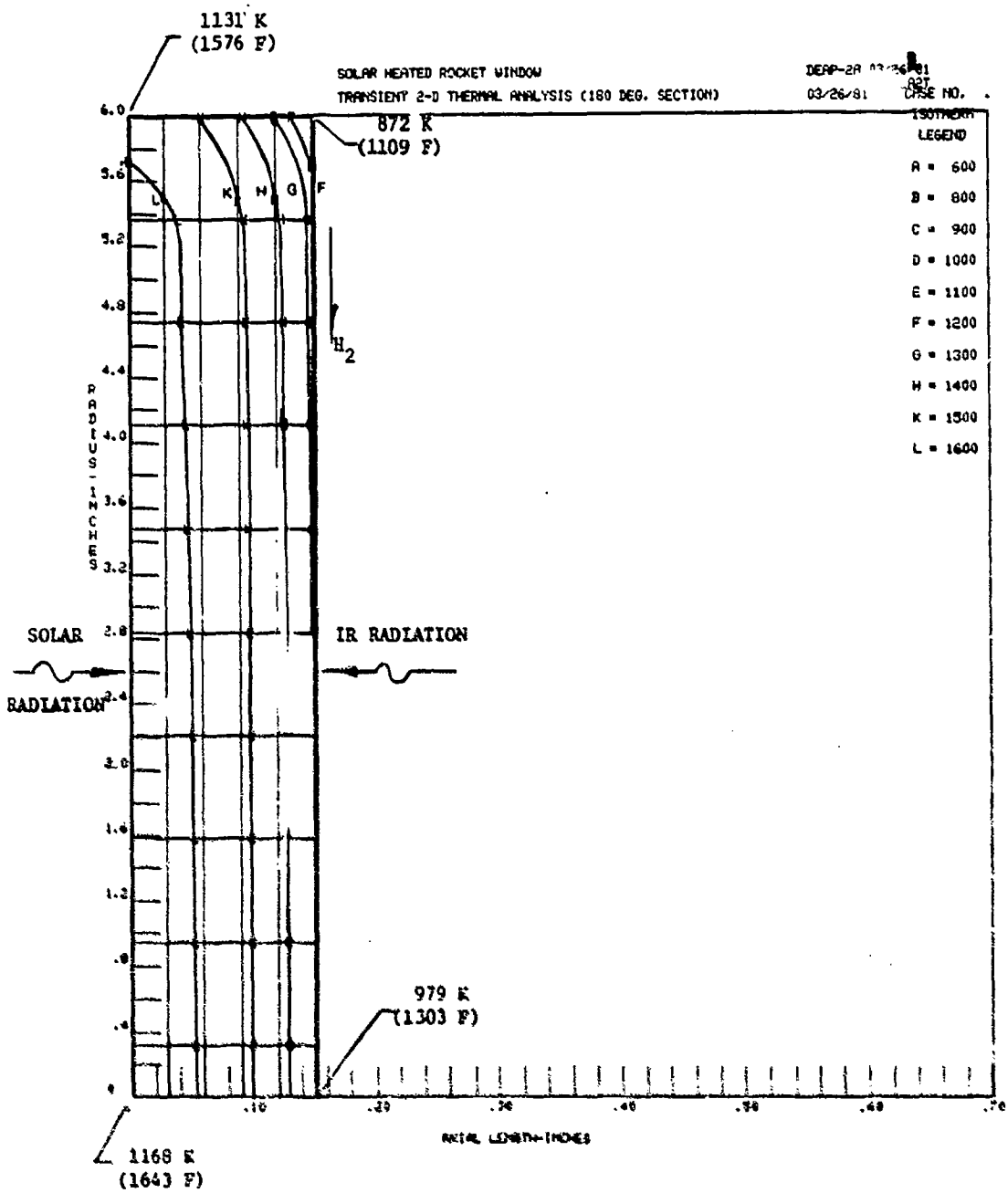

Figure 61. Window (Quartz) Temperature Distribution for Rotating Bed Concept — Hemispherical Window with 85% IR Reflectivity and 20% Window Coolant

TABLE 2. ROTATING BED CONCEPT WINDOW COOLING ANALYSIS SUMMARY

$T = 3889$ K (7000R)
$P_c = 34.47$ N/cm^2 (50 psia)
Propellant: H_2
Window Material: Quartz

Temperature \ Window Configuration	Single Pane (10% Coolant)	Double Pane (10% Coolant)	Hemispherical (10% Coolant)	Hemispherical (20% Coolant)
$(T_{WALL})_{MAX}$, K (F)	1264 (1816)	1189 (1681)	1197 (1694)	1168 (1643)
$(\Delta T_{AXIAL})_{CENTER\ LINE}$, K (F)	273 (491)	566 (1019)	117 (210)	189 (340)
$(\Delta T_{AXIAL})_{EDGE}$, K (F)	491 (883)	491 (884)	192 (346)	259 (467)

that a constant IR reflectivity was assumed independent of the IR source temperature. In reality, a high IR source temperature will result in a majority of the radiation at a lower effective wave length and therefore less IR absorption.

Seedant Evaluation

The basic approach of the rotating bed concept is to continually heat the particles, which in turn heat the hydrogen by extracting heat from the heated particles. The long term exposure of the particles to high temperatures may preclude the use of carbon particles. Chemical reaction of carbon with hydrogen generally form hydrocarbon gases which would significantly reduce the solar radiation absorbing characteristics. However carbide particles such as tantalum carbide and hafnium carbide will tend to form solid hydride coatings on the particle surface which would tend to slow further chemical reactions. Therefore, for the rotating bed concept, the more nonreactive particles such as tantalum carbide would be preferred.

Particle Bed Analysis

The cylindrical configuration of the rotating bed solar radiation absorption surface results in the capture of only a portion of the incoming radiation. The remainder of the solar radiation passes through to the cylinder bottom which must act as a heat exchanger. The influence of the amount of energy absorbed by the particle bed is shown in Fig. 62 as a function of the absorber length-to-diameter ratio (L/D). For the 1.5 L/D ratio desired for bed fluid dynamics, 72.5% of incoming energy is absorbed by the particle bed.

The basic philosophy in the rotating bed fluid dynamics was to operate the particle bed in a regime between where the bed surface becomes fluidized and the midbed point is fluidized. This approach retains a packed bed mode for the majority of the bed adjacent to the cylinder wall to provide an insulative layer of particles to protect the porous cylinder wall. The resulting bed

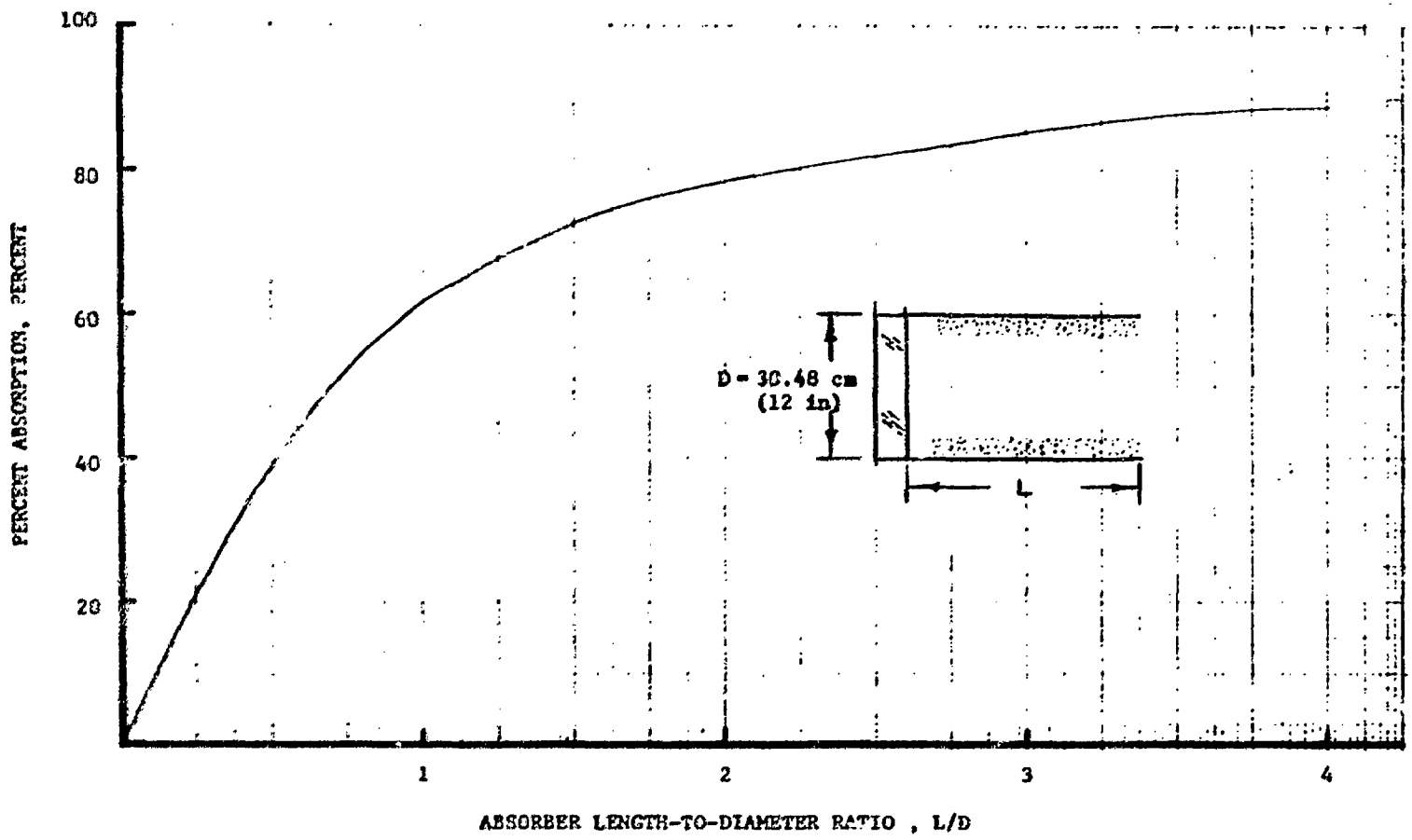

Figure 62. Rotating Bed Concept Solar Radiation Absorption

speed for carbon and tantalum carbide particles is shown in Fig. 63. The tantalum carbide particles only required approximately 1/3 the rotation speed due to their higher density. As the hydrogen flowrate is reduced (reduced radial velocity), the bed rotational speed is reduced.

The calculation of the rotational speed of the porous cylinder involved an iterative analytical procedure using the Galileo number and the particle Reynold's number. The basic criterion in the analysis was to balance the forces on the innermost particles to prevent loss of particles. The forces balanced were the radially outward centripetal force on the particles created by the rotation and the radially inward force caused by the incoming hydrogen flow. The influence of void fraction, geometry, hydrogen temperature, and pressure were included in determining the radially inward force. The hydrogen temperature variation through the bed was approximated by an overall thermal analysis and by assuming a linear gradient through the bed.

The in-bed pressure gradient was computed using the standard Ergun relationship (Ref. 3) for large particle sizes (>500mm) and the Carman-Kozeny relationship (Ref. 4) for smaller particles and laminar flow. As shown in Fig. 64, both relationships resulted in approximately the same pressure gradient.

A regenerative cooling analysis of the thruster indicated that the hydrogen entering the porous cylinder was approximately 1089 K (1500 F). Therefore, the bearings and seals associated with the rotating porous cylinder would be subject to this thermal environment. An overall bed thermal analysis revealed that bed exit hydrogen temperatures approaching 3889 K (7000 R) were theoretically attainable.

Thruster Thermal Analyses

The thermal analysis of the rotating bed concept thruster was performed for a final hydrogen temperature of 3889 K (7000 R) and a 100-to-1 nozzle area ratio. A conventional tapered tube thrust chamber was analyzed in which the axial rhenium tube array would be welded or brazed into a tubular assembly.

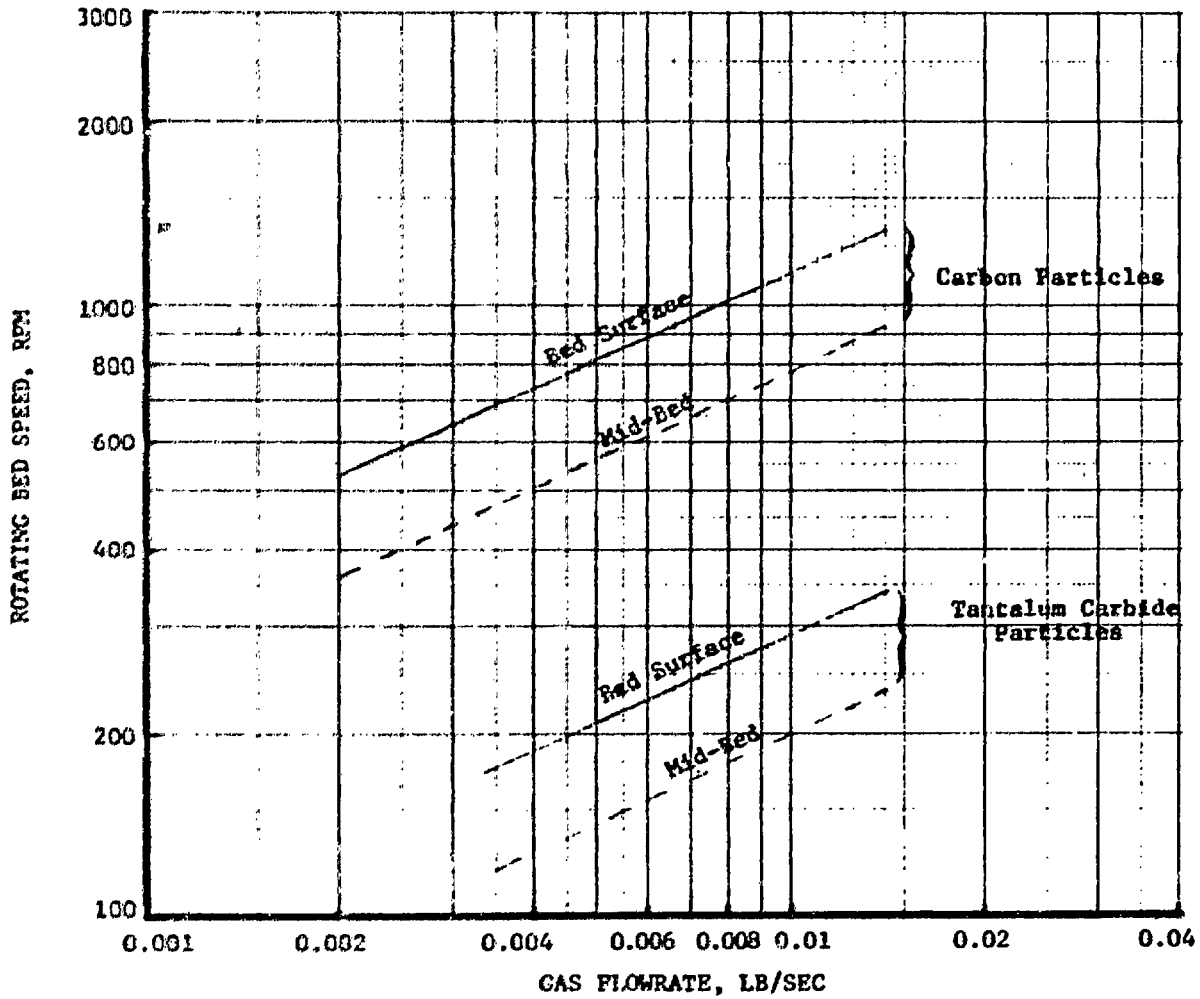

Figure 63. Rotating Bed Speed Requirements

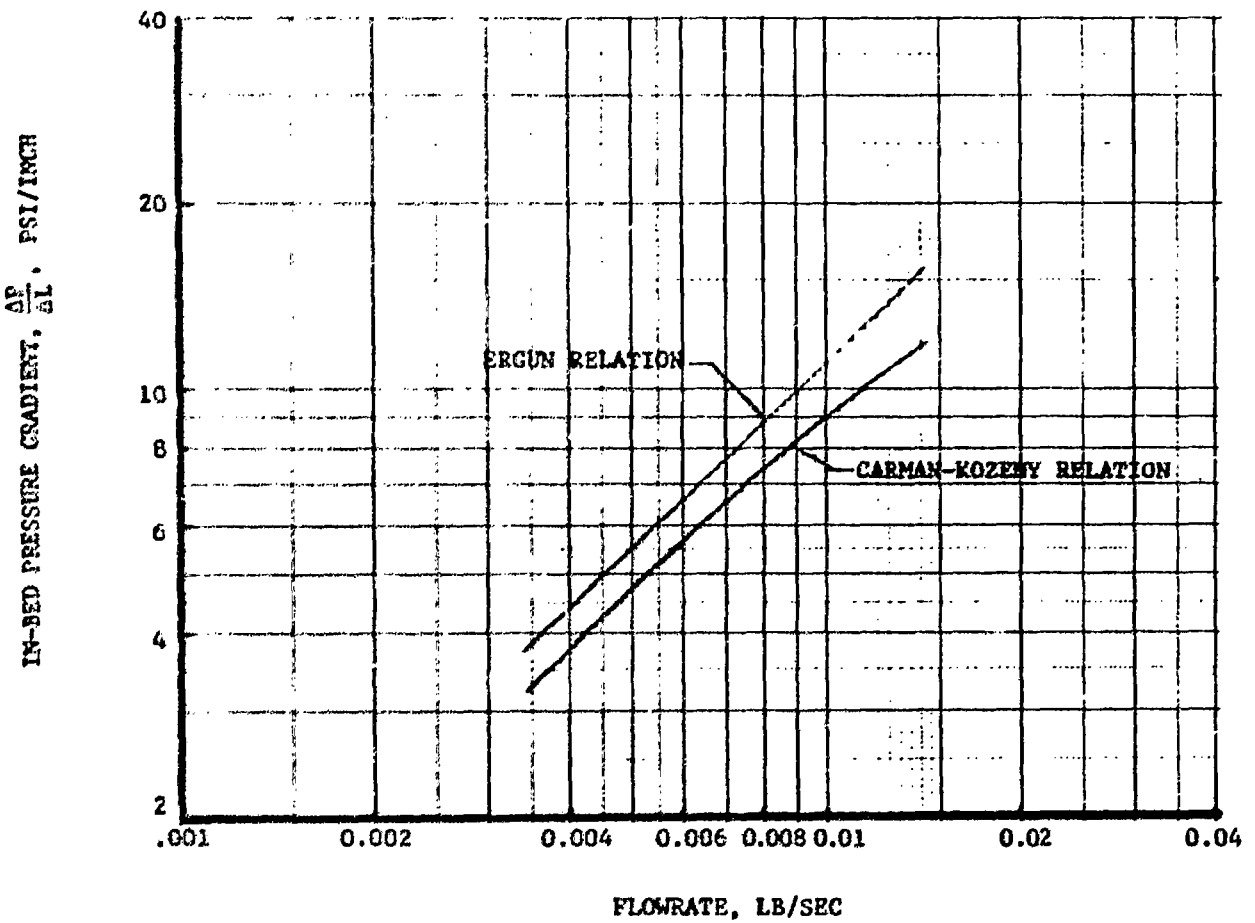

Figure 64. In-Bed Pressure Gradient

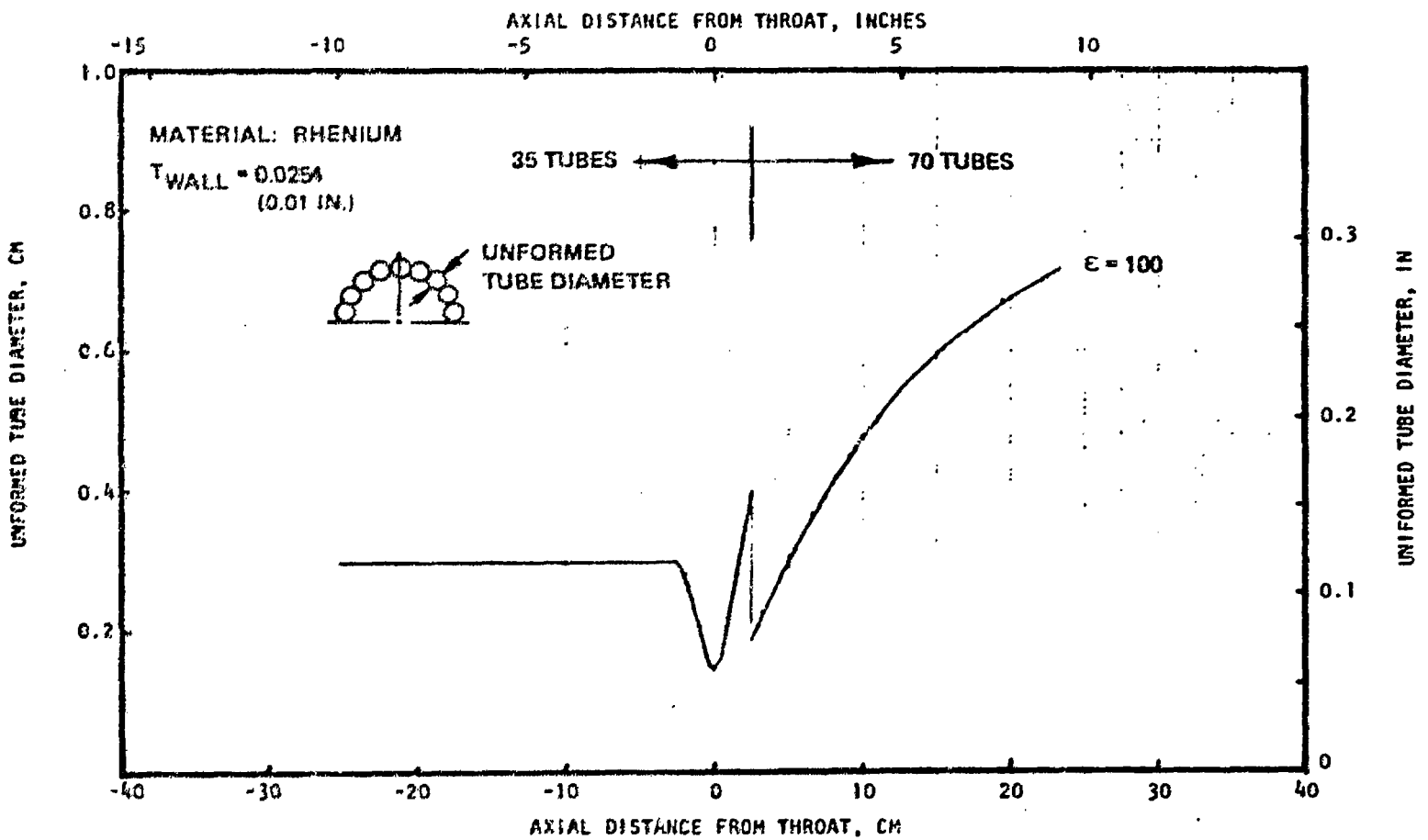

Figure 65. Tube Dimensions for Rotating Bed Thruster

A tubular thrust chamber will have tubes filling the entire circumference of the thrust chamber, as illustrated in Fig. 65. To accomplish this at each axial location with a varying internal diameter, a varying tube diameter (tapered tube) is required. The axial tube diameter variation is shown in Fig. 65 and the resulting axial temperature and pressure distributions are presented in Fig. 66 and 67, respectively. The maximum wall temperature of 2667 K (4340 F) occurred near the thruster sonic point and the thruster coolant pressure drop was only 11 N/cm^2 (16 psi).

Thruster Performance

The thruster-delivered specific impulse and thrust variation with hydrogen temperature and percent window cooling are shown in Fig. 68 and 69, respectively. At a hydrogen temperature of 3889 K (7000 R), the rotating bed absorber/thruster achieved a delivered specific impulse of 10591 N sec/kg (1080 lbf sec/lbm) with 20% window cooling and a thrust of approximately 67 N (15 lbf). This specific impulse performance was the highest of all concepts evaluated.

Concept Evaluation Summary

The results of the rotating bed concept evaluation are summarized as follows:

• Window Cooling	Marginal with hemispherical window (20% window coolant)
• Seedant	100 μm diameter carbon (if feasible), tantalum carbide or hafnium carbide Essentially 100% particle retention during mainstage
• Absorber Efficiency	73% direct solar radiation absorption plus heat exchange and minimum IR radiation loss
• Delivered Specific Impulse	Up to 10,591 N sec/kg (1080 lbf sec/lb_m)
• Thrust	Approximately 66.7 N (15 lbf) at 3889 K (7000 R)
• Absorber/Thruster Cooling	Regenerative cooling using rhenium tubes, $T_{w_{max}}$ = 2667 K (4340 F)

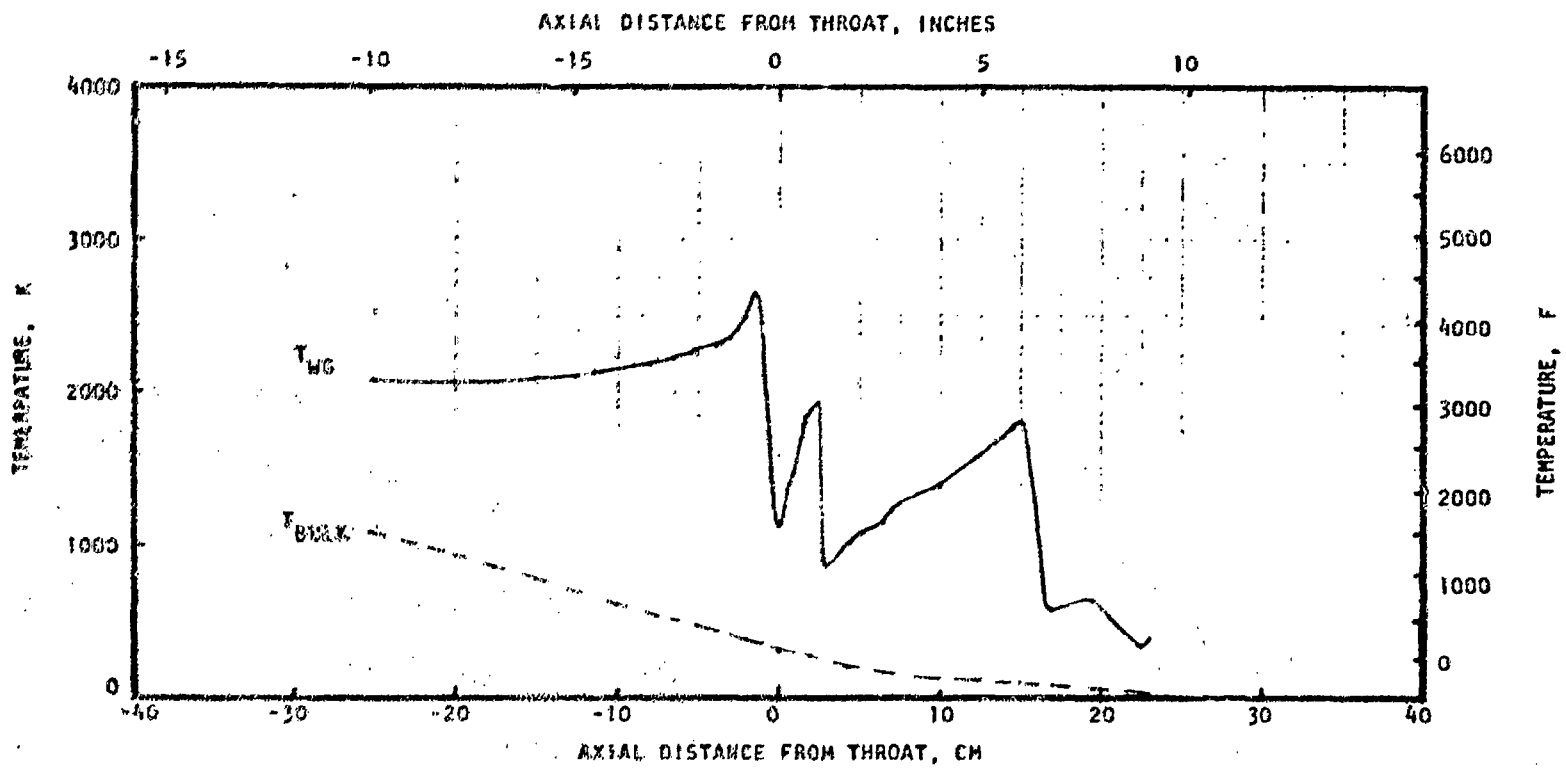

Figure 66. Temperature Distribution for Rotating Bed Thruster

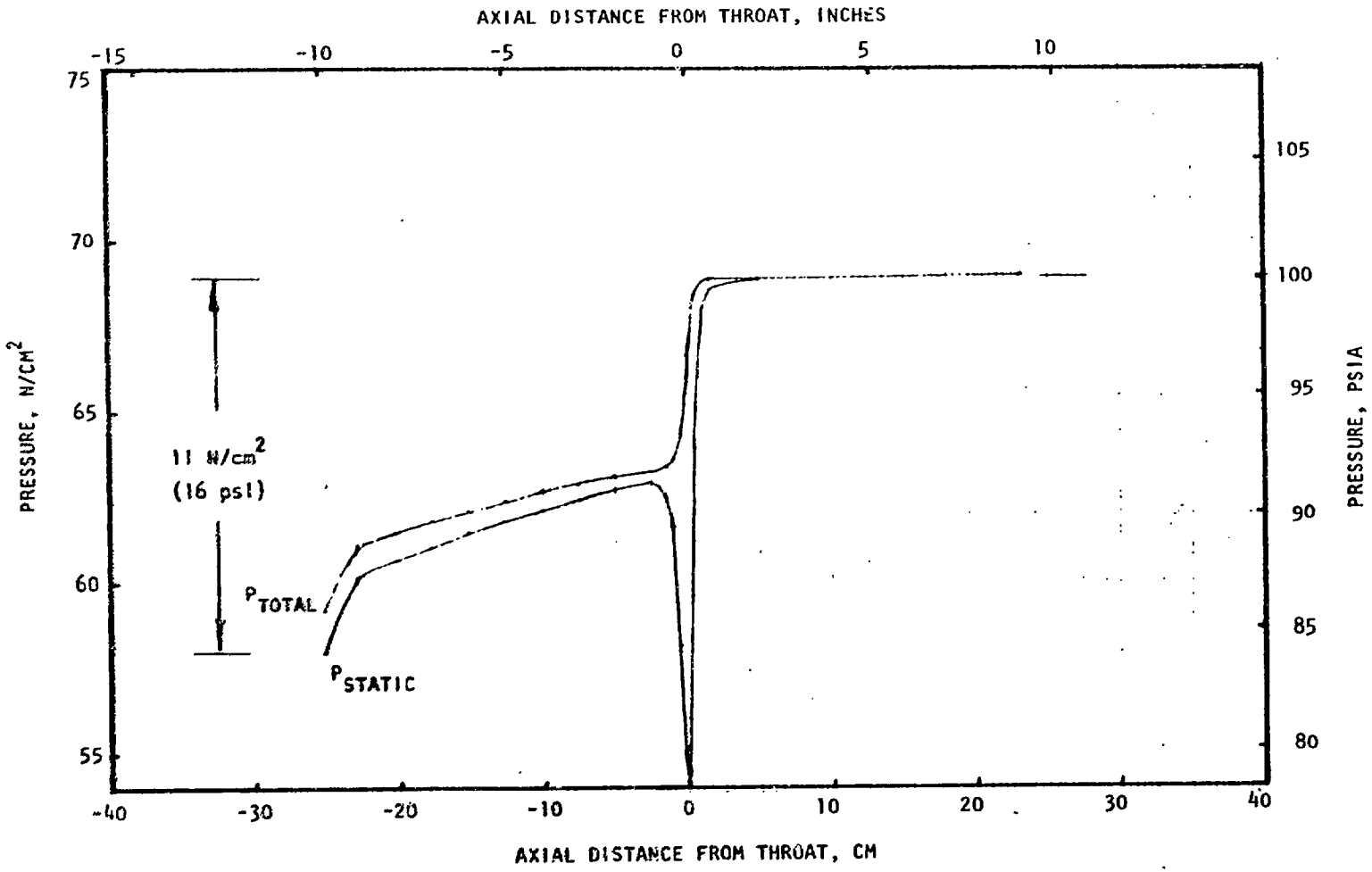

Figure 67. Thruster Coolant Pressure Distribution for Rotating Bed Thruster

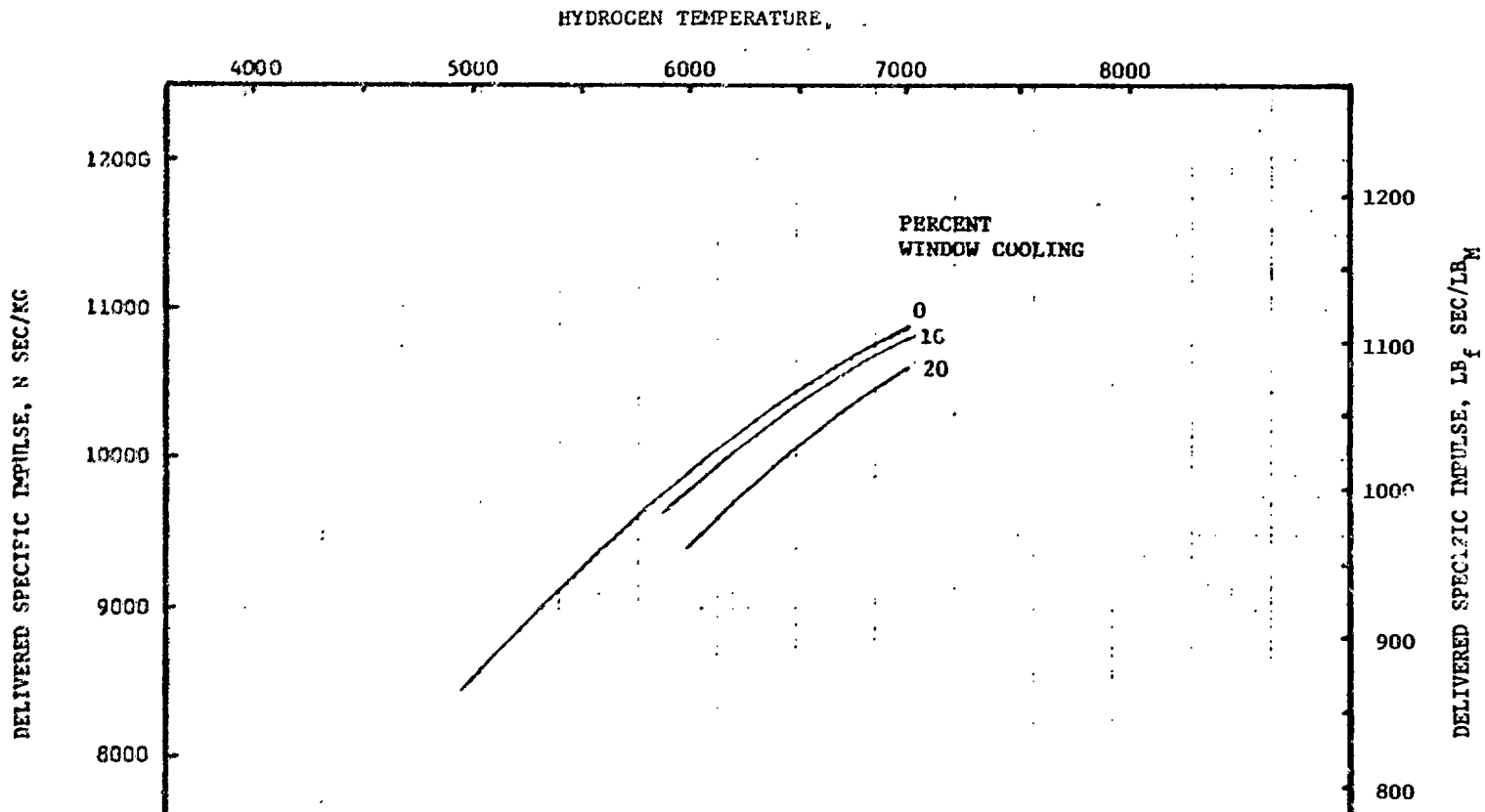

Figure 68. Delivered Specific Impulse for the Rotating Bed Absorber/Thruster

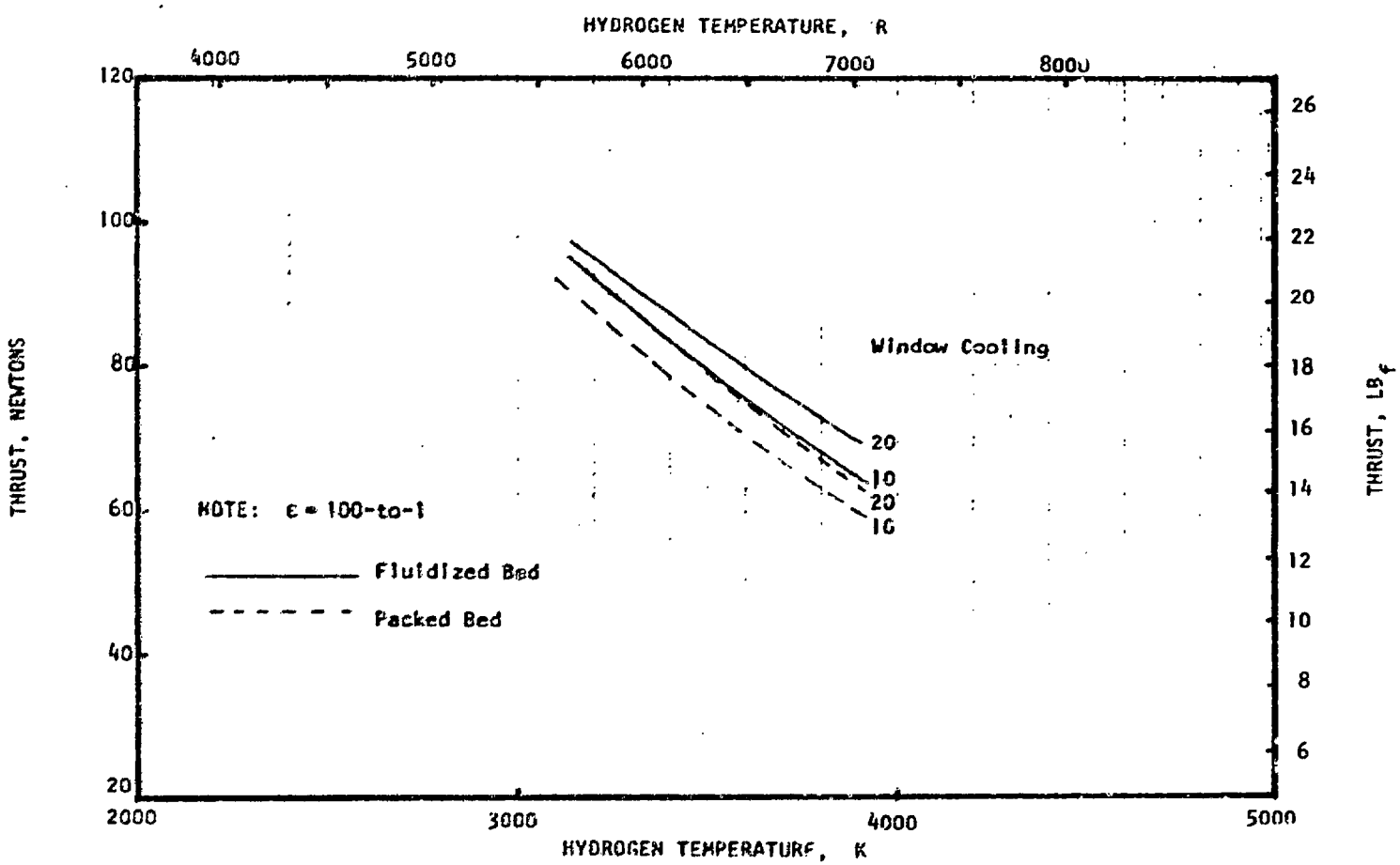

Figure 69. Delivered Thrust for Rotating Bed Absorber/Thruster

- Limitation — Window cooling
  Rotating Bed Operation
  Bearing life
- Other Features — No discharged seed during mainstage
  Relatively low absorber wall temperature

Conceptual Design

Utilizing the preceding analysis results, a conceptual design of the rotating bed concept was prepared (Fig. 70) for a 30.48 cm (12-inch) diameter absorber and with two absorbers feeding one thruster. The main propellant, hydrogen, first cools the thruster entering at the nozzle exit and after the thruster splits and cools the absorber-to-thruster transition tube and the cylinder end. This heated hydrogen flow is then split for each absorber between the turbine inlet and the downstream porous cylinder inlet. The magnitude of this flow split is dependent on the flow required to maintain a constant speed for the rotating bed and is controlled by the turbine bypass valve.

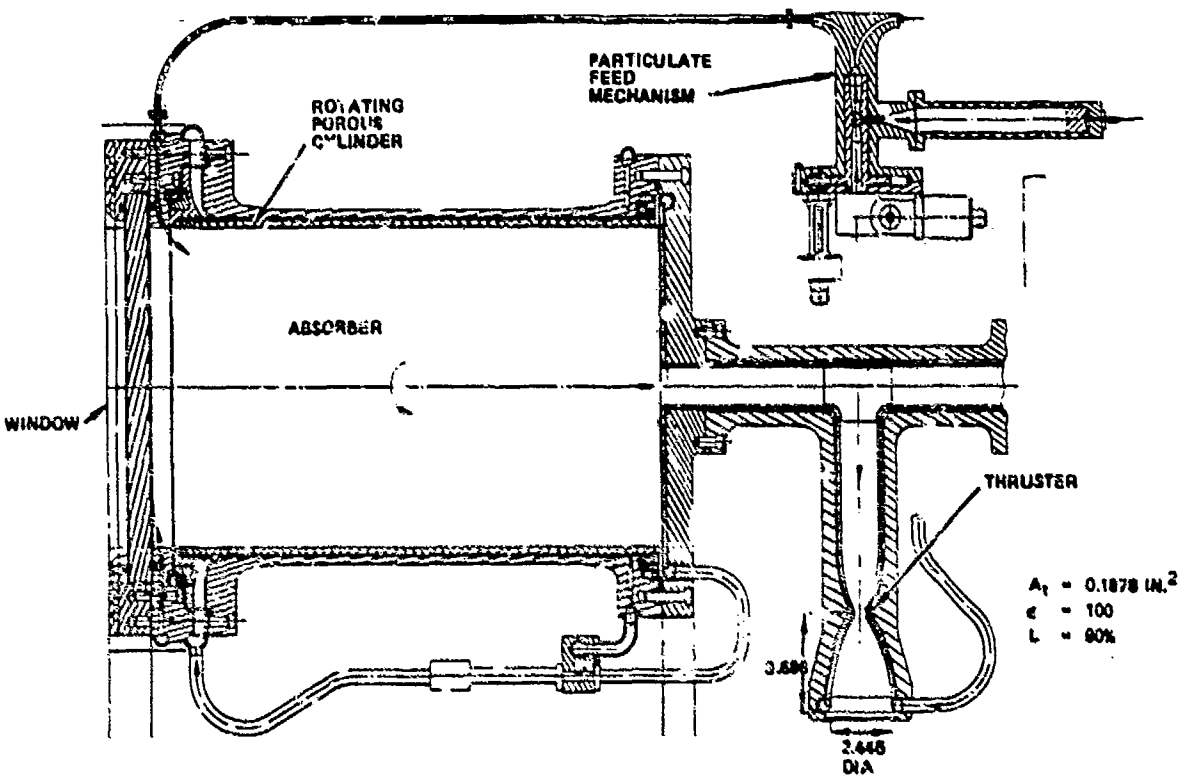

Figure 70. Rotating Bed Absorption Concept

The particulate feed mechanism (Fig. 71) provides the initial charge of particles and any subsequent make-up particles. The system transports the particles pneumatically using a portion of the hydrogen flow. Gently curved passages (Fig. 70) are provided in the particulate feed system to prevent local buildup of particles.

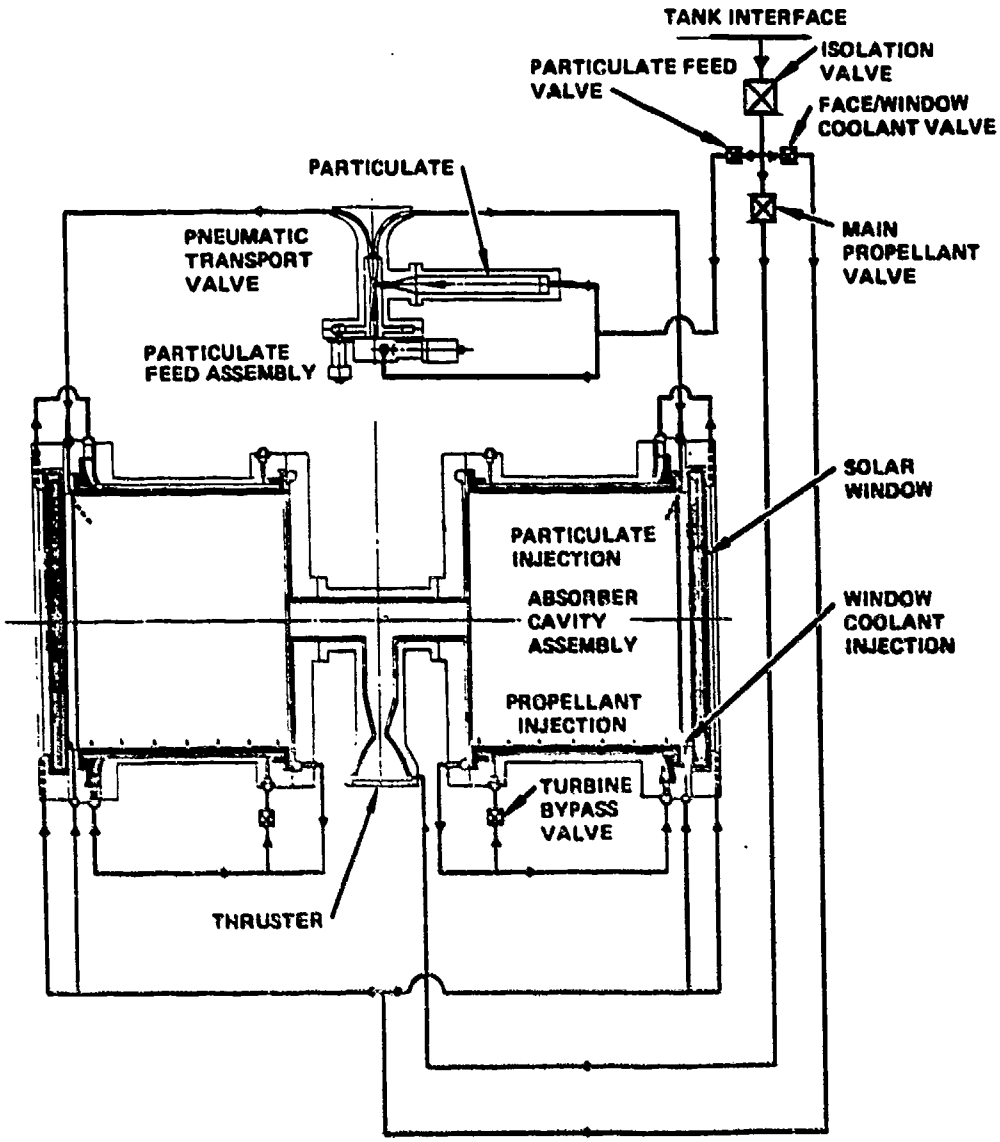

Figure 71. Rotating Bed Absorption Concept Schematic

Although a conventional sleeve bearing arrangement is illustrated in Fig. 70, the foil bearings shown in Fig. 72 offer the most promising bearing approach since this type of bearing has been tested in a 978 K (1300 F) temperature environment. The foil bearing consists of a series of compliant foil segments attached to the stationary housing and are cooled and lubricated by the hydrogen flow.

ADDITIONAL ADVANCED ABSORBER/THRUSTER CONCEPTS

In the process of evaluating the AFRPL-identified absorber/thruster concepts, other advanced concepts were identified that could potentially solve technical difficulties associated with the current concepts. The difficulties addressed were (1) solid window cooling; (2) excessive cavity reradiation; and (3) high-temperature rotating components. These identified advanced absorber/thruster concepts were not evaluated in detail and will require further analytical evaluation to verify their potential advantages.

Stationary Porous Cylinder

In the process of evaluating the rotating bed concept and the windowed heat exchanger cavity concept, a rather simple approach was defined which replaces the rotating porous cylinder and particle bed with a stationary porous cylinder. The solar radiation heats the porous cylinder and the hydrogen is heated as it flows through the porous cylinder. For this concept, the maximum hydrogen temperature achieved would be dependent on the porous cylinder material temperature limit. A porous carbon-carbon composite cylinder could be treated to form a carbide coating (such as tantalum carbide) to possibly withstand temperatures approaching 3889 K (7000 R).

Reduced IR Radiation View Factor

The marginal window cooling difficulty encountered with the high performance potential windowed absorber/thruster concepts led to the reduced IR radiation view factor configurations shown in Fig. 73 which can be utilized for a variety of windowed concepts. The approach, using a 90-degree bend with a specular reflector, would reduce the diffuse IR reradiation from the high-temperature particle/gas mixture and yet not influence the incoming solar radiation. The reduction of this diffuse emitter/window view factor permits a

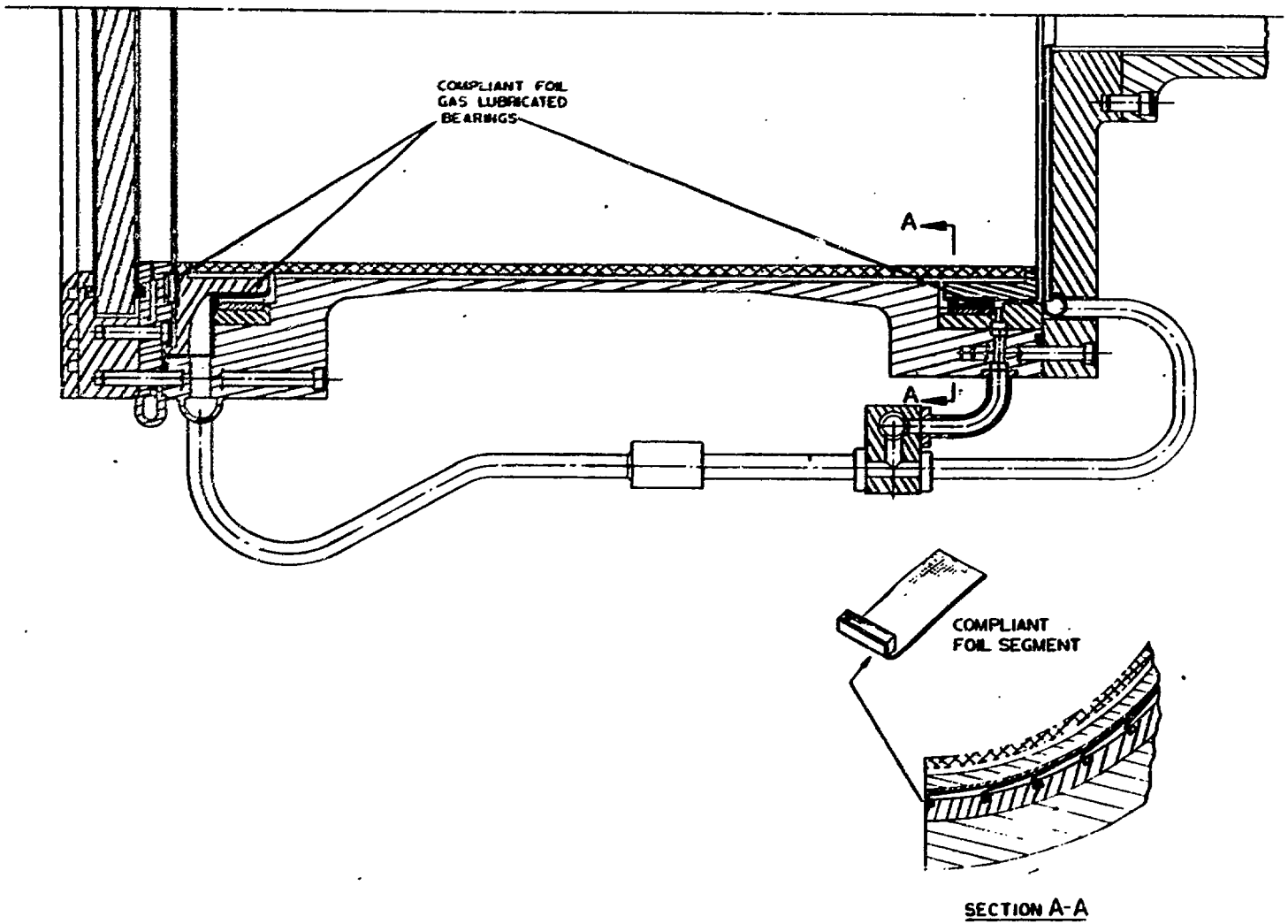

Figure 72. Rotating Bed Foil Bearing Approach

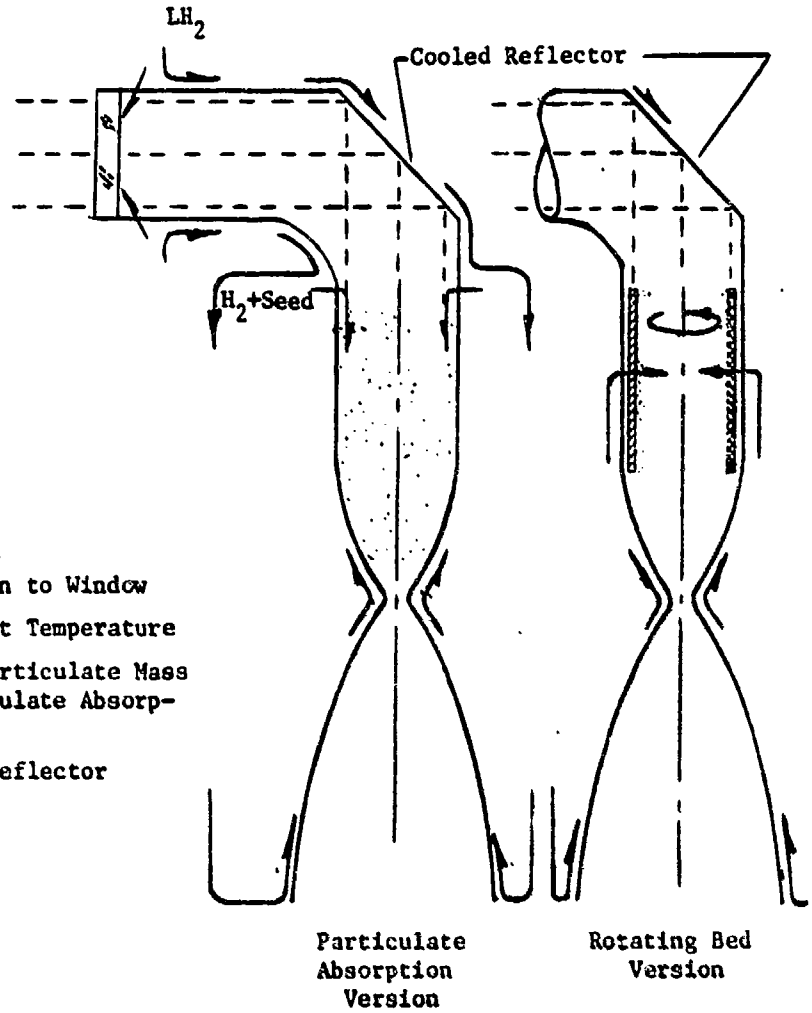

FEATURES

- Reduced IR Radiation to Window
- Increased Propellant Temperature
- Possibly Reduced Particulate Mass Fraction for Particulate Absorption Concept
- Requires a Cooled Reflector

Figure 73. Reduced IR Radiation View Factor Configurations

window temperature reduction and increases the absorber thermal efficiency over an equivalent length straight absorber configuration.

The implementation of this advanced concept requires the added component of a cooled reflector. The cooling of the reflector is necessary in order to maintain the reflector's structural integrity in a high-temperature environment. However, the advantages offered by this concept of reducing window temperatures and increasing absorber efficiency are significant.

Aero Window/Absorption

Another potential approach to alleviate the window cooling difficulty is to utilize an aerodynamic window. Nozzles are used to provide supersonic flow across the window opening and the flow of the nozzles is received and diffused in the absorption chamber. The aerodynamic window has been successfully used in laser systems and typically has 5 to 10% leakage flows. Aerodynamic window flow leakage losses become proportional to the opening size of the window aperture, which in turn is related to solar beam focusing ability. Based on developing laser technology, the reduction in the aperture to a minimum can be accomplished by providing the incoming beam focal point at the window aperture plane through the utilization of a secondary reflector, as shown conceptually in Fig. 74. The focusing of the solar radiation is limited to overall concentration ratios of 40,000 to 50,000, which leads to an approximate aerodynamic window-to-thruster throat diameter ratio of 50 to 1 for currently envisioned thruster chamber pressures. The resulting aerodynamic window still may be too large to provide a reasonable design. Therefore, although the aerodynamic window may solve the window cooling difficulty with advanced concepts, a detail analysis of aerodynamic window flow leakages and trades of lower chamber pressure need to be performed to assess the overall feasibility of this concept. This approach can be applied to any of the windowed absorber/thruster concepts.

Also, elimination of the solid window and its associated difficulties can make this approach potentially applicable to other advanced energy beam propulsion concepts having extremely high propellant temperatures.

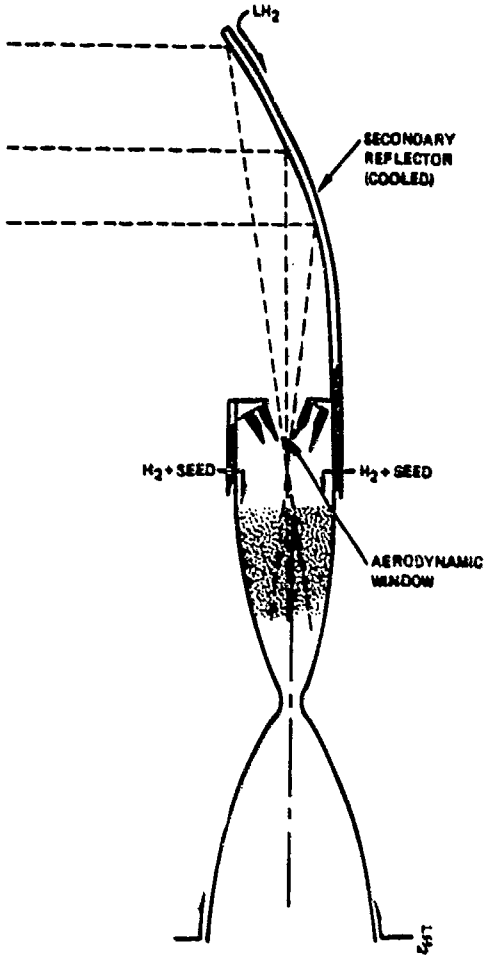

FEATURES

- Not Limited Due to Window Cooling
- Applicable to all Windowed Approaches
  - Particulate Absorption
  - Rotating Bed
  - Stationary Porous Cylinder
- Potential Application to Extremely High Propellant Temperature Propulsion Concepts
- Added Components
  - Aerodynamic Window
    - Replaces Solid Window
  - Supersonic Flow Nozzle
    - Creates Supersonic Flow for Aerodynamic Window
  - Cooled Secondary Mirror

Figure 74. Aerowindow/Absorption Concept

The disadvantage of this concept is the increased complexity created by the added components (aerodynamic window, supersonic flow nozzle, and the cooled secondary mirror). Also obviously with these added components, added technology unknowns exist.

Concept Evaluation Summary

The results of the stationary porous cylinder and the aero-window advanced concepts are summarized as follows:

Stationary Porous Cylinder Concept

• Window Cooling	Marginal with hemispherical window (IR reflectivity coating with angled cooling jets)
• Absorber Efficiency	Similar to rotating bed concept
• Delivered Specific Impulse	Up to 10385N sec/kg(1059 lbf sec/lbm)
• Thrust	Approximately 71N(16 lbf) at 3778 K (6800 R)
• Limitation	Window cooling
	Porous cylinder material (chemical reaction with H_2, temperature)
• Other Features	No moving parts
	No seedant required
	Relatively low absorber wall temperature

Aerowindow/Absorption Concept

• Potential	High I_s
	Application to other modes of beamed energy propulsion
• Limitation	Reradiation
	Aerodynamic window flow loss
• Other Features	No solid window
	No moving parts

MATERIALS AND FABRICATION ASSESSMENT

The high operating temperatures of the absorber/thruster concepts evaluated ($\geq$ 5000 R) required specific assessment of possible materials and fabrication techniques which could be utilized. Two areas requiring special attention were window and absorber/thruster wall materials and fabrication.

Window Materials

A summary of pertinent material properties for candidate absorber/thruster window materials are presented in Table 3. Desirable window properties are high transmittance, low absorption coefficient, high melting temperature, high modulus of rupture, and high thermal conductivity. Typically a high transmittance and a low absorption coefficient go together and will minimize the heat absorbed by the window and reduce the window cooling requirements. A high modulus of rupture reduces the window thickness required to withstand a given pressure differential and this reduced thickness will reduce the window heat absorption. A high melting temperature typically permits a higher allowable operational temperature, and a higher thermal conductivity improves the effectiveness of the cooling and reduces the thermal gradients.

The fluoride materials, which are primarily used for laser windows, are highly transmissive in ultraviolet wavelength range although the high transmissive characteristics may extend into the visible solar range. As shown in Table 3, all the fluorides have lower melting temperatures and lower strengths than either quartz or sapphire. Barium fluoride (BaF_2) and calcium fluoride (CaF_2) begin to soften at temperatures considerably below their melting points, approximately 833 K (1500 R) for calcium fluoride and 811 K (1460 R) for barium fluoride. Lithium fluoride has the lowest melting temperature of the window material candidates.

Sapphire (Al_2O_3) has the highest melting temperature and modulus of rupture; however it also has a high average absorption coefficient over the wavelength range of interest. Quartz (SiO_2) has the second highest melting temperature, a relatively low average absorption coefficient, and the second

TABLE 3. WINDOW MATERIAL PROPERTIES

MATERIAL	MELTING POINT, K	0.3 TO 2.5 MICROMETER WAVELENGTH			AT 811.1 K (1000 F)	
		APPROXIMATE TRANSMITTANCE, %	APPROXIMATE REFLECTIVITY, %	APPROXIMATE ABSORPTION COEFFICIENT PER CM (PER INCH)	MODULUS OF RUPTURE, Kg/cm2 (PSI)	THERMAL CONDUCTIVITY CAL/CM SEC K (BTU/IN. SEC R)
SAPPHIRE (Al_2O_3)	2323 (4182)	87	8	0.0130 (0.03302)	3516.4 (50,000)	0.025 (1.39×10^{-4})
QUARTZ (SiO_2)	1901 (3422)	92	8	0.00126* (0.0032)	660 (9885)	0.0048 (2.69×10^{-5})
BARIUM FLUORIDE (BaF_2)	1628 (2940)	92	~3	0.00188** (0.004572)	274*** (3900)	~0.573 (0.0032)
CALCIUM FLUORIDE (CaF_2)	1700 (3053)	94	~4	0.003** (0.00762)	507*** (7200)	~0.573 (0.0032)
LITHIUM FLUORIDE (LiF)	1121 (2018)	95	-	-	<599*** (<8000)	0.86 (0.0048)
STRONTIUM FLUORIDE (SrF_2)	1736 (3125)	~70	-	0.0015** (0.0038)	387*** (5500)	1.189*** (0.0066)

*BASED ON COMMERCIAL GRADE VALUES AT ROOM TEMPERATURE
**AVERAGE VALUE AT 2.5 μm
***VALUE AT ROOM TEMPERATURE

highest modulus of rupture. Therefore based on this evaluation of window materials, sapphire and quartz appear to be the most promising window materials with quartz the preferred material.

As discussed earlier, an IR reflective coating of Indium tin oxide coating on the inner window surface is an attractive approach to reduce energy losses and reduce window heating. Several vendors contacted indicated the feasibility of applying the coating and a realistic effectiveness IR reflectivity of 85%. The IR reflectivity is a function of coating thickness and is dependent on thickness uniformity. More recent vendor contacts by AFRPL personnel resulted in aditional Indium tin oxide data that indicated an unaccounted-for absorption in the visible wavelength range and the transition wavelength region between transmission and reflection. Therefore, although a highly IR reflective coating shows promise, other coating materials need to be evaluated.

Absorber/Thruster Wall Materials

Material requirements for this application are that the material be capable of withstanding temperatures up to 2778 K (5000 R) with sufficient strength, be compatible with hydrogen, and be fabricable. The first requirement eliminates all but a few refractory metals and a few carbon-based materials. There are four elements with melting points above 3056 K (5500 R): tungsten, tantalum, rhenium, and carbon. Tungsten has the highest melting temperature (3683 K or 6630 R) of any metal and is not susceptible to hydrogen embrittlement and is the most resistant to hydrogen permeation. Tungsten-rhenium alloy also has similar characteristics. The primary disadvantage of tungsten and its alloys is the difficulty of fabricating components. Tungsten can be welded but undergoes recrystallization during welding and loses ductility. Therefore, component fabrication and joining presents a major problem with tungsten.

Carbon and rhenium have the next highest melting temperature (greater than 3667 K or 6600 R and 3450 K or 6210 R, respectively). Rhenium has similar high-temperature strength characteristics to tungsten and is ductile at room temperature and also ductile after welding. Carbon-carbon composite presents an attractive wall material with excellent high-temperature strength characteristics, but does require a protective layer for use with hydrogen.

Tantalum has a melting temperature (3269 K or 5885 R) less than those of rhenium and carbon, and has significantly lower ultimate tensile and creep strengths.

Therefore, of the refractory metals, rhenium is the most logical wall material candidate and in addition a carbon-carbon composite with a high temperature carbide coating for the carbon-based material is an attractive candidate.

Rhenium. Since rhenium is a metal, it offers many advantages over carbon. Rhenium is very ductile and can be machined and formed by standard techniques. It can be brazed and welded. Because rhenium has a high melting point 3458 K (6224 R) and a close-packed structure, it is expected to be very resistant to the permeation of hydrogen. Though rhenium has a lower tensile strength than carbon-carbon composites at 2778 K (5000 R), its strength is adequate for currently considered configurations. Using representative rhenium tube samples, leak and proof tests have been conducted at room temperature and elevated temperatures approaching 2778 K (5000 R). No noticeable leaks were encountered. Also rhenium tube samples were joined using a welded sleeve with excellent results. Therefore, from a fabrication standpoint, current technology is sufficient to build a rhenium absorber/thruster.

Carbon-Carbon Composite. At 2778 K (5000 R) carbon-carbon composite is probably the highest strength material available. This material is lightweight and easily machined. However, since carbon-carbon composites are porous, a permeation-resistant coating is required. Carbide coatings can be deposited by chemical vapor deposition but the small coolant passages required in the absorber/thruster would be very difficult to coat uniformly. In addition the absorber/thruster would require the joining of several carbon-carbon composite pieces. The joining of composites can be accomplished with an adhesive, threads, or a combination of the two. The bonding adhesive is typically a carbon pitch or a pliable graphite material. As with most adhesive bonds, the bond joint is weaker than the material and the strength of such a bond at 2778 K (5000 R) is questionable.

The material cost per pound is comparable for rhenium and carbon-carbon composite; both typically are in excess of $1000/pound. However, the coating and joining of the carbon results in an absorber/thruster approximately twice the cost of a comparable rhenium unit.

High temperature hydrogen compatibility tests with carbon-carbon composites revealed the existence of a significant carbon-hydrogen reaction. This indicates that a carbon-carbon composite absorber/thruster would require a surface coating to retard the carbon-hydrogen reaction and to provide a hydrogen seal.

Therefore, rhenium was recommended for the near term application and carbon-carbon composite as a potential future material pending on the success of sealing internal passages, the carbon-hydrogen reaction, and high temperature carbon-carbon composite joints.

CONCEPT COMPARISON AND SELECTION

Based on the results of the previous concept evaluations for a flight configuration, some general conclusions were reached and are summarized in Table 4. Specific impulse performance and thrust varied over a range for the concepts evaluated. Cooling of the absorber, window, and thruster appeared feasible with proper design and selection of materials. Rhenium appeared the best near-term choice of material for the absorber/thruster while carbon-carbon composites with a high temperature carbide coating appeared attractive for the future. Quartz with an Indium tin oxide IR reflective coating appeared the best choice for window material.

For each of the candidate absorber/thruster concepts, the technology unknowns were defined as shown in Table 5. The windowless heat exchanger cavity concept had the least number of unknowns and the aerowindow/absorption and rotating bed concepts had the largest number of unknowns.

TABLE 4. PHASE I, GENERAL CONCLUSIONS

SOLAR RADIATION ABSORBER

- EFFICIENCY

  >60% ARE ACHIEVABLE

- COOLING

  FEASIBLE WITH COILED TUBE CONFIGURATION

  REGENERATIVE

  REASONABLE COOLING PRESSURE DROP

WINDOW

- COOLING

  HEATING DUE TO A COMBINATION OF INCOMING SOLAR RADIATION AND INTERNAL IR RADIATION

  HEMISPHERICAL WINDOW ACHIEVED LOWEST TEMPERATURE

  MAJORITY OF CONCEPTS WERE FEASIBLE WITH IR REFLECTIVE COATING

THRUSTER

- DELIVERED SPECIFIC IMPULSE: 850 TO 1100 LBF SEC/LBM FOR $\varepsilon = 100$
- THRUST: 62.4 TO 266.7 N SEC/KG (14 TO 60 LBF)
- COOLING

  UNCOOLED RHENIUM FOR $T_{PROP} = 2778$ K (5000 R)

  REGENERATIVE WITH RHENIUM FOR $T_{PROP} > 3611$ K (6500 R)

A comparison of the delivered specific impulse and thrust (for space application) versus achievable propellant temperature of the four primary absorber/thruster concepts are shown in Fig. 75. The rotating bed concept achieved the highest delivered specific impulse due to the higher achievable propellant temperature without the loss of seedant. Figure 76 shows the respective performance losses. An interesting fact shown in this figure is that for the concepts involving the higher propellant temperatures, the largest individual performance loss was the reaction kinetic loss. Therefore, efforts to reduce this loss could possibly net a significant performance improvement.

TABLE 5. TECHNOLOGY UNKNOWNS

WINDOWLESS ABSORBER/THRUSTER		WINDOWED ABSORBER/THRUSTER				
				SEEDED CONCEPTS		
HEAT EXCHANGER CAVITY	* AEROWINDOW/ ABSORPTION	HEAT EXCHANGER CAVITY	* STATIONARY POROUS CYLINDER	PARTICULATE/ MOLECULAR ABSORPTION (DISCHARGED SEED)	VORTEX FLOW (RETAINED SEED)	ROTATING BED (RETAINED SEED)
•FABRICATION •COOLING WITH DISSOCIATED H_2	•AEROWINDOW LEAKAGE •SECONDARY MIRROR DESIGN COOLING, AND FABRICATION •DIFFUSER RECOVERY •SAME COMMENTS AS FOR SEEDED CONCEPTS	•WINDOW COOLING & SEALING -IR REFLECTIVE COATING •POROUS LINER DESIGN, FAB AND OPERATION •COOLING •FABRICATION	•WINDOW COOLING, SEALING AND PARTICLE DEPOSITION -IR REFLECTIVE COATING •POROUS LINER DESIGN, FAB AND OPERATION -HIGH TEMP MATERIAL -H_2 REACTION RATE •COOLING •FABRICATION	•WINDOW COOLING, SEALING, AND PARTICLE DEPOSITION -IR REFLECTIVE COATING •PARTICLE DEPOSITION ON SOLAR COLLECTORS •PARTICLE FEED MECHANISM -SOLID/GAS MIXER •THROAT DEPOSITION OR EROSION •SOLAR RADIATION ABSORPTION PROCESS -SEED/H_2 REACTION •COOLING •FABRICATION	•PARTICLE LOSS -COLLECTOR DEPOSITION -ENGINE START & SHUTDOWN •WINDOW COOLING, SEALING, AND PARTICLE DEPOSITION -IR REFLECTIVE COATING •ABSORBER PARTICLE UNIFORMITY •COOLING •FABRICATION	•WINDOW COOLING, SEALING AND PARTICLE DEPOSITION -IR REFLECTIVE COATING •ROTATING BED -APPROACH FEASIBILITY -DESIGN -FABRICATION -OPERATION (SPEED CONTROL) •HIGH TEMPERATURE BEARINGS (LIFE) •PARTICLE LOSS -COLLECTOR DEPOSITION -ENGINE START AND SHUTDOWN -PARTICLE/H_2 REACTION •PARTICLE FEED MECHANISM •COOLING •FABRICATION

*SECONDARY CONCEPTS

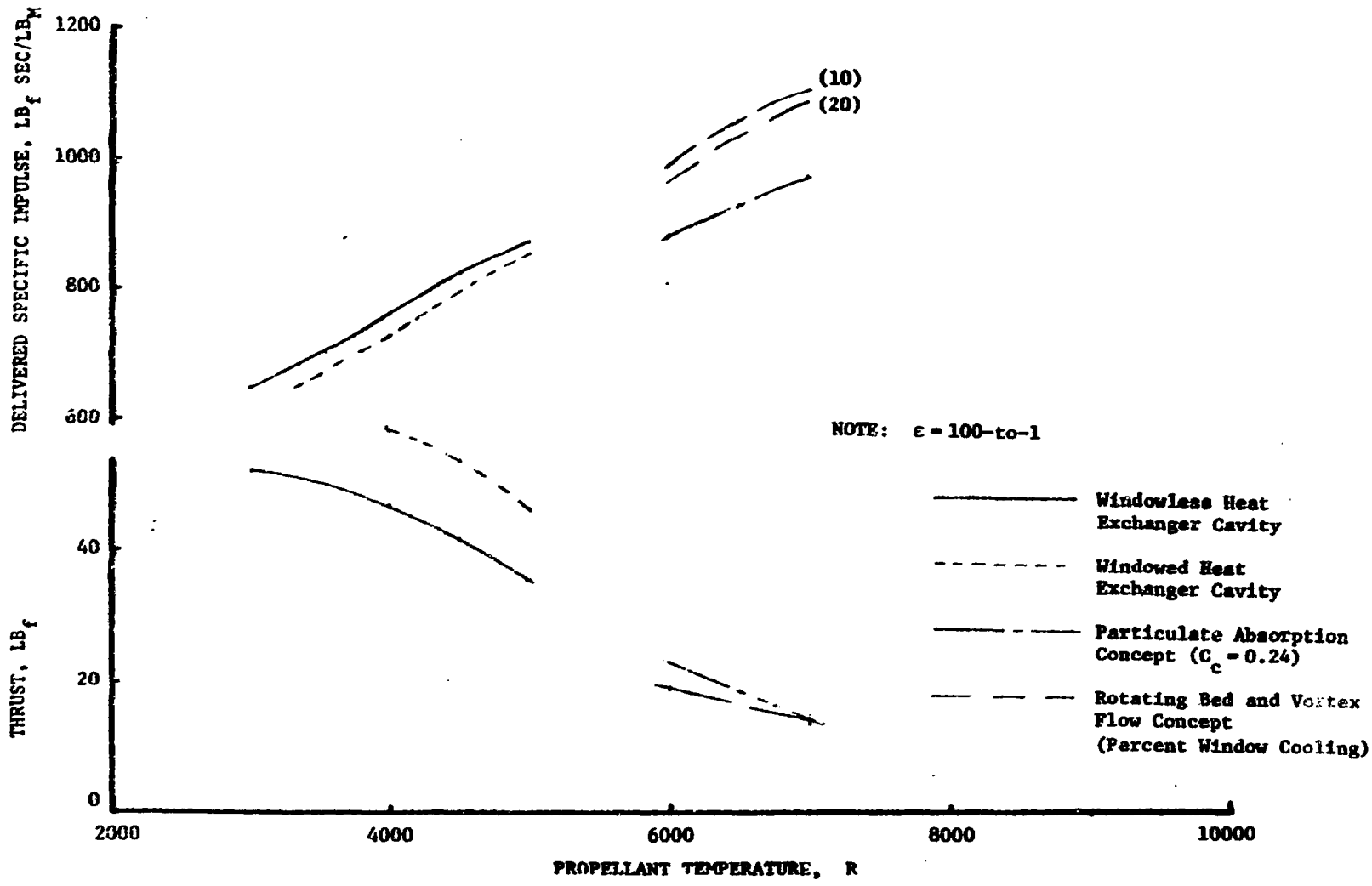

Figure 75. Solar Thermal Rocket Concept Performance Comparison

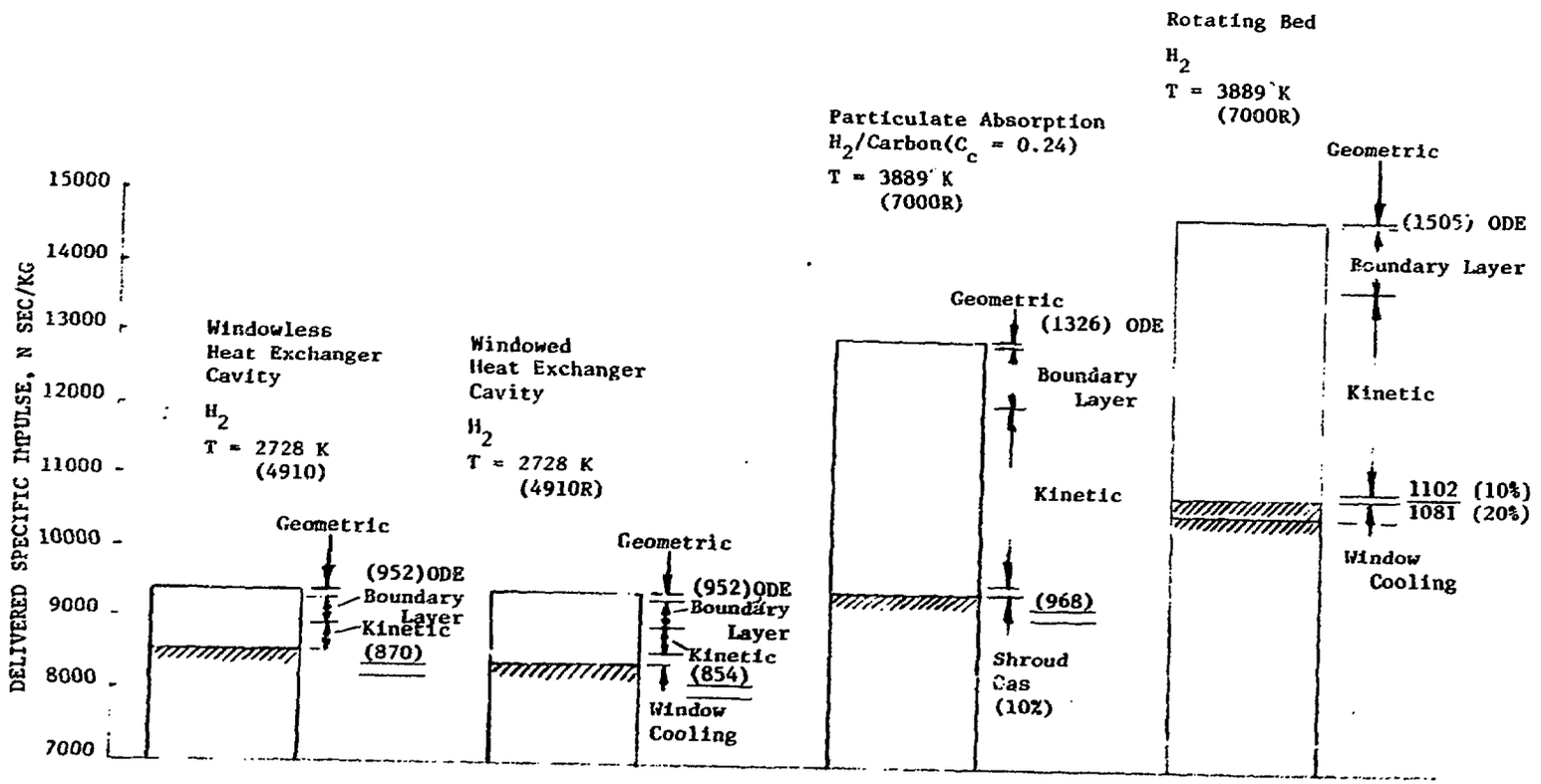

Figure 76. Delivered Specific Impulse Comparison

In the comparison of the seven candidate absorber/thruster concepts, the parameters compared were:

1. Achievable propellant temperature
2. Delivered specific impulse
3. Thrust
4. Maximum heat flux
5. Maximum absorber/thruster wall temperature
6. Maximum window temperature

These pertinent parameters were tabulated for the highest propellant temperature condition for each concept and are presented in Table 6.

The highest propellant temperatures were achieved by the seeded windowed concepts and the aerowindow/absorption concept. These same concepts achieved the highest delivered specific impulse and the lowest thrust level. The lowest heat flux was experienced by the windowless heat exchanger cavity concept. The absorber/thruster wall temperatures were all approximately the same varying from 2533 K (4100 F) to 2778 K (4540 F).

These same parameters were transformed into a comparative rating with the maximum heat flux and wall temperature data formulating a durability rating. Concept complexity, technical risk, and relative cost were added to complete the overall rating criteria and were based on the concept configuration and technology unknowns previously discussed. As shown in Table 7, the combined specific impulse, thrust, durability rating resulted in the two heat exchanger cavity concepts having the highest ratings. In adding complexity, technical risk, and relative cost ratings the highest overall rating was achieved by the windowless heat exchanger cavity absorber/thruster. Therefore, for the test hardware, the design and fabrication of this concept was recommended.

The windowless heat exchanger cavity concept (Fig. 77) represented the most viable near-term concept and can provide hardware flexibility through the conversion to other windowed concepts as shown in Fig. 78 (windowed heat exchanger cavity) and Fig. 79 (stationary porous cylinder).

TABLE 6. ABSORBER/THRUSTER COMPARISON

	WINDOWLESS ABSORBER/THRUSTER		WINDOWED ABSORBER/THRUSTER				
					SEEDED CONCEPTS		
	HEAT EXCHANGER CAVITY	AEROWINDOW/ ABSORPTION	HEAT EXCHANGER CAVITY	STATIONARY POROUS CYLINDER	PARTICULATE/ MOLECULAR ABSORPTION (DISCHARGED SEED)	VORTEX FLOW (RETAINED SEED)	ROTATING BED (RETAINED SEED)
ACHIEVABLE PROPELLANT TEMPERATURE, K (R)	$\leq$ 2728 (4910)	$\leq$ 3889 (7000)	$\leq$ 2667 (4800)	$\leq$ 3778 (6800)	$\leq$ 3889 (7000)	$\leq$ 3889 (7000)	$\leq$ 3889 (7000)
DELIVERED I_{SP} CAPABILITY, N SEC/KG, $\epsilon = 100$ $\left(\frac{LB_f \text{ SEC}}{LB_M}\right)$	$\leq$8532 (870)	$\leq$ 10591 (1080)	$\leq$ 8336 (850)	$\leq$ 10385 (1059)	$\leq$ 9493 (968)	$\leq$ 10591 (1080)	$\leq$ 10591 (1080)
THRUST CAPABILITY, N (LB_f)	~ 156 (~ 35)	~ 67 (~ 15)	205 (~ 46)	~ 71 (~ 16)	~ 62 (~ 14)	~ 67 (~ 15)	~ 67 (~ 15)
$(q/A)_{MAX}$, WATTS/CM^2 (BTU/IN^2 SEC)	$\leq$ 82 (Cavity) (0.5)	$\leq$ 490 (Estimated) (3)	$\leq$ 163 (Cavity) (1.0)	$\leq$ 1015 (Throat) (6.2)	$\leq$ 1090 (Throat) (6.7)	$\leq$ 1128 (Throat) (6.9)	$\leq$ 1128 (Throat) (6.9)
$(T_{WALL})_{MAX}$, K(F)	2778 (4540)	~ 2667 (~ 4340)	2778 (4540)	~ 2533 (~ 4100)	~ 2667 (~ 4340)	2667 (4340)	2667 (4340)
$(T_{WINDOW})_{MAX}$, K(F)	-	-	799 (979) Single Plane	~ 1170 (~ 1650)	927 (1208) Hemispherical	~ 1168 (~ 1643)	1168 (1643) Hemispherical

TABLE 7. ABSORBER/THRUSTER RATING

	WINDOWLESS ABSORBER/THRUSTER		WINDOWED ABSORBER/THRUSTER				
					SEEDED CONCEPTS		
	HEAT EXCHANGER CAVITY	AEROWINDOW/ ABSORPTION	HEAT EXCHANGER CAVITY	STATIONARY POROUS CYLINDER	PARTICULATE/ MOLECULAR ABSORPTION (DISCHARGED SEED)	VORTEX FLOW (RETAINED SEED)	ROTATING BED (RETAINED SEED)
I_{SP} RATING	8	10	7	10	9	10	10
THRUST RATING	8	4	10	4	4	4	4
DURABILITY RATING	8	5	7	5	6	5	5
COMPLEXITY RATING	10	2	8	7	6	6	2
TECHNICAL RISK RATING	10	4	8	7	5	1	4
RELATIVE COST RATING	10	2	7	6	4	4	2
TOTAL I_{SP}, F, DURABILITY RATING	24	19	24	19	19	19	19
OVERALL RATING	54	27	47	39	34	30	27

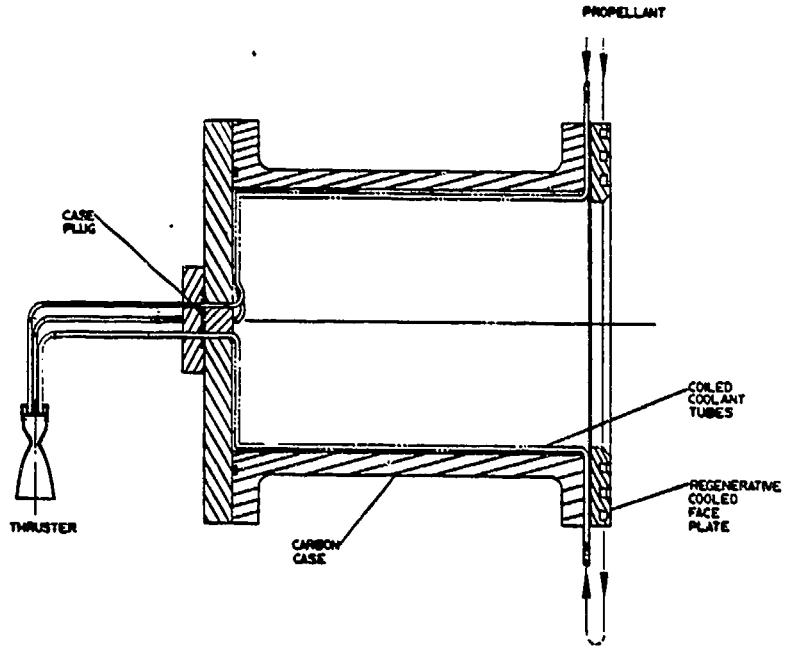

Figure 77. Windowless Heat Exchanger Cavity Absorber/Thruster

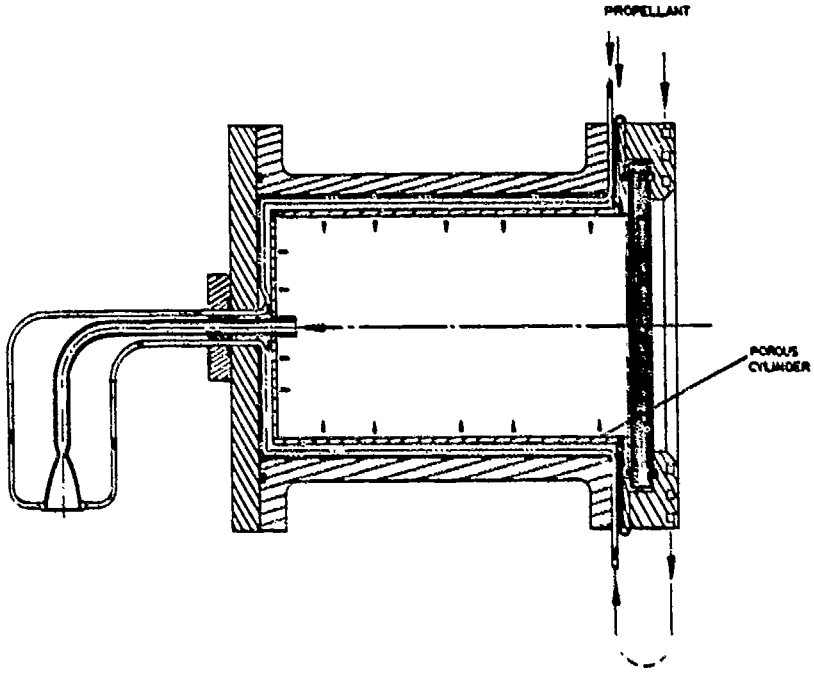

Figure 78. Conversion to Windowed Heat Exchanger Cavity Wth Porous Liner

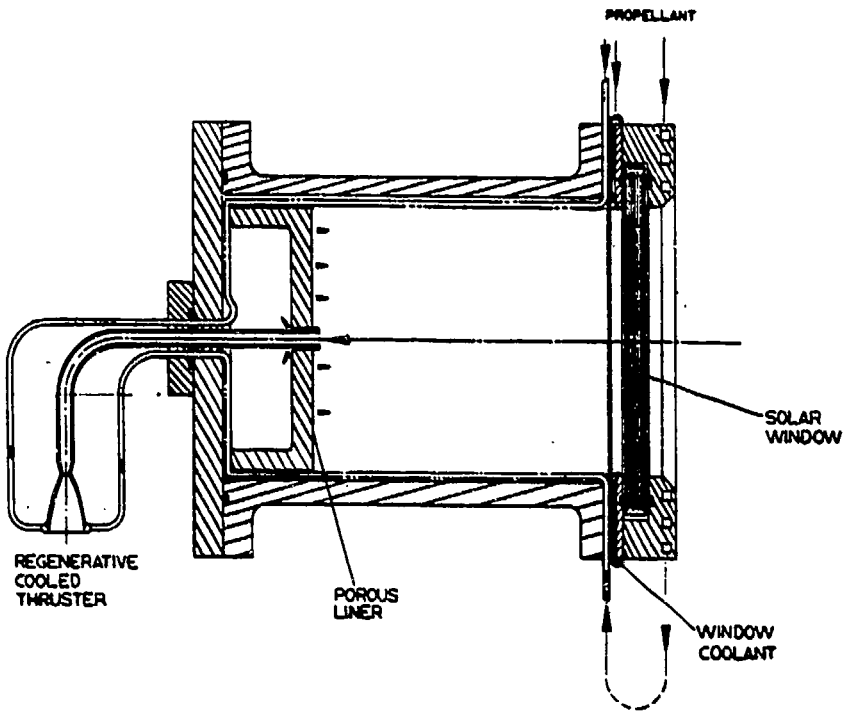

Figure 79. Conversion to Windowed Absorber/Thruster With Stationary Porous Cylinder

In addition, continued advanced absorber/thruster technology was recommended to further evaluate concepts which potentially offer the highest delivered specific impulses. Technology recommended was primarily related to specific component analysis and experimental testing to answer technology unknowns and provide confidence to develop a complete absorber/thruster system. The components included the window, porous cylinder, rotating bed, aerodynamic window, and secondary reflectors.

PHASE II, ABSORBER/THRUSTER DESIGN

As a result of the Phase I studies, an absorber/thruster concept was selected for detailed design. The concept selected was the windowless heat exchanger cavity absorber/thruster.

In Phase II, the design effort, together with all supporting analyses, was performed to provide specifications and drawings for subsequent fabrication of a subscale absorber/thruster ground test article. By definition, the design was to have a single-beam entry aperture which was scaled to the power and flux distribution characteristics of the Omnium-G 6-meter-diameter solar concentrator. The Omnium-G was the solar collector designated for testing of the absorber/thruster ground test article by the Air Force Rocket Propulsion Laboratory at the time of the study, however, later it was decided that other collectors will be used for testing.

Design philosophies consistent with the proof of principle requirement were incorporated into the ground test article configuration.

The effort was initiated with a definition of the absorber/thruster configuration followed by design layout and detail design. Concurrent supporting efforts included thermal, stress, material and fabrication processes, and performance analyses.

CONFIGURATION DEFINITION

To accomplish the detailed analysis and design of the selected concept, several absorber/thruster configuration definition areas were resolved: These areas included:

1. Solar flux/thruster orientation
2. Omnium-G solar concentrator characteristics
3. Absorber geometry and size determination based on efficiency

The analysis results of each of these areas follow.

Solar Flux/Thruster Orientation

An absorber/thruster configuration having the thruster in line with the incoming solar radiation (instead of oriented 90 degrees with respect to the incoming radiant energy) was evaluated for possible benefits (Fig. 80). The in-line thruster configuration offers some distinct advantages which include:

1. Minimum solar radiation blockage. The 90-degree orientation with a diffuser/ejector could result in partial radiant energy blockage caused by the diffuser/ejector pipe

2. Minimizes thruster thermal radiation to uncooled components. The in-line thruster configuration permits the radiation shield to be extended and surround the thruster and absorber. This also could be accomplished in the 90-degree thruster configuration but would complicate the radiation shield design

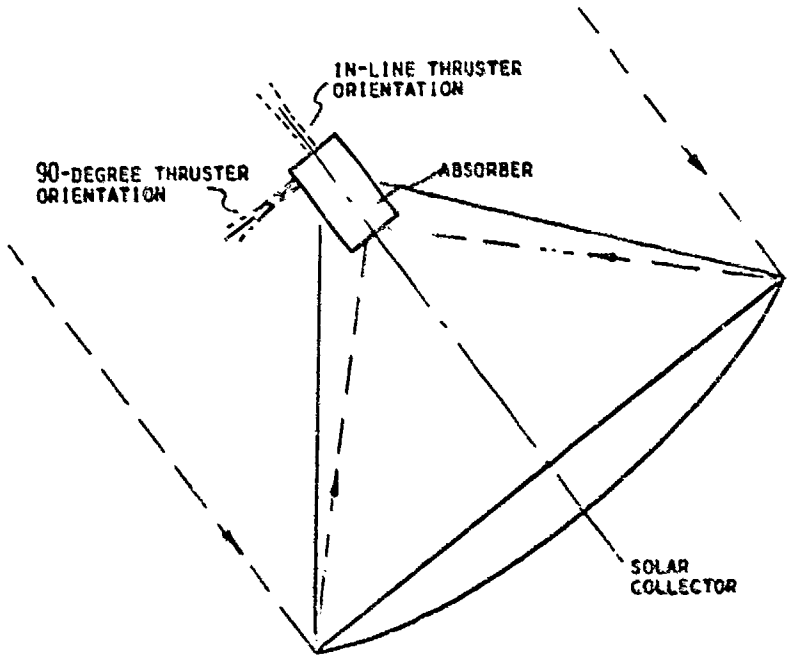

Figure 80. Thruster Orientation

The 90-degree thruster orientation also was briefly evaluated to determine design complications and benefits of incorporating this thruster configuration into the solar absorber and regenerative-cooled radiation shield design approach. From an absorber/thruster design and fabrication standpoint, only added complications were found when compared to the in-line thruster configuration and these included:

1. Added design and fabrication complexity to the regenerative-cooled radiation shield
2. A separate thruster nozzle exit joint cooling circuit would be required
3. Increased design and fabrication for the incorporation of the uncooled radiation shields

Based on the results listed above, the configuration with thruster centerline in-line with the incoming solar flux provided a simpler absorber/thruster design. Therefore, since the 90-degree orientation did not offer any significant test operational advantages and introduced additional design complications, the in-line thruster configuration was selected for the ground test hardware.

Ominium-G Solar Concentrator

The Omnium-G concentrator design parameters are shown in Table 8. The focal plane heat flux density and the resulting power distribution as a function of radius were plotted in Fig. 81 and 82. These data are only advertised concentrator characteristics, which was the only data available at the time of the study. These data provide the radiant solar energy input to enable the determination of absorber efficiency. The peak heat flux was 1160 watts/cm^2 (7.1 Btu/in.^{2}sec) which is, of course, located on the centerline. As shown in Fig. 82, 100% of the incoming solar energy is intercepted with a radius of 5.4 cm (2.13 inches).

TABLE 8. OMNIUM-G REFLECTOR

DIAMETER	6 METERS (236.2 INCHES)
FOCAL LENGTH	4 METERS (1575 INCHES)
CENTRAL OBSTRUCTION DIAMETER	1 METER (39.4 INCHES)
MAXIMUM POWER OUTPUT	24.7 kW (23.42 Btu/SEC)

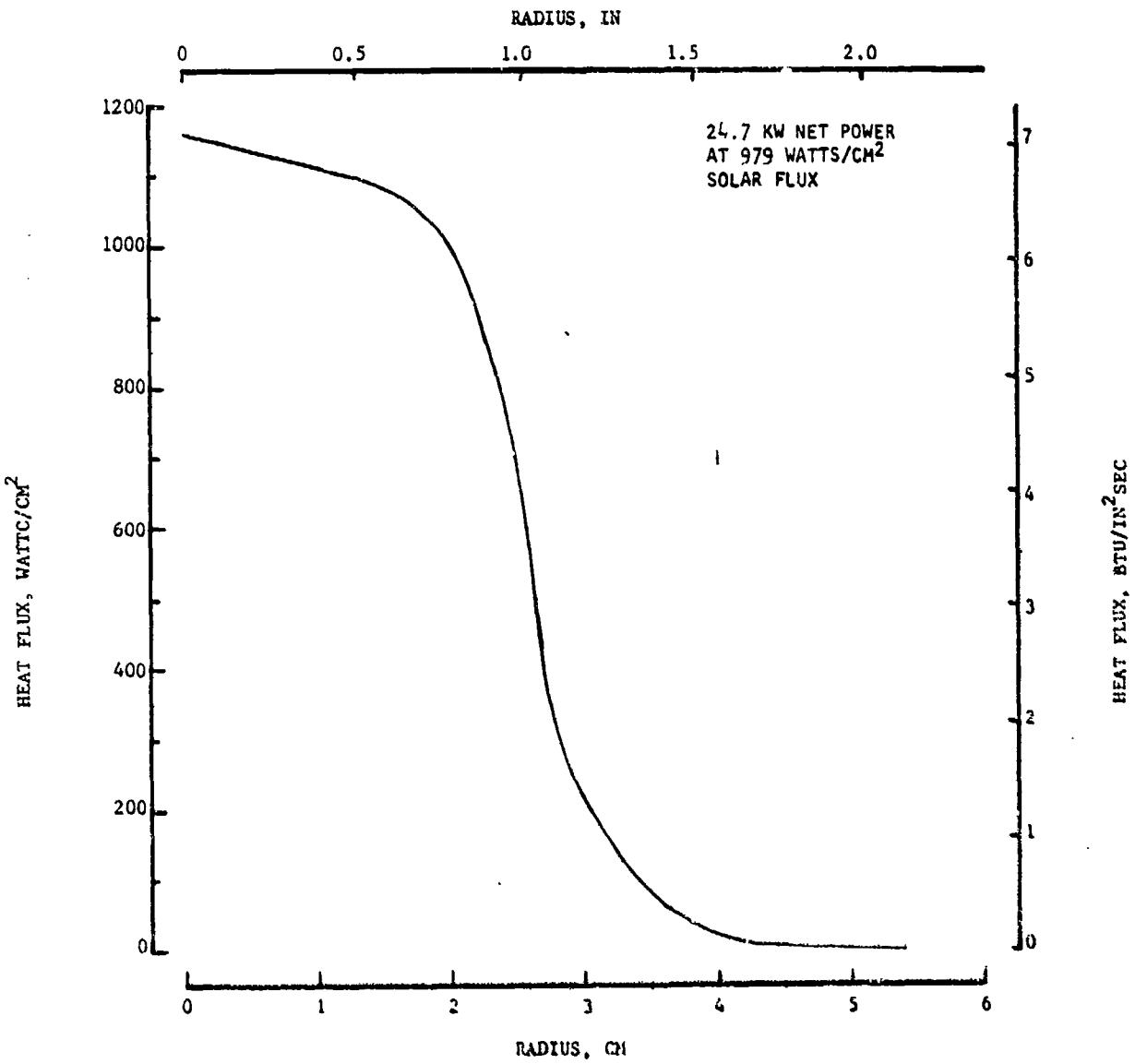

Figure 81. Omnium-G Focal Plane Heat Flux Distribution

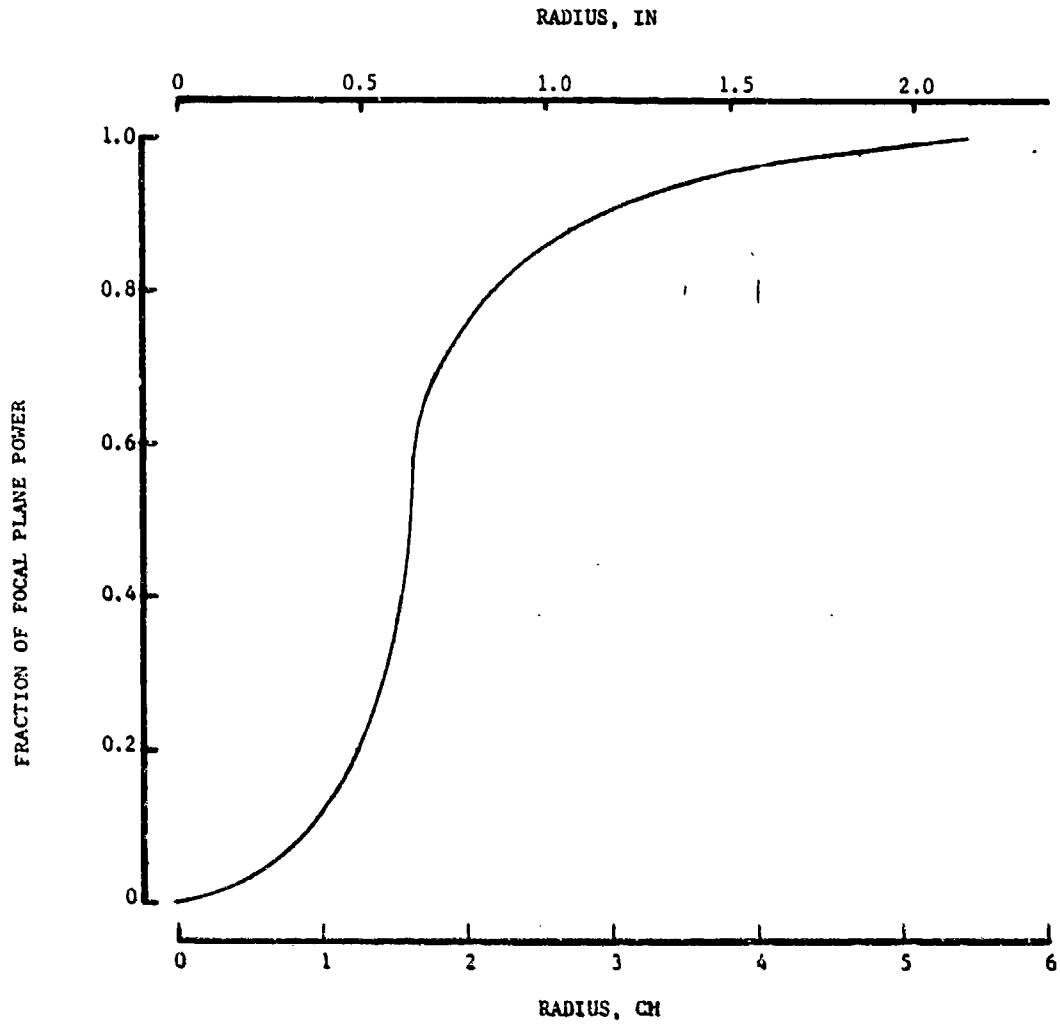

Figure 82. Omnium-G Focal Plane Power Distribution

Absorber Geometry

To define an absorber cavity size achieving a high absorber total efficiency, a relatively simple thermal model tailored after the Phase I model was utilized. The model determined the total absorber efficiency for a given open-ended cylinder geometry considering the incoming intercepted radiant heat, heat absorbed, and the heat radiated out of the cylinder opening. The total absorber efficiency is defined as the heat absorbed divided by the total collector solar energy output.

Based on the heat flux distribution, the test hardware absorber size efficiency trends were analyzed using the simplified thermal model. As shown by the results presented in Fig. 83 and 84, the optimum absorber radius was between 3.56 cm (1.4 inches) and 4.06 cm (1.6 inches). This influence is the result of the tradeoff of the larger radii intercepting more of the incoming radiation and the larger radii cavity losing more heat due to reradiation. To ensure optimum heat absorption and some dimensional tolerance for the test hardware, a radius of 4.06 cm (1.6 inches) was selected. Using this absorber radius, some low heat flux radiation will impinge on portions of the absorber external surfaces. These exposed surfaces are to be kept to a minimum in designing the absorber.

For all absorber radii analyzed, longer cylinder lengths resulted in higher absorber efficiencies. However, the rate of efficiency increase with increased length-to-diameter ratio decreased slightly for L/D greater than 2.5. Therefore, a cylinder length of 20.32 cm (8 inches) was chosen for the test hardware absorber which was predicted to achieve a total absorber efficiency of 72%. The geometry is illustrated in Fig. 85.

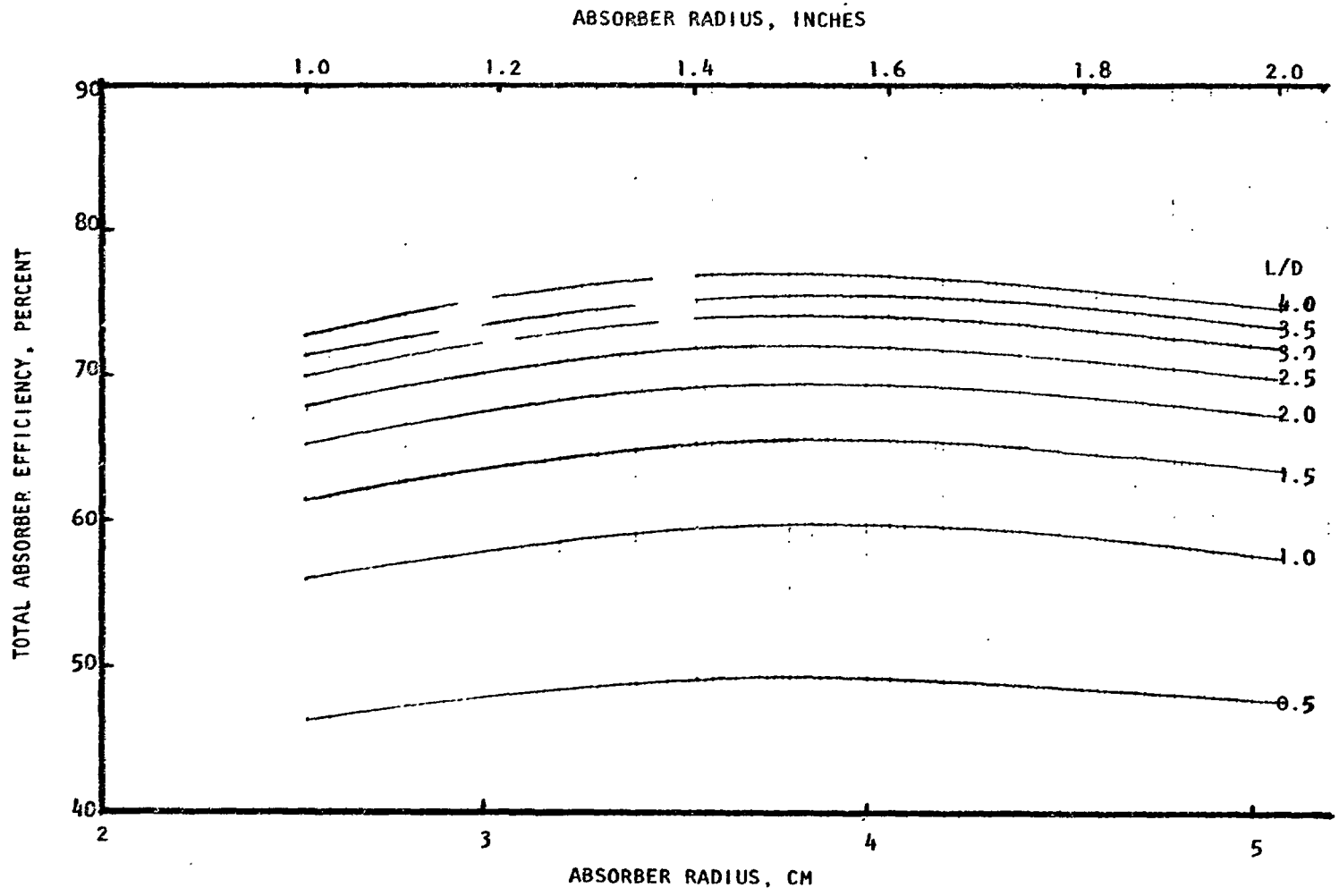

Figure 83. Absorber Efficiency Versus Geometry

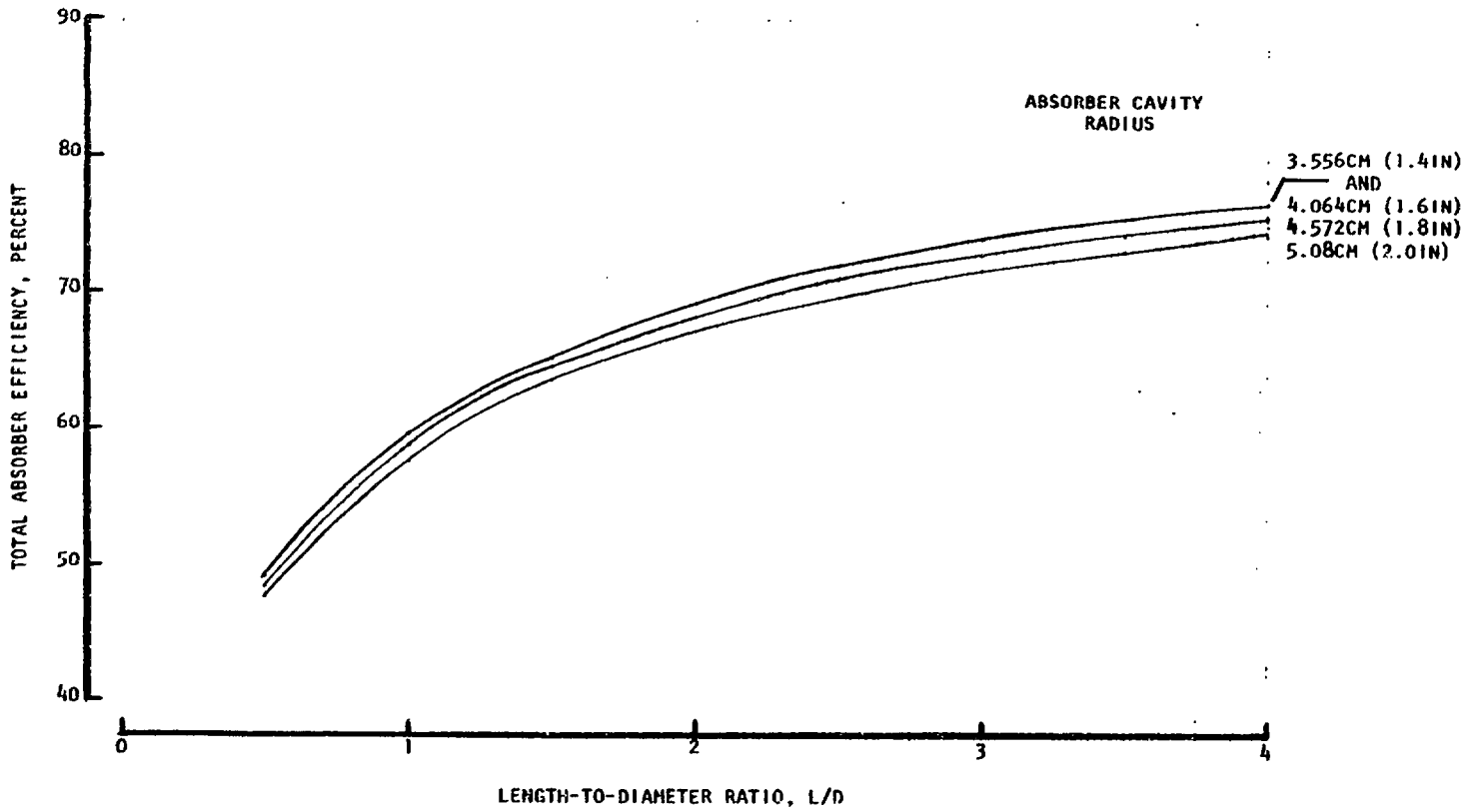

Figure 84. Test Hardware Absorber Efficiency Trends

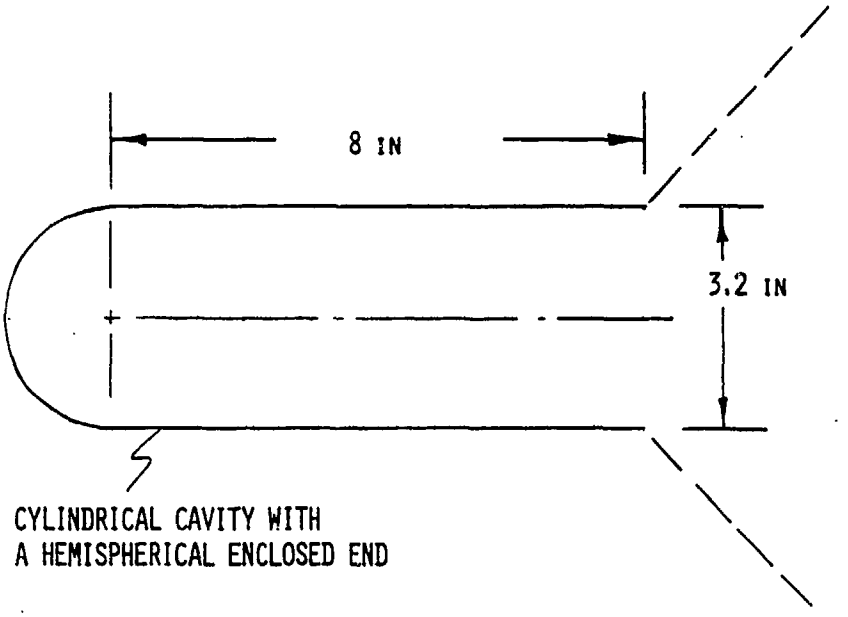

Figure 85. Test Hardware Absorber Geometry and Size

DESIGN LAYOUT AND DETAILED DESIGN

The absorber/thruster basic design features a cavity heat exchanger formed by coiled rhenium tubing with a thruster. The unit is surrounded by a number of heat shields designed to reduce the radiation heat losses from the absorber/thruster assembly. The absorber coil is encased in a rhenium coated graphite case which in turn is surrounded by a series of radiation shields and an insulation layer. This assembly is enclosed by a regeneratively-cooled vacuum chamber shell which serves as the final radiation shield. The solar flux enters the absorber through a quartz window (the window completes the vacuum chamber vessel). A window is required for ground testing to provide a vacuum even though a windowless concept was selected. Since rhenium oxidizes in air at fairly low temperatures, testing in an earth environment requires that the rhenium be contained in an inert or an evacuated environment (vacuum) which requires that the assembly have a transparent window. Therefore the window is considered a test equipment item. The design provides for minimization of thermal strains and utilizes state-of-the-art technology to maintain fabricability.

Design layout refinement through 12 individual configurations provided the final design layout from which the detailed component drawings were prepared.

Design Layouts

The initial design layout of the test hardware for the in-line thruster configuration is presented in Fig. 86. The absorber is a cylindrical cavity with a hemispherical enclosed end formed by coiling five tubes in parallel. A cooled carbon plug is used to fill the hole in the enclosed end which is left due to the minimum bend radius limitation on the rhenium tube of approximately 0.762 cm (0.2 in.). The coiled tube assembly was enclosed in a carbon shell which was in turn contained in a hydrogen cooled radiation shield.

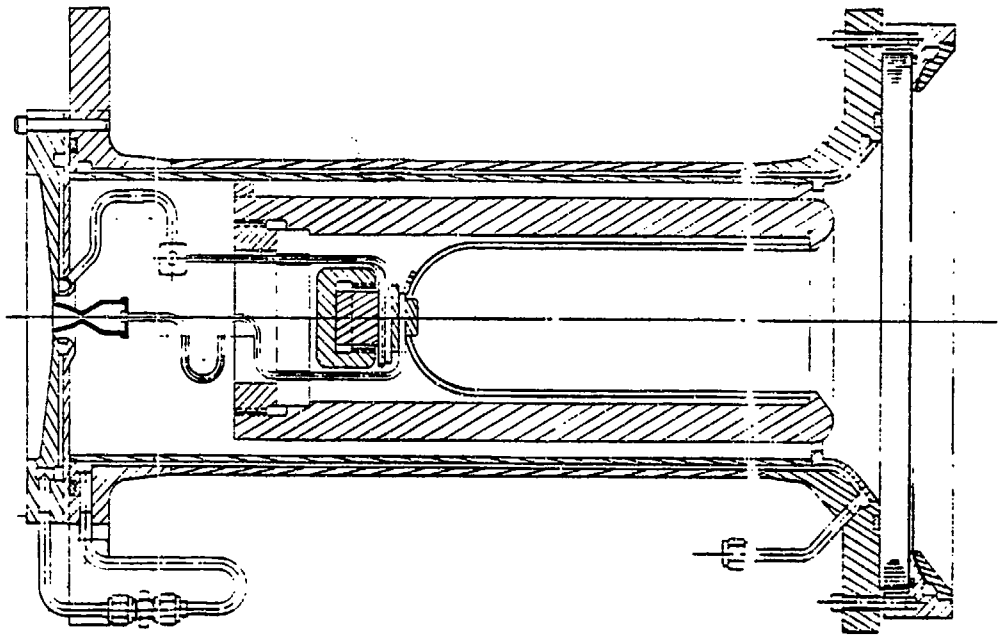

Figure 86. Solar Absorber/Thruster Experimental Layout

As shown in Fig. 86, the in-line thruster configuration provided a rather simple design completely enclosing the absorber and thruster within the regenerative-cooled radiation shield. Also this configuration provided an effective approach to cooling the nozzle exit-to-vacuum enclosure joint. In this design the radiation shield assembly becomes the vacuum enclosure and houses the window. To maintain the thruster region of the radiation shield at a reasonable temperature, a series of high temperature, uncooled cylindrical shields could be placed around the thruster to provide a staged radiation shield approach.

The thermal analysis, which was conducted in parallel with the design effort (discussed in a later section), indicated the need for a series of intermediate radiation shields between the carbon shell and the regenerative-cooled radiation shield. The modified configuration of Fig. 87 shows four intermediate radiation shields plus a sandwiched insulation layer (aluminum oxide) around the absorber carbon shell to minimize heat losses.

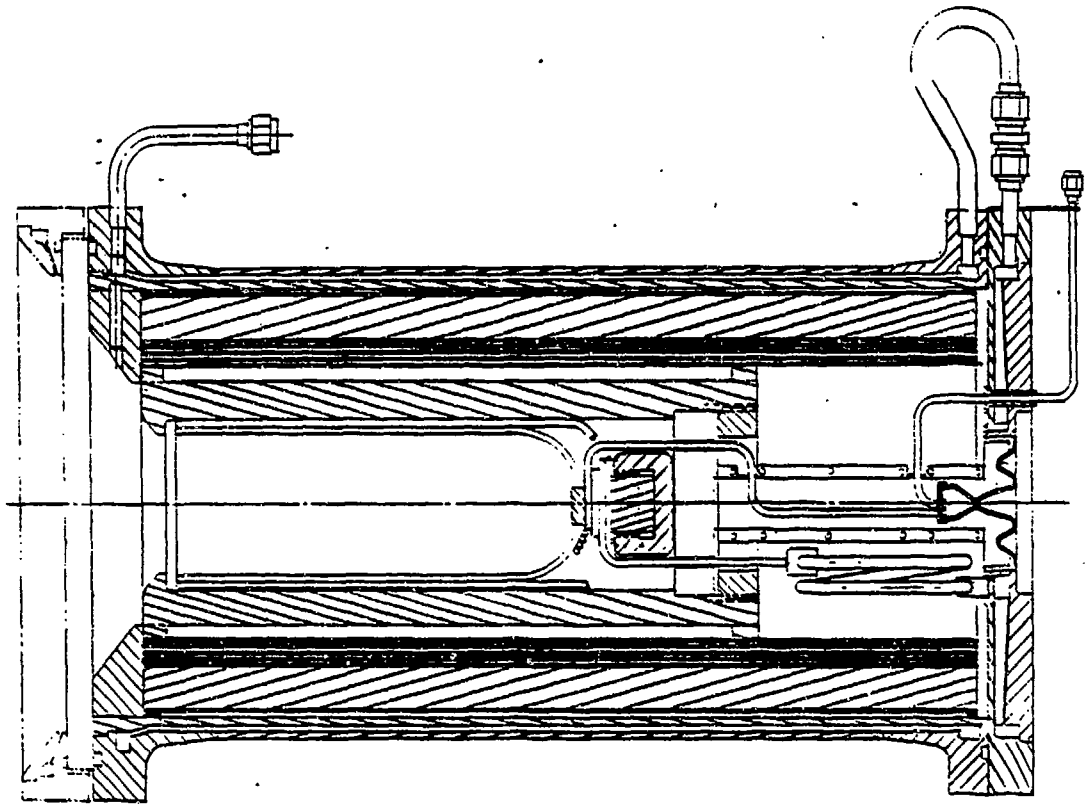

Figure 87. Modified Absorber/Thruster Design Layout

Figure 87 incorporates the following additional modifications: (1) a radiation shield around the absorber-to-thruster propellant lines again to minimize heat losses, (2) a coiled inlet propellant feed line to reduce strain due to thermal growth, (3) an expansion gap in the forward end (near the window) of the absorber carbon shell to permit minimum restrained thermal growth of the absorber coil, and (4) a carbon shell retainer ring at the forward end of the carbon shell.

As discussed later in the thermal analysis section, the heat loss from the five propellant lines from the absorber to the thruster directly influences the final hydrogen temperature achieved in the thruster, and therefore the delivered specific impulse. A design effort was undertaken to minimize this line length to reduce this heat loss. The resulting final absorber/thruster design layout is shown in Fig. 88. The carbon plug, carbon ring stabilizer, and the carbon ring set retainer were modified to shorten the line length.

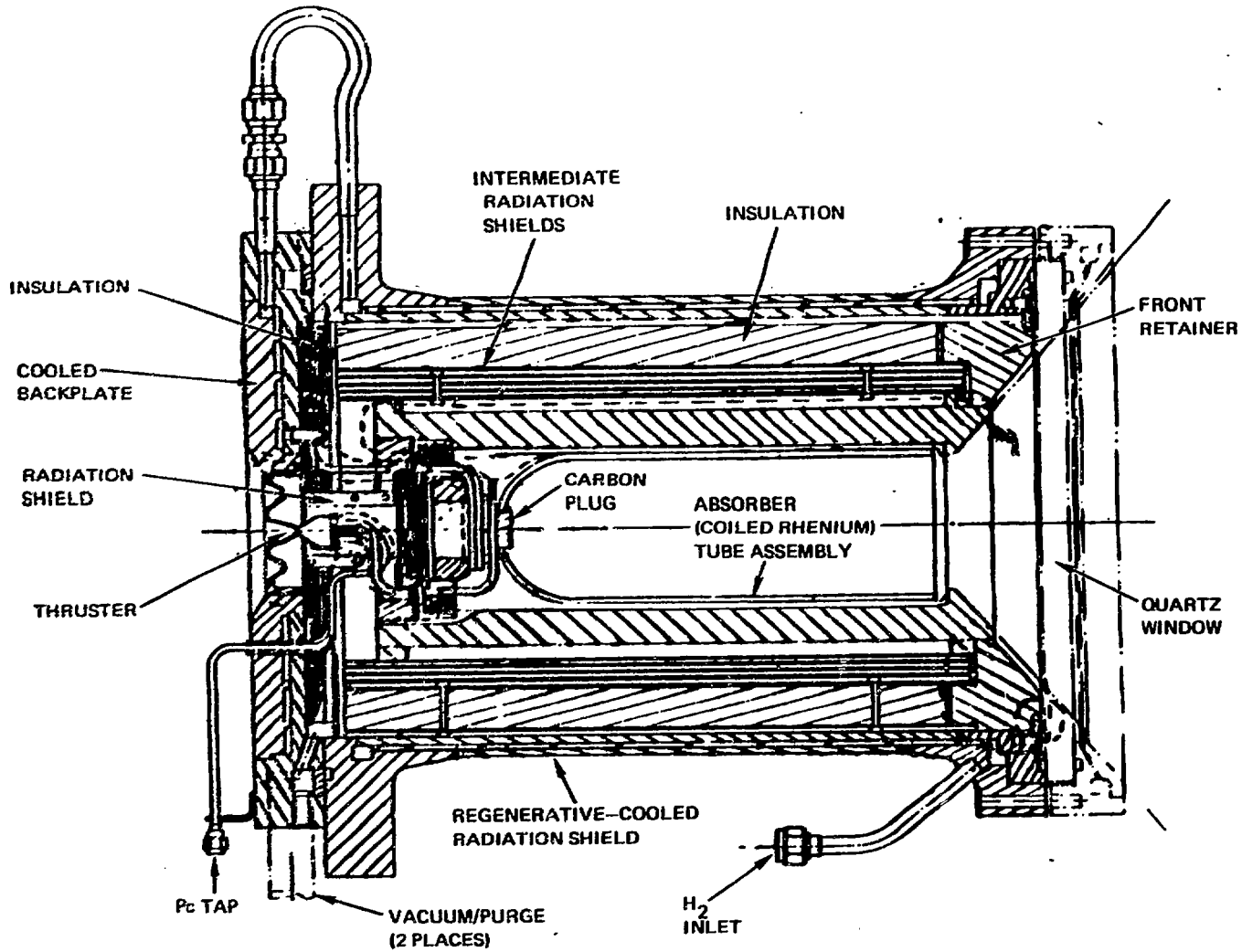

Figure 88. Final Absorber/Thruster Design Layout

Also, the long coiled inlet propellant line to the thruster was eliminated in favor of short lines to reduce the absolute magnitude of thermal growth. Also, a split aluminum oxide insulation disk was added to the backplate to further minimize heat losses. A comparison of Fig. 87 and 88 distinctly illustrates the reduced line length.

Additional final iterations of the ground test absorber/thruster layout were completed and incorporated into the final layout drawing shown in Fig. 88. Modifications made included: (1) increasing the diameter of the backplate insulation to the diameter of the cylindrical shield/insulation package, (2) modifying the front retainer ring (absorber inlet insulation) to consist of six pieces (to prevent cracking) which are held in place by a metal ring and metal radiation shields, (3) the coolant passage in regenerative-cooled backplate is formed by a spiraling coolant channel, (4) the flange thickness on the regenerative-cooled cylinder was increased to ensure structure integrity, and (5) ports for the vacuum/purge and the thermocouples were incorporated.

Final Configuration Material Selections. A Phase II design review resulted in finalization of material selection in several critical areas.

Graphite Components. All the graphite components of the absorber/thruster assembly were changed from ATJ graphite to fine grained POCO graphite. The change was made to more closely match the thermal expansion coefficient of the graphite with that of the rhenium coating. POCO graphite has a significantly lower expansion coefficient than ATJ graphite.

Thruster Radiation Shield. Since the maximum shield temperature was close to the melting temperature of TZM, tantalum was substituted.

Vacuum Chamber Backplate Assembly. To increase the material strength at the elevated temperatures predicted, Incoloy 903 was substituted for the 430 CRES. Also, Incoloy 903 provides a closer match to rhenium in terms of the thermal expansion coefficient. The rhenium thruster is brazed to the backplate.

Backplate Insulation. To increase the high temperature characteristics of the backplate insulation, a stabilized zirconium oxide was selected to replace the Mullfrax material. Zirconium oxide has a 833 K (1500 F) higher maximum use temperature than Mullfrax.

Hydraulic Circuit. The propellant/coolant circuit is shown in Fig. 89. The hydrogen enters the vacuum chamber regenerative circuit at the window end of the absorber and exits the vacuum chamber at the far end of the chamber where a transfer line carries the hydrogen into the outer perimeter of the vacuum chamber back plate. The hydrogen exits the back plate through a five-tube manifold since the solar absorber is a five-parallel-tube heat exchanger. The hydrogen flows through the five tubes which pass through a graphite absorber plug (the hydrogen is used to cool the plug). Having passed through the plug, the hydrogen is carried to the inlet end of the absorber and is then spiraled back toward the graphite plug through the five-parallel-wrapped tube system. The five parallel tubes are finally terminated in the thruster head cap so that the hydrogen can then be discharged through a conventional convergent/divergent nozzle after having been heated in the absorber.

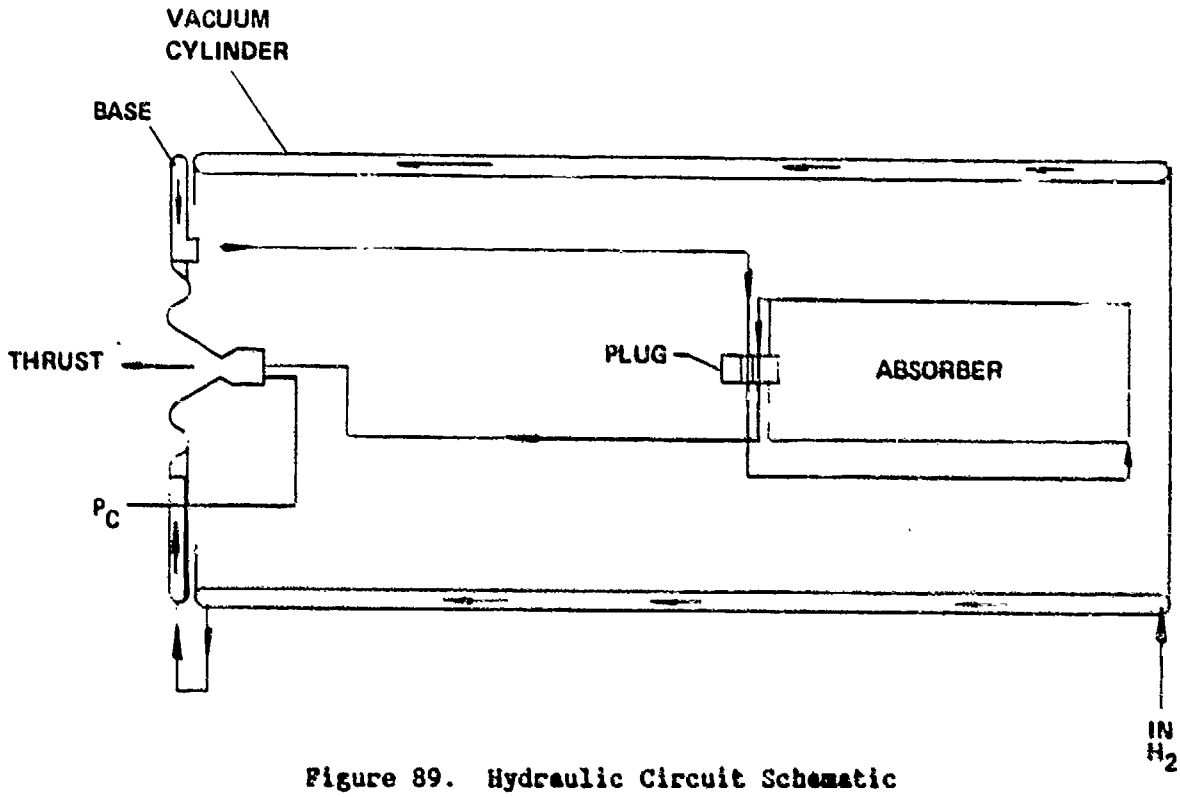

Figure 89. Hydraulic Circuit Schematic

Detailed Design

The assembly (Fig. 90 and 91) consists of an integral solar absorber and thruster. The absorber is a coiled rhenium tube subassembly and the thruster is rhenium converging/diverging nozzle. As shown isometrically in Fig. 92, this basic assembly is surrounded by various heat shields designed to reduce the radiation heat losses from the absorber/ thruster assembly. The absorber is encased in rhenium coated graphite, which in turn is encased in various refractory (metallic and non-metallic) materials. The entire system is then enclosed in a regeneratively cooled vacuum chamber. A complete drawing list is shown in Table 9.

The absorber tubing and thruster utilize chemically vapor deposited (CVD) rhenium material. Jumper lines (Incoloy 903 material) are furnace-brazed to the rhenium tubes. The use of the jumper lines was necessitated by the requirements to attach the rhenium absorber tubes to the Incoloy 903 material backplate. The difference between the coefficients of expansion of the Incoloy 903 and the rhenium material created a problem which was solved by joining the rhenium to the Incoloy 903 in a thin wall configuration.

The vacuum chamber incorporates a double wall construction (Fig. 92), which allows the hydrogen propellant to flow from the absorber inlet end to the vacuum chamber backplate end, thus recovering a majority of the heat being radiated from the various internal insulations. The flow path in the jacket is spiral, similar to the backplate flow path. The propellant passes from the vacuum chamber body to the vacuum chamber backplate via a crossover line. The hydrogen inlet end of the vacuum chamber is estimated to operate at 403 K (266 F). This temperature will increase along the wall toward the back, such that the back end of the vacuum chamber will operate at 811 K (1000 F). In addition to the axial temperature gradient in the chamber wall, there is also a temperature gradient between the inner and the outer wall of the chamber. An extensive stress analysis was conducted of the induced thermal stresses in the structure. The result of this analysis was the selection of the inner and the outer wall thicknesses to balance out the stresses to an acceptable level.

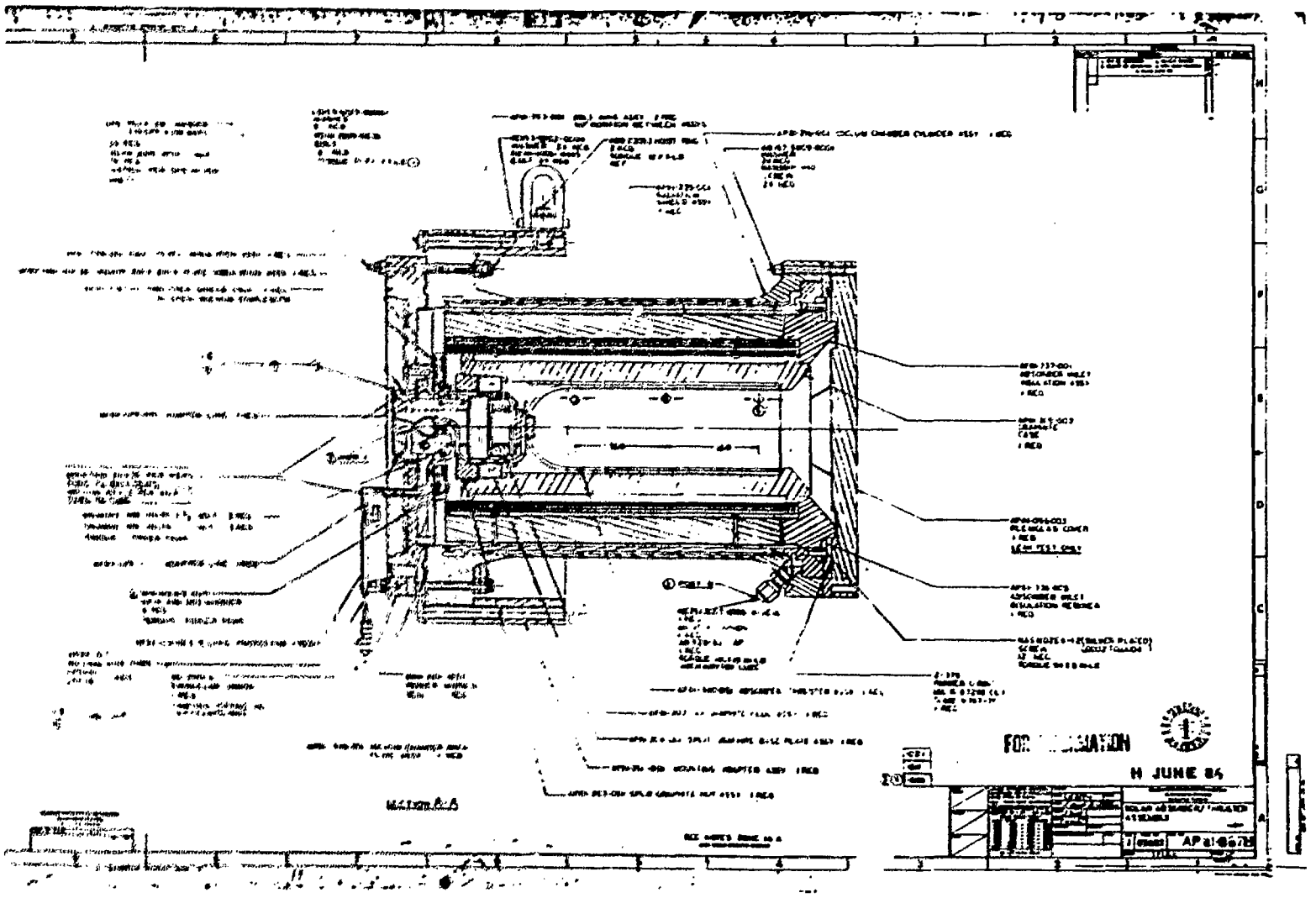

Figure 90. Solar Absorber/Thruster Assembly (Side View)

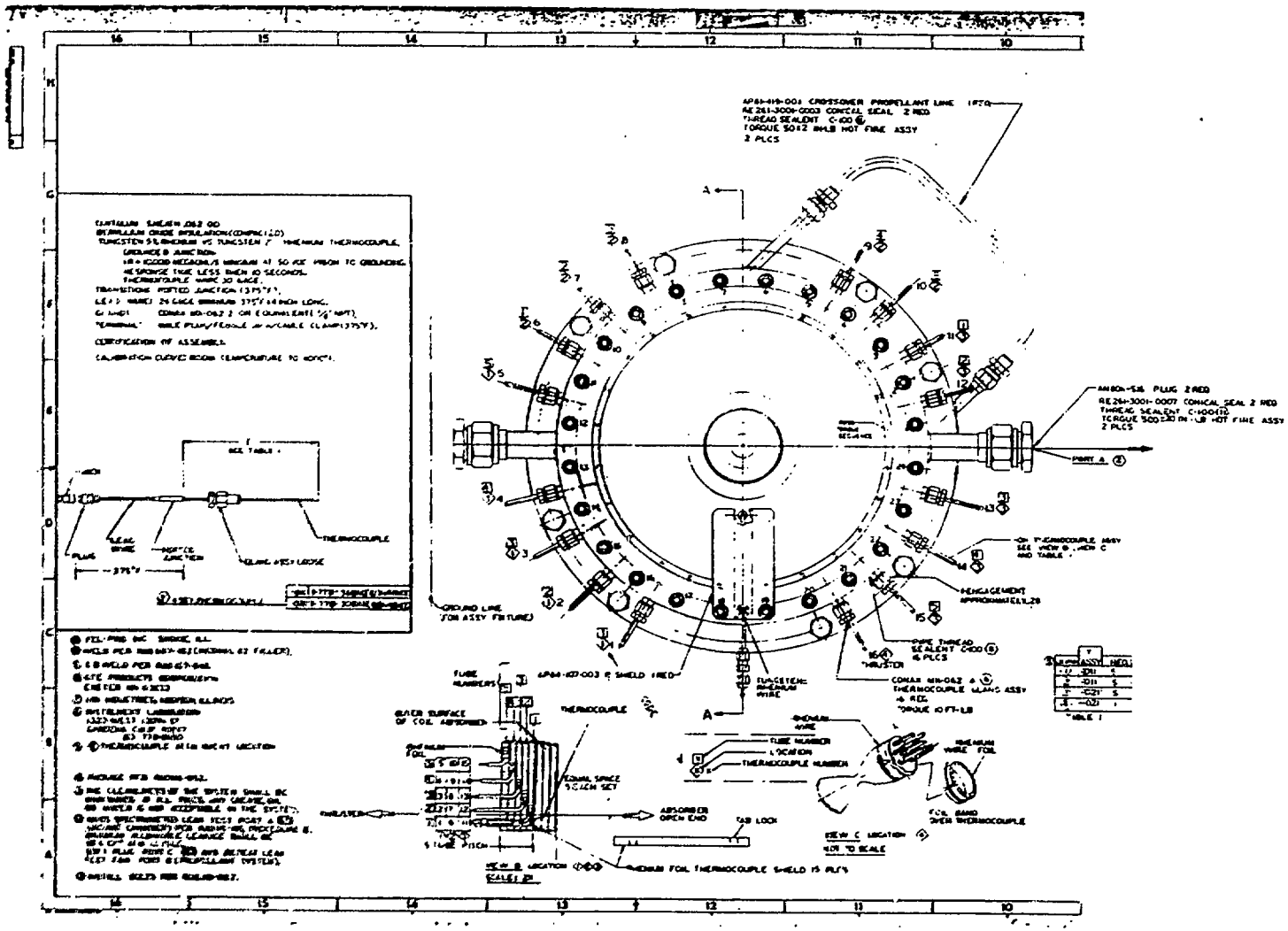

Figure 91. Solar Absorber/Thruster Assembly (End View)

TABLE 9. SOLAR ROCKET DRAWINGS

DRAWING NUMBER	TITLE
AP82-067	FINAL ASSEMBLY SOLAR ROCKET
-202	GRAPHITE PLUG ASSEMBLY, SOLAR ROCKET
-203	GRAPHITE NUT ASSEMBLY, SOLAR ROCKET
-204	GRAPHITE BASEPLATE ASSEMBLY, SOLAR ROCKET
-205	GRAPHITE CASE, SOLAR ROCKET
-216, 218	VACUUM CHAMBER CYLINDER ASSEMBLY, SOLAR ROCKET
-335	RADIATION SHIELD, SOLAR ROCKET
-336	ABSORBER INLET INSULATION RETAINER, SOLAR ROCKET
-337	ABSORBER INLET INSULATION ASSEMBLY, SOLAR ROCKET
-338	THRUST SHIELD, SOLAR ROCKET
-339	BASEPLATE INSULATION ASSEMBLY, SOLAR ROCKET
-340	ABSORBER/THRUSTER ASSEMBLY, SOLAR ROCKET
-349	VACUUM CHAMBER BACKPLATE ASSEMBLY
-391	MOUNTING ADAPTER, SOLAR ROCKET
-393	BOLT RING ASSEMBLY, SOLAR ROCKET
-409	STUD/WASHER ASSEMBLY, SOLAR ROCKET
-419	CROSSOVER PROPELLANT LINE, SOLAR ROCKET
AP83-090	SOLAR ABSORBER P/T ASSEMBLY
-352	ADAPTER RING
-258	ASSEMBLY CRADLE
AP84-029	INCOLOY 903 ADAPTER LINE
-046	SECONDARY (BASEPLATE) INSULATION
-057	SPLIT NUT INSTALLATION TOOL
-096	PLEXIGLAS COVER
-103	CHAMBER-PRESSURE EXTENSION, SOLAR ROCKET
-107	CHAMBER-PRESSURE TUBE SHIELD

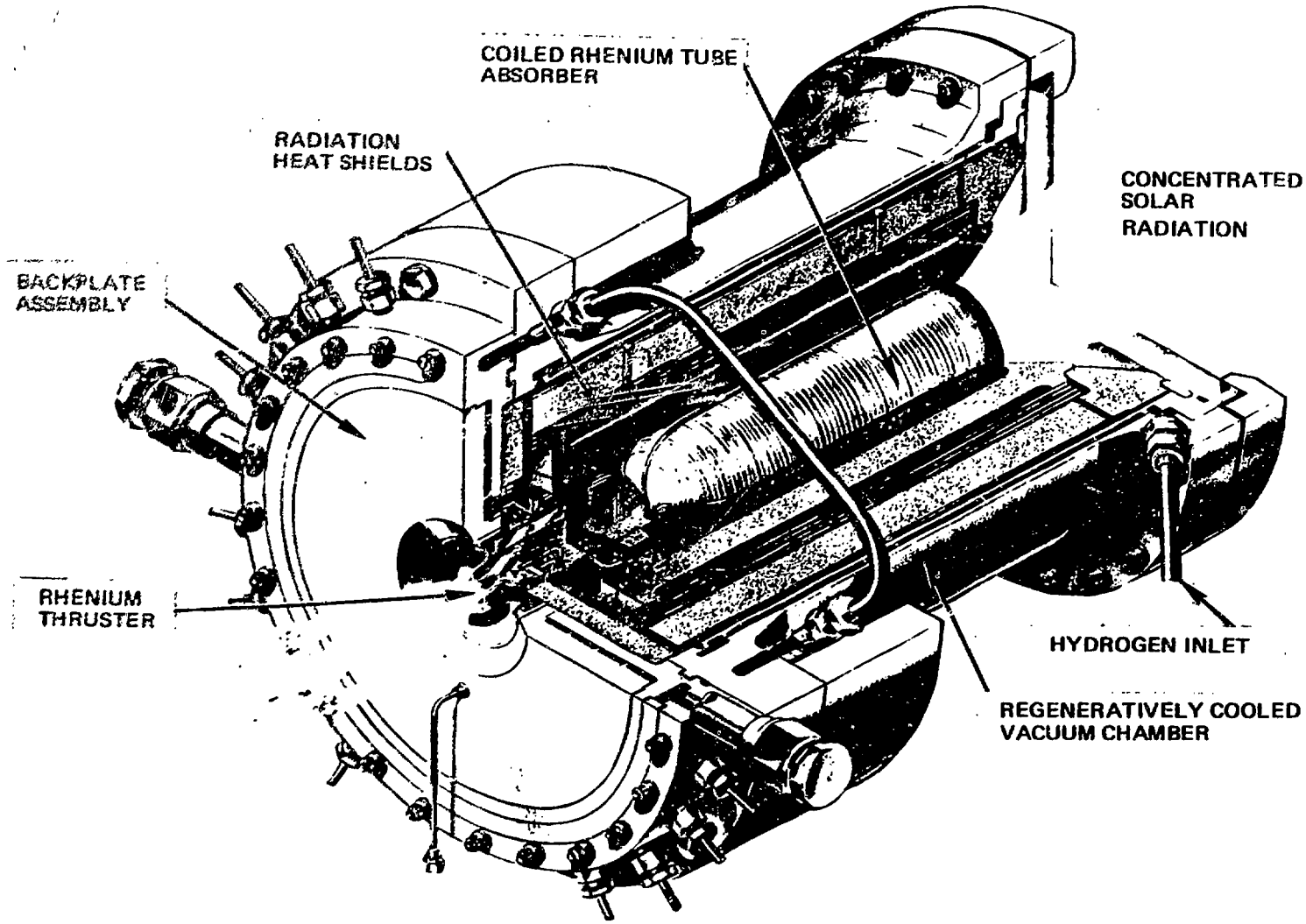

Figure 92. Solar Absorber/Thruster Assembly

The vacuum chamber backplate (Fig. 92) is fabricated from two plates of Incoloy 903 material, which has a thermal expansion approximately mid-way between rhenium and stainless steel at the hardware operating temperature. The backplate is essentially a double wall structure through which the hydrogen propellant spirals from the outer perimeter to the inner perimeter, where it is discharged into a fivehole absorber tube manifold. The backplate is estimated to operate at a temperature of 1000 K (1350 F) at the furnace braze joint between the rhenium thruster and the adapter ring. The selection of Incoloy 903 material was to reduce the thermal stress between the thruster and the backplate by matching the thermal expansion of the two parts as close as practical.

The vacuum chamber backplate is insulated with rigidized zirconium oxide board. The primary insulation (the insulation next to the backplate) is a two-piece assembly held to the backplate by six tungsten nut/screw/washer assemblies. The secondary insulation (the basic purpose of which is to insulate the Incoloy 903 material jumper line braze joint to the rhenium tubes) is held to the primary insulation by tungsten-rhenium staples. The secondary insulation is a six-segment assembly Slots are cut in both the primary and the secondary insulation for thermocouple routing through the backplate.

The rhenium tube coil absorber is surrounded by a rhenium coated graphite case as shown in Fig. 90 and 92. The graphite forms the first radiation thermal barrier around the absorber. The rhenium coating serves two purposes. The first purpose is to prevent the formation of rhenium carbide between the graphite and the absorber tube material. The second purpose is to prevent the sublimation of the graphite (which is operating at a high temperature in a vacuum). The maximum expected temperature of the graphite is approximately 2533 K (4100 F). Slots are machined into the graphite case to provide (Fig. 90) the tunnels through which the thermocouples exit the graphite envelope surrounding the absorber.

As shown in the assembly drawing, Fig. 90 and the isometric drawing in Fig. 92, the rhenium coated graphite case is surrounded by a radiation heat shield, consisting of six refractory tubes and one cast insulator. From the inner diameter to the outer diameter, the layers are: Tungsten 0.051 cm (0.020 in.) thick, tungsten 0.025 cm (0.010 in.) thick, molybdenum 0.025 cm (0.010 in.) thick, molybdenum 0.051 cm (0.020 inch) thick, molybdenum 0.025 cm (0.010 in.) thick, Alfrax BI No. 57 2.69 cm (1.057 in.) thick, and molybdenum 0.025 cm (0.010 in.) thick. The effect of the radiation shield is to drop the temperature approximately 30% at the cold end (absorber inlet) to approximately 46% at the hot end (thruster end).

As shown in Fig. 90, the hemispherical end of the absorber is closed out with a split graphite plug. The relatively cool hydrogen, 894 K (1150 F), coming from the backplate through the five parallel tubes is passed through the split plug in order to keep the temperature of the graphite within limits. The split graphite plug is backed up by a split graphite base and a split graphite nut is used to hold the assembly of graphite together.

The absorber inlet face area (Fig. 90) is insulated by a six-segment ring of Mulfrax 202. The segmentation of the ring is dictated by the temperature gradient through the Mulfrax. The ring dovetails into the radiation shield (with the Alfrax), however, standoffs have been cast into the Mulfrax to limit the amount of heat conduction into the Alfrax. The Mulfrax ring is held in place by a stainless steel retainer.

The thruster (Fig. 90 and 92), is surrounded by a tantalum heat shield (of split construction). The shield is expected to operate at 2376 K (3800 F). The heat shield is held between the graphite baseplate and the graphite nut. The other end of the heat shield is retained by the backplate insulation. The retention of the thruster heat shield in the backplate insulation is part of the support system for the absorber/graphite assembly. The six legs on the graphite case form a backup support system.

To reduce radiation to the thermocouple sheathing, rhenium foil strips were placed between the rhenium tubes of the absorber and the thermocouples (Fig. 91). Each strip has two radial tabs cut into the strip and these tabs are wrapped around the thermocouple sheathing so that they remain in position. The axial placement of the thermocouples on the absorber are shown in Fig. 90.

THERMAL ANALYSIS

Thermal analyses were completed to determine overall absorber/chamber heat input/output characteristics with resulting performance and on individual component areas to establish their thermal behavior. Eight localized regions were analyzed as illustrated in Fig. 93.

Special detailed thermal models were developed for the complex interrelationships such as between the absorber and window and between the carbon shell and radiation shields. The analysis results established a feasible design, acceptable absorber/thruster temperatures, reasonable pressure drop and maximized performance.

Absorber Cooling Analysis

A regenerative-cooling analysis was performed for five different coiled rhenium tube absorber designs with selected absorber dimensions. The five designs consisted of three, four, five, six and seven tubes. The rhenium tube size was selected based on previous weld joint and minimum tube bend radii evaluations. The tube had the following dimensions:

Outside tube diameter:	0.304 dm (0.12 inch)
Inside tube diameter :	0.254 cm (0.10 inch)
Wall thickness :	0.0254 cm (0.01 inch)

The basic absorber dimensions were the same for each case with a cylindrical length of 20.32 cm (8 inches) and a diameter 8.3 cm (3.2 inches).

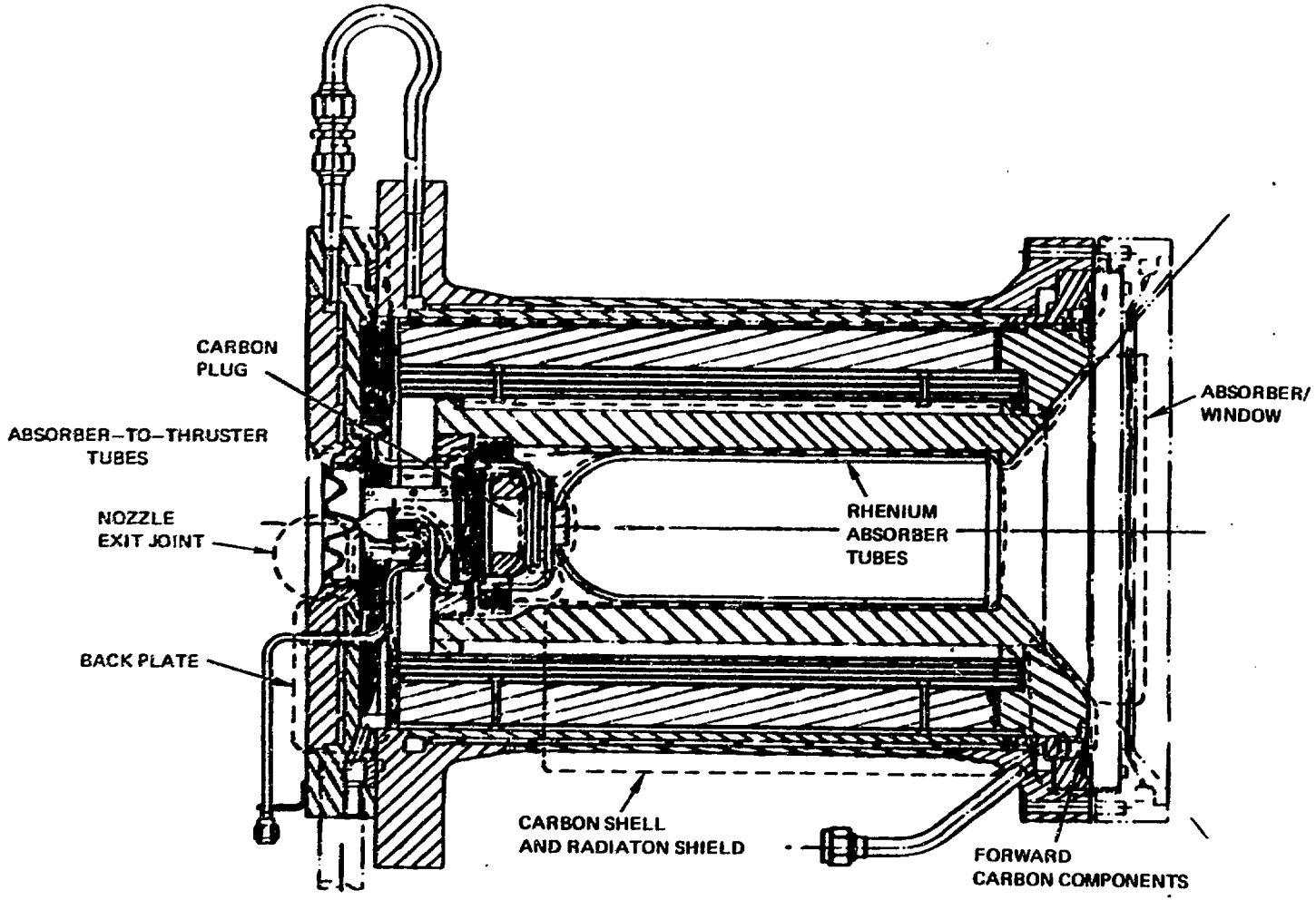

Figure 93. Thermal Analysis Regions

The coolant pressure drop results for the five absorber designs are presented in Table 10. The three- and four-tube designs resulted in high coolant pressure drops and although the six- and seven-tube designs greatly reduced the coolant pressure drop, the increased number of tubes would complicate the coiling of the tubes. Therefore, the five-tube design was selected as a compromise in minimizing the coolant pressure drop and minimizing the number of tubes to ease fabrication.

TABLE 10. RESULTS OF COIL-TUBE PROPELLANT FLOW AT DIFFERENT CONFIGURATIONS (TUBE DIAMETER = 0.1 ID)

NUMBER OF TUBES	TUBE LENGTH (IN)	DISCHARGE MACH NO.	ΔP (PSI)
3	268.1	> 0.7	> 100
4	201.1	0.2	> 100
5	160.8	0.1	53
6	134.0	0.078	40
7	114.9	0.065	25

Total pressure and propellant temperature along the axial distance are shown in Fig. 94 for the five-tube configurations. Tube wall temperatures along the tube coil are shown in Fig. 95. The maximum tube wall temperature was 2750 K (4950 R) to achieve a final hydrogen propellant temperature of 2722 K (4900 R).

Detailed Absorber/Window Thermal Model

The heat exchange between the coiled tube cylindrical absorber cavity and the window of the vacuum enclosure was modeled using the Differential Equation Analyzer Program (DEAP). The absorber cavity assumed to be a gray diffuse surface which can absorb a portion of the incoming radiation and emit and reflect the spectral radiation toward adjacent cavity surfaces and toward the quartz window of the vacuum enclosure. The heat balance on the quartz window is shown in Fig. 96.

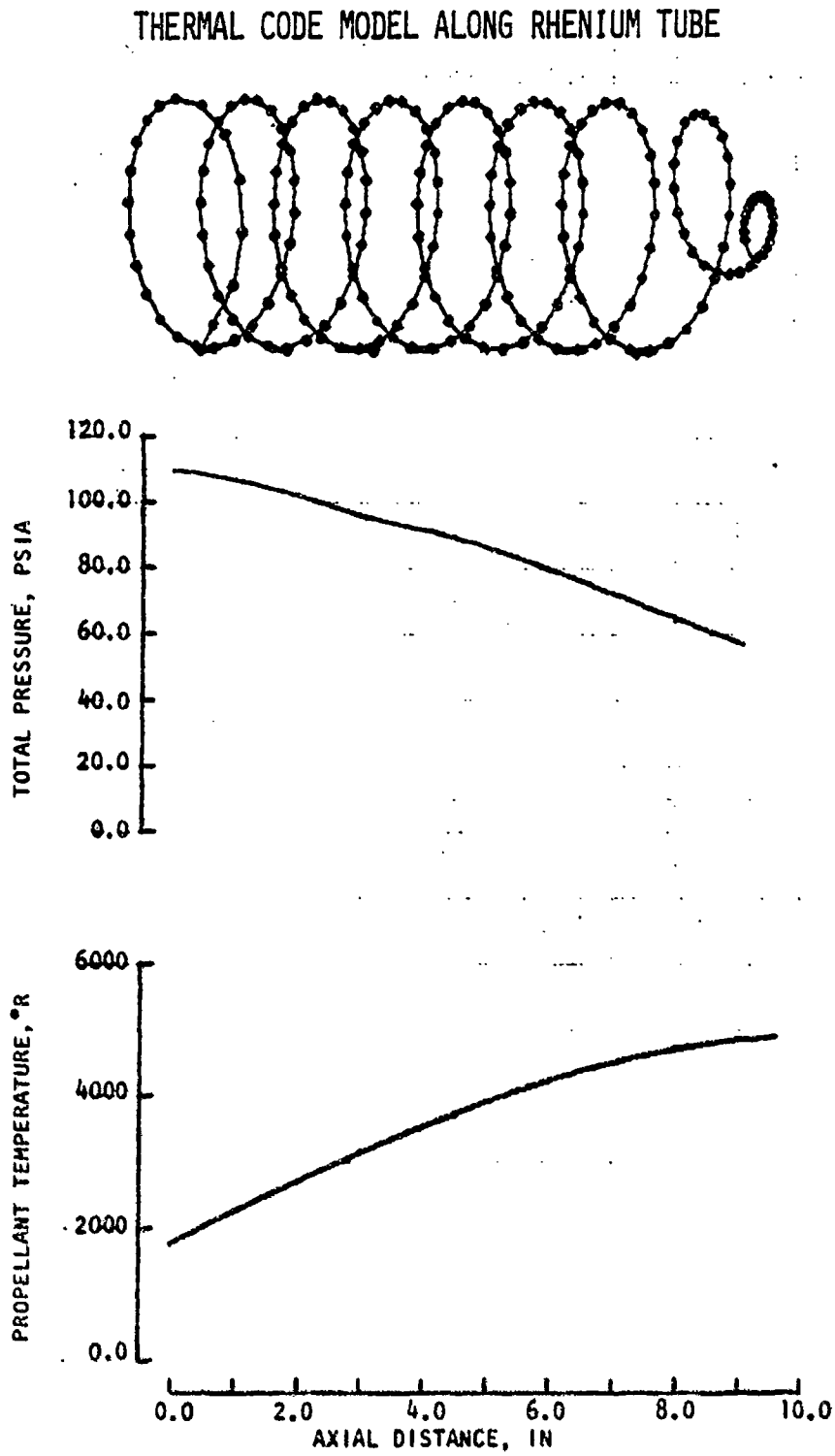

Figure 94. Results from Regen Computer Output for Absorber/Chamber With L/D = 2.5 and Tube of 0.254 cm (0.1 inch) ID

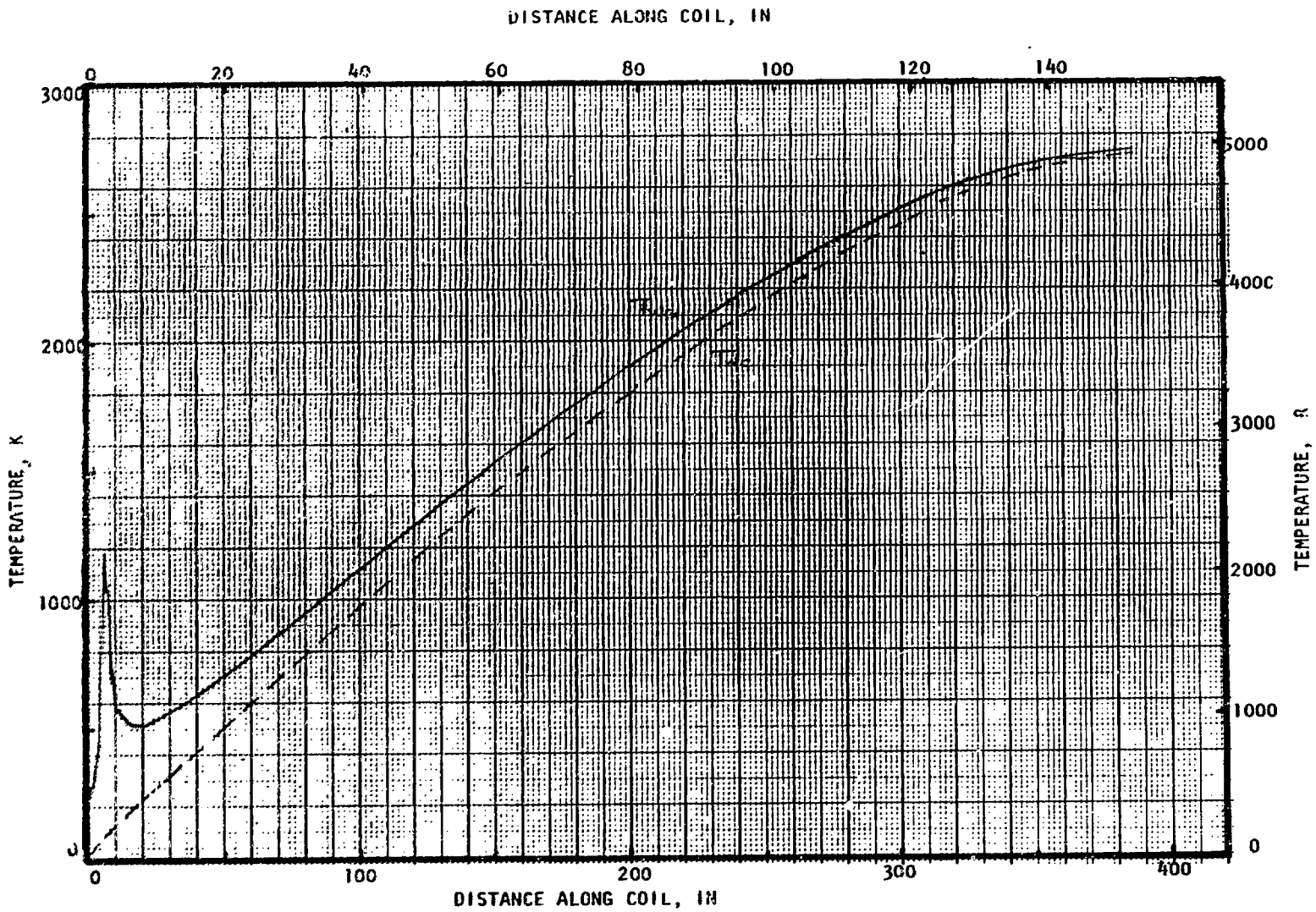

Figure 95. Temperature Distribution for Five-Tube Absorber Design (L/D = 2.5)

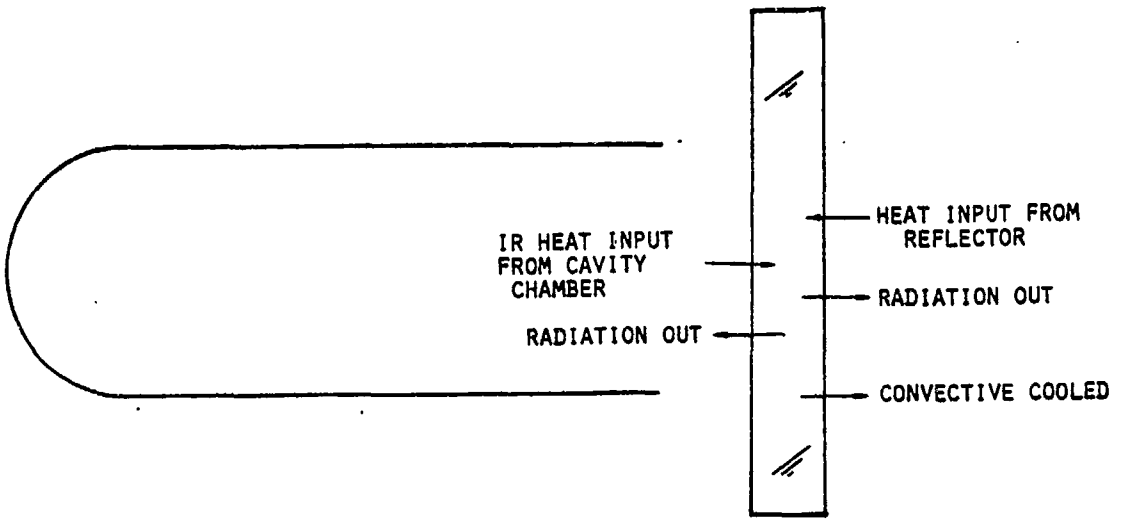

Figure 96. Heat Balance on Quartz Window

To analyze the heat exchange within the cavity in a detailed but efficient manner, the absorber was divided into seven thermal zones. Each zone represents a region with a different uniform temperature. The regenerative cooling analysis computer program used in the previous cooling analysis of the absorber was used to provide the average absorber zone temperatures for the combined thermal model. The energy exchange factors between the different cavity zones were computed within the model. The radiation heat flow resistance within the absorber was described by the general relationship,

$$R_{ij} = \frac{1 - \epsilon_i}{\epsilon_i A_i} + \frac{1}{E_{ij} A_i} + \frac{1 - \epsilon_j}{\epsilon_j A_j} \quad \text{for } i = 1 \text{ to } 7, \; j = 1 \text{ to } 7$$

where

ϵ_i = emissivity at surface i

E_{ij} = exchange factor between surface i and j

A_i = surface area of zone i

The vacuum enclosure quartz window transmits, reflects and absorbs energy from the incoming solar radiation, the absorber cavity, and the ambient surroundings. The detail thermal model of the window is illustrated in Fig. 97 and 98. On the earth's surface, the nominal solar heat flux is approximately 1 kW/M^2 (or equivalent to an effective sun temperature of 5113 K or 9203 R).

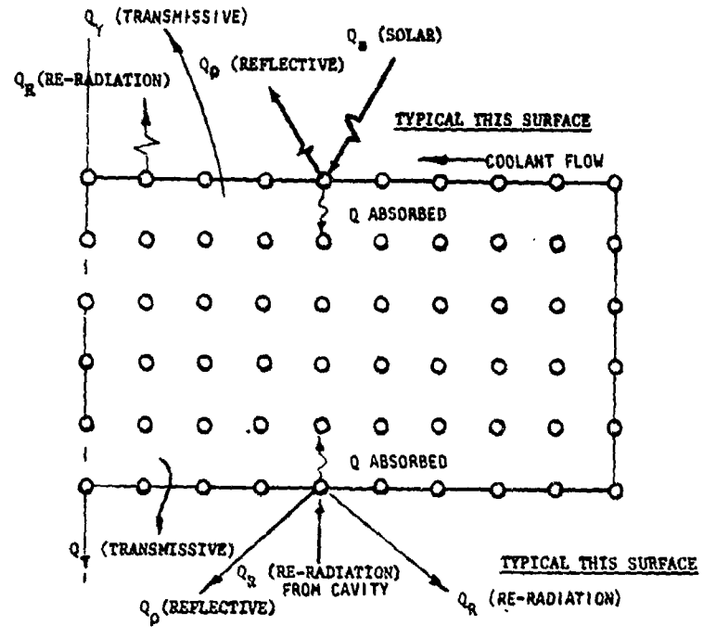

Figure 97. Absorber/Thruster Window Thermal Model Nodal Network

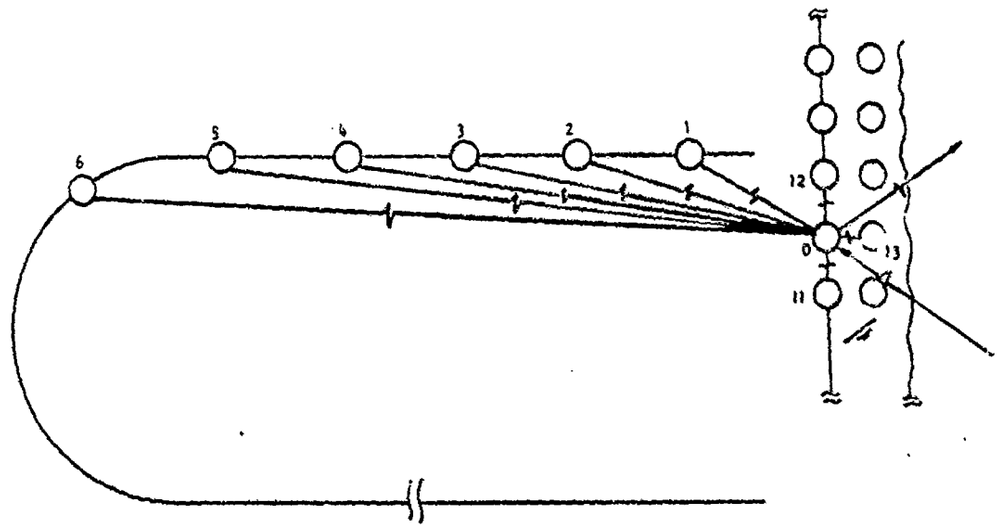

R_{0-i} = THERMAL RADIATIVE RESISTANCE $\quad i = 1, 2, 3, 4, 5$

R_{0-j} = THERMAL CONDUCTIVE RESISTANCE $\quad j = 11, 12, 13$

Figure 98. Quartz Window Thermal Model

As a result, approximately 92% of the total solar emissive power is distributed within the 0 to 2 μM wavelength band spectral band. The average quartz absorptivity for this wavelength band is approximately 0.01 (1%). However, for the infrared (IR) wavelength region, the average absorptivity will be high. To aid in cooling the window, a thin IR reflective coating can be placed on both the inner and outer window surfaces. The exchange factors between the cavity and the window consist of both the view factors and the reflective factors.

$$E_{ij} = F_{ij} + \rho F_{(i-o)-j}$$

All these interrelated effects (effective sun temperature, window coating characteristics, absorber cavity wall temperatures, emissivities, and absorber size) formulate the inputs to the combined thermal model.

$$q_{ij} = \frac{\dfrac{\varepsilon_i \quad \sigma T_i^4}{\tau_j \ \alpha_j} - \sigma T_j}{\left[\dfrac{1}{E_{ij} \ A_i \ \alpha_j \tau_j}\right]}$$

where

α_j = window absorptivity

τ_j = surface boundary infrared coating transmissivity

T_i = quartz window temperature

T_j = cavity zone temperature

The window heating rate (heat absorption) from the solar concentrator is

$$q_o = \alpha_k \ \tau_k \ Q_o$$

where

$\alpha_k \ (T_s)$ = absorptivity

T_s = effective sun temperature

$\tau K \ (T_s)$ = coating transmissivity

Q_o = heat flux from concentrator

Absorber/Window Thermal Analysis

Utilizing the above-described model, combined thermal analysis of the absorber and the quartz window was performed to determine window temperatures, window cooling requirements, and IR coating requirements. As shown in Fig. 99, an IR

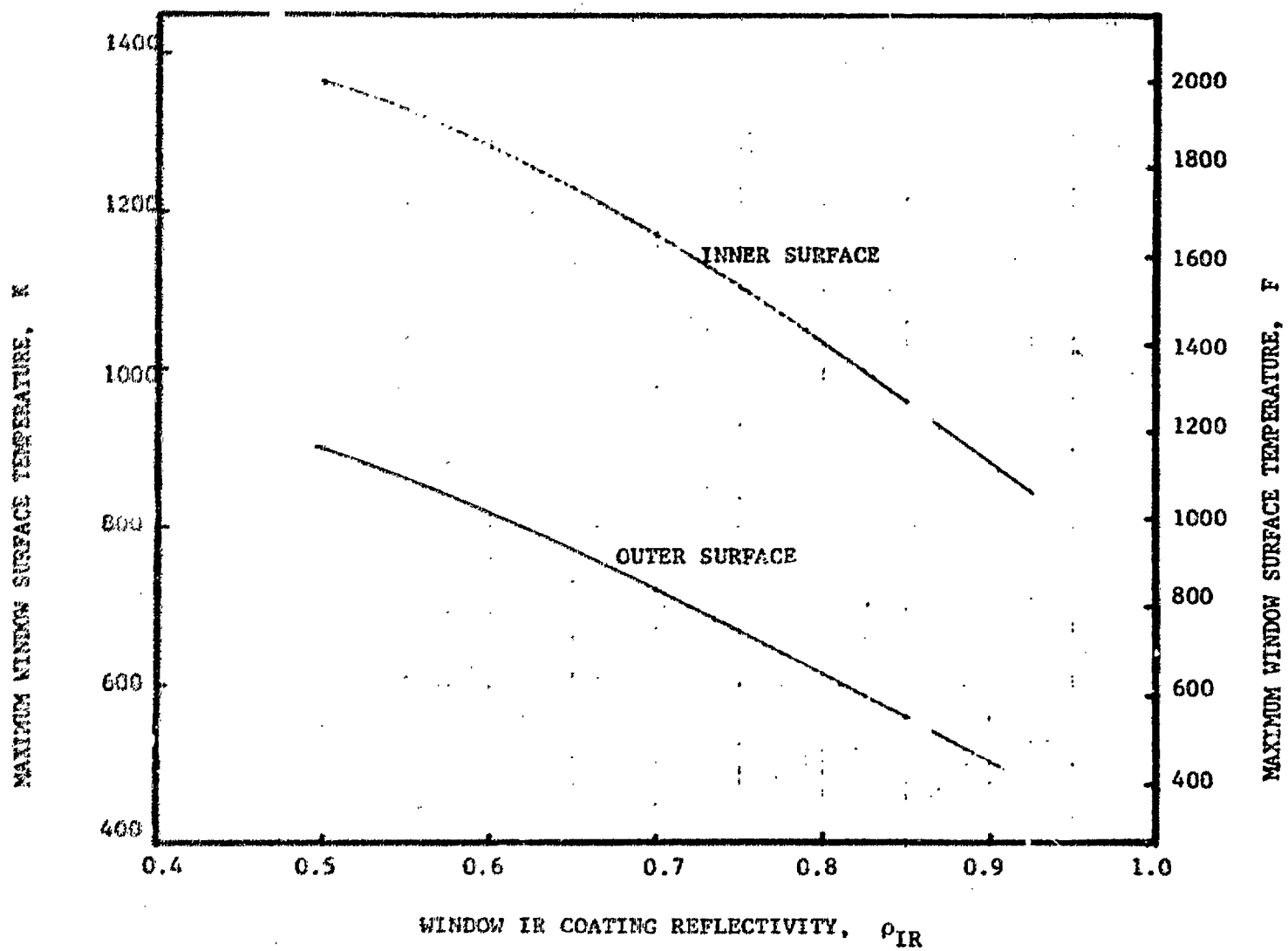

Figure 99. Window Temperature Variation with IR Coating Reflectivity
[$h_{c_{GH_2}}$ = 0.0000581 kCal/cm^{2}sec K (0.000826 Btu/inch^{2}sec F)]

coating is required to achieve satisfactory window temperatures. Due to reradiation from the internal absorber surface and the gaseous nitrogen convective cooling on the outside window surface, the inner window surface temperature is higher than that of the outside surface.

A typical absorber and quartz window temperature distribution is presented in Fig. 100 using absorber and window geometry previously presented and an 85% IR reflectivity coating. The window was 1.905 cm (0.75 inch) thick and the heated surface was 23.724 cm (9.34 inch) in diameter. The aperture end of the absorber was 4.445 cm (1.75 inch) from the window. The lower window temperatures at the larger radii should enable the use of conventional seal materials.

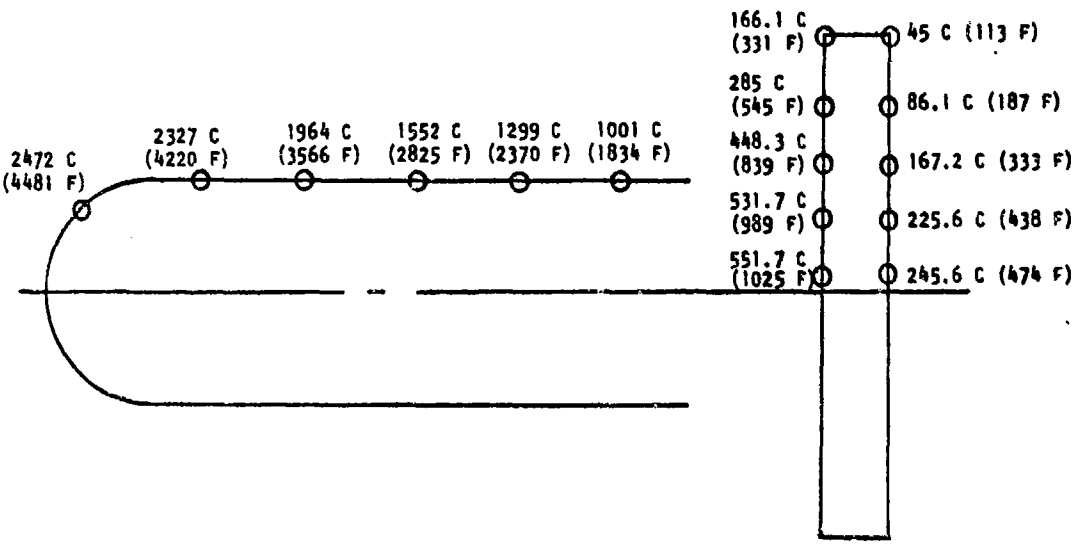

- WINDOW IR COATING REFLECTIVITY = 0.85
- WINDOW FILM COOLING COEFFICIENT = 0.00001162 KCAL/CM^2-SEC- R (0.00016528 BTU/IN^2-SEC- F)
- WINDOW THICKNESS = 0.75 INCH

Figure 100. Typical Absorber/Window Temperature Distribution

Analysis results determined that the quartz window temperatures were significantly lower than the material critical temperature. However, a substantial temperature gradient across the window thickness was encountered due to the low thermal conductivity of quartz as shown in Fig. 101. Analysis which eliminated the convective cooling indicated that a reasonably low window temperature can be achieved without the undesirable axial temperature gradient. As shown in Fig. 102, each of the isotherm lines of this quartz window configuration (no convective cooling) are parallel to an axial centerline indicating very little thermal gradient. The maximum temperature occurred at the center region and decreases radially. In this configuration the quartz window was kept from overheating by the protection of IR coating on both sides. The required coating reflectivity was 0.85. Therefore it was concluded that window cooling was not required with use of IR coatings and this approach was adopted for the design.

Carbon Shell and Radiation Shields

The carbon shell with a rhenium coating on the inner surface serves as a thermal shield to reduce the heat loss from the absorber and acts as a high temperature housing to contain the coiled rhenium tube assembly. In determining the regenerative cooled radiation shield temperatures, three variables were influential. These were: (1) reflectivity of the coating on the inner wall of the carbon shell, (2) reflectivity of the radiation shield, and (3) hydrogen coolant velocity within the regenerative-cooled radiation shield. The first two variables determined the heat flux on the shield and the third parameter defined the cooling capability of the shield.

A study was made of the various high temperature coatings which could be applied to the carbon shell and other carbon components of the absorber as discussed in more detail in the subsequent Materials and Processes section. Of the possible candidates, chemically vapor-deposited rhenium appeared to be the most attractive. The coefficient of thermal expansion of the rhenium is close to that of the graphite, thereby minimizing the risk of thermal mismatch problems. The ductility of the rhenium will more than allow for any thermal

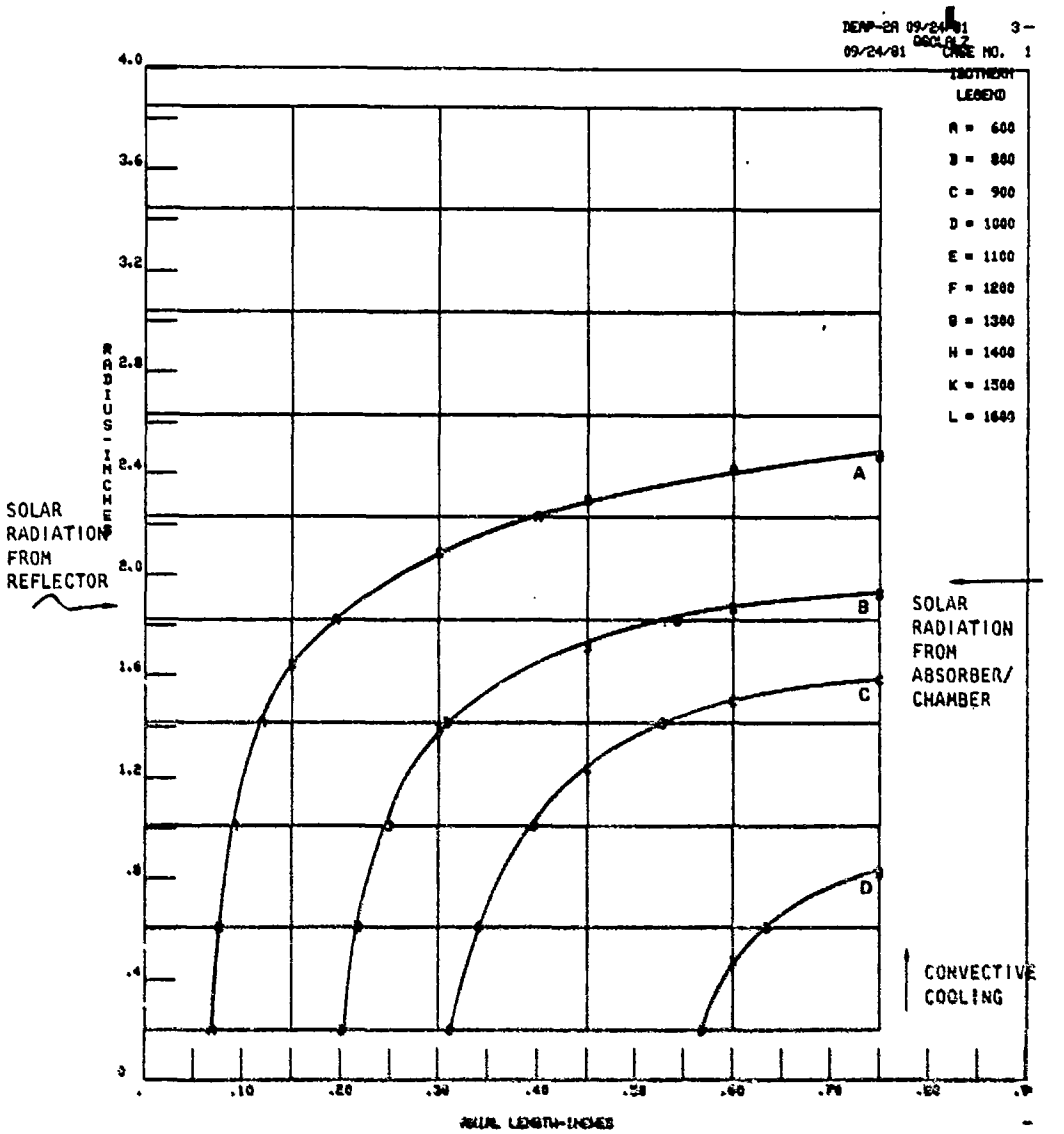

Figure 101. Quartz Window Temperature Distribution with 30.48 cm (12 inches) Diameter and 85% IR Reflectivity

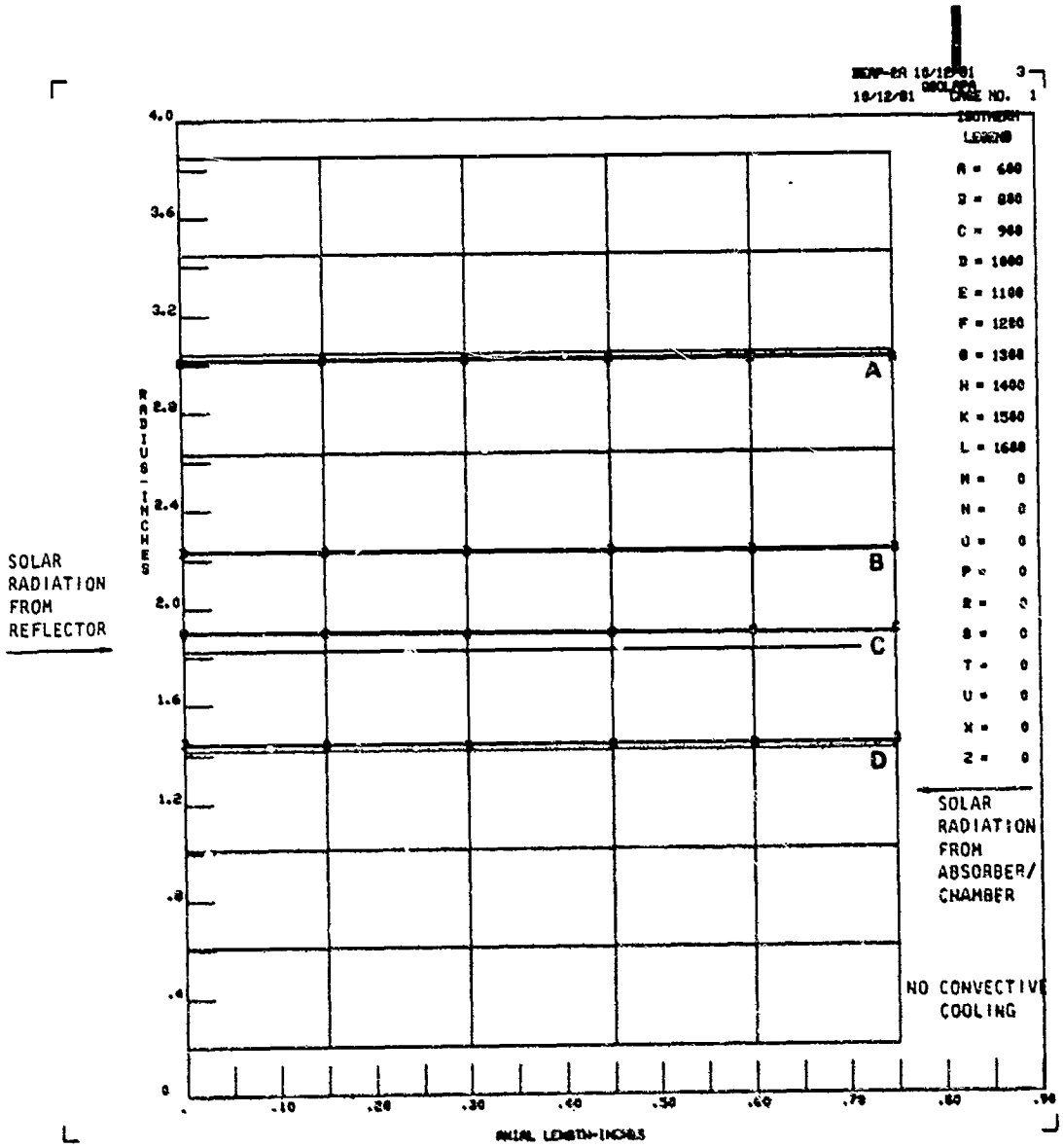

Figure 102. Quartz Window Temperature Distribution with 30.48 cm (12 inches) Diameter and 85% IR Reflectivity

mismatch which may exist. In addition, of the coatings considered, rhenium is the only one that does not form a carbide. The interface layer between the rhenium and carbon will be a stable eutectic. The rhenium coating will prevent sublimation of the carbon because the surface is 100% dense. Based on the survey made, a coating emissivity value of 0.3 was used for the thermal analyses.

The thermal analysis indicated that the carbon shell was heated close to 2284 K (3651 F) at steady state (Fig. 103). The low thermal conductivity of the carbon results in a relatively large resistance to axial heat conduction; however heat is transferred radially through radiation. The net heat flux dissipated from the carbon shell was intercepted by the regenerative-cooled radiation shield and resulted in an excessive propellant bulk temperature rise in the shield. To reduce this heat input, the benefit of a series of intermediate thermal shields (between the carbon shell and the regenerative-cooled radiation shield) were analyzed and the corresponding thermal results are presented in Fig. 103.

The intermediate shields were assumed to be fabricated from TZM with a 0.1016 cm (0.04 inch) wall thickness. The shields were also assumed to be polished on both sides to achieve an emissivity no more than 0.3. The fairly high thermal conductivity of this material resulted in small thermal gradients across the shields (0.11 K or 0.2 F). The effectiveness of the number of intermediate shields used is illustrated by the data presented in Fig. 104. The heat input through the radiation shield significantly decreased for one and two shields but tended to level off for more than four intermediate radiation shields. This result was similar to the one-dimensional solution for a series of equal area flat plate radiation shields. In this simple problem the heat transferred through the shields decreased proportional to 1/(n+1) where n is the number of shields.

The heat input shown in Fig. 104 is the heat absorbed by the hydrogen in the cooled shield plus that lost externally through radiation. With four intermediate shields, the total heat input for this section of the regenerative-cooled radiation shield was 3.11 kw (2.95 Btu/sec).

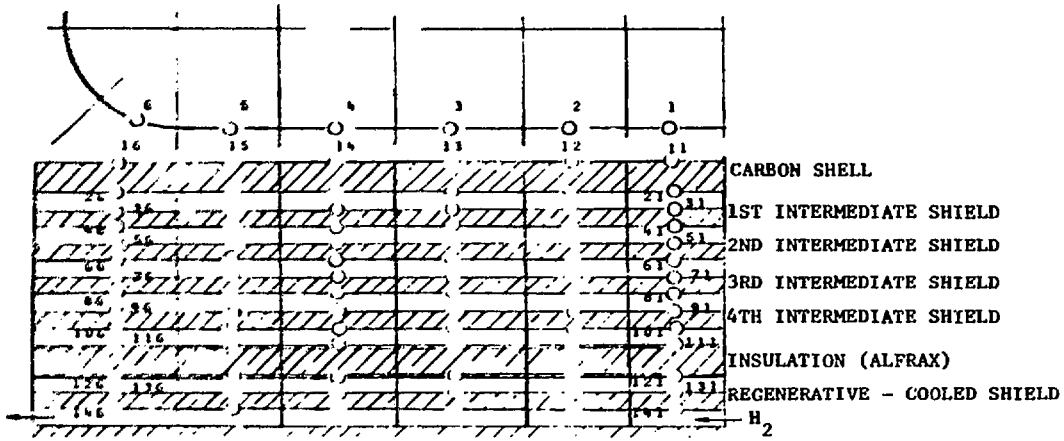

SHIELD CONFIG.	T_{11} °K(°F)	T_{16} °K(°F)	T_{21} °K(°F)	T_{26} °K(°F)	T_{31} °K(°F)	T_{36} °K(°F)	T_{51} °K(°F)	T_{56} °K(°F)	T_{71} °K(°F)	T_{76} °K(°F)	T_{91} °K(°F)	T_{96} °K(°F)	T_{111} °K(°F)	T_{116} °K(°F)	T_{121} °K(°F)	T_{126} °K(°F)	T_{131} °K(°F)	T_{136} °K(°F)	T_{141} °K(°F)	T_{146} °K(°F)
NO INT. SHIELD	1278 (1841)	2284 (3651)	1283 (1849)	2177 (3459)													477 (399)	1573 (2371)	474 (393)	1563 (2353)
ONE INT. SHIELD	1340 (1952)	2336 (3745)	1350 (1970)	2237 (3566)	1286 (1855)	2051 (3232)											477 (398)	1419 (2095)	473 (392)	1411 (2079)
TWO INT. SHIELDS	1378 (2020)	2427 (3908)	1392 (2046)	2342 (3756)	1382 (2028)	2041 (3214)	1299 (1878)	1866 (2899)									476 (396)	1207 (1712)	473 (391)	1199 (1699)
FOUR INT. SHIELDS	1426 (2107)	2461 (3969)	1446 (2142)	2382 (3827)	1481 (2205)	2131 (3376)	1465 (2177)	1998 (3137)	1407 (2073)	1853 (2875)	1302 (1884)	1687 (2576)					473 (391)	1032 (1398)	469 (385)	1027 (1389)
FOUR INT. SHIELDS & INSUL.	1662 (2531)	2514 (4065)	1637 (2577)	2456 (3960)	1726 (2646)	2292 (3665)	1724 (2644)	2212 (3522)	1696 (2592)	2132 (3378)	1639 (2491)	2053 (3235)	1553 (2335)	1249 (3096)	1249 (1788)	1451 (2152)	403 (266)	802 (984)	401 (261)	799 (978)

Figure 103. Absorber Intermediate Radiation Shield Thermal Analysis Results

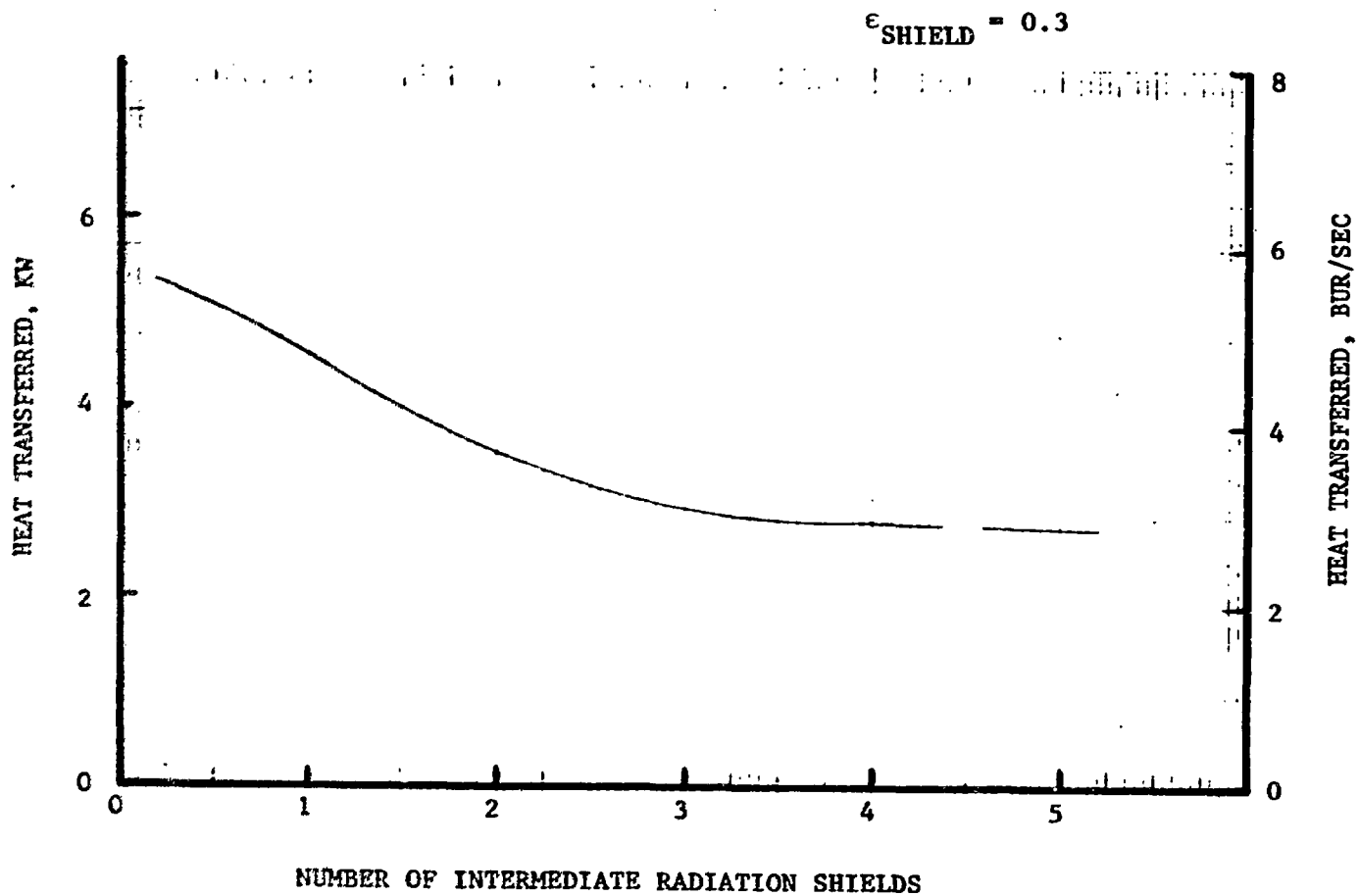

Figure 104. Influence of Number of Intermediate Radiation Shields on Heat Transferred to Regenerative-Cooled Shield (Cylindrical Portion)

To determine the heat input to the remaining portion of the cooled shield, the heat loss from the five absorber-to-thruster propellant tubes was estimated assuming that the five tubes were arranged in a row and the four intermediate shields were extended aft to surround the thruster. The resulting heat input was 2.01 kw (1.9 Btu/sec). Approximately 6.5% of this loss reflected back to the propellant lines and remainder reflected within the cylindrical shield and to the back plate of the regenerative-cooled radiation shield or absorbed through the radiation shields.

Therefore, the total heat input to the regenerative-cooled radiation shield was 5.23 kw (4.85 Btu/sec). The heat lost externally from the back side of this shield was determined to be 1.16 kw (1.1 Btu/sec) or approximately 5% of the total incoming solar radiation. This results in a 3.96 kw (3.85 Btu/sec) net heat input to the hydrogen in the cooled shield which resulted in approximately a 978 K (1300 F) hydrogen exit temperature. Therefore, to improve cooling of the shield, further reductions in the net heat input were desirable.

The current regenerative-cooled radiation shield design offers several radiation shield cooling approaches as schematically outlined in Fig. 105. All the approaches lose 28% of the total incoming solar radiation through reradiation and reflection through the window. The first approach is the regenerative-cooled method using only the nominal absorber/thruster hydrogen flowrate (ambient inlet). As discussed previously, this approach results in an additional 5% heat loss due to the high hydrogen bulk temperature within the shield which translates into a 71% absorber efficiency.

Using two times the nominal hydrogen flow to cool the cylindrical part of the cooled shield and dumping half the flow at the exit (second approach), the hydrogen shield exit temperature could be reduced to approximately 617 K (650 F). However, an additional 4% heat loss is incurred and also an uncertainty in measuring the actual thruster flowrate is introduced by the bypass cooling technique.

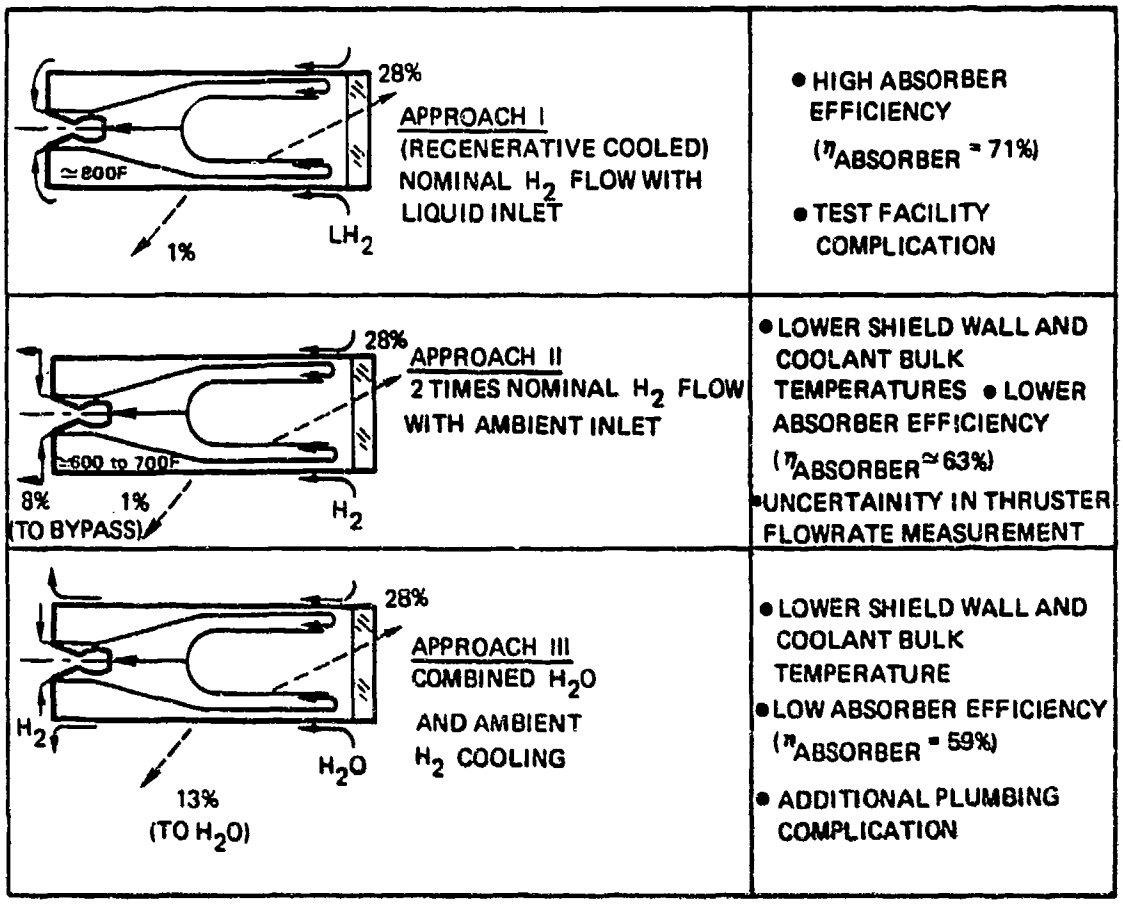

Figure 105. Radiation Shield Cooling Approaches

The third alternative shield cooling approach is to cool the cylindrical portion of the shield with water and use an ambient hydrogen inlet for the regenerative-cooled back plate. This approach reduces the shield coolant bulk temperature but increases the external heat loss to 13% (absorber efficiency of 59%) since the heat absorbed by the water is not utilized in the system.

Therefore, to achieve the desired high absorber efficiency and accurate propellant flowrate measurement, the regenerative cooling approach (Approach I) was preferred based on achievable absorber efficiency.

In an attempt to further reduce the heat input to the regenerative-cooled radiation shield and the external heat loss, the incorporation of an insulative layer (aluminum oxide) was analyzed. The insulation was evaluated in three basic configurations which included: (1) intimate contact with the fourth intermediate shield with a gap between the insulation and the regenerative-cooled shield, (2) intimate contact with the regenerative-cooled shield with a gap between the insulation and the fourth intermediate shield, and (3) a gap between both the fourth intermediate shield and the regenerative-cooled shield. The third configuration achieved the lowest heat loss. An insulative layer emissivity of 0.3 was assumed. This would necessitate a polished insulative surface or that the insulation be sandwiched between two cylinders of TZM shield material. Properties of two grades of aluminum oxide insulation (Mullfrax 202 and Alfrax B101) are given in Table 11.

TABLE 11. PROPERTIES OF ALUMINUM OXIDE RADIATION INSULATION

PARAMETER	MULLFRAX 202	ALFRAX B101
MAXIMUM HOT FACE TEMPERATURE	1815 C (3300 F)	1870 C (3400 F)
BULK DENSITY	2.8 G/CM^3 (175 LB/FT^3)	1.45 G/CM^3 (90 LB/FT^3)
THERMAL CONDUCTIVITY AT 1477 K (2200 F)	1.9 W/M K (13 BTU/HR/FT^2/IN F)	1.1 W/M K 7.5 BTU/HR/FT^2/IN F
SPECIFIC HEAT 0 to 1400 C (2550 F)	0.25 CAL/GM/C	0.28 CAL/gm/C
THERMAL EXPANSION COEFFICIENT (MEAN)	6.0x10^{-6} CM/CM/C (3.3x10^{-6} IN/IN/ F)	8.6x10^{-6} CM/CM/C 4.8x10^{-6} IN/IN F)
POROSITY	19.6%	62%

The total heat input to this section of the regenerative-cooled radiation shield was reduced from 3.11 kw (2.95 Btu/sec) to 2.93 kw (2.78 Btu/sec). More importantly, maximum regenerative-cooled shield temperature was reduced from 1032 K (1398 F) to 802 K (984 F).

The resulting carbon shell, shield, insulation, and regenerative-cooled shield temperatures are presented in Fig. 106. Since this shield configuration achieved the lowest heat loss and reduced wall temperatures on the regenerative-cooled shield, this configuration was incorporated into the ground test absorber/thruster design.

Absorber Forward Carbon Components

The inner IR radiation window coating influences the distribution of the radiation loss from the absorber. Eighty percent of the radiation from the absorber inner surface is reflected both diffusively and specularly from the window. Therefore, tracing this reflected energy was essential in determining the net heat load imposed on the absorber. Also, the radiant heating caused by this reflected radiation determined the temperature of the forward end of the carbon shell and the carbon retaining ring.

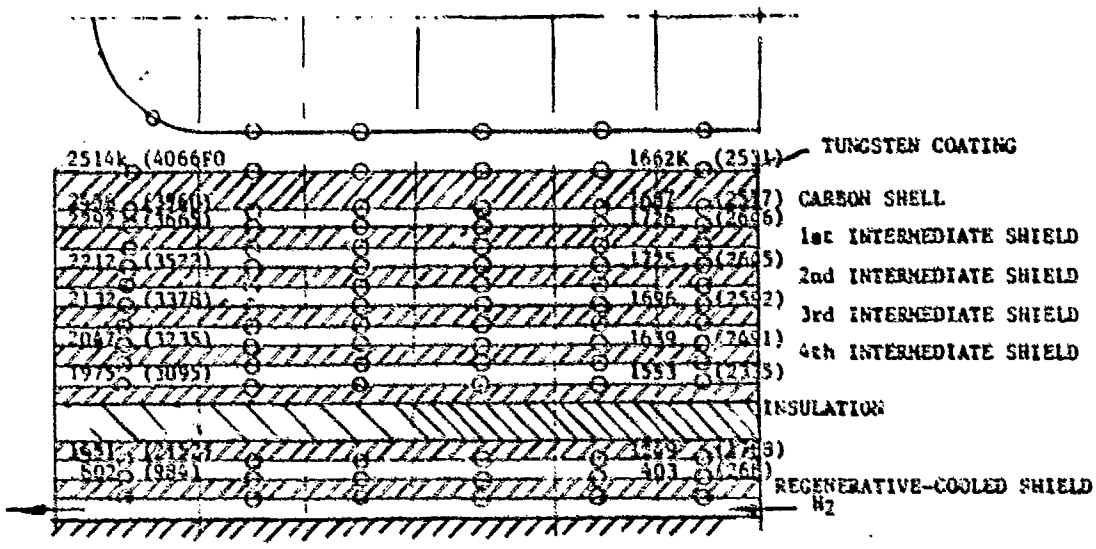

Figure 106. Absorber Shield Thermal Analysis Results (with Insulation)

The temperature of these carbon surfaces was computed using the thermal model presented in Fig. 107. Assumptions included in this analysis were:

1. Surface 3 is a black surface
2. Window coating reflectivity is 0.8
3. The specular and diffusive coating reflectivity were both 0.4

The pertinent dimensions of the model geometry were:

r_1 = 4.064 cm (1.6 inch)

r_2 = 9.843 cm (3.875 inches)

h = 4.445 cm (1.75 inch)

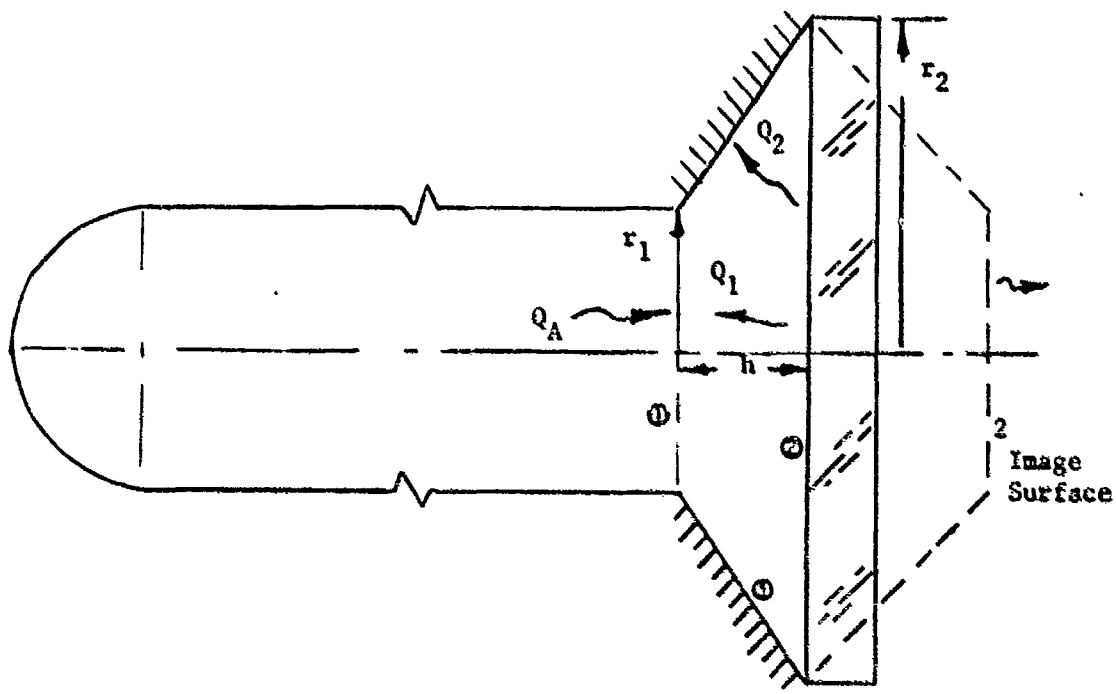

Figure 107. Thermal Schematic of Absorber Forward End

The respective surface view factors were computed and the radiative heat balance established. The heat reflected back into the absorber (Q_1) was calculated to be 9.34% of the radiation from the absorber. The heat reflected onto the front portion of the carbon shell and the carbon retainer ring (Q_2) was 69.5% of the heat radiated from the absorber. The other 21.16% is transmitted through the window. The equilibrium temperature of the carbon components was computed to be 1311 K (1900 F) and therefore should not present a problem.

Carbon Plug

The carbon plug acts to block off solar radiation not captured by the rhenium tubing. One may ask if the carbon plug was eliminated, what percentage of the total heat would pass through the remaining hole. A brief thermal analysis indicated that 0.8% of the total heat would be radiated from adjacent absorber surfaces out the hole. The percentage of direct solar radiation passing through the hole would be dependent on the diffuse nature of the radiation source. The total heat through the hole was determined to be approximately 6% of the total heat input for a collimated radiation source and 1% for a 180-degree diffuse source. A ±45-degree radiation source should result in an average of 3.5% heat passing through the hole.

Heat Loss from the Absorber-to-Thruster Tubes

The heat loss from the absorber-to-thruster tubes to the cylindrical portion of the absorber shield configuration with the first modified absorber/thruster design (with radiation shield around the tubes) was calculated to be 0.88 kw (0.83 Btu/sec). At this time, it was realized that the obvious solution to reducing this heat loss was to shorten the distance between the absorber and the thruster. The final design layout shown in the Design Section accomplished this objective (Fig. 88).

The main improvement in the design layout was incorporation of the advantages of having minimum heat loss and higher thruster nozzle performance. The main efforts in reducing the heat-loss was to keep the overall thruster/vacuum

chamber short to minimize the heat loss from heated propellant tubes from the absorber to the thruster. For the five tubes arranged in a circle, the emitting surface area of the propellant discharge line was area = 1.67 RL

where R = outer-tube radius, inch
L = tube length, inch

Since the tube radius was determined as 0.1524 cm (0.06 inch), the line length became the important parameter in calculating the emitting surface area. In this final design layout, the line length was reduced from 10.92 cm (4.3 inches) to 1.58 cm (0.62 inch) such that the emitting surface area was reduced by a factor of 6.94.

The total heat loss from these lines decreases as the emitting surface area and the potential nonlinear temperature difference driving force are decreased. The average temperature difference between the tube and enclosure surface (radiation shield) is approximately 250 K (450 F). Hence the estimated heat loss can be calculated approximately as 0.686 kw (0.65 Btu/sec).

Thruster and Nozzle Exit Joint

Due to potential thermal expansion and life fatigue problems of the nozzle exit joint region, where the rhenium nozzle joins to a Inco 903 base, a thermal model consisting of 37 nodes was constructed (Fig. 108) to determine the steady-state temperature profile in this region. Heat conduction was the primary mode of heating in this region. The radiation heat source was not dominant due to the fact that the emitting surface area and temperature are not large [the radiation heat source is only 1644 K (2500 F) and less]. The peak temperature point at the joint surface area was estimated to be less than 998 K (1797 R) which was determined to be a satisfactory condition.

Backplate

In the thermal design of the enclosure backplate, the heat distribution inside the enclosed cavity was evaluated based on the surrounding wall temperatures

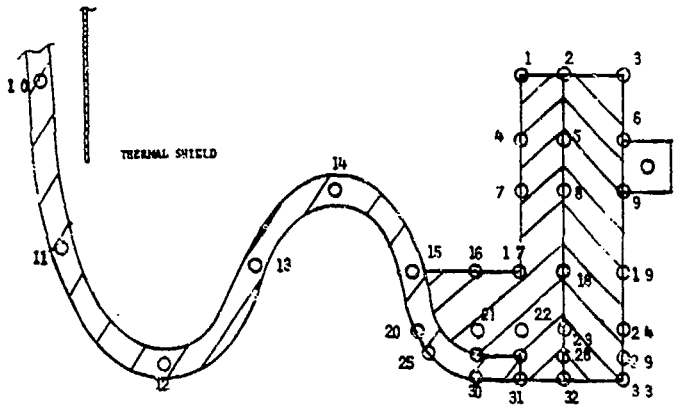

T_1	1307°F	T_{18}	1328°F
T_4	1313°F	T_{19}	1303°F
T_5	1311°F	T_{20}	1397°F
T_6	1294.7°F	T_{21}	1395°F
T_7	1323°F	T_{22}	1353°F
T_8	1318°F	T_{23}	1331°F
T_9	1291°F	T_{24}	1305°F
T_{10}	2570°F	T_{25}	1391°F
T_{11}	2540°F	T_{26}	1389°F
T_{12}	2083°F	T_{27}	1353°F
T_{13}	1814°F	T_{28}	1332°F
T_{14}	1609°F	T_{29}	1306°F
T_{15}	1450°F	T_{30}	1387°F
T_{16}	1423°F	T_{31}	1354°F
T_{17}	1347°F	T_{32}	1337°F

Figure 108. Typical Results of Nozzle Joint Temperature Distribution

as well as the surface area and geometry (Fig. 109). Since the thruster radiation shield had a temperature close to that of the combustor thruster wall, the net heat transfer into the internal shield was from absorber to thruster propellant lines. The temperature difference along the carbon shell was the main driving force to contribute the heat transferred into this cavity. However, the heat transfer into the backplate was designed to be minimized using a 1.524 cm (0.6 inch) thick low thermal conductivity insulation placed on the plate. This enables the backplate to be maintained at the reasonable low operating temperature range. To achieve desired temperature gradient across the insulation, the coolant flow path illustrated in Fig. 110 was developed. The hydrogen enters the backplate at the outer diameter and flows spirally and is discharged into a manifold near the center. This coolant flow absorbs majority of the heat load which is being transferred into the cavity.

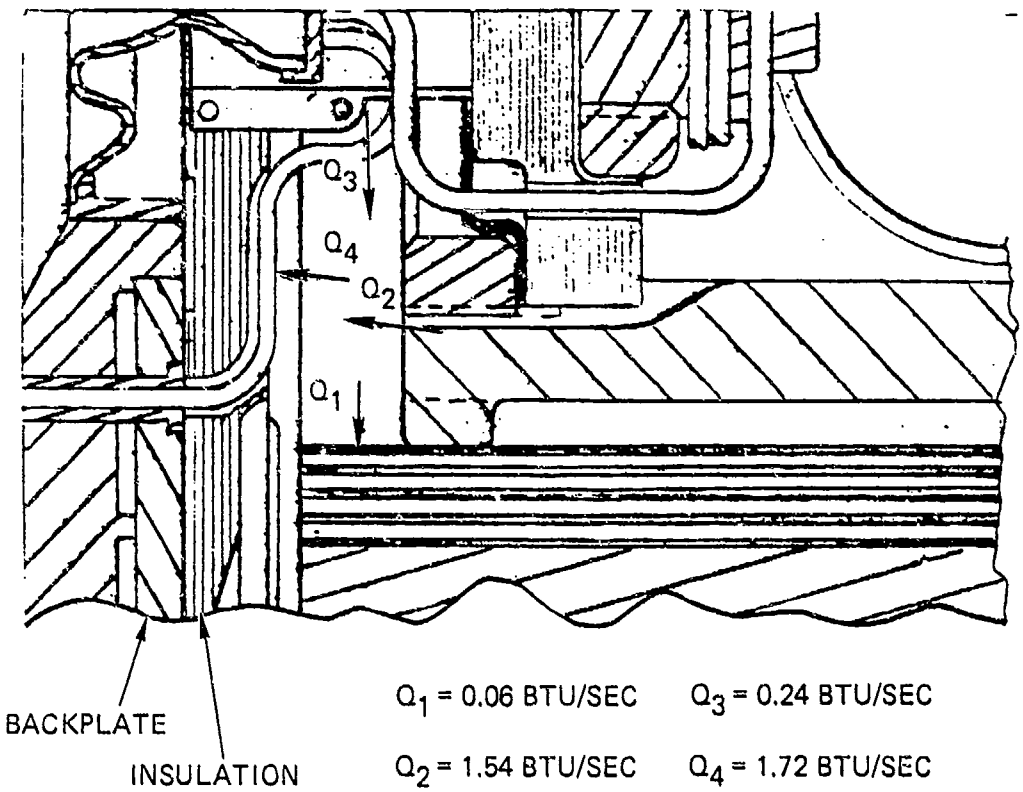

Figure 109. Heat Distribution at the End Enclosure Cavity

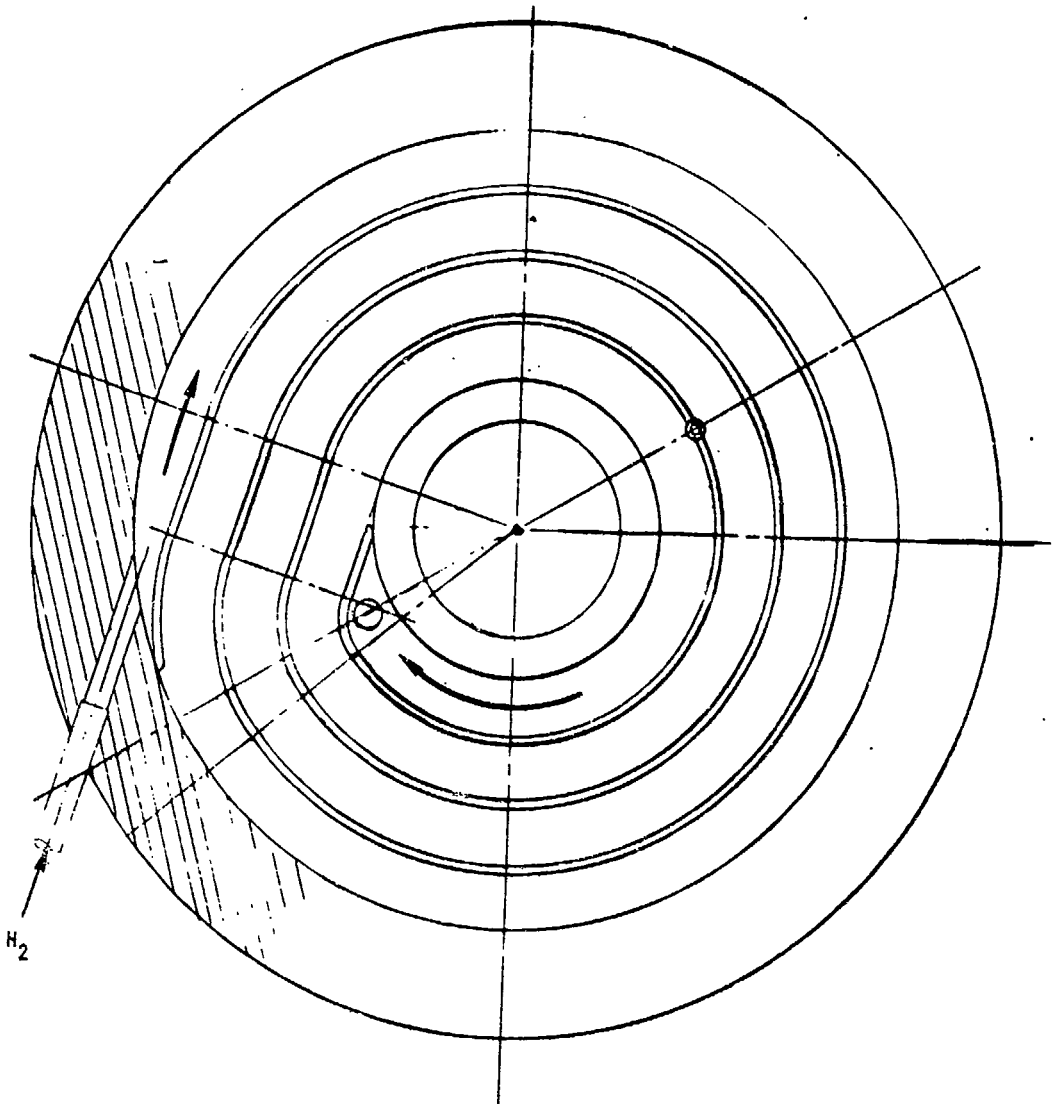

Figure 110. Cooling Passages Design for Cavity Chamber Closeout Plate

Overall Absorber/Thrust Temperature and Pressure Distribution

Based on the individual analyses discussed previously, the overall heat distribution in the absorber/thruster was established and is shown in Fig. 111. Figure 112 shows the temperatures and pressures throughout the assembly. It may be noted that the required hydrogen propellant inlet pressure was 79.3 N/cm^2 (115 psia) at a flowrate of 0.000467 kg/sec (0.00103 lb/sec) and that the maximum temperature within the assembly was 2745 K (4481 F) on the absorber rhenium tubes.

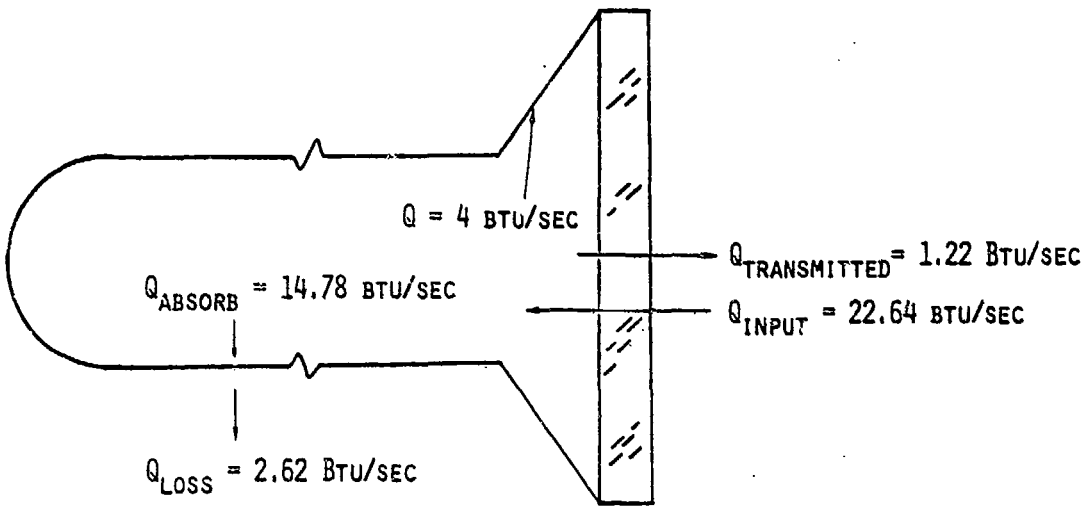

Figure 111. Overall Heat-Distribution in Absorber/Chamber

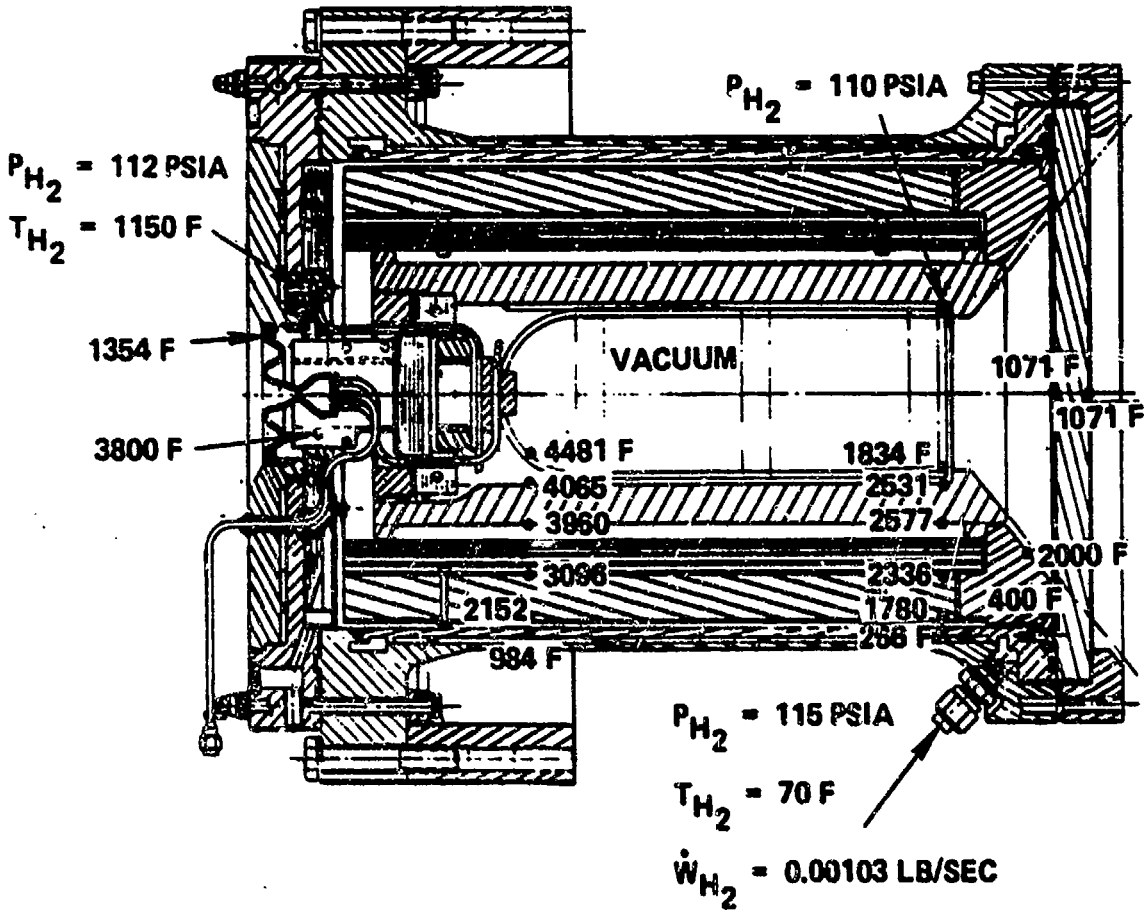

Figure 112. Overall Temperatures and Pressures

STRESS ANALYSIS

Detailed stress analyses were completed on critical component areas of the absorber/thruster assembly. Seven localized regions were analyzed, as illustrated in Fig. 113, to determine loads due to pressure and thermal growth. The structural design criteria and factor of safety requirements are summarized below:

FS_u	≥ 3.0
FS_y	≥ 1.5
FS 10-HOUR RUPTURE STRESS	≥ 2.0
STRESS RUPTURE LIFE	$\geq$40 HOURS

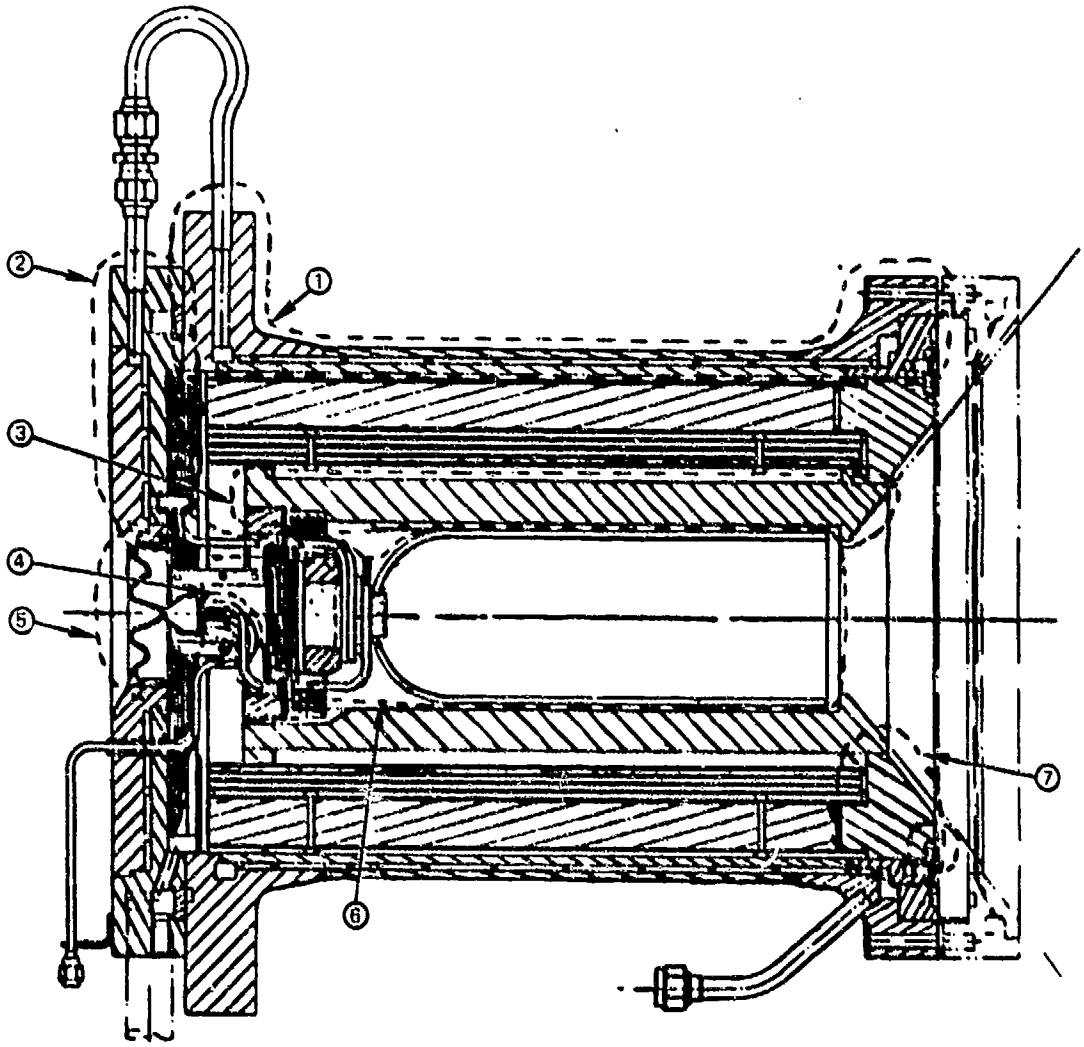

Figure 113. Stress Analysis Regions

Rhenium Tubing

A finite element model of a single rhenium tube (Fig. 114) was constructed and incorporated the coiled rhenium tube as well as absorber inlet and outlet lines. The absorber feed line that runs perpendicular to the rhenium tube coil was conservatively modeled as a straight tube.

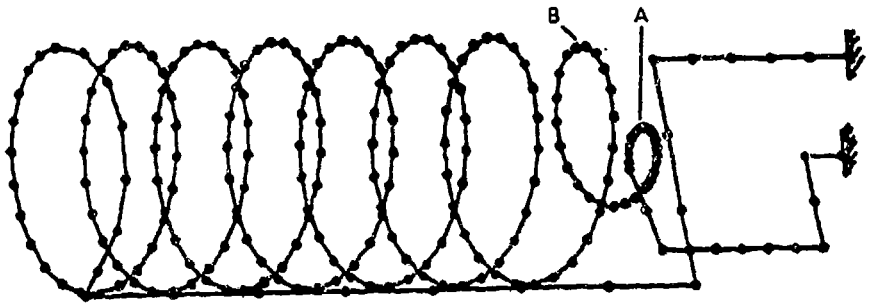

• FACTORS OF SAFETY

MECHANICAL STRESS

LOCATION	STRESS YIELD	ULTIMATE	10 HOUR RUPTURE STRESS	TIME TO – RUPTURE	TEMPERATURE 2756K (4500F)
A	2.42	5.33	2.18	70 HOURS	

STRAIN LOCATION	EMAX	TEMPERATURE 2756K (4500F)
B	0.17%	

Figure 114. Rhenium Tube Finite Element Model and Analytical Results

The finite element model of the rhenium tube was used to determine tube stresses/strains resulting from thermal, pressure, and dead weight loadings. Results are summarized in Fig. 114. The stress results at location A are based on an internal pressure of 41.4 N/cm^2 (60 psia). The maximum predicted strain resulting from thermal loading is 0.17% (location B) compared to a material elongation of 2%. The thermal load analysis included the effects of thermal gradients across the tube diameter. As noted in Fig. 114, factor of safety requirements were met.

Regenerative-Cooled Radiation Shield

Initial analysis of the four intermediate radiation shield design configurations indicated that an Inconel 625 regenerative-cooled radiation shield was structurally acceptable but that a 300 series cres steel shield was unacceptable. This latter material could be made structurally acceptable if a bellows arrangement was incorporated to relieve the differential thermal growth between the inner and outer walls of the cooled shield.

Analysis of the regenerative-cooled radiation shield was revised to reflect the shorter shell length and lower shield temperatures of the final configuration. Results indicated that the lower shield temperatures allowed the use of 347 cres for the radiation shield shell material. During the initial thermal cycle, the outer cylinder will yield in tension. However, on subsequent cycles it will function elastically. The inner cylinder will remain elastic at all times to prevent instability resulting from the combination of compressive thermal and pressure induced stresses. Factors of safety on mechanical stresses for the radiation shield shell and backplate are summarized in Fig. 115 and 116 and were indicated to be satisfactory.

Thruster and Nozzle Exit Joint

A finite element model of rhenium nozzle exit joint was constructed to facilitate the prediction of nozzle pressure and thermal stresses (Fig. 117).

Initially, analysis was conducted based on the use of 347 CRES for the cooled backplate. However, the large difference between coefficients of thermal expansion for rhenium (3.7×10^{-6} in./in./F) and 347 cres (10×10^{-6} in./in./F) resulted in excessive thermal strains in both materials. To reduce strains, the backplate material was changed to Custom 450 CRES (coefficient of thermal expansion of 6.5×10^{-6} in./in./F).

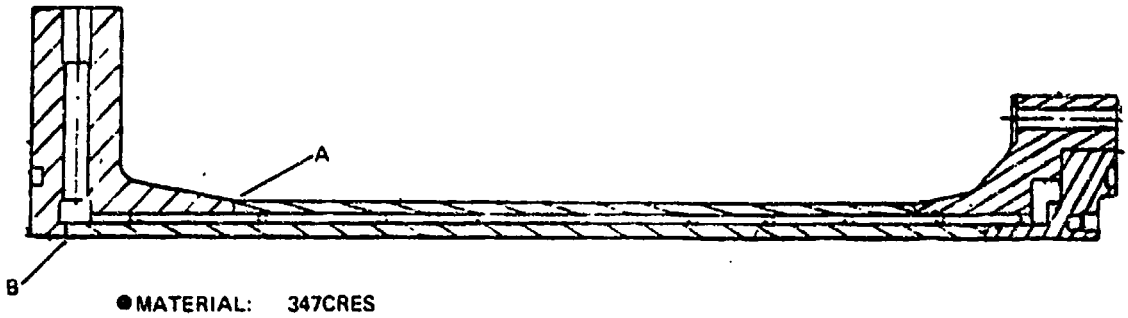

- MATERIAL: 347CRES
- FACTORS OF SAFETY

LOCATION	YELD	ULTIMATE	TEMPERATURE
A - WELD	2.10	5.00	700K (800F)
B - WELD	3.29	8.32	811K (1000F)

Figure 115. Solar Absorber/Thruster Radiation Shield Shell

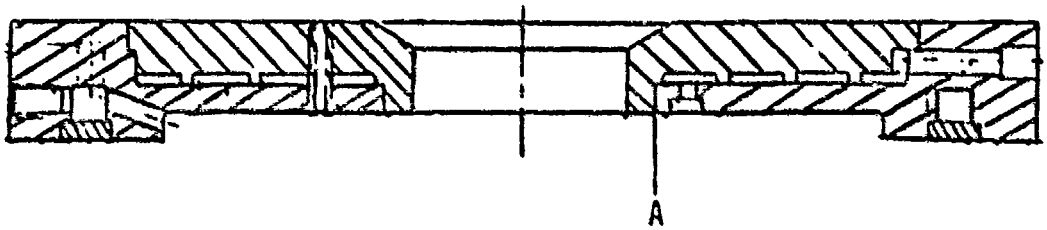

- MATERIAL: CUSTOM 450 CRES
- FACTORS OF SAFETY

LOCATION	YIELD	ULTIMATE	TEMPERATURE
A - EB WELD	1.65	3.11	978K (1300F)

Figure 116. Radiation Shield Back Plate Factors of Safety

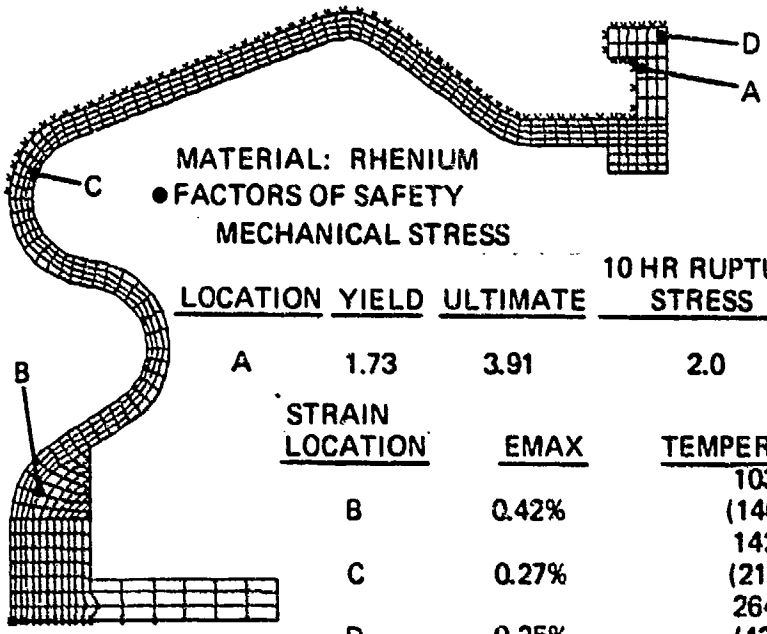

MATERIAL: RHENIUM

● FACTORS OF SAFETY

MECHANICAL STRESS

LOCATION	YIELD	ULTIMATE	10 HR RUPTURE STRESS	TIME TO RUPTURE	TEMPERATURE
A	1.73	3.91	2.0	40 HOURS	2478K (4000F)

STRAIN LOCATION	EMAX	TEMPERATURE
B	0.42%	1033K (1400F)
C	0.27%	1422K (2100F)
D	0.25%	2644K (4300F)

Figure 117. Nozzle Finite Element Model and Analytical Results

Analysis results for critical locations are given in Fig. 117 and indicated a satisfactory design. Stress results at location A include the effects of loads imposed by the absorber tubes. Maximum strains for combined pressure and thermal loadings are given for three locations. At the braze joint (location B) the maximum strain in the rhenium is 0.42%, compared to a material elongation of 5%. At locations C and D the maximum strains are 0.27 and 0.25%, respectively, compared to a material elongation of approximately 2% at both locations.

Carbon Shell

Analysis of the carbon shell indicated that thermal stresses in the shell resulting from the temperature gradients along the shell length and through the shell thickness was not a problem.

Summary Comments

The results of the absorber/thruster stress analysis indicated the assembly to be structurally adequate. The minimum ultimate and yield factors of safety occurred in the backplate at values of 3.11 and 1.65, respectively. The minimum time to rutpure was 40 hours and occurred in the thruster.

A weight breakdown analysis of the solar rocket assembly is shown in Table 12. The absorber/thruster assembly weight was estimated at 111 kg (244 lb) and the window assembly hardware, which was considered to be test equipment provided by the Air Force Rocket Propulsion Laboratory, was estimated at 14 kg (31 lb).

TABLE 12. SOLAR ROCKET WEIGHT BREAKDOWN

	kg	POUNDS
VACUUM CHAMBER		
CYLINDER	60	(132)
BASE PLATE	24	(52)
SHIELDS		
CYLINDER ASSEMBLY	11	(25)
THRUSTER ASSEMBLY	0.5	(1)
INSULATION		
BASE PLATE	2	(4)
ENTRY CONE	4	(8)
GRAPHITE		
CYLINDER	5	(11)
PLUG ASSEMBLY	1	(2)
ABSORBER/THRUSTER		
ABSORBER	1	(3)
THRUSTER	0.5	(1)
LOOSE HARDWARE	2	(5)
	111	(244)
WINDOW ASSEMBLY		
QUARTZ WINDOW	3	(6)
RETAINER	10	(22)
LOOSE HARDWARE	1	(3)
	14	(31)

MATERIALS AND FABRICATION PROCESSES

In parallel with the previously discussed design, thermal and stress analyses, evaluations were conducted to define required critical materials and verify the required fabrication processes. Effort was primarily focused on the critical material selected in Phase I for the absorber tubing (rhenium). The quartz window with an IR reflecting coating also was considered critical and was assessed during the Phase I effort. During Phase II, material and fabricability was further verified by contact and discussions with various window and coating vendors. Data and information were provided to the Air Force Rocket Propulsion Laboratory who will procure the window for the solar rocket testing.

All primary material callouts for the absorber/thruster assembly are shown in Fig. 118.

Rhenium Tube Coiling

One of the crucial steps in the fabrication of the coiled tube absorber is the coiling of the rhenium tubes. A potential difficulty was projected in coiling five tubes simultaneously and with material spring back creating excessive gaps between adjacent coils. Therefore, a tool for the absorber was designed (Fig. 118 and 119) and fabricated to evaluate tube coiling procedures.

As shown in Fig. 119 and 120, the tooling consisted of an aluminum mandrel for coiling the cylindrical absorber with a hemispherical enclosed end. The cap on the hemispherical end simulated the carbon plug and provided a tool to align the tubes to the thruster. The plate with the five pins is the tool to form the thermal expansion bends between the thruster and the absorber (Fig. 120).

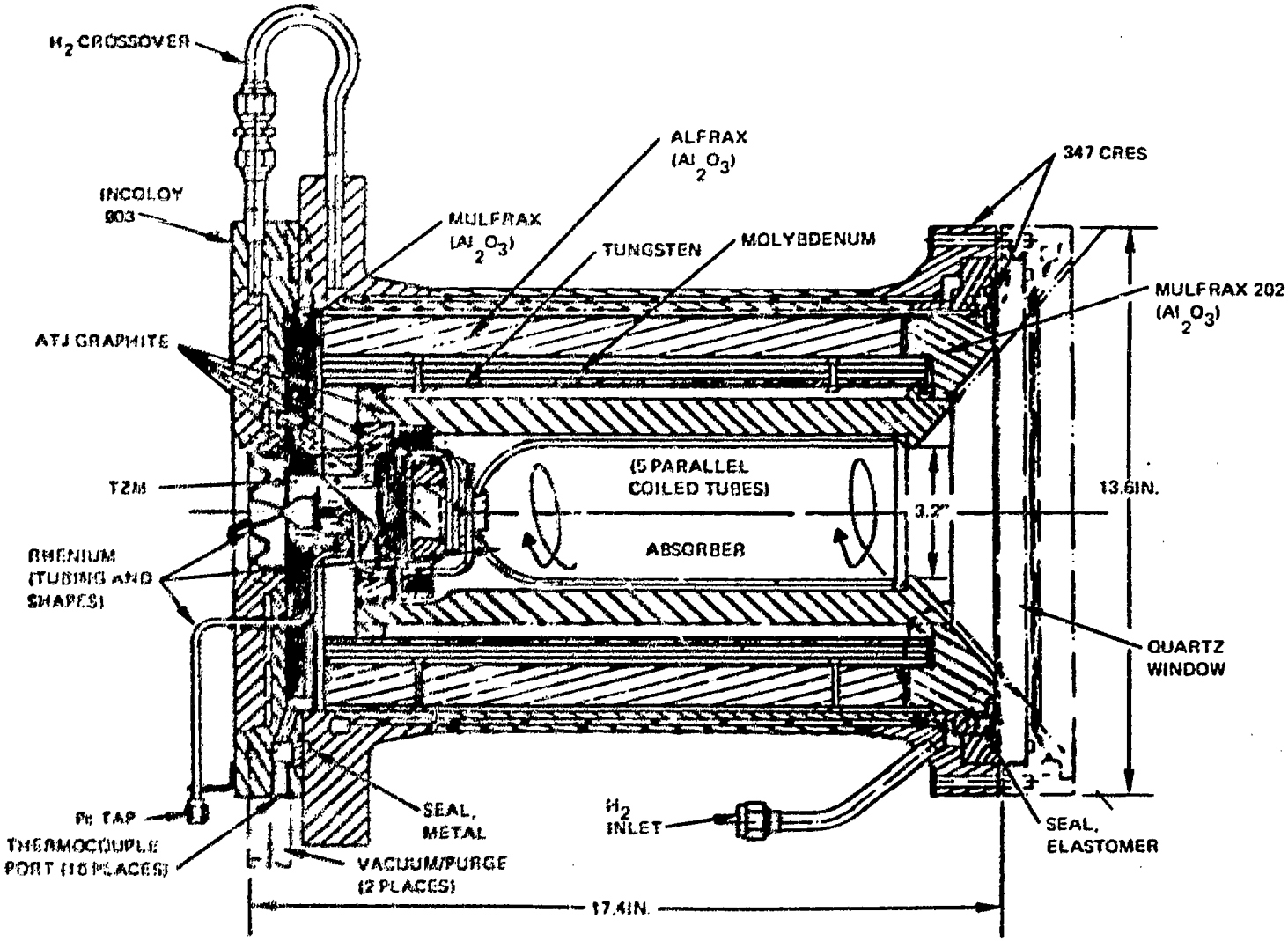

Figure 118. Absorber/Thruster Materials.

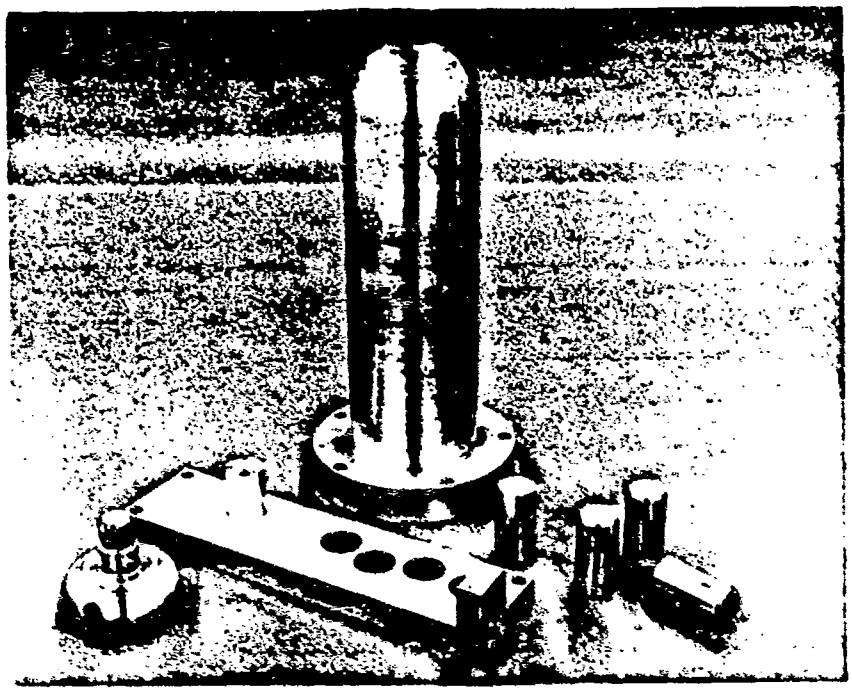

1XZ91-7/14/81-C1A

Figure 119. Absorber Tooling

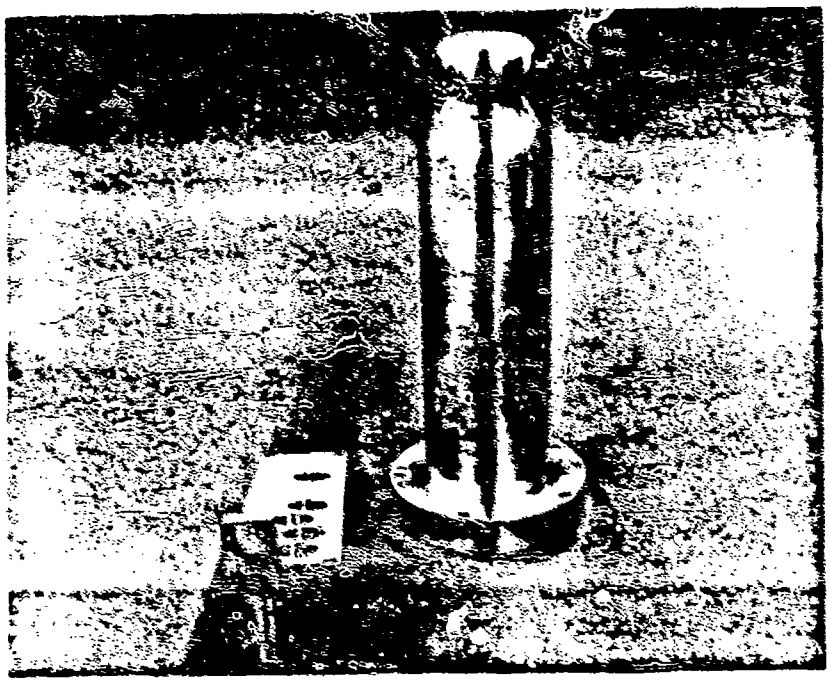

1XZ91-7/14/81-C1B

Figure 120. Absorber Mandrel With Plug Installed

The first attempt in coiling the hemispherical end of the absorber with five 321 CRES tubes (simulating rhenium) is shown in Fig. 121. The thruster would be at the top of the photo and the sixth tube (on the left side) is the thruster chamber pressure instrumentation line. The spring back of the 321 CRES tubes was significant (believed to be higher than that for rhenium) and resulted in a rather loose coil. An evaluation of the rhenium tubing spring back was subsequently performed and verified the assumption. Additional stainless steel tube coiling was performed in Task III and resulted in complete mockups of the absorber coil assembly.

Rhenium Tube-to-Tube Joint

Three fabrication approaches to provide the long length rhenium tubing were considered and are illustrated in Fig. 122. The first approach was the use of a welded sleeve which was successfully demonstrated in the Phase I material evaluation effort. The second approach consisted of a chemically vapor deposited (CVD) joint. Successful sample joints were completed by the vendor. The CVD joint was observed to be longer than the welded sleeve joint and, due to the change in tube thickness caused by the joint, tended to bend less uniformally. The success of the CVD joint led to the third suggested approach of a continuous CVD tube of the final desired length. This would essentially provide a tube without any joints, however, attempts at this approach proved unsuccessful. The welded sleeve approach (Fig. 123) was judged best and selected for the design.

Rhenium Tube Strength, Leak and Bend Tests

Laboratory test evaluations of the rhenium tube material were conducted to evaluate creep characteristics, potential porosity with leakage, and ability to bend to the required radii. The test results verified the suitability of rhenium for the tube material. The test conditions are summarized in Table 13.

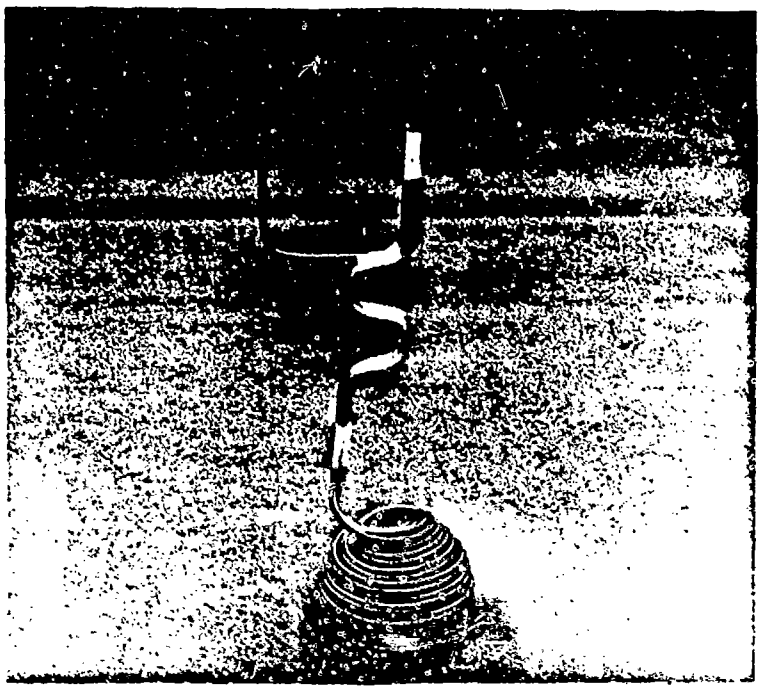

1XZ91-7/14/81-C1C

Figure 121. First Tube Coiling Attempt (321 CRES Tubes)

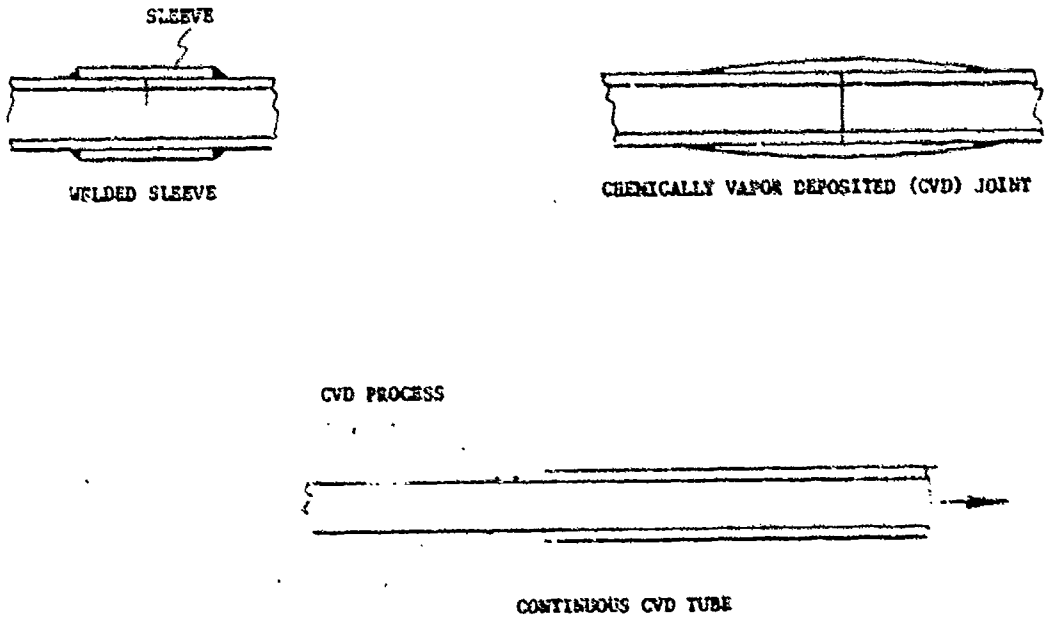

Figure 122. Rhenium Tube Joint Approaches

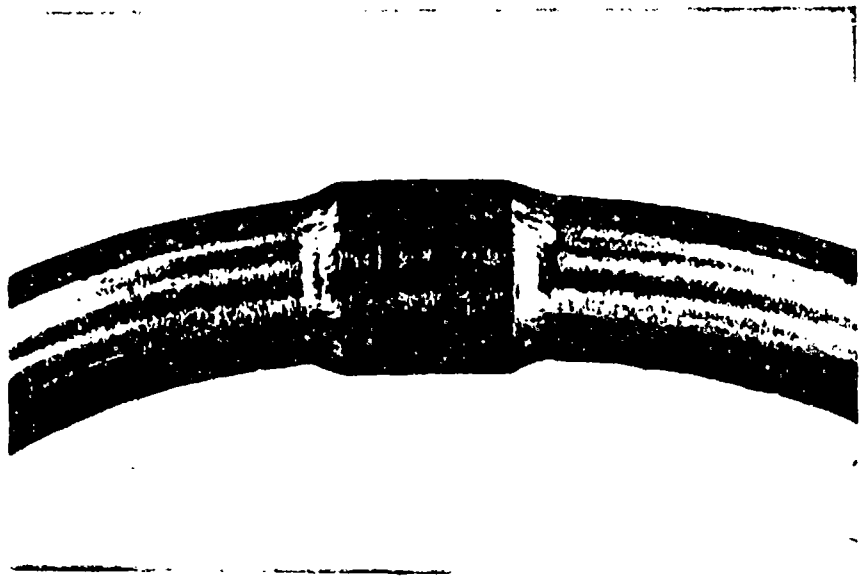

1XZ65-3/12/81-C1D

Figure 123. Welded Sleeve

TABLE 13. SOLAR THRUSTER RHENIUM TESTS

HIGH TEMPERATURE PROOF (AND CREEP) TESTS	
MAXIMUM TEMPERATURE	2667 K (4800 R) $^{+0}_{-83}$ $\left(^{+0}_{+150}\right)$
MAXIMUM PRESSURE	62 N/cm^2 (90 PSI)
TIME AT TEMPERATURE AND PRESSURE	1 HOUR
NO MEASURED DIAMETRAL EXPANSION	
HIGH TEMPERATURE LEAK TESTS	
SAME CONDITIONS AS ABOVE	
BEND TESTS (NO INTERMEDIATE ANNEALING)	
MINIMUM BEND RADIUS	0.76 TO 1 0 CM (0.3 TO 0.4 INCH)
TUBE FILLED WITH SHOT	0.053 CM (0.021 INCH)
TUBE ID	0.25 CM (0.100 INCH)
TUBE WALL	0.025 CM (0.010 INCH)

Carbon Component Coating

A literature search on the sublimation characteristics of carbon indicated significant sublimation could occur for the absorber/thruster carbon components. Carbon component sublimation could result in subsequent deposition onto adjacent surfaces. Coating of the inner surface of the vacuum chamber window with carbon could result in overheating the window and/or carbon depositing on the various radiation shields could influence their reflective characteristics. Vapor pressure data for graphites are presented in Fig. 124. As shown in this figure, the carbon will sublime at 2500 K (4500 R) if the pressure is below 1.6×10^{-5} mm Hg. Although the majority of the components are below this temperature, a coating was planned for all carbon components to ensure that carbon sublimation does not occur.

To verify the sublimation characteristics of carbon, high temperature 2278 K (4100 R) exposure tests were conducted on samples in a hydrogen environment. A weight loss of 2 to 3% resulted with an exposure time of 1 hour, thus substantiating the need for a coating.

Several approaches to coat the carbon components were investigated and included:

1. Chemical vapor deposition (CVD) of tungsten
2. Plasma sprayed tungsten
3. Plasma sprayed or chemically vapor deposited tantalum/tungsten
4. Chemically vapor deposited rhenium

The interface layer between the metallic coating and the graphite will form a eutetic in each of the cases. The rhenium and tungsten eutectics melt at about 2500 C (4500 F), whereas the tantalum eutectic melts at about 2800 C (5100 F). In the case of chemical vapor deposition of tungsten, a small amount of carbide may be formed in addition to the eutectic due to the

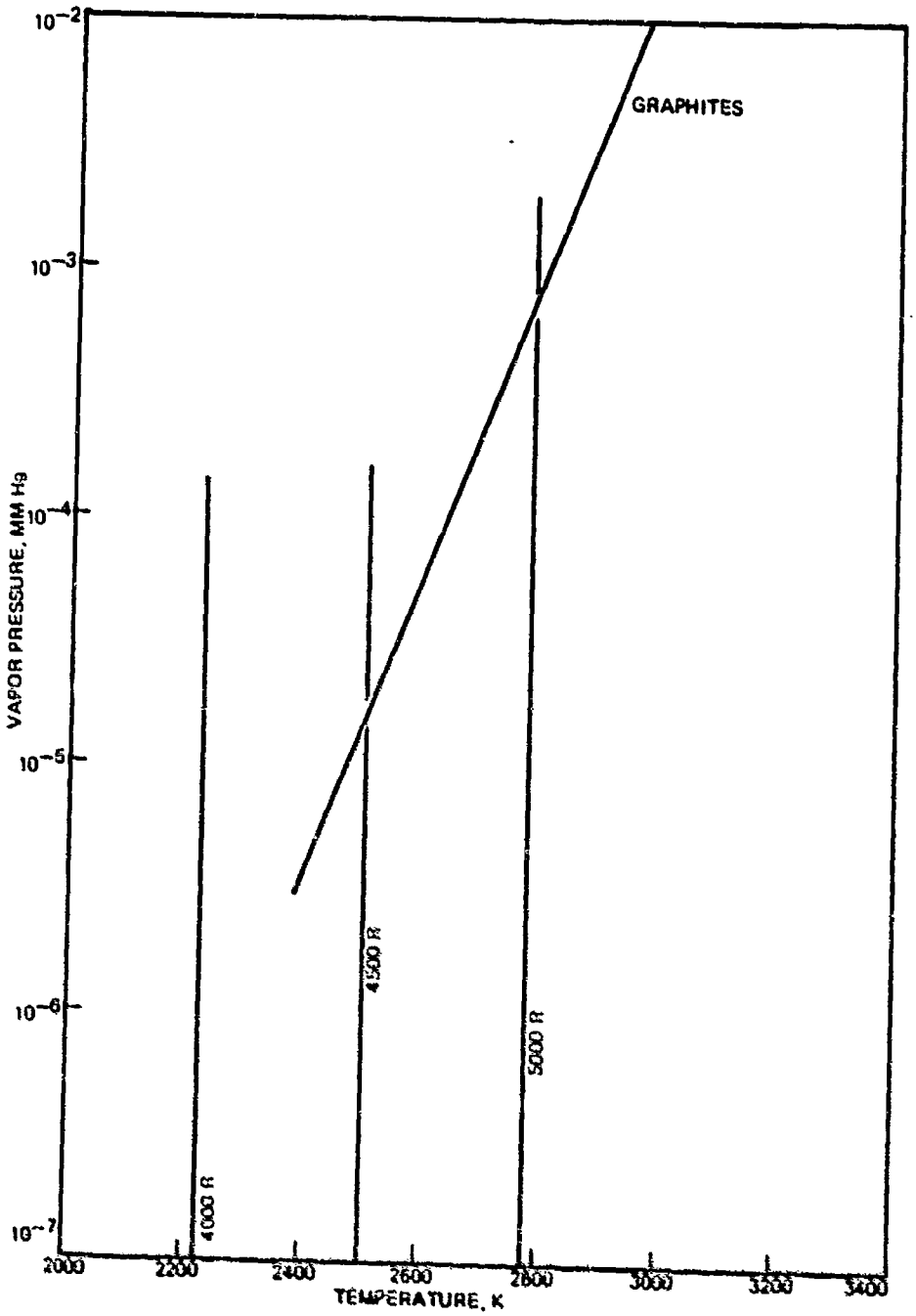

Figure 124. Graphite Vapor Pressure Variation With Temperature

presence of the vaporization gas. In any case, the eutectic or the carbide layer is not expected to pose a problem. A slight gas pressure will build up under the surface of the outer metallic layer. The contained gas will be at a high enough pressure to prevent sublimation of the carbide or eutectic and at a low enough pressure to prevent further carbide formation. Both CVD and plasma spray techniques have been used successfully in the past for high temperature carbon hardware.

Of the possible candidates, chemically vapor-deposited rhenium appeared to be the most attractive. The coefficient of thermal expansion of the rhenium is close to that of the graphite, thereby minimizing the risk of thermal mismatch problems. The ductility of the rhenium will more than allow for any thermal mismatch which may exist. In addition, of the coatings considered, rhenium is the only one that does not form a carbide. The interface layer between the rhenium and carbon will be a stable eutectic. The rhenium coating will prevent sublimation of the carbon because the surface is 100% dense.

PERFORMANCE ANALYSIS

Performance analyses were completed to determine thruster performance for variation in nozzle expansion ratio and hydrogen propellant temperature. These results led to the final definition of the ground test absorber/thruster projected performance. Analyses were performed to define the required test facility diffuser/ejector system, and approaches were investigated to vary the final hydrogen temperature to minimize hardware risk during initial testing. Evaluation was also made of instrumentation requirements of the absorber/thruster assembly for performance determination and to ensure safe test operation.

Thruster Performance

To achieve representively high delivered specific impulse values with the ground test hardware, the nozzle area ratio is an important influencing parameter. Ground testing without a diffuser/ejector system would result in a nozzle area ratio of approximately 2-to-1 for a chamber pressure of 34.47 N/cm^2 (50 psia). As shown in Fig. 125, the theoretical specific impulse for a 2-to-1 area ratio is below the design minimum goal of 7845.3 Nsec/kg (800 $lb_f sec/lb_m$). Although nozzle area ratios of 100-to-1 or greater were desirable, the diffuser/ejector system complications and ejector flow requirements necessitated a compromise. A nozzle area ratio of 20-to-1 enabled a more reasonable ejector design and achieved a theoretical specific impulse of 9120.2 Nsec/kg (930 $lb_f sec/lb_m$) which should provide a delivered value greater than 7845.3 Nsec/kg (800 $lb_f sec/lb_m$). Due to the small physical size, the test hardware will result in lower delivered specific impulse values as compared to the flight design due to increased boundary layer and reaction kinetic losses.

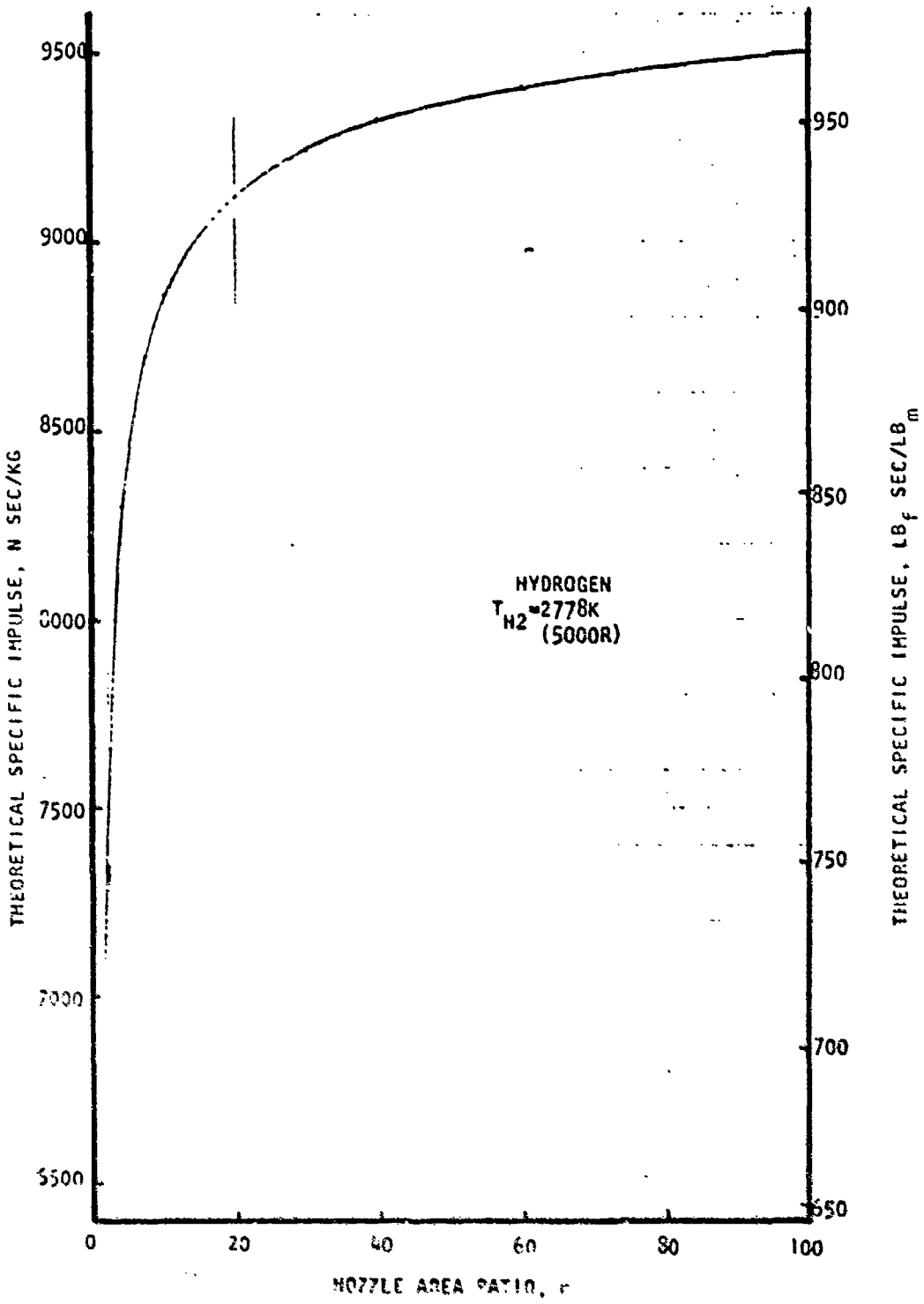

Figure 125. Theoretical Specific Impulse Variation With Area Ratio for Hydrogen at 2778 K (5000 R)

Specific Impulse Variation With Hydrogen Temperature

Using the simplified JANNAF performance prediction procedure (Fig. 126) the delivered specific impulse for the 20-to-1 and the 100-to-1 area ratio nozzles was determined as a function of the final hydrogen temperature by computing the individual thruster losses (Fig. 127). The nozzle geometric efficiency (η_g) was determined using the Rocketdyne aerodynamic design and analysis computer programs. The 100-to-1 area ratio nozzle achieved a 0.6% higher geometric efficiency. Both nozzles were assumed to have an 80% length. The boundary layer loss (Δ_{BL}) was obtained using Rocketdyne's integral boundary layer analysis computer program assuming laminar flow. As shown in Fig. 127, the longer and larger 100-to-1 area ratio nozzle resulted in almost double the boundary layer loss of 20-to-1 area ratio nozzle. The reaction kinetic efficiency (ηK) for the two thrusters was determined using the one dimensional kinetic (ODK) computer program. The increased amount of dissociated hydrogen at the higher temperatures and the subsequent recombination in the nozzle resulted in lower reaction kinetic efficiencies.

$$I_{S_{DEL}} = I_{S_{THEOR}} \left| \eta_G \, \eta_K - \Delta_{BL} \right|$$

WHERE

$I_{S_{DEL}}$ = DELIVERED SPECIFIC IMPULSE

$I_{S_{THEOR}}$ = THEORETICAL SPECIFIC IMPULSE AT CHAMBER CONDITIONS

η_G = GEOMETRIC OR TWO-DIMENSIONAL THRUST CHAMBER EFFICIENCY ← ROCKETDYNE'S NOZZLE ANALYSIS PROGRAM

η_K = REACTION KINETIC EFFICIENCY ← ONE-DIMENSIONAL KINETIC (ODK) PROGRAM

Δ_{BL} = BOUNDARY LAYER LOSS ← ROCKETDYNE INTEGRAL BOUNDARY LAYER PROGRAM

Figure 126. Simplified JANNAF Procedure

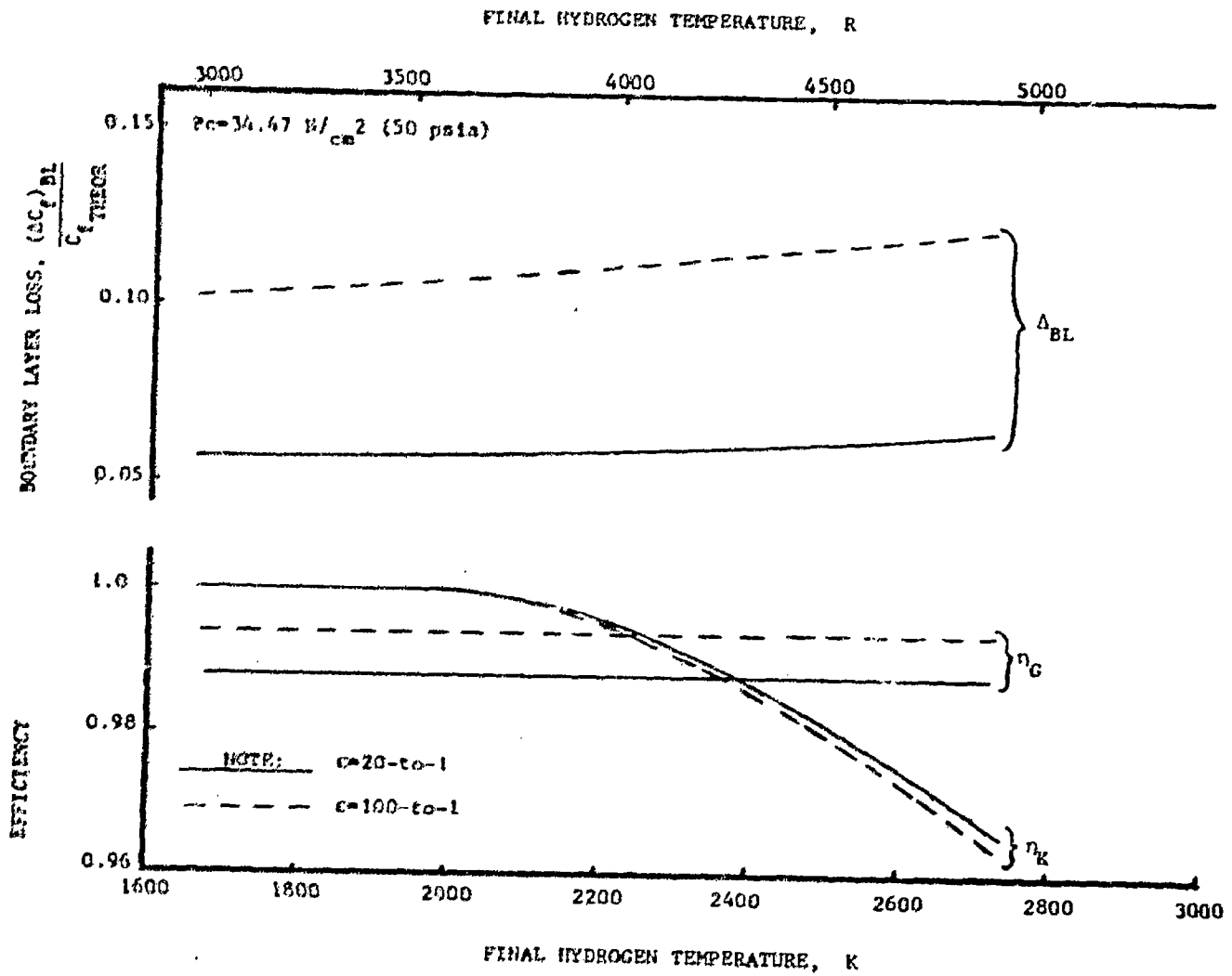

Figure 127. Thruster Performance Losses

Combining these individual thruster losses with the theoretical performance values, the resulting delivered specific impulse was computed. The variation of the delivered specific impulse with the final hydrogen temperature is shown in Fig. 128. As a result of the higher boundary layer loss of the 100-to-1 area ratio nozzle, the delivered specific impulse for this thruster was lower than that of the 20-to-1 area ratio nozzle. Therefore, based on these results and the test diffuser ejector flow requirements analyzed below, the 20-to-1 area ratio nozzle was selected as the test hardware baseline. As shown in

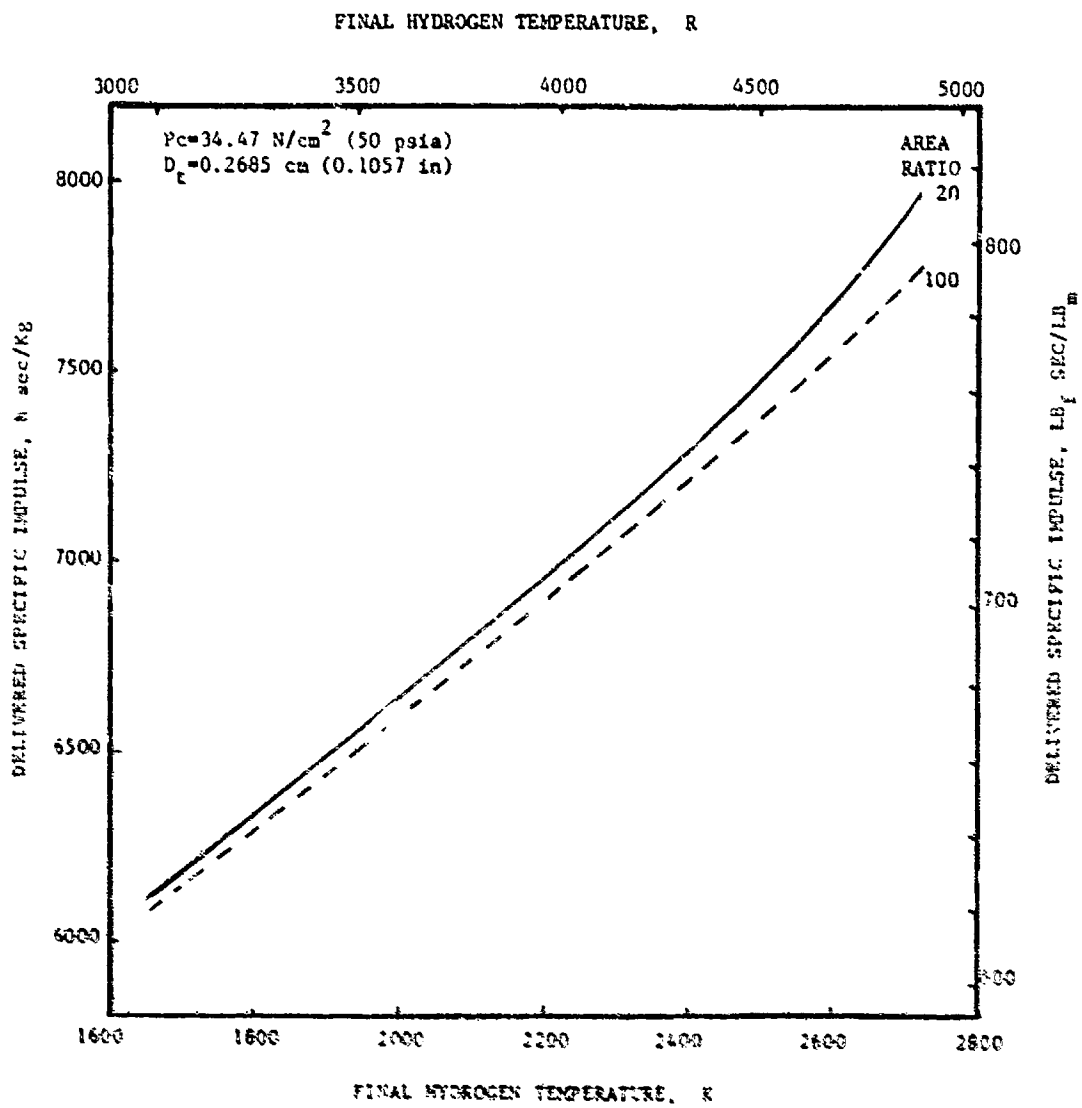

Figure 128. Delivered Specific Impulse Variation With Final Hydrogen Temperature

Fig. 127, the delivered specific impulse value for this thruster varied from 6132 N sec/kg (625.3 lb_fsec/lbm) at 1667 K (3000 R) to 7962 N sec/kg (811.9 lb_f sec/lbm) at 2722 K (4900 R).

The variations of the hydrogen flowrate and thrust are shown in Fig. 129 and 130, respectively. The flowrate varies by 35% and the thrust was essentially constant over the temperature range evaluated.

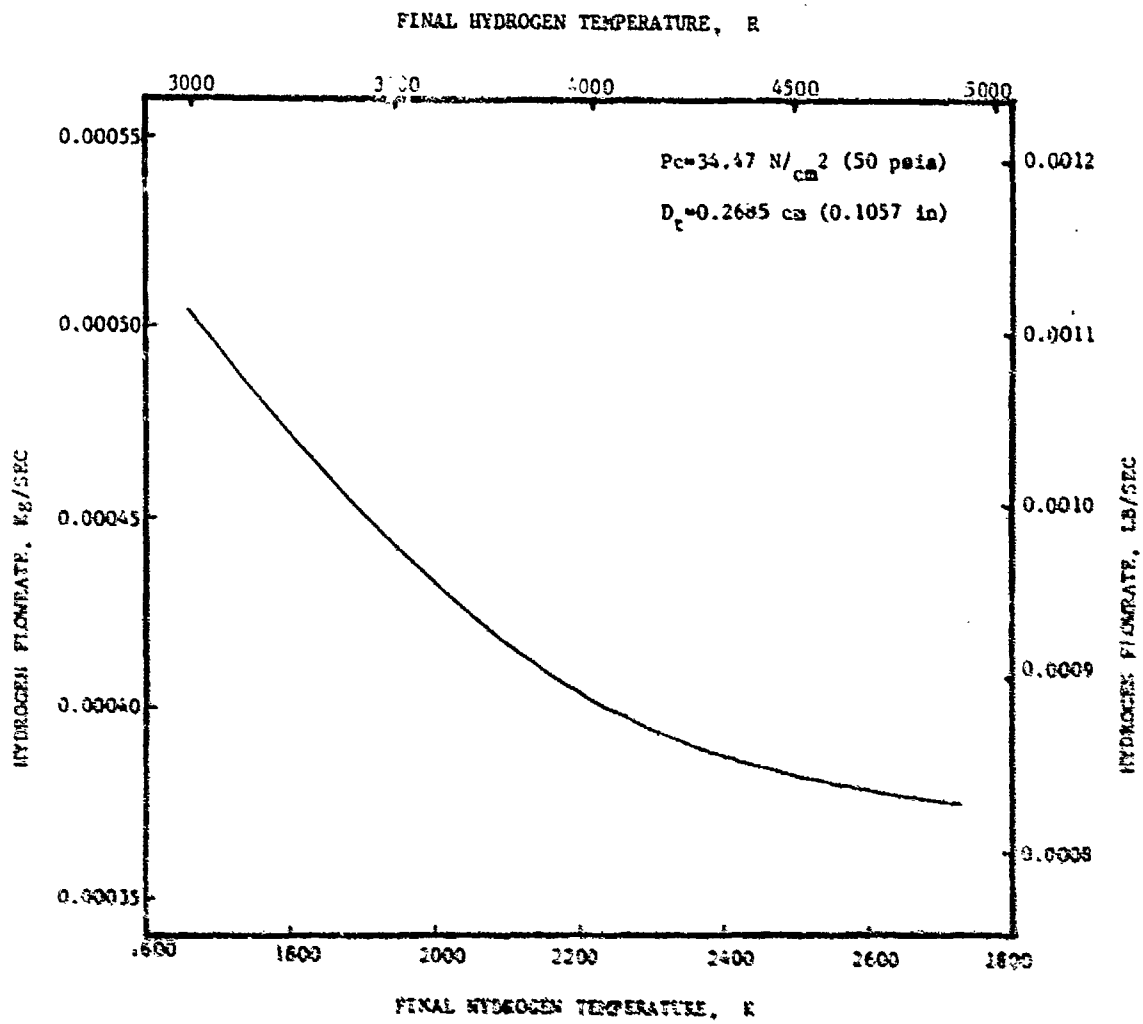

Figure 129. Hydrogen Flowrate Variation With Final Hydrogen Temperature

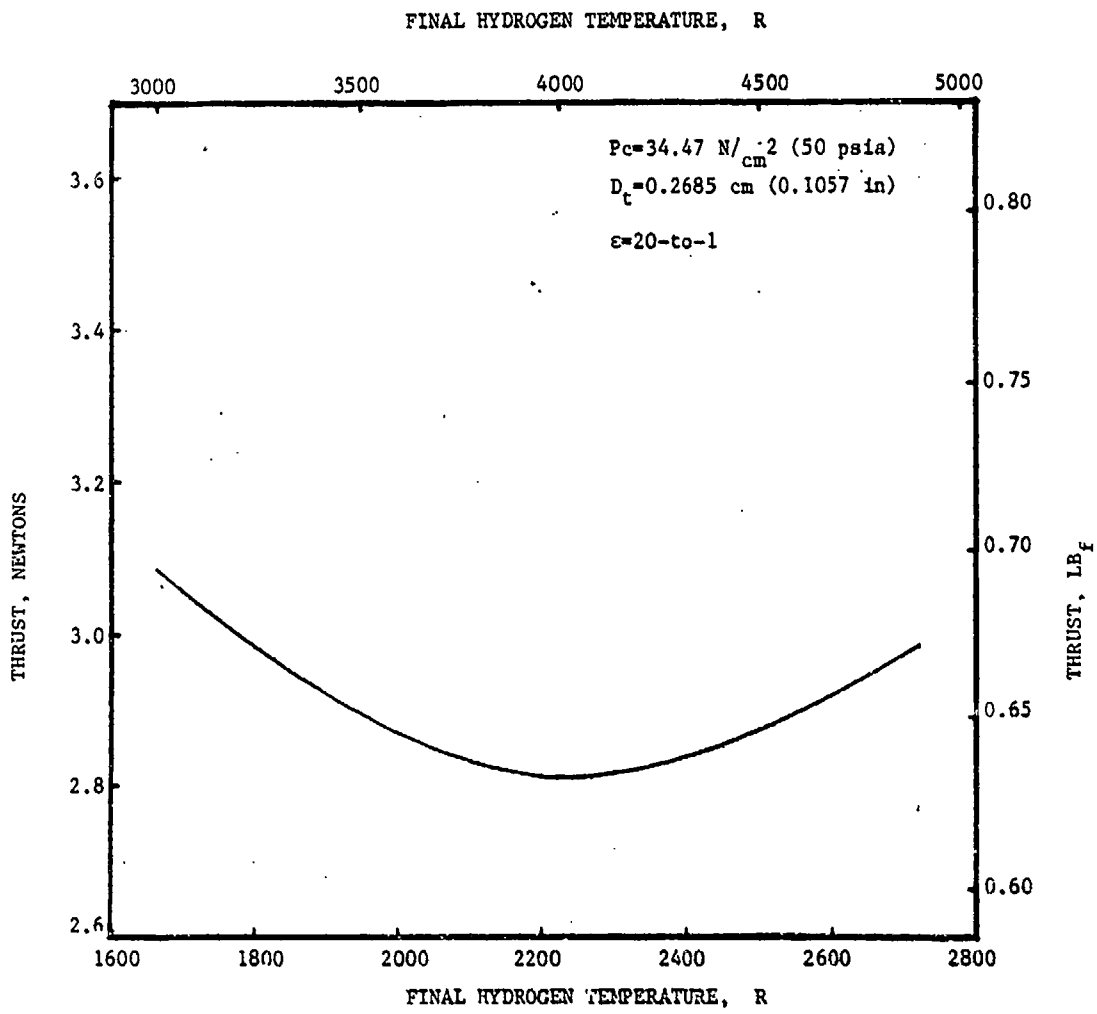

Figure 130. Thrust Variation With Final Hydrogen Temperature (20-to-1 Area Ratio)

Thruster Diffuser/Ejector Analysis

Preliminary diffuser/ejector analyses have indicated that the 100-to-1 nozzle area ratio required a two-stage ejector system with a total gaseous nitrogen flowrate of 0.381 gm/sec (0.839 lb/sec). Depending on the pressure recovery split between the two stages, the required ejector flowrate varied from 0.381 gm/sec (0.389 lb/sec) to 0.44 gm/sec (0.97 lb/sec). The complication of a two-stage system and the high ejector flow requirements are undesirable ejector features. Therefore the lower nozzle area ratio (ε = 20-to-1) was analyzed. This nozzle only required a single-stage ejector system and a gaseous nitrogen flowrate of 0.084 gm/sec (0.186 lb/sec) which is a factor of 4.5

lower than for the 100-to-1 area ratio nozzle. As shown in Table 14, a comparison of the recovery pressure and required ejector flows for different nozzle area ratios indicated that the required gaseous nitrogen ejector flow is approximately proportional to the nozzle area ratio.

TABLE 14. DIFFUSER/EJECTOR ANALYSIS RESULTS

NOZZLE AREA RATIO	20	50	75	100
RECOVERY PRESSURE, $0.8\ P_{oy}$, N/cm^2 (psia)	2.103 (3.05)	0.869 (1.26)	0.579 (0.84)	0.441 (0.64)
REQUIRED GN_2 FLOW, [illegible]/sec (lb/sec)	0.084 (0.186)			0.381 (0.839)

Thruster Diffuser/Ejector Design

Using available analysis and design methods and the experience obtained on previous operational diffuser/ejector designs, a diffuser/ejector system for the ground test solar absorber/thruster was defined as shown in Fig. 131.

The ground test thruster is a 20-to-1 area ratio bell nozzle with an 80% length with the following one-dimensional nozzle exit conditions:

$$M = 3.97$$
$$P/Po = 0.0043$$
$$Poy/Pox = 0.0827$$

The design chamber pressure was 34.47 N/cm^2 (50 psia) which results in a one-dimensional nozzle exit pressure of 0.15 N/cm^2 (0.22 psia). Using the above parameters, the full normal shock recovery pressure was 2.83 N/cm^2 (4.1 psia).

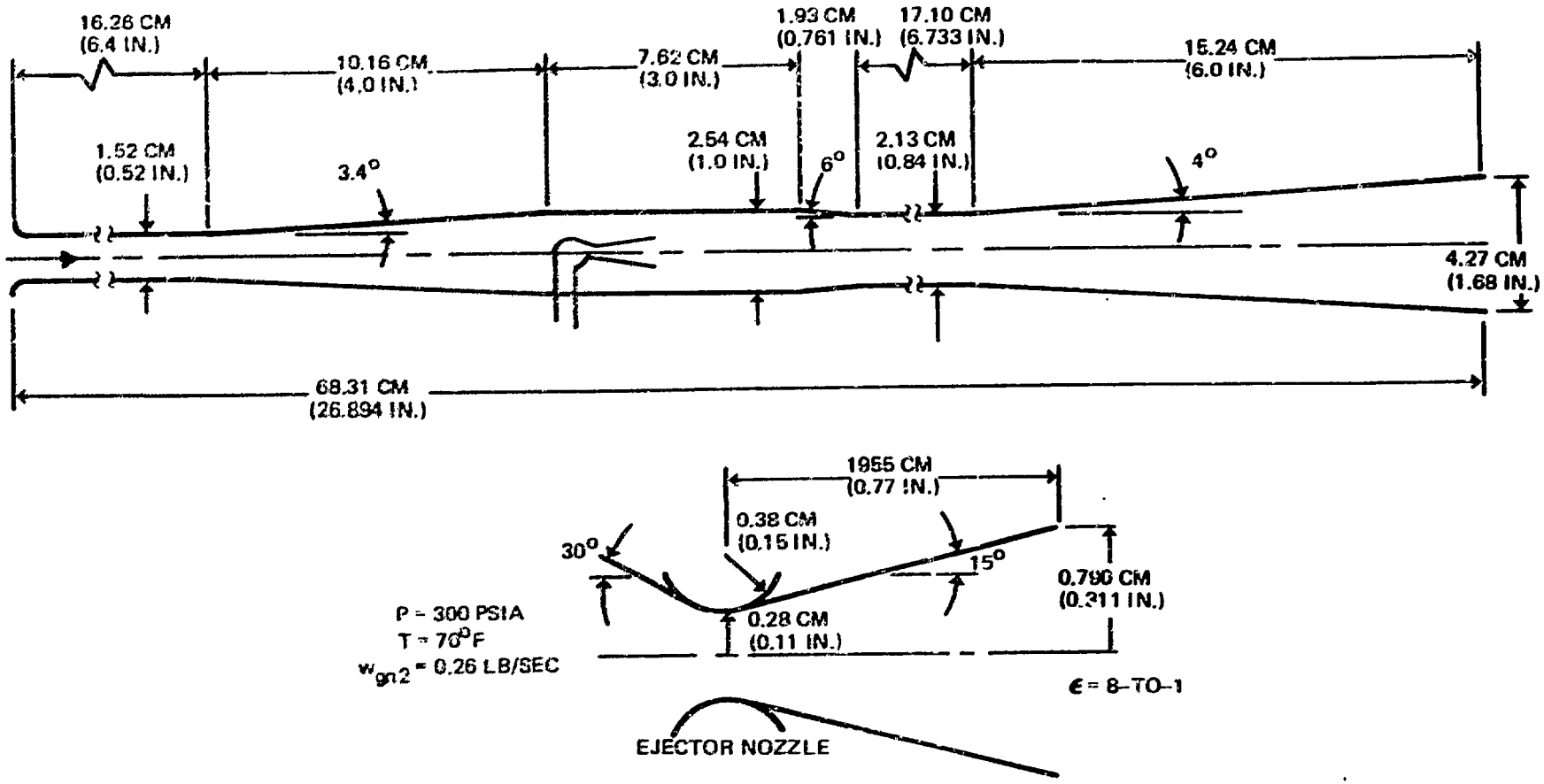

Figure 131. Diffuser/Ejector Design

The pertinent nozzle geometry and the axisymmetric nozzle exit boundary layer conditions were:

Nozzle Wall Exit Angle, θ_E	=	9 degrees
Thruster Throat Radius, R_t	=	0.134 cm (0.0528 inch)
Nozzle Exit Radius, R_E	=	0.601 cm (0.2364 inch)
Boundary Layer Velocity Thickness, δ	=	0.152 cm (0.06 inch)
Boundary Displacement thickness, δ_*	=	0.056 cm (0.022 inch)

To capture the nozzle exhaust plume which exits the nozzle at 9 degrees, a diffuser diameter of 1.321 cm (0.52 inch) was chosen (Fig. 132). This diameter provides 20% more flow area than the nozzle exit plane. To enhance pressure recovery, the diffuser area was kept small; however, no area contraction was incorporated due to boundary layer viscous considerations.

Also the constant diameter will tend to simplify construction. The diffuser length is 12 length-to-diameter ratios long. The diffuser subsonic section has an area ratio of 3.7 with a 3.4-degree half angle. The diffuser diameter increases from 1.321 cm (0.52 inch) to 2.54 cm (1.0 inch) in this subsonic section.

Based on the diffuser area to nozzle throat area ratio of 24.2, the predicted Pc/Pa start ratio is 18. For the nominal design chamber pressure of 234.47 N/cm^2 (50 psia), the expected static pressure recovery is 1.93 N/cm^2 (2.8 psia).

The ejector system for this configuration must be able to pump from the 1.93 N/cm^2 (2.8 psia) diffuser exit pressure to ambient pressure which was assumed to be 9.65 N/cm^2 (14 psia). Several design considerations were weighed prior to selecting the ejector drive nozzle shown in Fig. 132. These included: (1) the ejector flowrate for an ejector chamber pressure range of 103.4 N/cm^2 (150 psia) to 344.7 N/cm^2 (500 psia), (2) the ejector nozzle exit pressure to match the diffuser recovery, and (3) the ejector blank-off pressure (initial cell pressure).

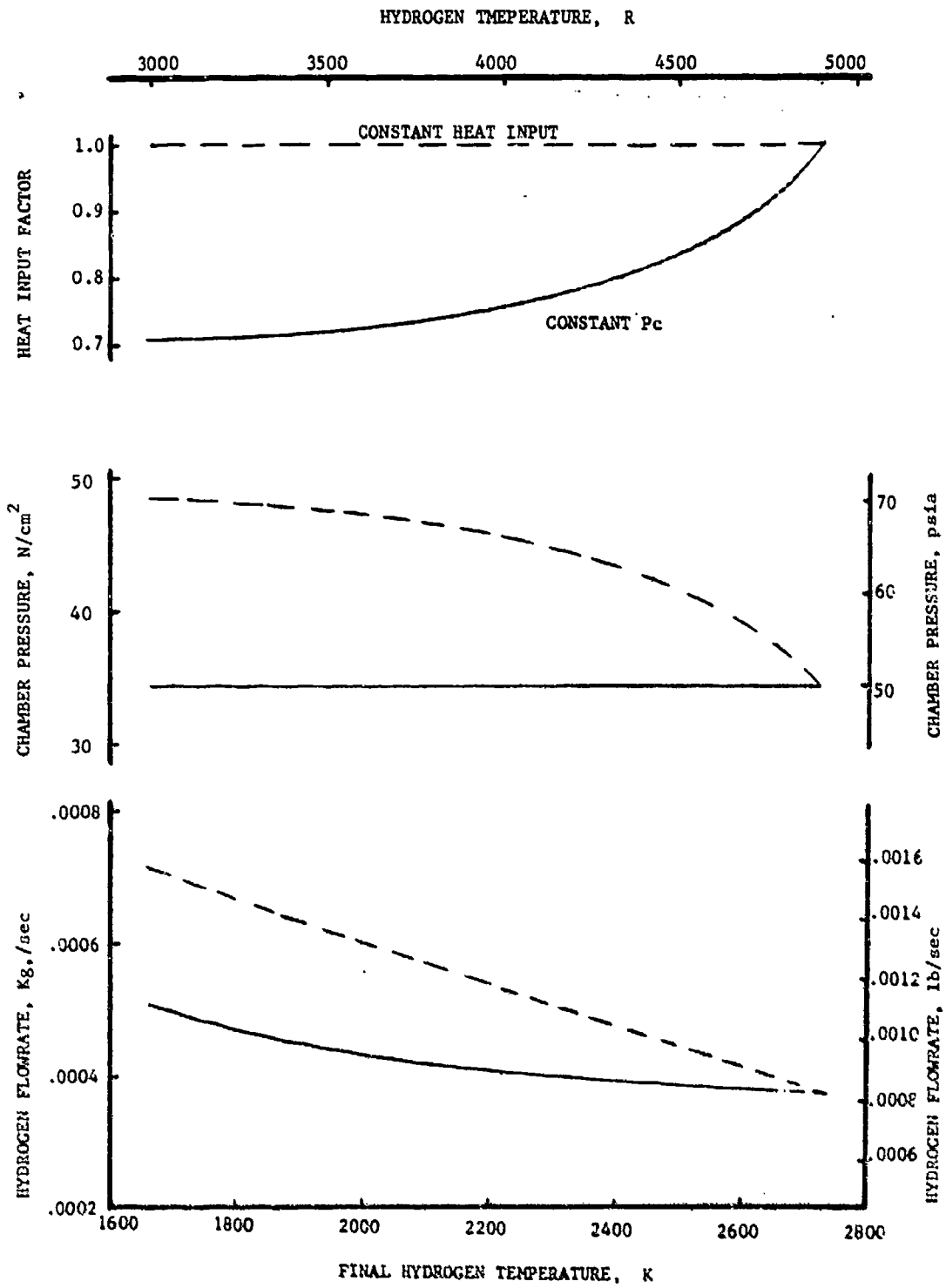

Figure 132. Parameter Variations With Final Hydrogen Temperature

The Rocketdyne ejector program, RODA, was used to size the ejector driver nozzle throat and expansion ratio. A mid-point ejector chamber pressure of 306.8 N/cm^2 (300 psia) was chosen to permit the flexibility of operating at higher or lower pressures if required. For this pressure, a mass flowrate (ambient gaseous nitrogen) of 0.118 kg/sec (0.26 lb/sec) was required with an ejector nozzle throat diameter of 0.559 cm (0.22 inch). The resulting nozzle was an 8-to-1 area ratio conical nozzle with a 15-degree half angle (see ejector nozzle detail in Fig. 131. An ejector diameter of 2.54 cm (1.0 inch) was selected to provide for the driver nozzle and secondary flow areas. At an ejector chamber pressure of 206.8 N/cm^2 (300 psia), the blank-off pressure would be 0.517 N/CM^2 (0.75 psia). Contraction to a minimum ejector diameter of 2.13 cm (0.84 inch) was obtained with a 6-degree convergence angle. The ejector contraction ratio is 0.7 and the length is 8 length-to-diameter ratios. The ejector subsonic area ratio is 4 and is achieved with a 4-degree conical half angle.

With no thruster flow, the ejector should start at an ejector pressure of 117.2 N/cm^2 (170 psia). The ejector throat is designed for the flow associated with the ejector design chamber pressure of 206.8 N/cm^2 (300 psia). If for some reason substantially more ejector flow is required to pump the thruster exhaust, the ejector throat could be machined larger and ejector contraction eliminated. Therefore, for the ejector nozzle and duct, sufficient material to permit this alteration should be provided although substantial margin has been incorporated in the diffuser/ejector design.

Absorber-to-Thruster Line Heat Loss Influence

The most important heat loss in the absorber/thruster configuration is the loss from the absorber-to-thruster propellant lines. Up to the absorber exit the propellant is being continually heated, but downstream of this location the heat loss will decrease the final hydrogen temperature and the delivered specific impulse. Therefore, thermal and design efforts were directed to minimize this heat loss.

The loss of 0.77 kw (0.73 Btu/sec) determined by thermal analysis resulted in a 16.7 K (30 R) decrease in final hydrogen temperature and approximately a 31.97 Nsec/kg (3.26 $lb_f sec/lb_m$) decrease in delivered specific impulse at the design conditions of 2722 K (4900 R) maximum hydrogen temperature and a 34.5 N/cm^2 (50 psia) chamber pressure. Since the delivered specific impulse is approximately 7945 Nsec/kg (810 $lb_f sec/lb_m$), these results indicate that the efforts to minimize the absorber-to-thruster line heat loss have reduced the delivered specific impulse loss to approximately 0.4%, which was considered acceptable.

Delivered Specific Impulse

The final individual thruster performance losses were computed at the chamber design condition for the 20-to-1 nozzle area ratio. The nozzle geometric efficiency remained unchanged at 0.988. Using the Rocketdyne integral boundary layer computer program, the boundary layer loss was determined to be 6.17%. The reaction kinetic efficiency was calculated to be 0.9668 using the one-dimensional kinetic (ODK) computer program. These losses combined with a theoretical specific impulse of 8875 Nsec/ky (905 $lb_f sec/lb_m$) resulted in a delivered specific impulse of 7929.7 Nsec/kg (808.6 $lb_f sec/lb_m$). The line heat loss contributes to only a 0.4% decrease in delivered specific impulse from the 2722 (4900 R) maximum hydrogen temperature condition. The major thruster performance loss was the boundary layer loss.

Assuming an ambient (294.4 K or 530 R) hydrogen inlet temperature, the resulting hydrogen flowrate was 0.000467 kg/sec (0.00103 lb/sec) and the thrust was 3.69 N (0.83 lb_f) with a thruster throat diameter of 0.2685 cm (0.1057 inch).

Test Approaches to Vary Hydrogen Temperature

In testing the hardware, the safest approach would be to start with a low final hydrogen temperature (absorber outlet temperature) and reduce the hydrogen flowrate until the design final hydrogen temperature is reached. This approach would minimize the risk of an over-temperature condition due to differences in the predicted and the actual absorber operational characteristics.

In reviewing the basic relationships describing the variation with the final hydrogen temperature, two approaches to accomplish this were apparent. The governing relationships are:

$$\dot{M}_{H_2} = \frac{Q}{\Delta H_{TH_2}} \tag{1}$$

and

$$P_c = \frac{c^* \dot{M}_{H_2}}{A_t g} \tag{2}$$

where

$\dot{M}_{H_2}$ = Hydrogen flowrate

Q = Heat absorbed by hydrogen

P_c = Chamber pressure

C^* = Hydrogen characteristic velocity

A_t = Thruster throat area

g = Gravitational constant

Using Eq. (1) in Eq. (2), Eq. (2) becomes,

$$P_c = \frac{C^* Q}{A_t g \Delta H_{TH_2}} \tag{3}$$

Therefore, for a fixed thruster (constant A_t) and a constant heat absorbed (Q),

$$P_c \propto \frac{C^*}{\Delta H_{TH_2}} \tag{4}$$

The thrust chamber pressure must be varied for the various final hydrogen temperatures.

Now if a fixed chamber pressure (P_c) is desired for the fixed thruster (A_t),

$$Q \propto \frac{\Delta H_{TH_2}}{C^*} \tag{5}$$

The heat absorbed must be varied.

Using the derived proportionalities (Eq. 4 and 5), pertinent parameter variations were determined for a fixed thruster (0.2685 cm or 0.1057 inch throat diameter) with a design condition of 2722 K (4900 R) final hydrogen temperature at 34.47 N/cm^2 (50 psia) chamber pressure. The results for the two approaches are presented in Fig. 132.

For the fixed heat absorbed case, the chamber pressure must be increased from 34.47 N/cm^2 (50 psia) at 2722 K (4900 R) final hydrogen temperature to 48.77 N/cm^2 (70.73 psia) at 1666.7 K (3000 R) final hydrogen temperature. The hydrogen flowrate would increase by a factor of 1.9 from the value at the design condition. In addition, the increased chamber pressure and flowrate would increase the absorber pressure drop by greater than a factor of 2 and increase the required inlet pressure by more than 60%. This increase in inlet pressure will increase the stress throughout the absorber/thruster hardware.

To maintain a constant chamber pressure, the solar heat input must be reduced for the lower hydrogen temperatures. As shown in Fig. 132, the heat absorbed must be reduced by 29.3% at the 1666.7 K (3000 R) final hydrogen temperature condition. The resulting hydrogen flowrate increase with decrease in hydrogen temperature was considerably less than in the fixed heat input approach (only 34% as compared to 190%). This translates into approximately a 10% increase in absorber pressure drop and a 3% increase in hydrogen inlet pressure.

Since the chamber pressure influence on the delivered specific impulse should not be significant, the delivered specific impulse versus hydrogen temperature calculations were performed assuming a constant chamber pressure.

Performance Analysis Summary

Based on the completed performancee analyses, the final nominal performance projections for the ground test absorber/thruster were established. The projections are summarized in Table 15. It may be noted that the specific impulse program goal of 7845.4 Nsec/kg (800 sec/lb_m) was exceeded.

TABLE 15. ABSORBER/THRUSTER NOMINAL PERFORMANCE SUMMARY

ABSORBER
EFFICIENCY, 76.9%
HYDROGEN FLOW, 0.000467 kg/sec (0.00103 lb/sec)
HYDROGEN TEMPERATURE, MAXIMUM 2722 K (4900 R)
THRUSTER
CHAMBER PRESSURE, 34.5 N/cm^2 (50 PSIA)
HYDROGEN FLOW, 0.000467 (kg/sec (0.00103 lb/sec)
HYDROGEN TEMPERATURE, 2705 K (4870 R)
NOZZLE EXPANSION AREA RATIO, 20:1 (80% LENGTH)
DELIVERED SPECIFIC IMPULSE, 7929.7 Nsec/kg (808.6 LF_F sec/LB_m)
THRUST, 3.69 N (0.83 LB_f)

Instrumentation Requirements

The primary objective of the ground test hardware is to provide proof-of-principle of the solar absorber/thruster design concept. This would include the determination of the absorber efficiency and the delivered specific impulse from measured data. Instrumentation required to provide these data and that required to ensure safe test operation and test hardware integrity was defined. Instrumentation and measurement provisions to be provided on the test hardware as shown schematically in Fig. 133 and 134. The propellant inlet and outlet pressures and temperatures will enable the calculation of the heat absorber performance and will define the thrust chamber conditions (chamber pressure and final hydrogen temperature). The tube for measuring chamber pressure (Fig. 134) passes out of the thruster heat shield, through the rigidized zirconium oxide insulation, through the vacuum backplate to exist outboard of the backplate.

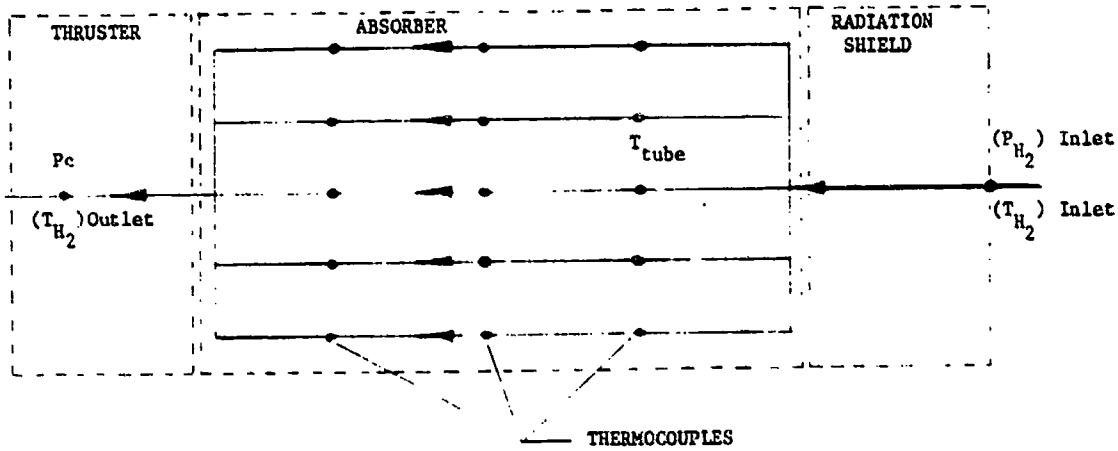

Figure 133. Absorber/Thruster Propellant Temperatures and Pressures

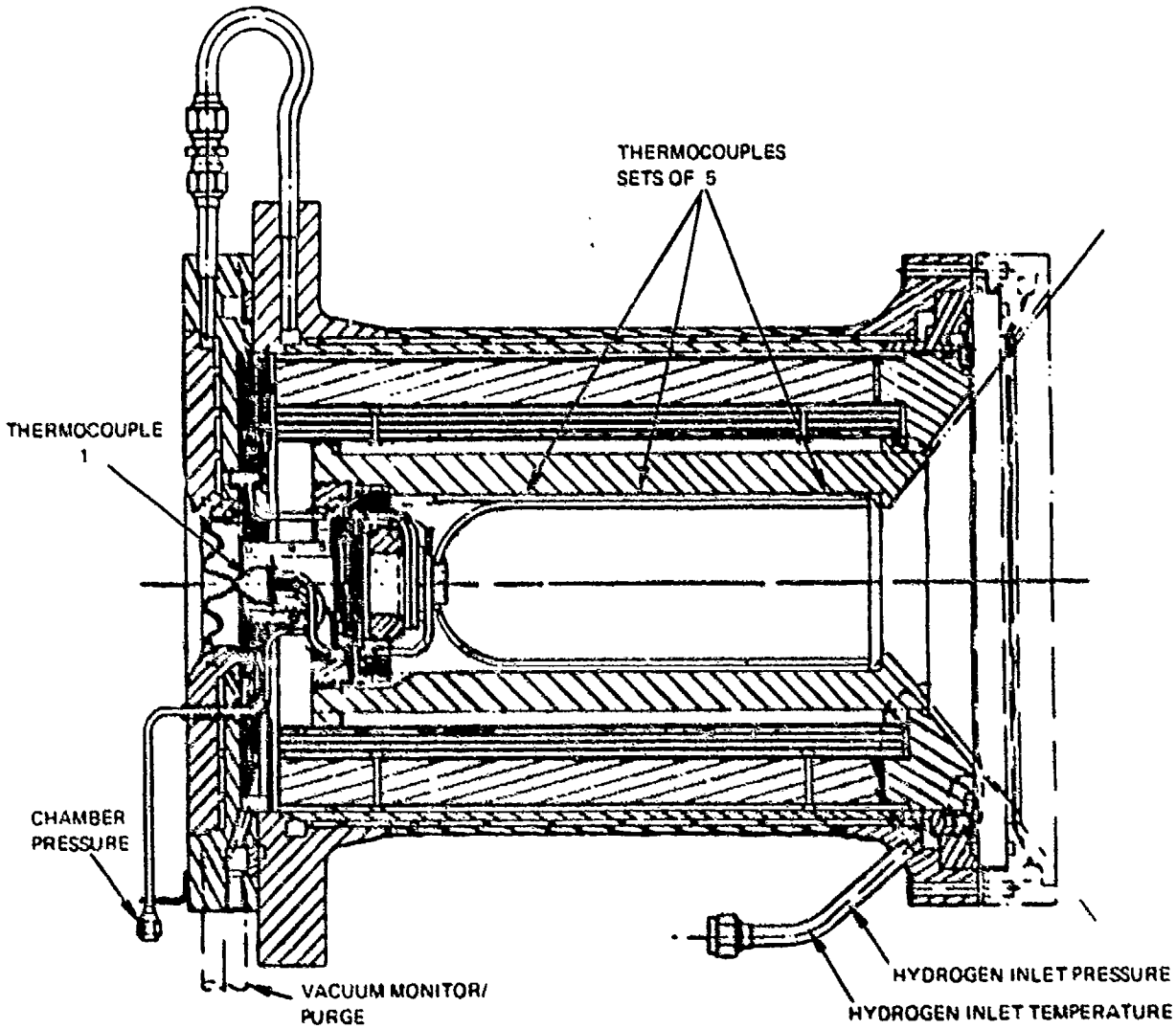

Figure 134. Instrumentation

The high temperature thermocouples will (1) verify the solar flux profile (axial) in the absorber, (2) verify the discharge temperature of the hydrogen, and (3) detect flow variations in the five tubes. The thermocouples are tungsten/tungsten 20% rhenium with grounded junctions, beryllium oxide insulation, and tantalum sheathing. The grounded junction, besides being welded, are mechanically locked, since such junctions tend to be brittle and separate after several thermal cycles. These thermocouples were considered to be state of the art for high temperature thermocouples. They were not metalurgically locked to the surface of the rhenium tubes (using such methods as welding or brazing). It is expected that the measurements made this way will be within 50 degrees of true value, since the solar assembly is very similar to a high temperature vacuum furnace.

One of the thermocouples was attached to the thruster and this is the thermocouple which should have the highest reading. Fifteen thermocouples were attached to the outer surface of the absorber. They were broken into sets of 5, and each set was at a designated axial location. This allowed the reading of a mean axial temperature, and the reading of a temperature distribution along each of the 5 rhenium tubes.

The absorber tube number and the axial location on the absorber of each of the thermocouples are denoted in Fig. 91 as it exits the vacuum chamber backplate assembly. As shown in Fig. 90, location No. 1 is the closest to the vacuum chamber window and location No. 3 is at the start of the hemispherical end of the absorber. Progressing clockwise from the bottom of the vacuum chamber (Fig. 91), the thermocouples are arranged in groups for the three axial locations. The path and installation of a typical absorber thermocouple at axial location No. 2 is illustrated in Fig. 135. The thermocouple is held adjacent to the absorber coil and is protected from direct solar radiation impingement by a rhenium foil strip. The thermocouple passes through the various rhenium-coated graphite components, through the backplate insulation and exits through the backplate assembly.

A discussion of the potential thermocouple error is presented in Appendix D.

Additional Instrumentation

Provision to measure the test chamber pressure (vacuum or positive pressure) must be provided. This pressure will enable the monitoring of the test chamber to ensure an oxygen-free environment. Detection of an increase in this pressure would result in an inert purge into the chamber to prevent high temperature oxidization of the rhenium.

Additional instrumentation recommended included direct or indirect methods of measuring the H_2 propellant flow and ejector (GN_2) flowrate and thrust (if possible). These measurements and their continual monitoring during testing would further ensure safe test operation and the direct calculations of delivered specific impulse.

Configuration Ground Test Setup

The planned overall ground test solar rocket configuration is illustrated in Fig. 136, and shows the absorber/thruster assembly and the diffuser/ejector. Because of the strong desire to measure thrust for performance evaluation, and because the thrust values will be quite small (approximately 3.7 N (0.83 lb), special consideration was given to the thrust measurement system by AFRPL. A altitude chamber will be provided by AFRPL to enclose the absorber/ thruster and the thrust measurement load cells and avoid external atmospheric loads (wind) on the ground test article. The hydrogen propellant supply instrumentation, vacuum and purge lines will be routed through the wind screen enclosure to the test article with flexible lines.

As shown in Fig. 136, a window (really two windows) are required for the ground test facility. AFRPL has elected to use an actively cooled window assembly with three windows. Coolant is placed between the second and third windows.

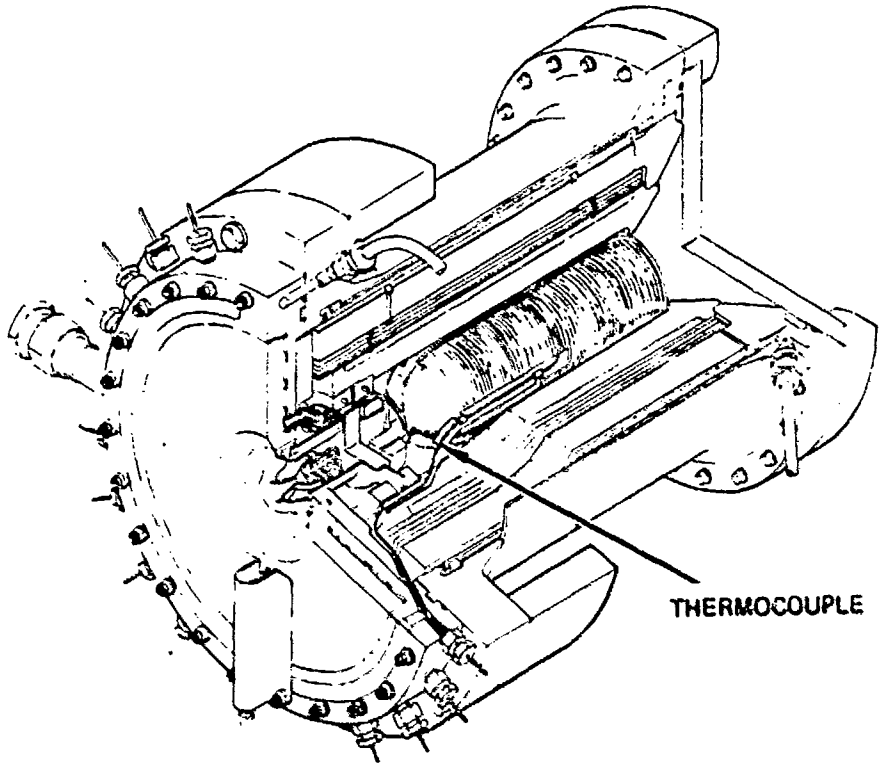

Figure 135. Typical Absorber Thermocouple Installation

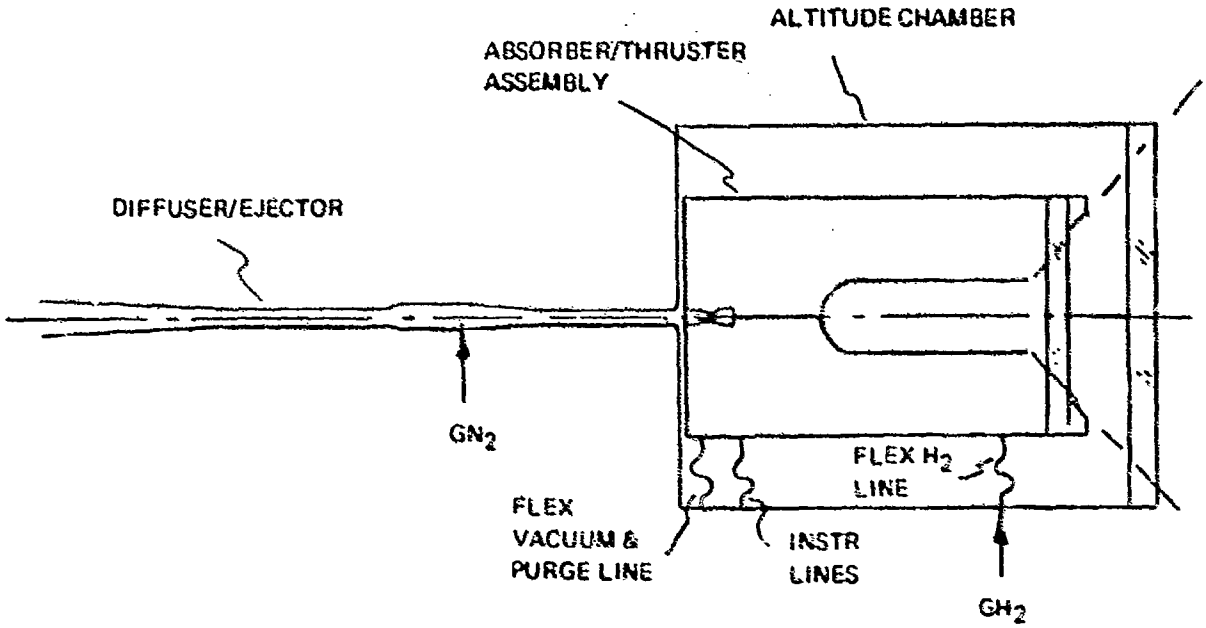

Figure 136. Overall Ground Test Solar Rocket Configuration

PHASE III, FABRICATION

This phase consisted of fabrication of the solar rocket ground test article according to the designs and specifications developed in Phase II. The completed assembly was to be delivered to the Air Force Rocket Propulsion Laboratory for acceptance and future test evaluation.

A simplified fabrication and assembly sequence is shown in Fig. 137. With release of the designs and specifications, components and parts fabrication was initiated. Completed rhenium tubes were assembled into the absorber coil subasembly and a high-temperature (1644 K, 2500 F) pressure/leak test conducted. The absorber coil subassembly was then assembled with thruster and backplate followed by final assembly of the remaining components using an assembly fixture. More detail assembly flow charts are presented in the later sections where the assembly procedures are discussed.

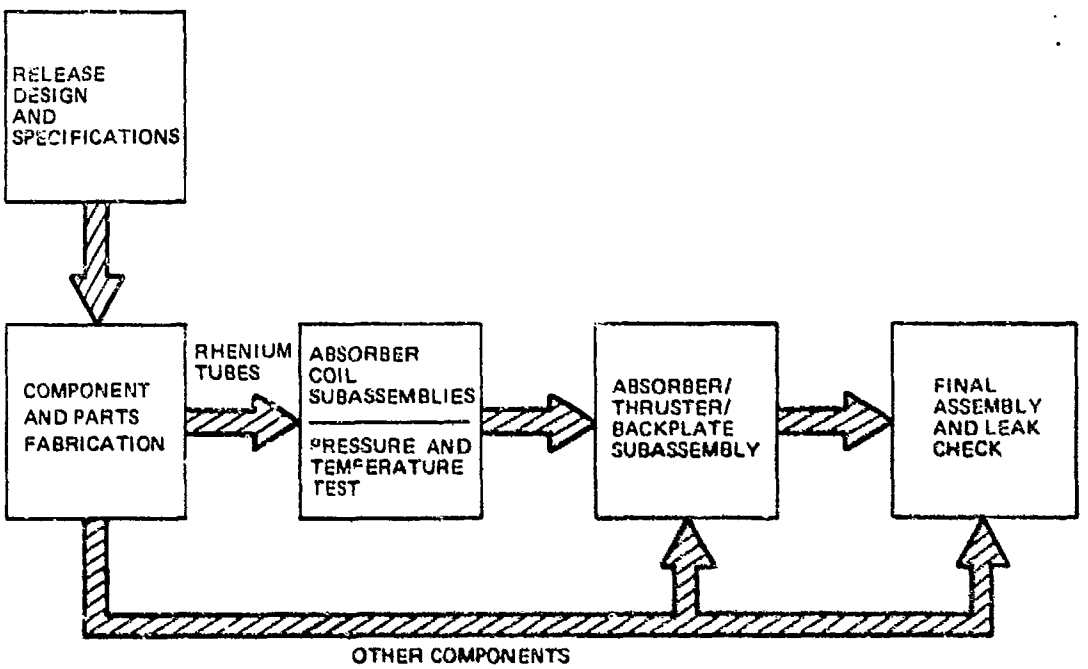

Figure 137. Simplified Fabrication and Assembly Sequence

The final assembly layout was updated for Phase III and is shown in Fig. 138. Table 16 shows the assembly parts list.

The vacuum chamber window specification is presented in Appendix A. While Rocketdyne did not provide this component as part of the solar rocket ground test article, recommendations were made on suppliers for the window and the IR coating.

COMPONENT FABRICATION

The major component groups for the solar rocket ground test article included the following:

1. Rhenium Tubing
2. Graphite Components
3. Vacuum Chamber
4. Radiation Shields
5. Inlet Insulation
6. Thermocouples
7. Rhenium Thruster

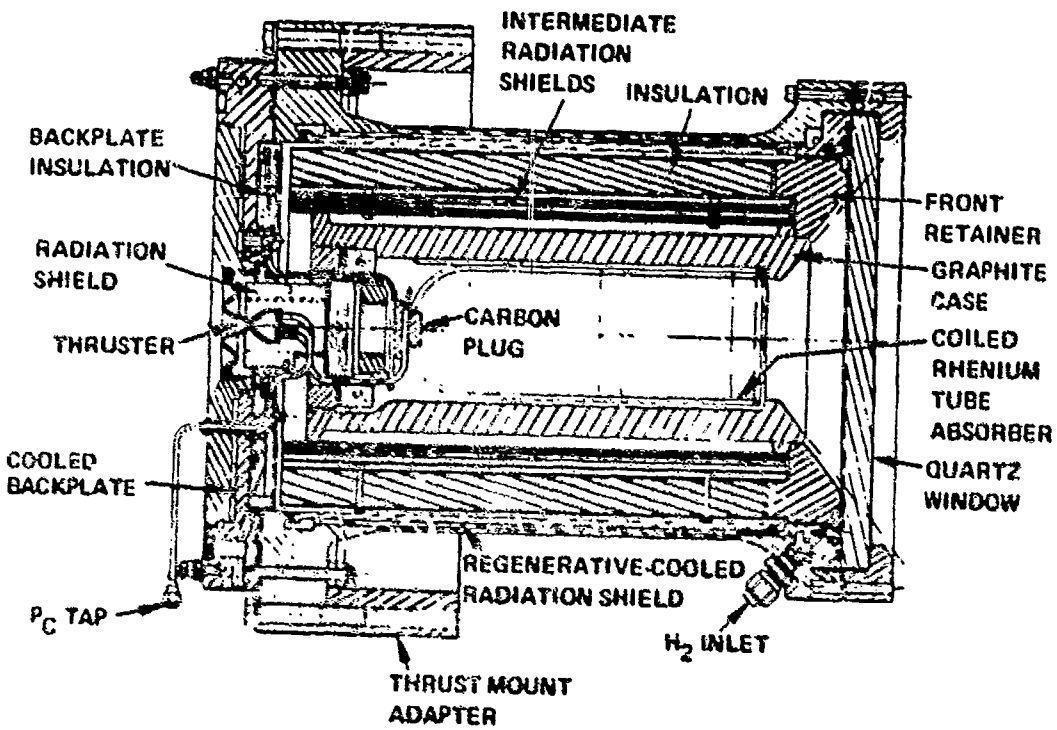

Figure 138. Final Absorber/Thruster Design Layout

TABLE 16. SOLAR ROCKET ASSEMBLY PARTS LIST

ITEM	DESCRIPTION	REQUIRED
AP81-067-011	T-77B-36BAE(8.1) N48 MOD THERMOCOUPLE (*)	10
AP81-067-021	T-77B-30BAE(8.1) N48 MOD THERMOCOUPLE (*)	6
AP81-202-001	GRAPHITE PLUG ASSEMBLY	1
203-001	GRAPHITE NUT ASSEMBLY	1
204-001	GRAPHITE BASEPLATE ASSEMBLY	1
205-003	GRAPHITE CASE	1
216-001	VACUUM CHAMBER CYLINDER ASSEMBLY	1
335-001	RADIATION SHIELD	1
336-005	ABSORBER INLET INSULATION RETAINER	1
337-001	ABSORBER INLET INSULATION ASSEMBLY	1
338-001	THRUST SHIELD	1
339-001	BASEPLATE INSULATION ASSEMBLY	1
340-051	ABSORBER/THRUSTER ASSEMBLY	1
349-001	VACUUM CHAMBER BACKPLATE ASSEMBLY	1
391-003	MOUNTING ADAPTER	1
393-001	BOLT RING ASSEMBLY	2
409-001	STUD/WASHER ASSEMBLY	1
419-001	CROSSOVER PROPELLANT LINE	1
AP83-029-003	ADAPTER RING	1
AP84-029-003		5
029-005	INCOLOY 903 ADAPTER LINE	1
046-001	SECONDARY (BASEPLATE) INSULATION	1
096-003	PLEXIGLAS COVER	1
103-	CHAMBER PRESSURE EXTENSION	1
107-003	CHAMBER-PRESSURE TUBE SHIELD	1
NAS 1102E4-12 (SILVER PLATE)	SCREW	12
NAS 1351N54 H 40	SCREW	24
RD111-1009-0836	BOLT	8
RD111-1006-0445	BOLT	24
RD114-8005-1004	NUT	24
RD153-5009-0001	WASHER	24
RD153-5002-0004	WASHER	24
LD153-0013-0006	WASHER	8
SPSPLI-4-2.9 (A286)	WASHER	24
SYLVANIA WB-110315 x 0.5	BOLT	3
SYLVANIA WN-110319	NUT	3
RE261-3005-1006	K-SEAL	1
PARKER 8914-2101-1250	MARK II SEAL	1
PARKER 2-379 (V747-75)	O-RING	1
AN815-6J	UNION	1
AN806-6J	PLUG	2
CRAWFORD FITTING CO. SS-200-6	SWAGELOK UNION	1
RHENIUM 0.007 DIAMETER	WIRE	5 FEET
RHENIUM 0.006 x 0.125	FOIL	7 FEET
RHENIUM 0.006 x 0.250	FOIL	15 FEET
RE261-3001-0003	CONICAL SEAL	2
RE261-3001-0007	CONICAL SEAL	2

(*)ARI INDUSTRIES

Fabrication of each of these component areas is discussed in the sections that follow. A flow chart for the rhenium components (tubing and thruster) is shown in Fig. 139.

Rhenium Tubing

Fabrication of the rhenium tubing for the absorber cavity was accomplished by a specialty vendor (Ultramet) using the chemical vapor deposition process (CVD). In this process, rhenium is built up by CVD on a vertical molybdenum mandrel of 0.204 cm (0.100 inch) OD to sufficient thickness to give the desired OD and wall thickness after final surface grinding. Generally, the process was interrupted once or twice and the mandrel inverted, since the CVD buildup tends to be greater toward one end. The mandrel and CVD buildup was just over 0.914 m (3 feet) in length. The deposition process itself took 1 to 2 days. Removal of the mandrel by chemical dissolution initially took over a week; however, introduction of a two-step dissolution process shortened this time somewhat. The individual 0.914 m (3 feet) lengths were centerless ground to the specified OD. The tubes were then annealed to give complete recrystallization.

Tube Inspection. All of the 26 tubes (approximately 25.6 m or 84 feet) received from the vendor were inspected for defects and all defects were characterized so that the best tubes could be placed in the "hot zone" of the absorber.

Typical tube defects are shown in photos in Fig. 140 through 142. Representative pits magnified 32-times are shown in Fig. 140. The numbers shown below each photo denote the tube number. Each tube was numbered so that the characteristics could be correlated with a particular tube. An example of the loosely deposited material is illustrated in Fig. 141 for tube No. 5. Nodules and depression defects are presented in Fig. 142. The depth of the pits was measured optically and a nominal wall thickness beneath the pits was established using vendor measurements of the tube outside diameter and assuming a concentric tube. The minimum wall thickness are presented in Table 17 and as shown, a few of the tubes were free of pits. The range of minimum tube wall thicknesses and the corresponding tube numbers are shown in Table 18.

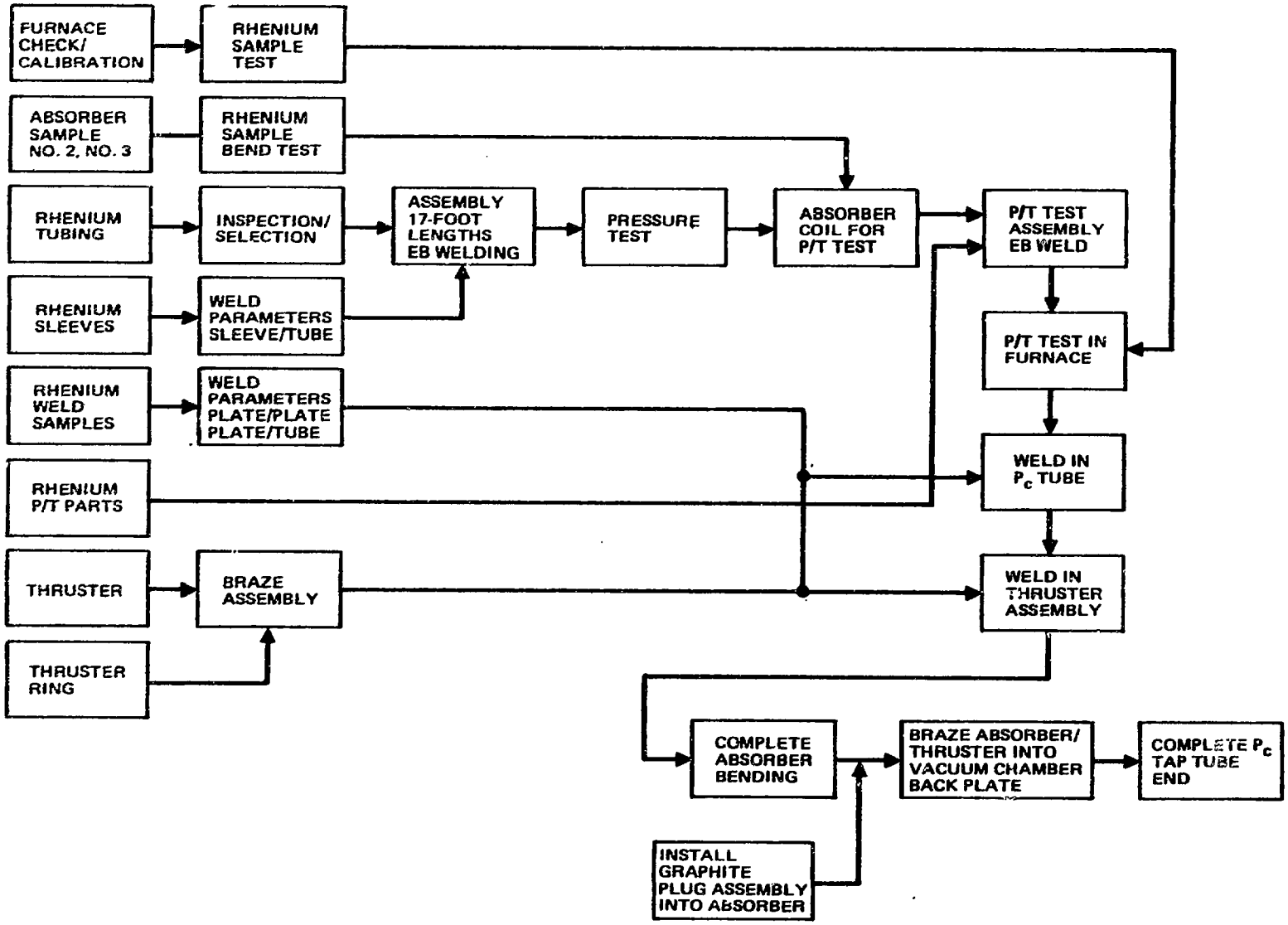

Figure 139. Rhenium Hardware Assembly Flow Chart

NO. 1 32 X FOREIGN PHASE BOTTOM

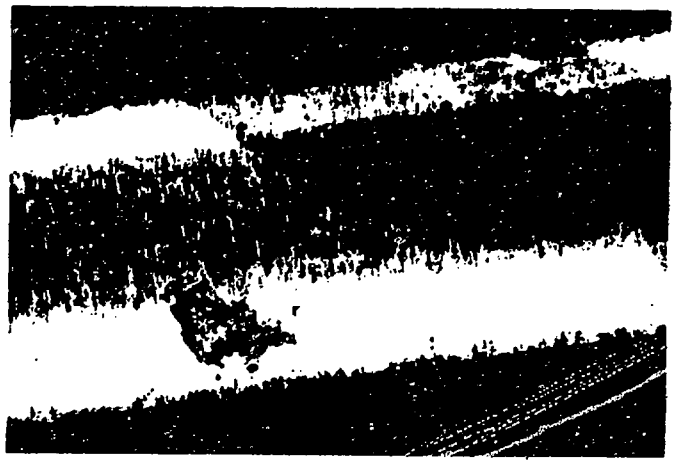

NO. 5 32 X

NO. 23 32 X 8 MILS

380-670

Figure 140. Typical Rhenium Tube Pit Defects

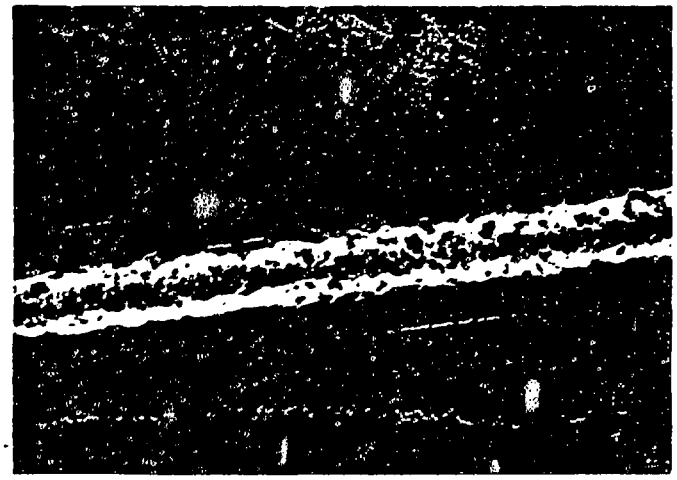

7.5 X

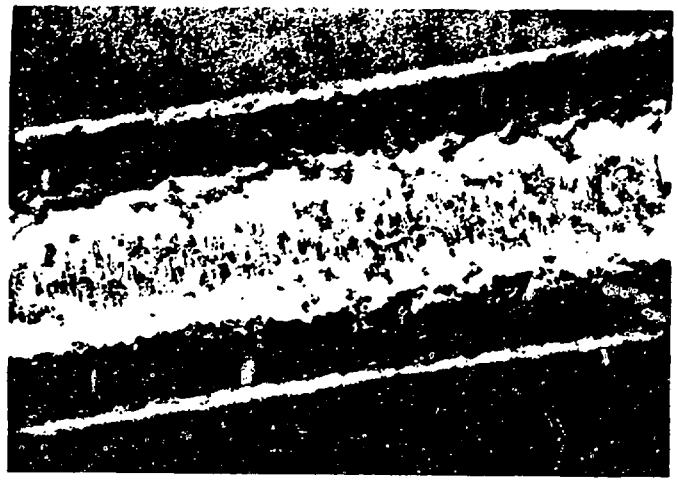

15 X

380-671

Figure 141. Representative Loosely Deposited Material Rhenium Tube Regions

NO. 9 15 X

NO. 24 15 X

NO. 8 15 X

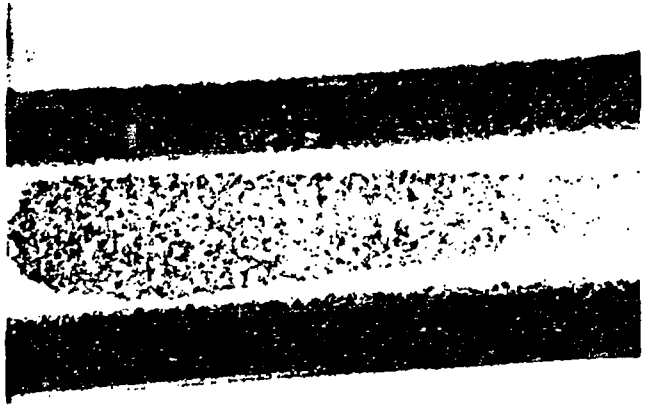

NO. 6 15 X

380-672

Figure 148. Typical Modules and Depression in Rhenium Tubing

TABLE 17. RHENIUM TUBE MINIMUM WALL THICKNESS DATA

Data based on a mandrel OD of 0.100 ±0.0005 inch, tube OD data measured by micrometer (supplier data).

Tube No.	Average OD, cm (inch)	Mandrel OD, cm (inch)	Wall Average, cm (inch)	Defect Depth, cm (inch)	Minimum Wall, cm (inch)
1	0.3110(0.12245)	0.254(0.100)	0.02845(0.0112)	0.0023(0.0009)	0.0262(0.0133)
2	0.3170(0.1248)	0.254(0.100)	0.0315(0.0124)	-	0.0315(0.0124)
3	0.3261(0.1284)	0.243(0.100)	0.0361(0.0142)	-	0.0361(0.0142)
4	0.3114(0.1226)	0.254(0.100)	0.0287(0.0113)	-	0.0287(0.0113)
5	0.3124(0.1230)	0.254(0.100)	0.0292(0.0115)	0.0074(0.0029)	0.0218(0.0086)
				0.0031(0.0012)	0.0262(0.0103)
				0.0206(0.0081)	0.0086(0.0034)
				0.0091(0.0036	0.0201(0.0079)
6	0.3246(0.1278)	0.254(0.100)	0.0353(0.0139)	0.0150(0.0059	0.0203(0.0080)
7	0.3109(0.1224)	0.254(0.100)	0.0285(0.0112)	-	0.0285(0.0112)
8	Data Lost				
9	Data Lost				
10	Data Lost				
11	0.3086(0.1215)	0.254(0.100)	0.0272(0.0107)	0.0142(0.0056)	0.0130(0.0051)
				0.0142(0.0056)	0.0130(0.0051)
				0.0051(0.0020)	0.0221(0.0087)
				0.0084(0.0033)	0.0188(0.0074)
				0.0097(0.0038)	0.0175(0.0069)
				0.0084(0.0033)	0.0188(0.0074)
				0.0140(0.0055	0.0132(0.0052)
12	0.3068(0.1208)	0.254(0.100)	0.0264(0.0104)	-	0.0264(0.0104)
13	0.3071(0.1209)	0.254(0.100)	0.0264(0.0104)	0.0051(0.0020)	0.0213(0.0084)
				0.0043(0.0017)	0.0221(0.0087)
				0.0048(0.0019)	0.0216(0.0085)
14	0.3155(0.1242)	0.254(0.100)	0.0307(0.0121)	0.0038(0.0015)	0.0269(0.0106)

TABLE 17. (Concluded)

Tube No.	Average OD, cm (inch)	Mandrel OD, cm (inch)	Wall Average, cm (inch)	Defect Depth, cm (inch)	Minimum Wall, cm (inch)
15	0.3155(0.1242)	0.254(0.100)	0.0307(0.0121)	0.0058(0.0023)	0.0249(0.0098)
16	0.3056(0.1203)	0.254(0.100)	0.0257(0.0101)	-	0.0252(0.0101)
17	0.3099(0.1220)	0.254(0.100)	0.0279(0.0110)	-	0.0279(0.0110)
18	0.3114(0.1226)	0.254(0.100)	0.0287(0.0113)	0.0132(0.0052)	0.0155(0.0061)
19	0.3071(0.1209)	0.254(0.100)	0.0264(0.0104)	0.0013(0.0005)	0.0252(0.0099)
20	0.3099(0.1220)	0.254(0.100)	0.0279(0.0110)	-	0.0279(0.0110)
21	0.3167(0.1247)	0.254(0.100)	0.0312(0.0123)	-	0.0312(0.0123)
22	0.3058(0.1204)	0.254(0.100)	0.0259(0.0102)	0.0203(0.0080)	0.0056(0.0022)
23	0.3104(0.1222)	0.254(0.100)	0.0282(0.0111)	-	0.0279(0.0111)
24	0.3185(0.1254)	0.254(0.100)	0.0323(0.0127)	0.0074(0.0029)	0.0249(0.0098)
				0.0140(0.0055)	0.0183(0.0072)
				0.0013(0.0050)	0.0136(0.0077)
				0.0081(0.0032)	0.0241(0.0095)
				0.0061(0.0024)	0.0262(0.0103)
25	0.3109(0.1224)	0.254(0.100)	0.0285(0.0112)	-	0.0285(0.0112)
26	0.3193(0.1257)	0.254(0.100)	0.0325(0.0128)	0.0038(0.0015)	0.0287(0.0113)

TABLE 18. RHENIUM TUBE MINIMUM WALL THICKNESS RANGE CHARACTERIZATION

Minimum Wall Thickness by Range: 0.0023 cm (0.0009 inch) Increments

Range, cm (inch)		Tube Numbers
0.0053-0.0076	(0.0021-0.003)	23
0.0079-0.0102	(0.0031-0.004)	5
0.0104-0.0127	(0.0041-0.005)	-
0.01295-0.0152	(0.0051-0.006)	11
0.0155-0.0178	(0.0061-0.007)	18
0.0180-0.0203	(0.0071-0.008)	6, 26
0.0206-0.0229	(0.0081-0.009)	13
0.0231-0.0254	(0.0091-0.010)	15, 19
0.0257-0.0279	(0.0101-0.011)	1, 12, 14, 16, 17, 20
0.0282-0.0305	(0.0111-0.012)	4, 7, 24, 27, 28
0.0307-0.0330	(0.0121-0.013)	2, 21
0.0333-0.0356	(0.0131-0.014)	-
0.0358-0.0381	(0.0141-0.015)	3

The minimum or sound wall thickness ranged from 0.0053 cm (0.0021 inch) to 0.0387 cm (0.015 inch) thick. A tube section with a sound wall thickness of 0.0155 cm (0.0061 inch) was selected for testing. The testing of this tube was conducted at 2000 C (3632 F) and 68.95 N/cm^2 (100 psi) internal Argon gas pressure, and the tube was bent with a 4.445 cm (1.75 inch) radius so as to apply the maximum tensile stress to the pit area. No leakage was recorded during this test. Therefore, it was decided to accept any tube with a sound wall thickness greater than 0.0178 cm (0.007 inch) with 0.0025 cm (0.001 inch) safety factor--15% of the tested article. On this basis, four tubes were rejected and were replaced by the vendor. In addition, three more tubes were ordered (and received) to accommodate the weld sample tests, the pressure/temperature tests and bend tests (by the absorber tube coiling vendor).

Investigation of the other two defects observed in the tubing (the low density surface and appearance of nodules) indicated these deflects would not affect the function of the tubing. The low density surface (fuzz) was only approximately 0.0051 cm (0.002 inch) deep. The tubes with nodules were subjected to a double annealing procedure, and this type of structure was felt to be stabilized and would not affect the function of the tubing.

Tube Weld Joining. Because the CVD rhenium tubing was only available in lengths of approximately 3 feet, the tube sections were required to be joined to form the total length required of approximately 5.18 m (17 feet). The tube joining by a weldment approach was based on the Materials and Process evaluation conducted in Phase II. Both electron beam welding and laser welding were considered for this process in Phase III.

Electron beam (EB) welding requires that operation be conducted in a vacuum to avoid beam distortion. Because of the long length of the tube assembly 5.18 m (17 feet), concern existed as to whether a facility with a sufficiently large vacuum chamber would be available.

In order to avoid solutions such as winding the tubes as they are welded, unwinding them and finally annealing the 5.18 m (17 feet) sections, laser welding was considered. Laser welding does not require a vacuum chamber and therefore allows the tubes to be welded in straight sections. Weld samples were prepared at Rocketdyne and a local vendor was identified to conduct the weld sample test.

Weld samples for both EB and the laser welding process were sectioned and micrographs prepared (Fig. 143 and 144). Evaluation of these samples indicated that the laser weld problems were material oriented and that acceptance criteria would need to be established. EB and laser welding were considered equivalent, except that EB welding in a vacuum environment should not result in weld contamination, while laser welding in an inert environment could result in contamination if the inert gas management is incorrect. Although the final total rhenium tube lengths were long (approximately 5.18 m [17 feet], a 9.14 m [30 feet]) vacuum chamber was located at an experienced EB welding vendor. As a result of this investigation, EB welding of the rhenium tube, using a sleeve joint configuration, was selected.

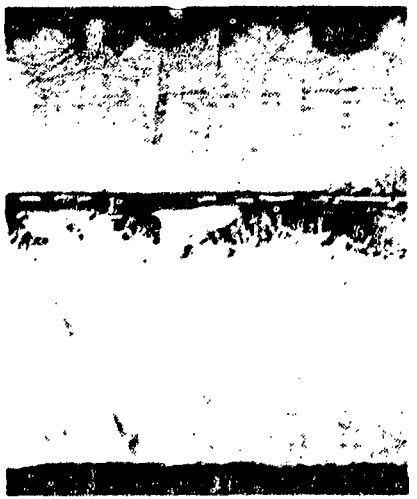

200X 10% OXALIC-ELECTROLYTIC

TYPICAL TUBE/SLEEVE

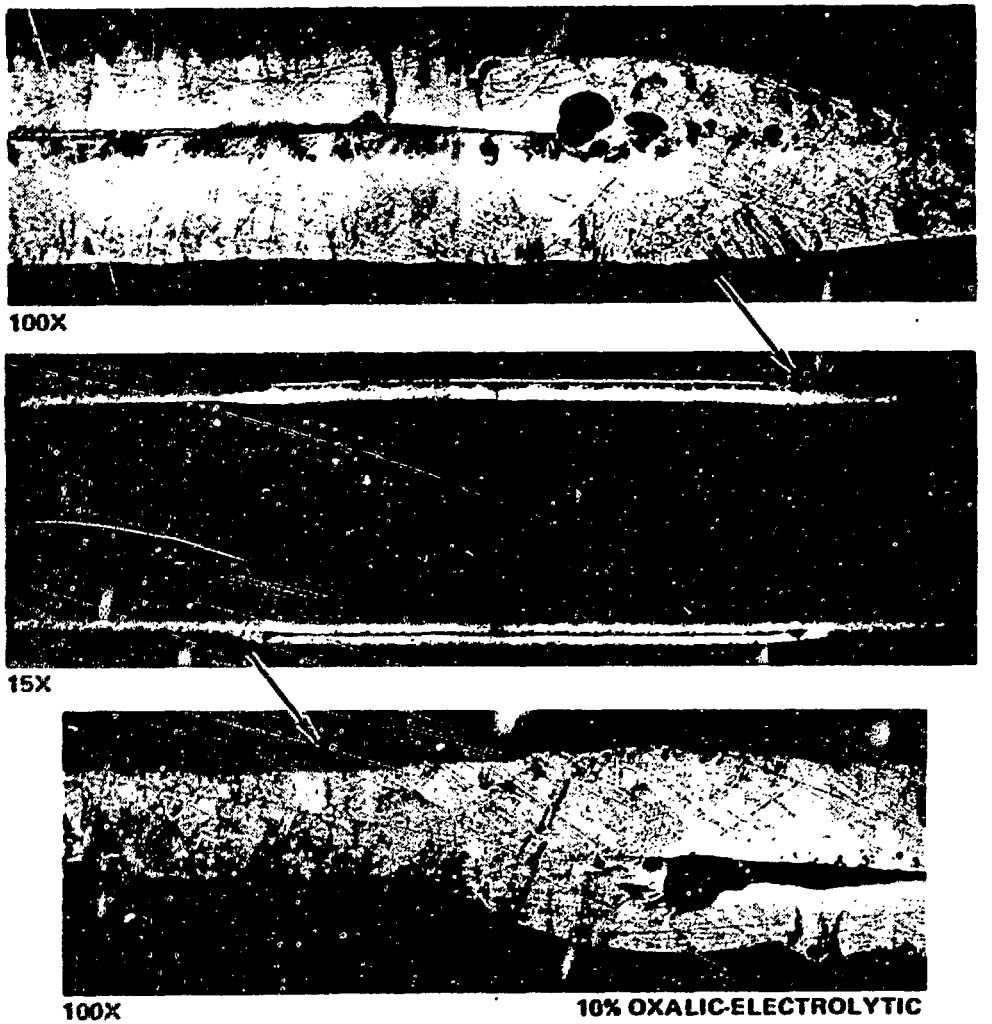

100X

15X

100X 10% OXALIC-ELECTROLYTIC

LASER WELDED SLEEVE SAMPLE

380-205

Figure 143. Rhenium Tube Weld Investigation A 380-205

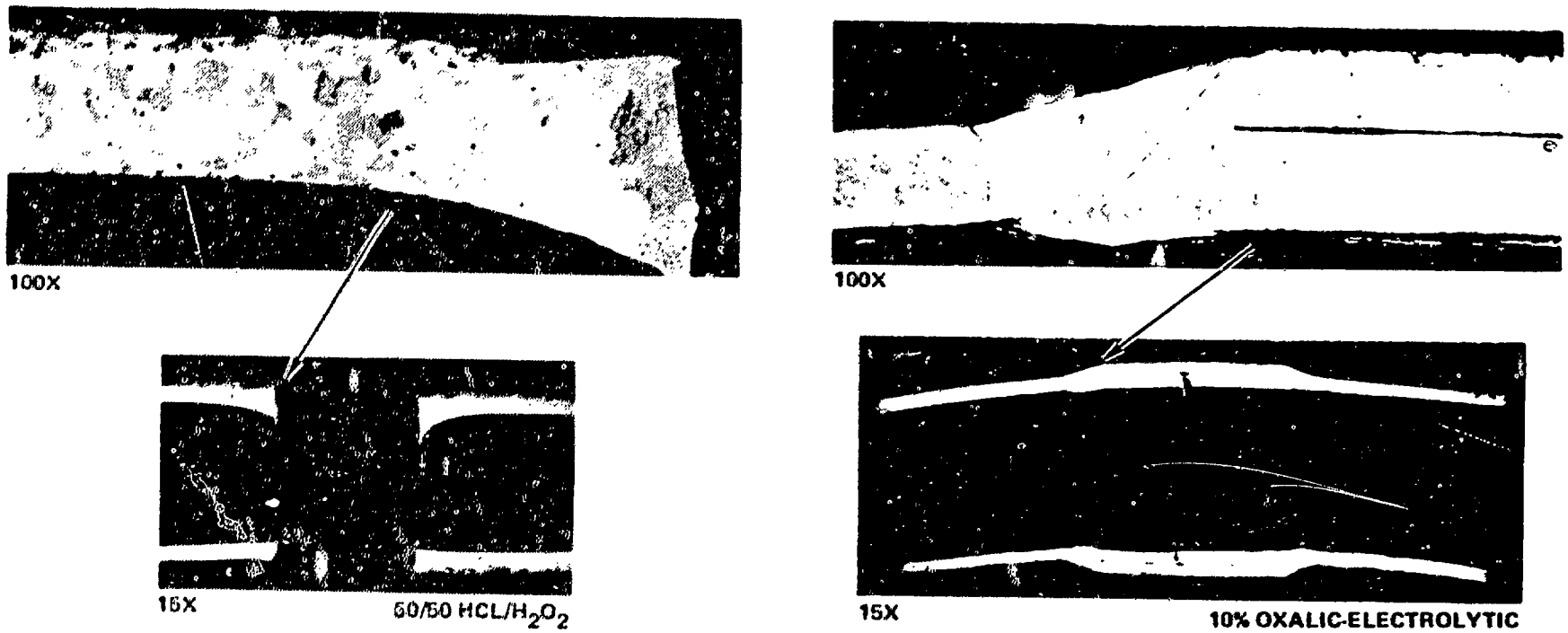

LASER WELDED BUTT SAMPLE

ELECTRON BEAM WELDED SLEEVE SAMPLE

380-206

Figure 144. Rhenium Tube Weld Investigation B

Rhenium Tube Sleeves. Because the outside diameter of the rhenium tubing varied from 0.305 cm (0.120 inch) to 0.326 cm (0.1285 inch), a number of different size sleeves was required. The number of sleeve sizes required to assemble the rhenium tubing into 5.18 m (17 feet) lengths was minimized at three. The ends of the tubes were reworked, as required, to fit the sleeves. This was much less expensive than ordering eight sizes of sleeves and also reduced pits, nodules or low density material in the weld region.

Tube Coiling. The feasibility of coiling the fire parallel-tube assembly was investigated during the Materials and Fabrication Process Evaluations of Phase II. To minimize the problems which could be encountered in coiling the rhenium tube assembly, further evaluation of tube coiling procedures was conducted in Phase III, using the previous tooling. Stainless steel tubing was used because it has coiling characteristics similar to rhenium.

Two absorber mockups were successfully coiled using stainless steel tubing. The first mockup unit is shown in Fig. 145.

It was determined from the mockup that the control of the inlet/discharge area geometry would require some template hardware. To this end, a dummy split plug and a dummy split plate were fabricated from aluminum. These templates assured that the inlet and discharge tubes were properly bent/located and allowed some minor modifications to the shape of the inlet tubes (an improvement in the bending procedure). The aluminum plug assembly was also used to size the tubes before the graphite plug was installed.

Graphite Components

The material selected for the plug, the nut, and the baseplate was POCO graphite to obtain high-strength carbon and thermal expansion characteristics similar to rhenium. Ultra-carbon YU-605T was selected for the absorber graphite case. All graphite components had a protective rhenium coating to prevent sublimation of the graphite during high-temperature vacuum operation.

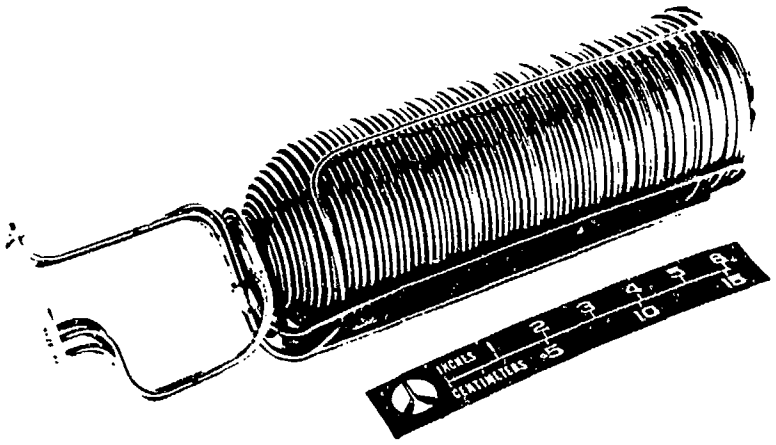

71AX61-4/6/83-C1A

Figure 145. Absorber Stainless Steel Mockup No. 1

Graphite Case. The graphite case which houses the coiled rhenium tube absorber was fabricated by Ultra-Carbon. A visual inspection indicated a well fabricated part and good fit-up with the graphite baseplate was obtained. The part is shown in Fig. 146. The rhenium coating of this part was accomplished by Ultramet and since certain portions of the cases were not initially coated, some recoating was required.

Graphite Plug. The graphite plug which closes out the hole in the hemispherical end of the coiled rhenium tube assembly was completed and received. After the rhenium coating was applied, an interference fit of the rhenium coated graphite plug and ring existed in the mating threads. The coated graphite plug was returned to the vendor for rework of the threads. The rework required stripping the coating and recoating after modification of the threads.

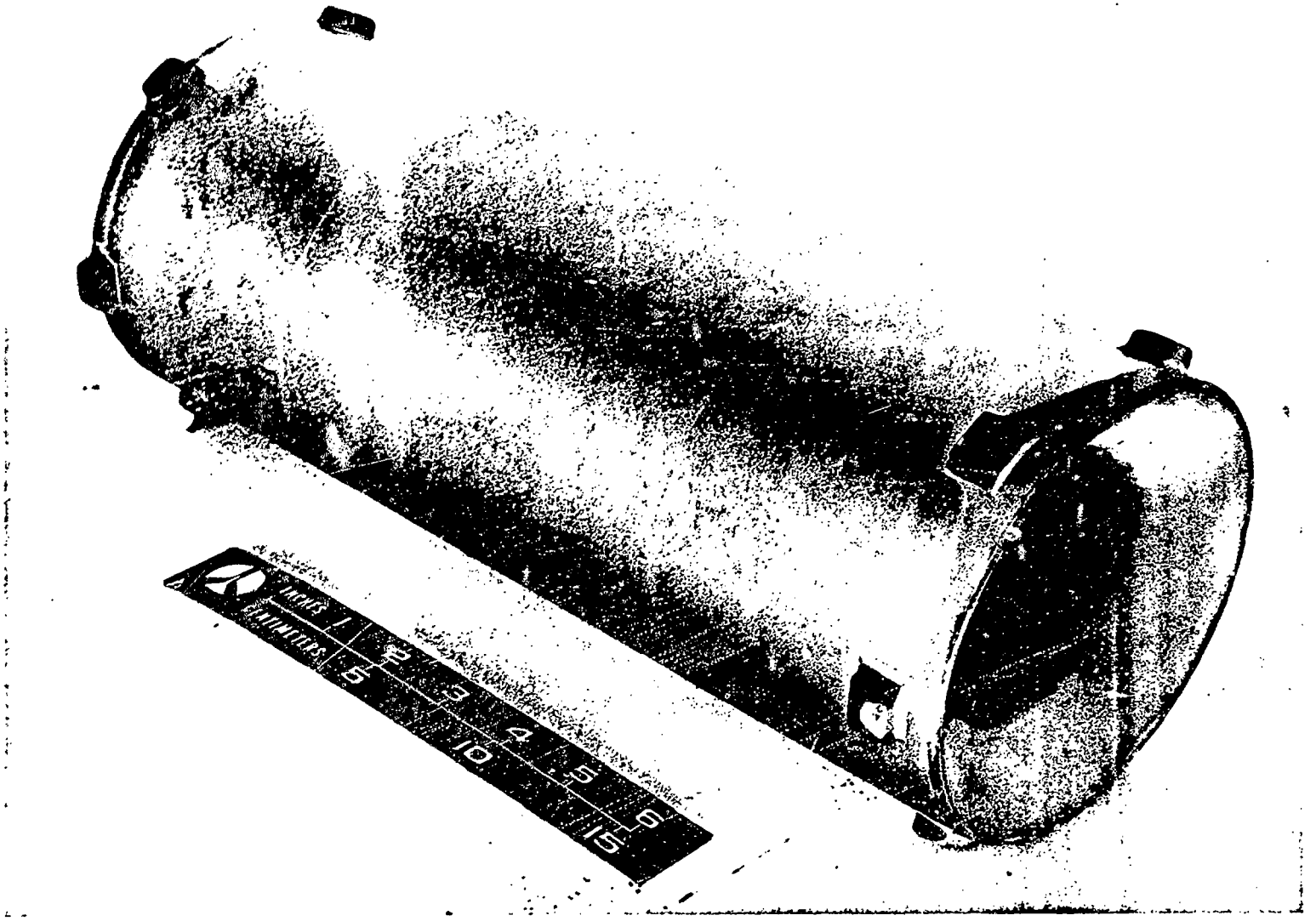

1XZ61-4/6/83-C1C*

Figure 146. Graphite Case

Graphite Nut and Split Baseplate. The absorber graphite nut and baseplate were completed and received from POCO. A visual inspection of the components indicated high quality, well fabricated parts. The split baseplate and nut are shown in Fig. 147, along with the threaded end of the graphite case. The baseplate is shown installed into the end of the graphite case in Fig. 148. These components were also coated with rhenium several times to provide complete coverage.

Vacuum Chamber

The vacuum chamber assembly included an outer shell and an inner cylinder, both fabricated from 347 corrosion resistant steel, and a backplate fabricated of Incoloy 903. The fabrication was completed by a vendor (Trimodels). The outer shell (Fig. 149) resulted in a length shorter than the design value and a fix involving a brazed spacer ring was required. The spiral wire which formed the spiral coolant passage was successfully welded to the inner cylinder also completing this part.

Vacuum Chamber Backplate. To reduce material cost and lead time for the Incoloy 903 material for the backplate, existing in-house forgings were utilized. To use the existing forgings, a slight design modification was required to the backplate design. The 903 Incoloy material for the part was slightly smaller in diameter than the original design. Therefore, the outer coolant passage was made narrower but its depth was increased to provide the same coolant flow area. The transition into the second spiral passage was accomplished by an increase in width and a decrease in depth.

Some difficulty was experienced in obtaining vendor bids on fabrication of the split backplate insulation. The primary concerns were: (1) small thickness leading to holes completely through the piece (material integrity), and (2) a warpage of the part due to the sintering of a small thickness-to-diameter ratio part. After considering alternative insulation materials, a satisfactory bid was received for rigidized zirconium oxide insulation which provided the desired low thermal conductivity material.

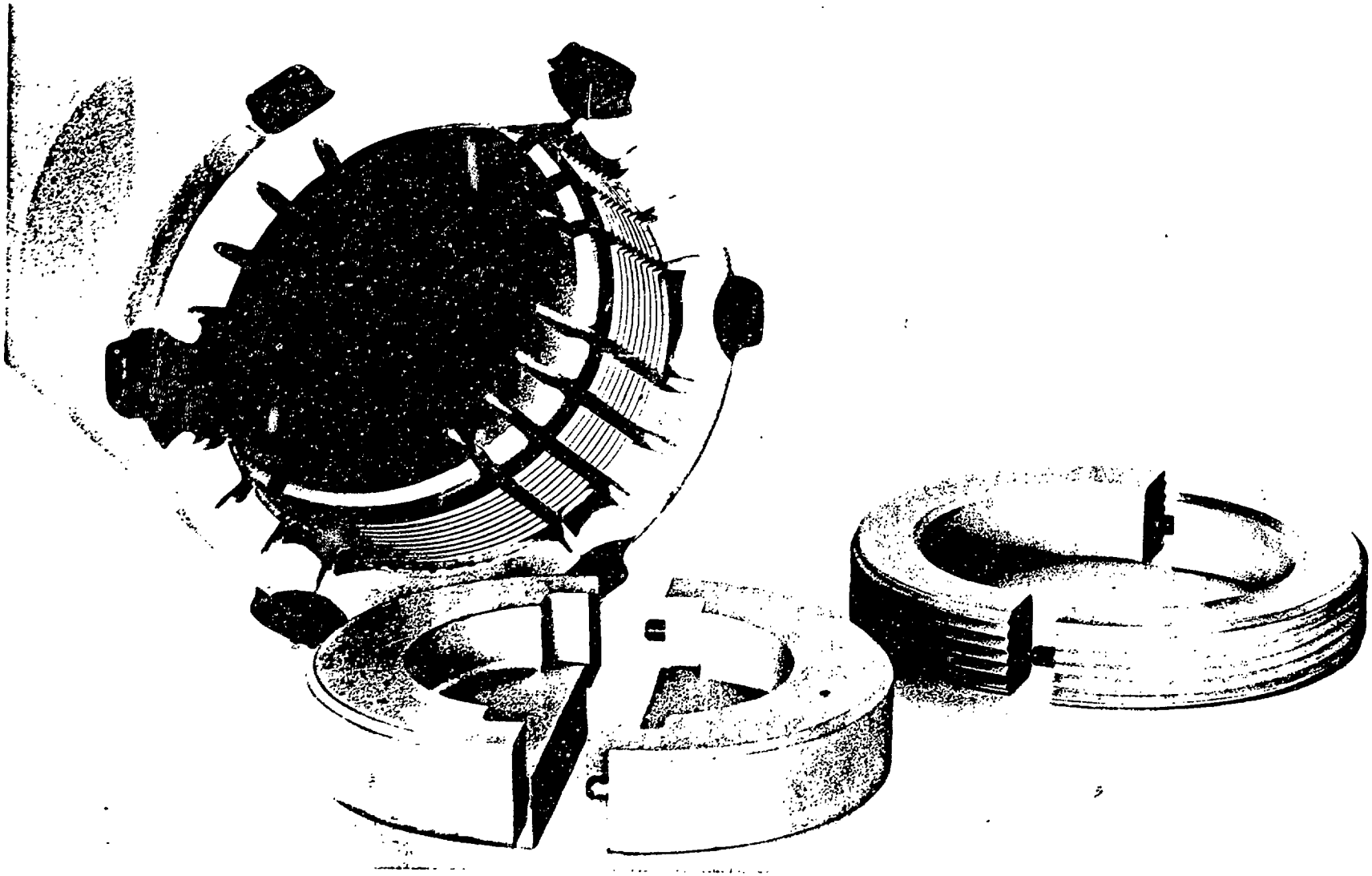

1XZ61-4/6/84-C1J*

Figure 147. Split Graphite Baseplate and Nut

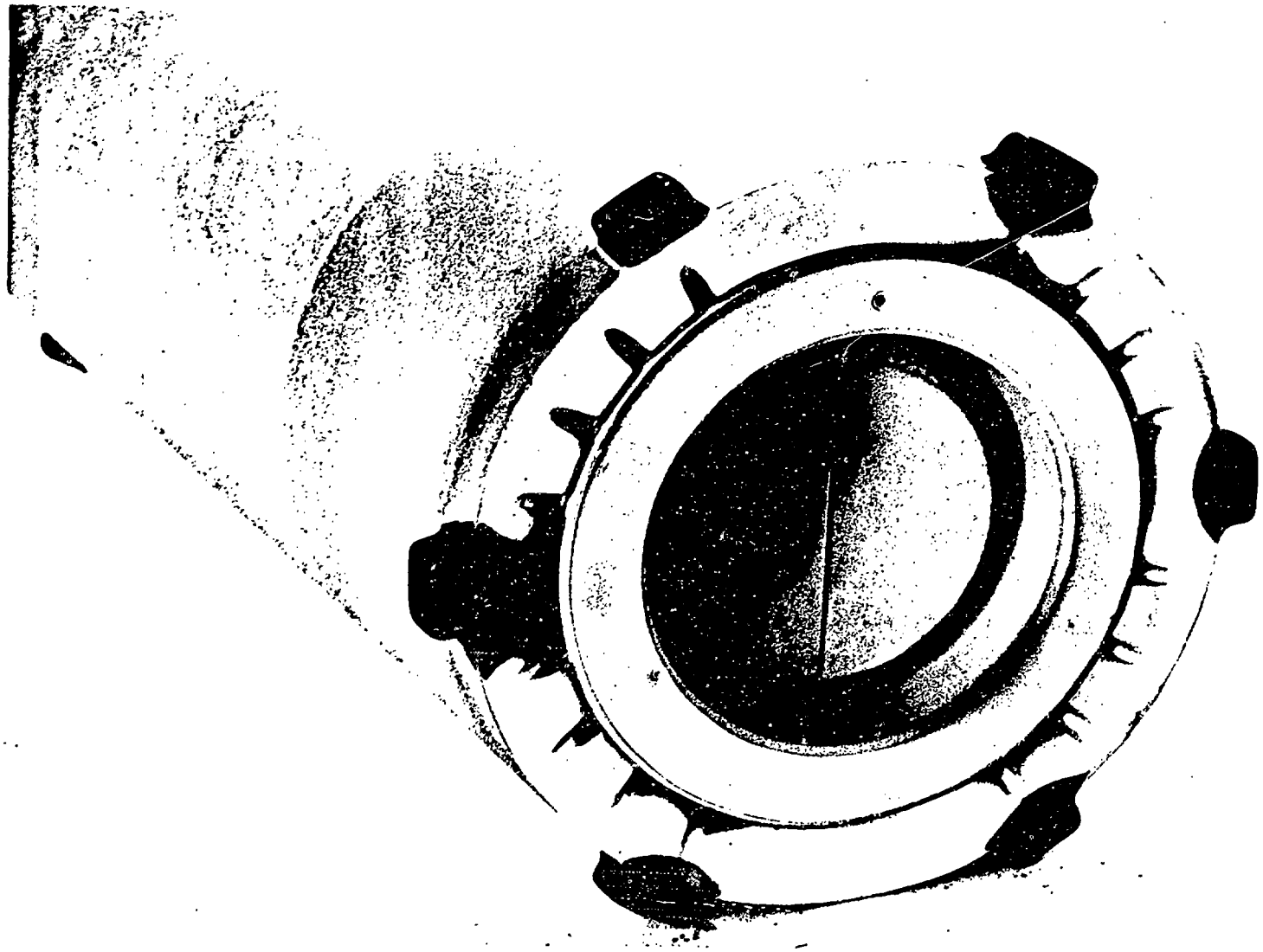

1XZ61-4/6/83-C1K*

Figure 148. Graphite Nut Installation in Graphite Case

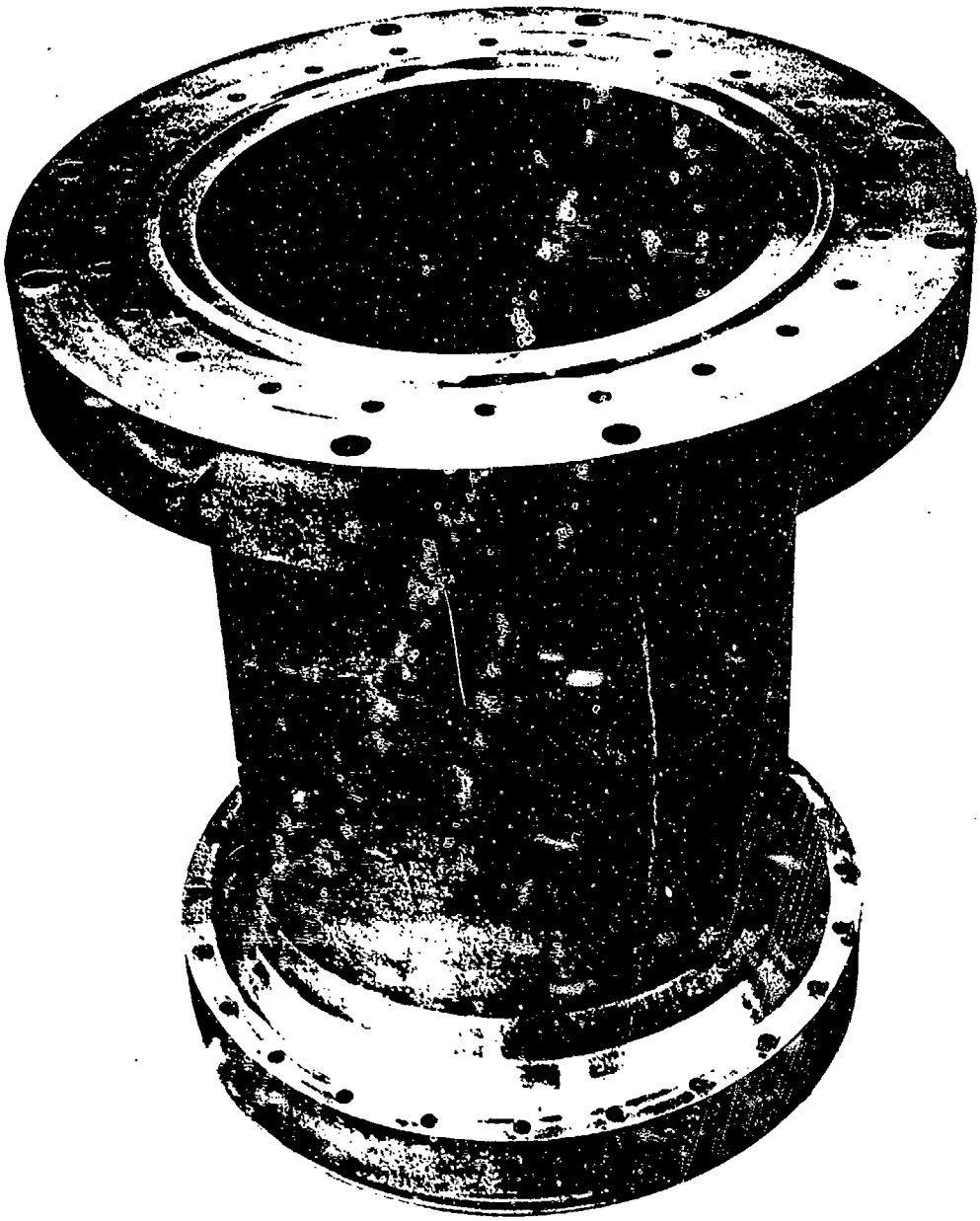

ESG44056-12

Figure 149. Vacuum Chamber Outer Shell

The insulation was held in place by six tungsten bolt assemblies attached to the backplate. The tungsten bolt assemblies were welded to the backplate.

As a result of a design change in the attachment of the rhenium absorber to the backplate, a secondary rigidized zirconium oxide insulation layer was added over the primary layer. The secondary layer is attached to the primary layer with high-temperature staples made from tungsten-rhenium.

Radiation Shields

Vendor fabrication (Sylvania) of the radiation shields included the shields for the absorber and for the thruster. The completed absorber radiation shield assembly is shown in Fig. 150 with the two tungsten and two molybdenum radiation shields and with Alfrax insulation sandwiched between two molybdenum shields.

The thruster shield, fabricated from tantalum, was to be rhenium coated to avoid hydriding in the event of a hydrogen leak. Investigation of this potential problem indicated the probability of tantalum hydride formation was small and should not present a problem if precautions (inert purges) are taken in the event of a hydrogen leak. Therefore, rhenium coating of the tantalum thruster radiation shield was eliminated. The thruster shield was received from the vendor and had a dimensional problem; a 0.129 cm (o.050-inch) gap between the bolting surfaces (2 places). The part was reworked to remove this gap between the bolting surfaces.

Inlet Insulation

Fabrication of the high density aluminum oxide inlet insulation (Mullfrax 202) was completed by the vendor (Carborundum). A stack-up of the insulation bricks with the heat shield and the inlet insulation retainer demonstrated an excellent fit. A cold temperature gap existed between each of the bricks which measured 0.051 cm (0.020 inch) to 0.076 cm (0.030 inch). Once the assembly was heated (including the heat shield), the gap was calculated to be 0.079 cm (0.031 inch) to 0.091 cm (0.036 inch). A zirconium oxide fiber material was used to fill and control the gaps.

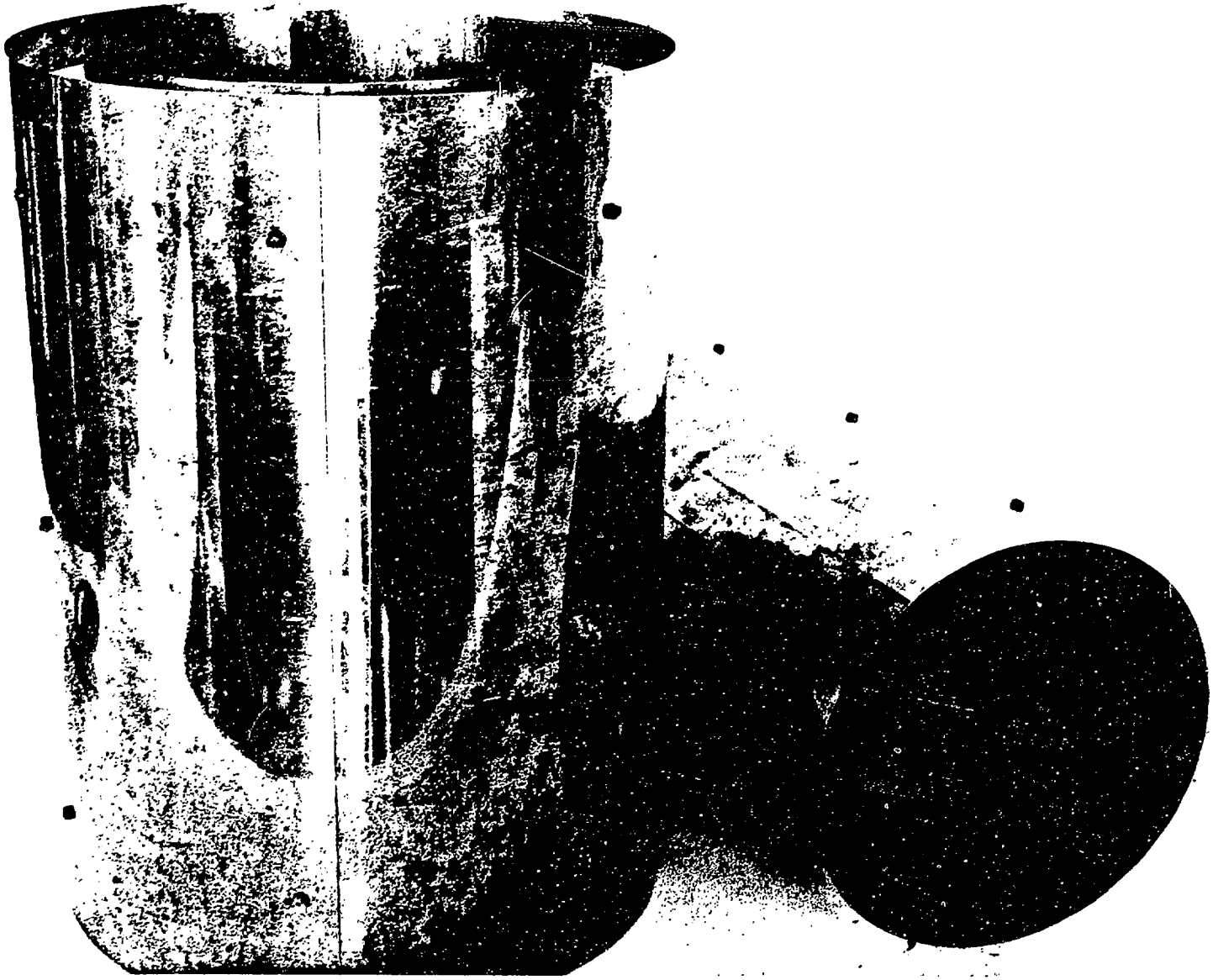

1XZ61-4/6/83-C1I*

Figure 150. Absorber Radiation Shield Assembly

The bricks, as received, had a reddish deposit on some of the brick surfaces (the material is white). Carborundum was contacted and indicated that the deposit is caused by a fuel flash in their oil-fired furnace. The bricks were heated in a vacuum furnace for 1 or 2 hours to drive off the vacuum removable material.

Thermocouples

Selection of the thermocouples to be used in the hardware was re-evaluated due to the very high temperature operation. Discussions with a thermocouple vendor indicated that the thermocouples required were not standard. All thermocouples pass through a region of 2478 K (4000 F) and six of the 16 thermocouples must be capable of measuring temperatures of 2644 K (4300 F) to 2756 K (4500 F). Although the environment is to be a vacuum, the thermocouples should be capable of tolerating high-temperature exposure to hydrogen in the event of a leak in the rhenium tube assembly. Otherwise the thermocouples would have to be replaced if a hydrogen leak occurred. This single failure environment created a material compatibility question with existing high-temperature thermocouple sheathing materials which included tantalum and moly-rhenium.

The investigation of tantalum carbide formation with the tantalum thruster radiation shield concluded the probability of formation was small and therefore tantalum appeared to be the best choice of material for the thermocouple sheathing. This choice was based on improved flexibility (ductility) at room temperature for thermocouple installation, compared to moly-rhenium sheath material, the other candidate. In addition, thermocouple cost was expected to be reduced.

The final configuration was the tantalum-sheathed tungsten/tungsten-rhenium thermcouples. The thermocouples were to be grounded junctions with a mechanical lock backup for the welded hot junction. This ensured an extended life expectancy for the junction as compared with a welded-only tip.

Rhenium Thruster

Fabrication of the rhenium thruster was successfully completed (Fig. 154) and dimensional checks were performed. Initial concern was that the thruster could not be chemically vapor deposited (CVD) in one piece due to the complex shape, but through unique gas flow tooling design a one-piece thruster was successfully fabricated by Ultramet (Fig. 151 and 152).

The results of the dimensional checks of the fabricated rhenium thruster are illustrated in Fig. 153 and indicated a variation of the thruster wall thickness from a minimum of 0.0889 cm (0.035 inch) to a maximum of 0.2413 cm (0.095 inch). The nominal design wall thickness was 0.1975 cm (0.062 inch). In the combustion chamber section, the wall was a maximum of 0.2413 cm (0.095 inch) and reduced to 0.1016 cm (0.04 inch) in the thruster throat. Also, the sine-wave section of the thruster exit resulted in a maximum wall thickness of 0.2159 cm (0.085 inch) on the inside crown and was 0.0889 cm (0.035 inch) at the thruster-to-backplate braze joint. Therefore, although the thruster had been fabricated in one piece by the CVD process, a wide range of thruster wall thicknesses resulted. A brief assessment of the structural characteristics of this as-deposited part indicated that a thicker actual minimum wall thickness was required.

To more thoroughly assess the structural adequacy of the thruster for the as-deposited configuration, the original finite element stress analysis model was modified. However, since it was felt that the 0.216 cm (0.085 inch) thickness in the sine wave section would result in an undesirable increase in thermal strains, a constant wall thickness of 0.089 cm (0.035 inch) was assumed for this region. This could be accomplished through grinding down of the thick section.

1XZ61-4/6/83-C1G*

Figure 151. Rhenium Thruster

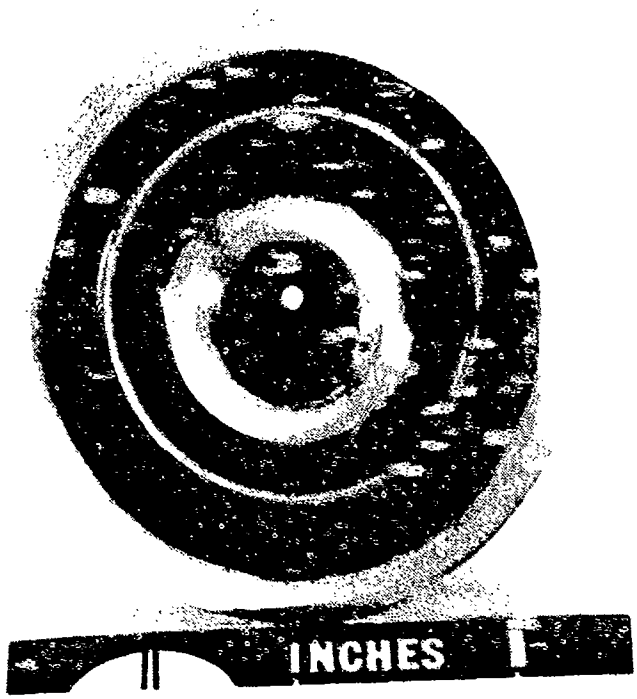

1XZ261-4/6/83-C1H*

Figure 152. Rhenium Thruster (Backside)

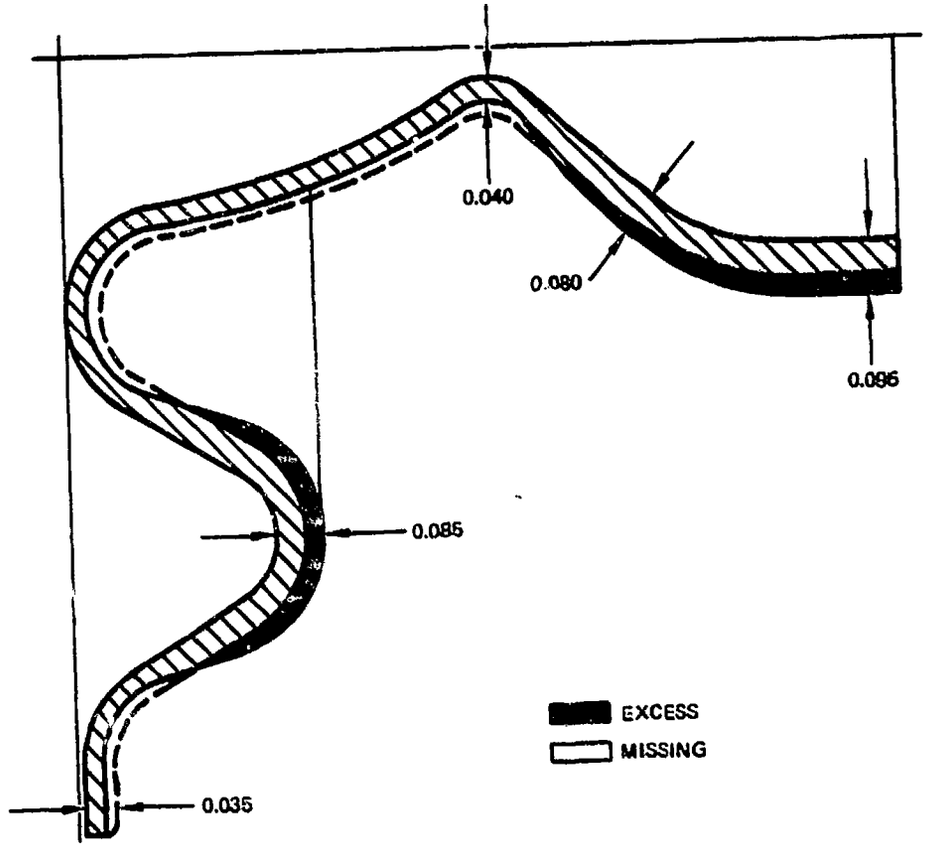

Figure 153. Nominal Rhenium Thruster Design and As-Deposited Configuration

In the finite element stress analysis, two load cases were considered:

1. Steady-state temperature distribution plus thruster internal pressure
2. 20.68 N/cm^2 (30 psi) purge pressure

Analysis results for the first load case are summarized in Fig. 154. The calculated strain values resulted in a minimum predicted life of 200 cycles based on predicted minimum material properties. Results for the second load case indicated that large factors of safety exist for a 20.68 N/cm^2 (30 psi) purge pressure (ultimate strength safety factor of greater than 25). Based on these results, and the fact that the changes in the thruster geometry should not adversely affect the stress-rupture life, it was concluded that the as-deposited thruster was structurally adequate once the sine-wave section was ground to 0.089 cm (0.035 inch) thickness.

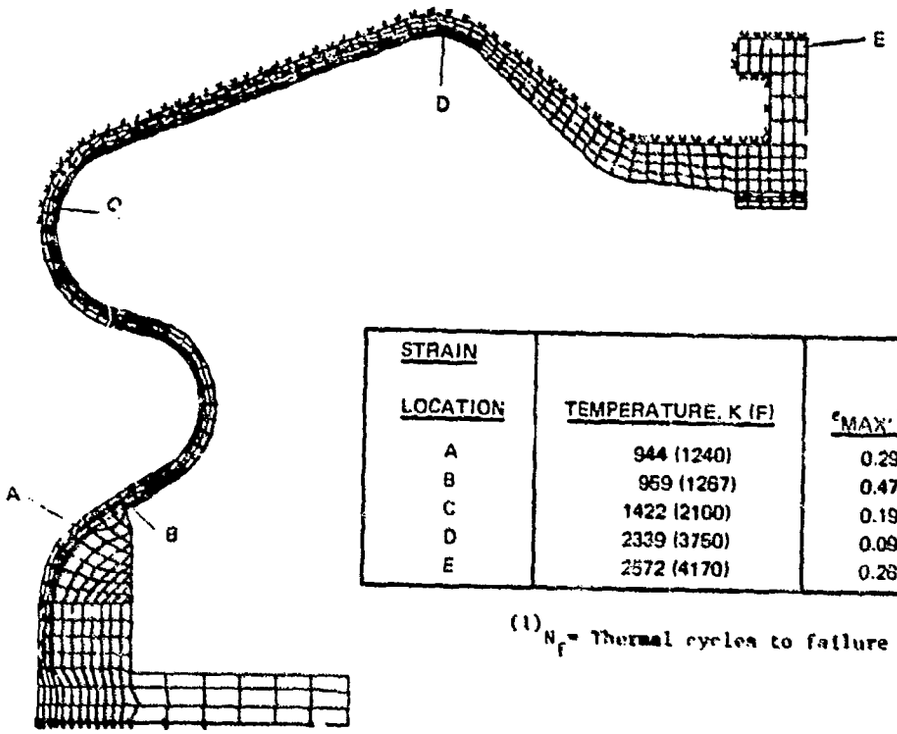

STRAIN LOCATION	TEMPERATURE, K (F)	ϵ_{MAX}, %	N_f (1)
A	944 (1240)	0.29	>1000
B	959 (1267)	0.47	500
C	1422 (2100)	0.19	>1000
D	2339 (3750)	0.09	>1000
E	2572 (4170)	0.26	200

(1) N_f = Thermal cycles to failure

Figure 154. Peak Strain Summary for Rhenium Thruster

Further inspection of the completed rhenium thruster in the region to be brazed to the Incoloy 903 adapter ring disclosed a depression (maximum of 0.022 cm or 0.085 inch) in the region of the braze joint. The depression could result in an unsatisfactory braze joint and therefore a rework was performed. The brazing joint surface was built up with additional rhenium and the surface satisfactorily reground.

Inspection also revealed that the axis of the thruster was approximately 3 degrees off from perpendicular to the base section. It was suspected that at some point in the various reworks, the thruster "oil canned" about the thin section in the base convolution. No rework could be performed to correct this discrepancy. The thrust misalignment of this nozzle was corrected by adjusting the orientation of the thruster within the vacuum chamber.

ABSORBER COIL SUBASSEMBLY

All of the rhenium tubes, including replacement tubes, were inspected, numbered, and grouped into 5.18 cm (17 foot) assemblies (Fig. 155). Two of the assemblies are made up of six tubes each and three of the assemblies are made up of five tubes each. The tubes were joined together using 0.508 cm (0.200 inch) long sleeves (EB-welded to the tubes). The maximum allowable gap between the tubes and the sleeve was 0.00254 cm (0.001 inch). Therefore, each of the tube assemblies was arranged to match tube end diameters as closely as possible. Some of the tube ends were reworked to fit the sleeves.

A 14-step fabrication sequence for the absorber was established, as shown in Table 19. The sequence was based on a "least-risk" approach. The initial sleeve welds (Step 3) assured that the right sleeve remained with the right tube. Step 5A allowed one of the more difficult bending operations to be completed on easy-to-handle short tube lengths (and also allowed the replacement or repair of the tube if a problem occurred).

Prior to proceeding with the actual tube-to-sleeve welds, weld samples were processed. Some weld craters were developed during the welding process; they apparently were caused by outgassing of the interlaminar region of the tubing. Some modifications in the welding procedure were suggested by Material and Processes personnel and were incorporated.

After modification in the rhenium tube welding procedure, the initial sleeve-to-tube welds were successfully completed (Step 3). Two of the tube welds experienced burn-through but were successfully reworked with replacement sleeves. Visual inspection of the welds indicated excellent fusion was achieved.

The tubes were forwarded to another vendor for annealing (Step 4) to ensure ductile tubes for the coiling process. The annealing (stress relieving) of all the rhenium tubes was successfully completed following the final selected annealing procedure in which the tubes were placed in a vacuum furnace at 1772 ±14 K (2730 ±25 F) for 3 hours and then furnace cooled to 311 K (100 F).

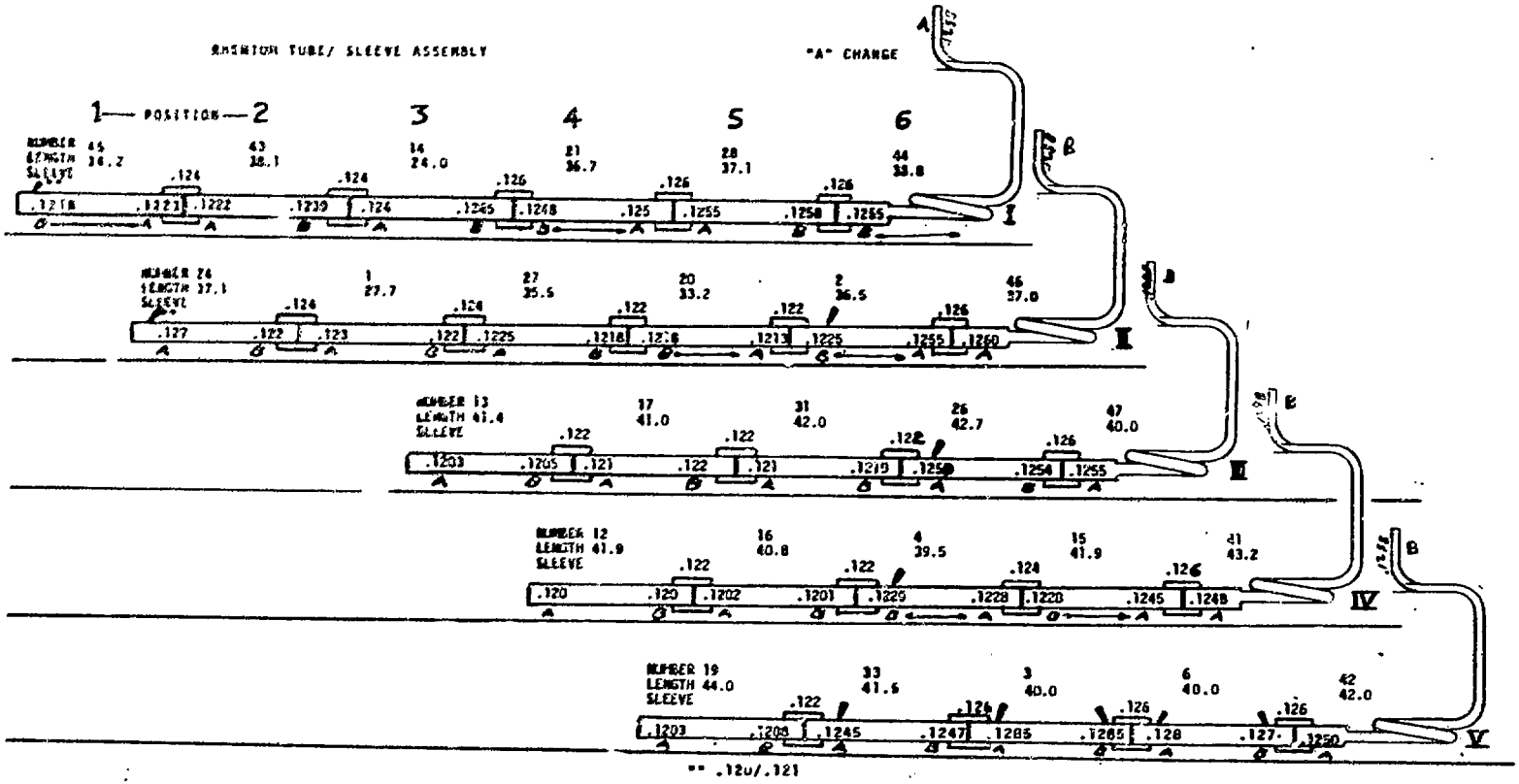

Figure 155. Rhenium Tube/Sleeve Assembly

TABLE 19. ABSORBER FABRICATION SEQUENCE

	1.	TUBE INSPECTION
	2.	ULTRAMET SLEEVE/TUBE FITUP
	3.	EB WELDING INCORPORATED TO WELD ONE SIDE OF SLEEVE ONLY
	4.	SCARROT HEAT TREAT, ANNEALING
	5a.	PRECISION TUBE BENDING TO PREBEND TUBES 44, 46, 47, 41, 42
	5b.	EB WELDING INCORPORATED TO COMPLETE 14 FOOT SUBASSEMBLY
A	6.	EB WELDING INCORPORATED TO COMPLETE 17 FOOT ASSEMBLIES
	7.	PRECISION TUBE BENDING TO FORM ABSORBER FOR P/T TEST
B	8.	EB WELDING INCORPORATED TO ASSEMBLY P/T FITTINGS TO ABSORBER
C	9.	TO PERFORM P/T PROBE TEST
	10.	TO PERFORM P/T TEST
	11.	ULTRAMET TO REMOVE P/T FITTINGS EXCEPT THRUSTER HEADER
	12.	EB WELDING INCORPORATED TO ASSEMBLE P_c TUBE AND THRUSTER TO ABSORBER
	13.	PRECISION TUBE BENDING TO COMPLETE INLET BENDS TO ABSORBER
D AND E	14.	ROCKETDYNE TO ASSEMBLY ABSORBER/THRUSTER TO VACUUM CHAMBER BACKPLATE

NOTES:

A. 18-FOOT RIGID SHIPPING CONTAINER REQUIRED
B. WELD SAMPLES REQUIRED
C. ESTABLISH P/T TEST PROCEDURES AND ASSEMBLY TEST EQUIPMENT
D. PROVIDE MANDREL FOR ABSORBER
E. INSTALL GRAPHITE PLUG PRIOR TO ASSEMBLY

The five tubes identified to be located in the hot end of the absorber (attached to the thruster) were delivered to the tube bending vendor for preliminary forming (Step 5). The prebending on tubes 44, 46, 47, 41 and 42 was successfully completed and the tubes were then sent to the welding vendor (Steps 5b and 6). Following successful welding, the tubes were leak-checked and sent to the tube coiling vendor (Step 7) where they were coiled into the solar absorber configuration (Fig. 156) as defined by the requirements for the subsequent pressure/temperature test.

Rhenium Header Plates

To complete the absorber assembly for the pressure/temperature test, rhenium header plates were required. The initial design configuration is illustrated in Fig. 157. In this configuration, the rhenium tubes were individually EB welded into the Powder Metallurgy (PM) header plate at both the thruster and the inlet end of the coiled rhenium tube absorber. The tube-to-plate weld was located at the end of the tube. The subsequent fabrication step was to EB-weld the closeout cap (PM rhenium to the header plate.

Two rhenium powder metallurgy billets were procured for the header plates. The parts fabricated from this material are shown in Fig. 158 (zones 6 and 7). Figure 158 depicts the inlet end (cold end) and the discharge end (hot end) of the absorber as it was configured for the pressure/temperature test. The cut line shown was where the closeout plate could subsequently be removed so that the thruster could be welded in place for the final assembly.

Following evaluation of PM weld samples, the coiled rhenium tube absorber was assembled and the rhenium tube-to-thruster cap welds and the closeout welds successfully completed for the pressure/temperature test. The pressure/temperature configuration is depicted in Fig. 159.

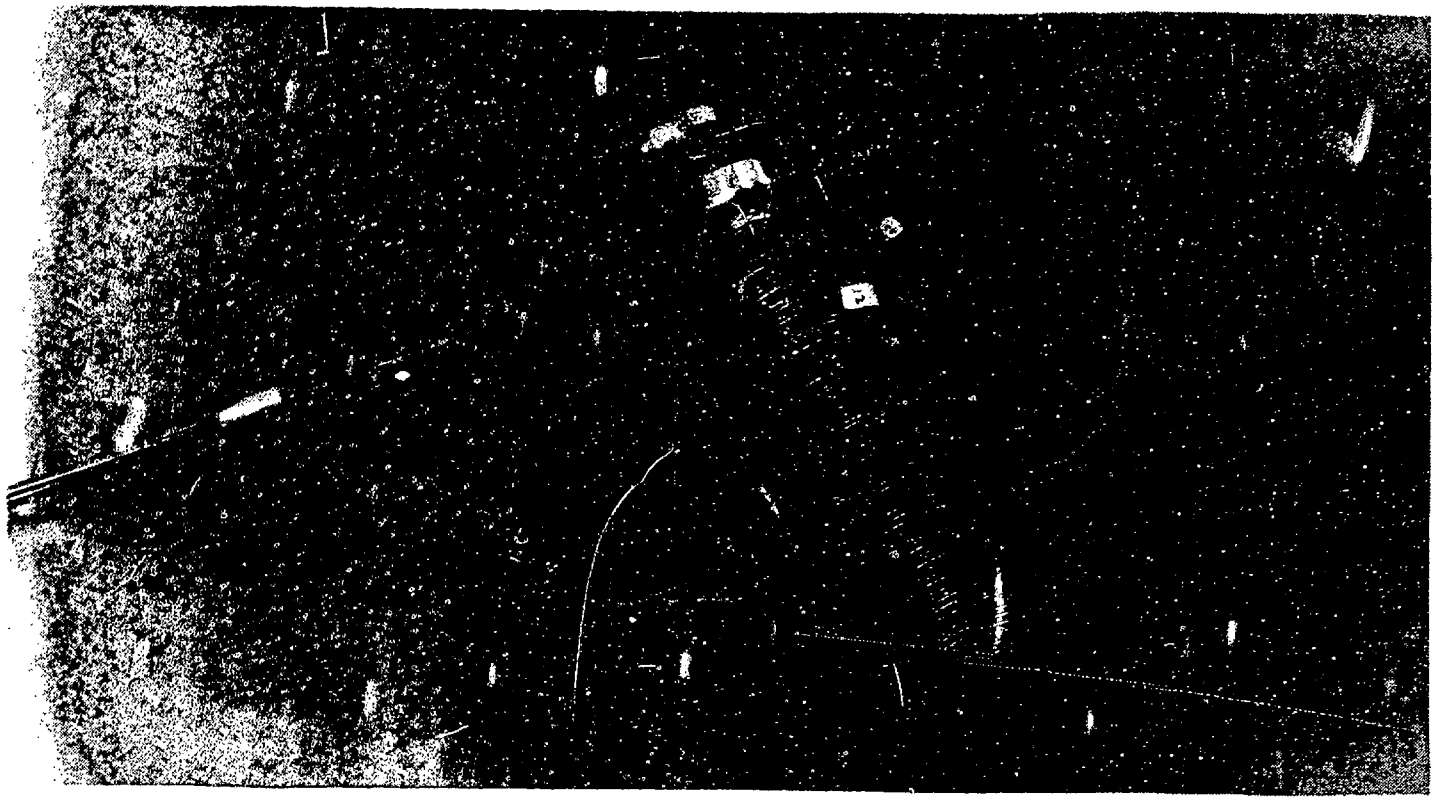

Figure 156. Coiled Rhenium Tube Assembly (High Temperature Leak Test Configuration)

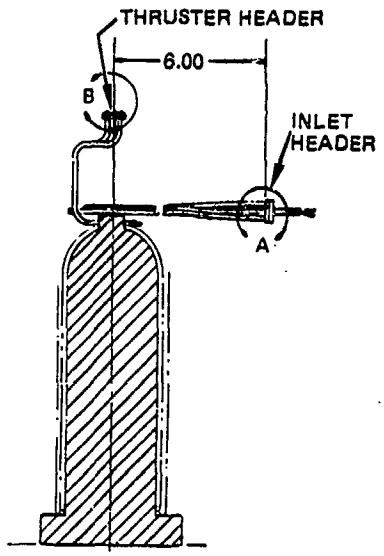

PRESSURE/TEMPERATURE TEST

Figure 157. Rhenium Tube-to-Header Plate Design Configuration

Absorber Coil Subassembly Pressure/Temperature Test

The absorber coil subassembly was subjected to an intenal pressure of 100 psig helium with the assembly in a vacuum chamber at approximately 1644 K (2500 F). This test is essentially a high-temperature leak test of the assembly. The test plan included checkout of the vacuum furnace for leaks and maximum temperature and then testing the vacuum furnace with a section of rhenium tubing at the test conditions prior to running the test on the absorber.

The equipment required to build up the absorber for the pressure/temperature test included a graphite support mandrel (Fig. 157). To prevent the formation of rhenium carbide between the mandrel and the absorber, it was planned to coat the mandrel with titanium carbide. However, this coating was tested in a vacuum furnace and found to be unsatisfactory and a zirconium-oxide coating was substituted.

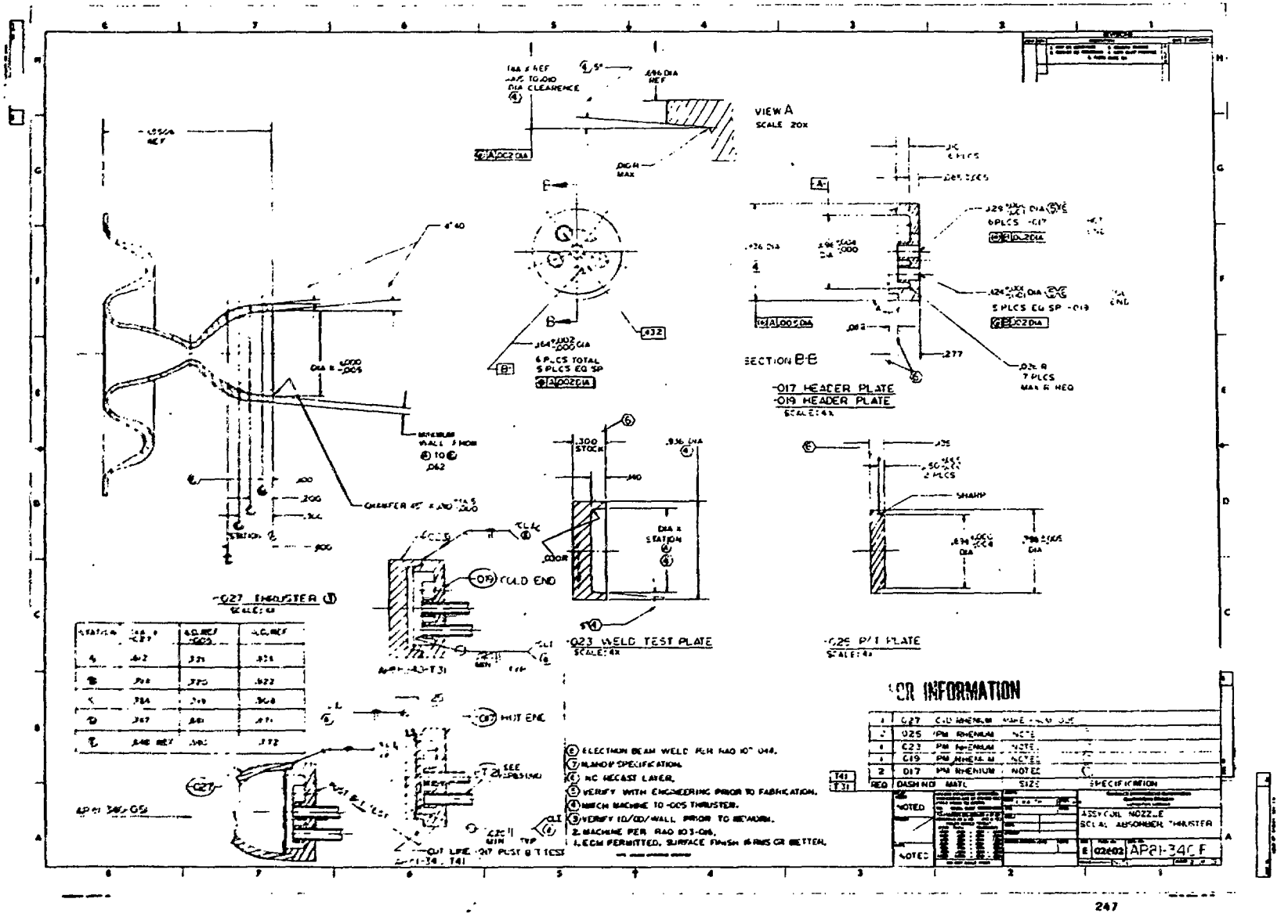

Figure 158. Rhenium Thruster Assembly

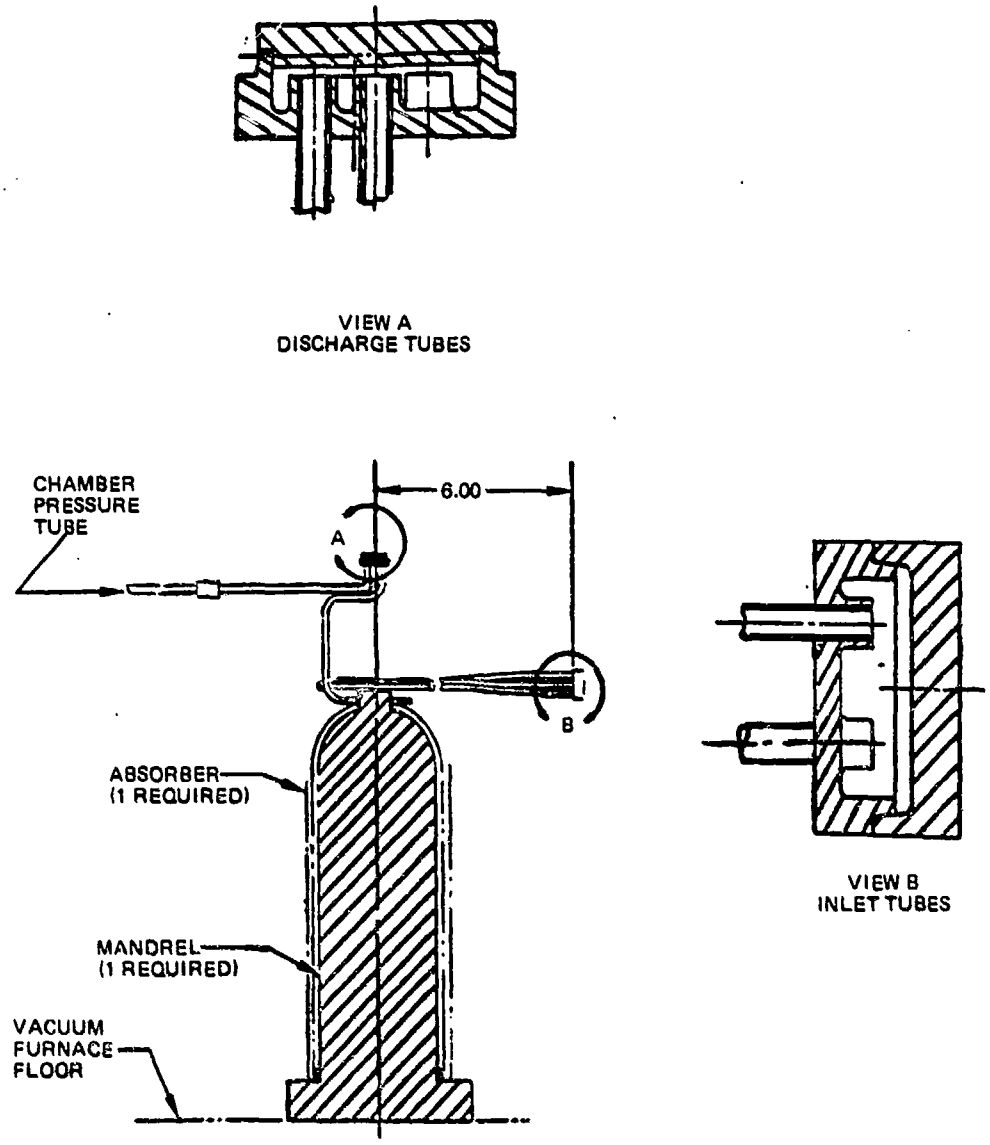

Figure 159. Pressure/Temperature Test Configuration

Figure 160 is a schematic of the test configuration. Prior to testing the actual absorber, a rhenium tube probe sample was run in the furnace to verify that the furnace system operated as required and no rhenium oxidation occurred. Additionally, the rhenium wire attachment of the tungsten-rhenium thermocouples to the absorber tube was tested. The schematic of the probe test configuration is shown in Fig. 161.

The test was run with the coiled tube absorber supported on an alumina crucible. The pressure/temperature test of the absorber coil subassembly was satisfactorily completed. The subassembly was tested in a vacuum chamber at 1473 K (2500 F), and with an internal tube pressure of 68.9 N/cm^2 (100 psi) helium. Two small leaks were detected in the tubing. The estimated leak rate was 10^{-6}% of total flow, which was deemed acceptable.

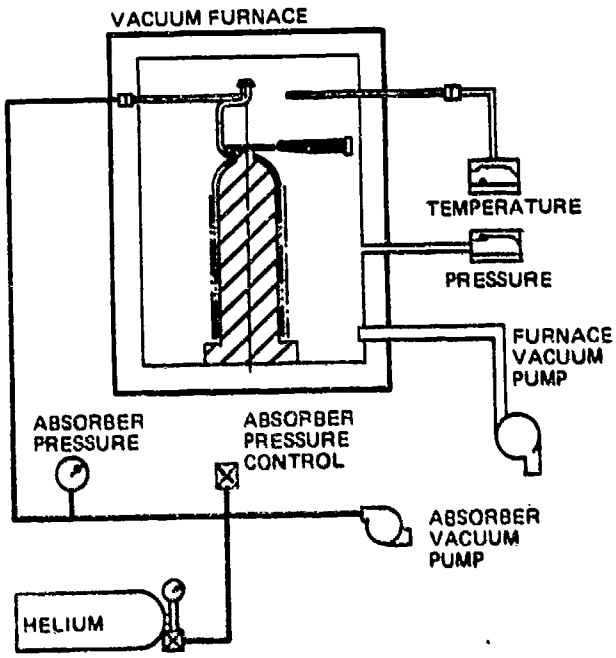

Figure 160. Pressure/Temperature Furnace Assembly

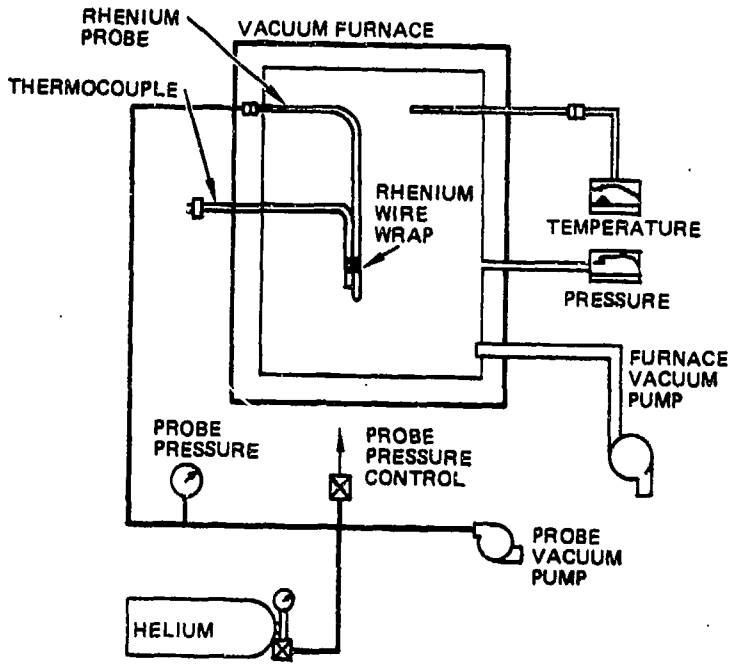

Figure 161. Probe/Thermocouple Test Furnace Assembly

The absorber coil subassembly was prepared for assembly to the thruster adapter ring and the vacuum chamber backplate. The subassembly was returned to the tube bending vendor where the inlet tubes were formed to the final configuration. The Incoloy 903 absorber inlet lines (and the chamber pressure line) were nickel plated on the sleeve ID. The inlet lines were then bent to their final configuration and nickel plated on their OD. The chamber pressure jumper tube was kept in the straight condition, but it was also plated on its OD.

ABSORBER/THRUSTER/BACKPLATE SUBASSEMBLY

The assembly procedure was to braze the adapter ring to the thruster at high temperature, then to induction-braze the inlet tubes and the chamber pressure tube and to EB-weld the thruster to the absorber tubes and finally EB-weld the adapter ring with the thruster to the backplate. The subassembly is illustrated in Fig. 162.

The braze alloy used in the brazing of the Incoloy 903 adapter ring to the rhenium thruster was evaluated with sample tests. The selected braze alloy was Palniro ONE (50% gold, 25% nickel and 25% paladium) and the braze temperature was 1408 K (2075 F). Palniro ONE proved to be a less agressive (less diffusion into the parent material) alloy with the Incoloy 903 than Palniro SEVEN which was also evaluated. On the basis of the braze sample evaluation, design was completed on tooling to braze the adapter ring to the thruster (Fig. 163). The thruster/adapter ring brazing was successfully completed.

The five propellant inlet tubes to the absorber coil and the thruster chamber pressure tube were to be induction-brazed to the vacuum chamber backplate. In addition to the evaluation of the braze samples, an extensive study was conducted of the joint between the rhenium tubes and the Incoloy 903 manifold. A stress analysis indicated a possible low-cycle fatigue problem. The low-cycle fatigue question was solved by adding a short Incoloy 903 jumper line between the rhenium tubes and the manifold. The configuration is illustrated in Fig. 164. A thermal analysis of the joint between the rhenium tube and the Incoloy 903 sleeve indicated an operational temperature of 1256 K (1800 F). Since this temperature is not acceptable, based on the strength of Incoloy 903 (the material shows very little strength at 1089 K/1500 F), the jumper line was completely insulated, as shown in Fig. 164. The thermal analysis of this insulated configuration indicated an operational temperature of 933 K (1220 F). This new design balances the expansions and the elasticity of the two materials (using wall thickness) to reduce the stress/strain at the joint to an acceptable limit. Following evaluation of the Incoloy 903 induction braze samples the actual tube braze was satisfactorily completed.

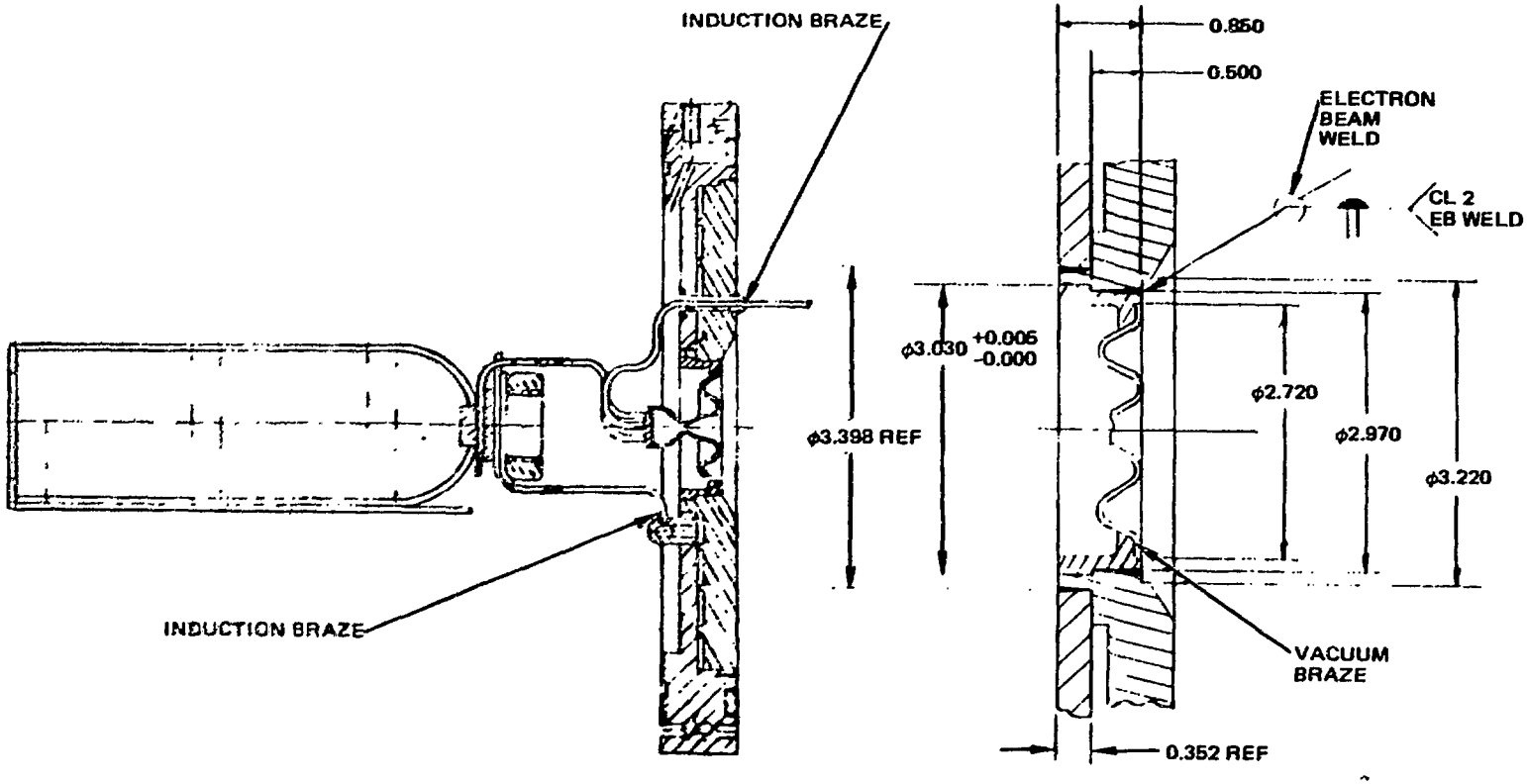

Figure 162. Thruster/Backplate Assembly

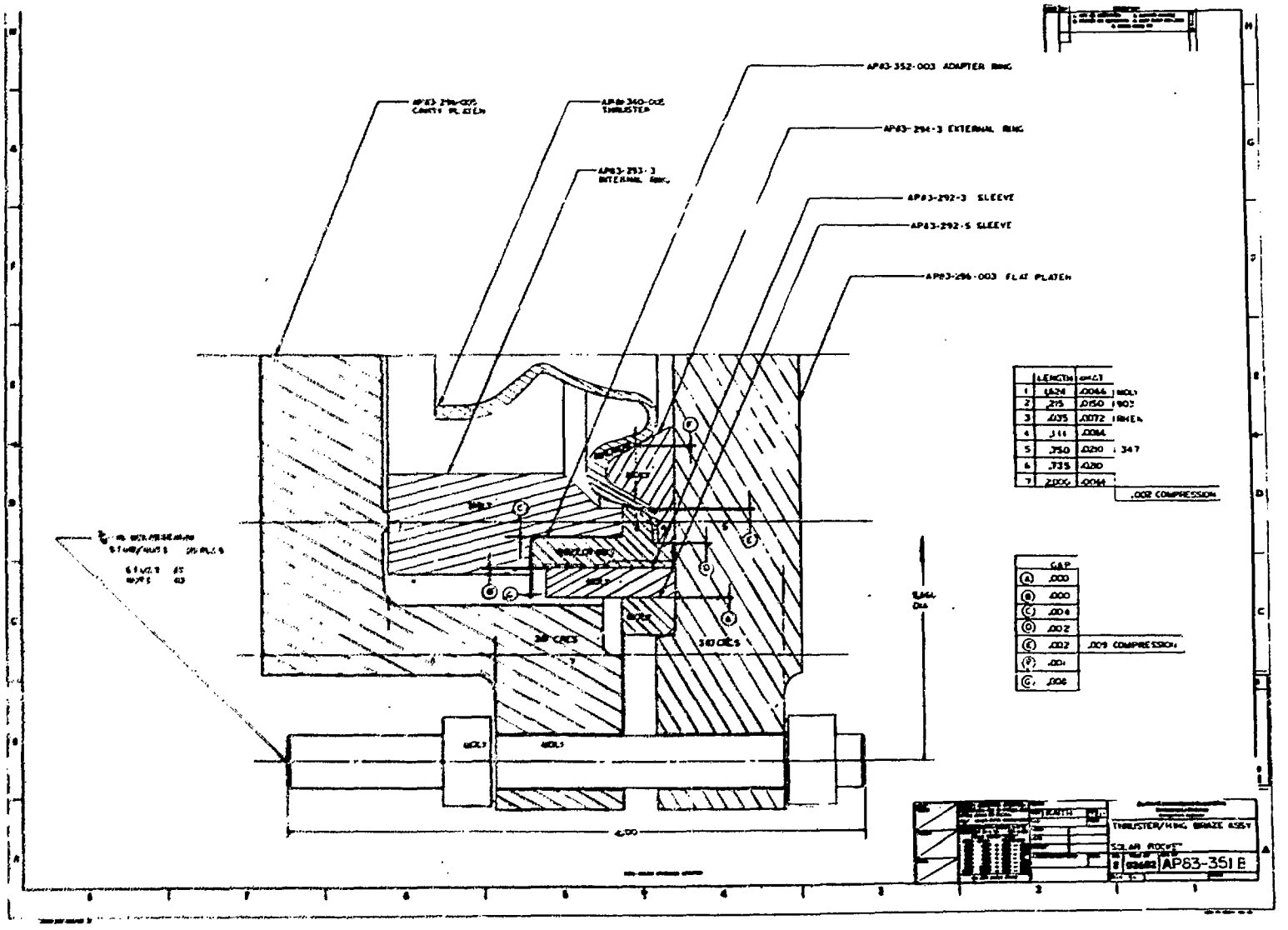

Figure 163. Thruster/Ring Brazing Tooling

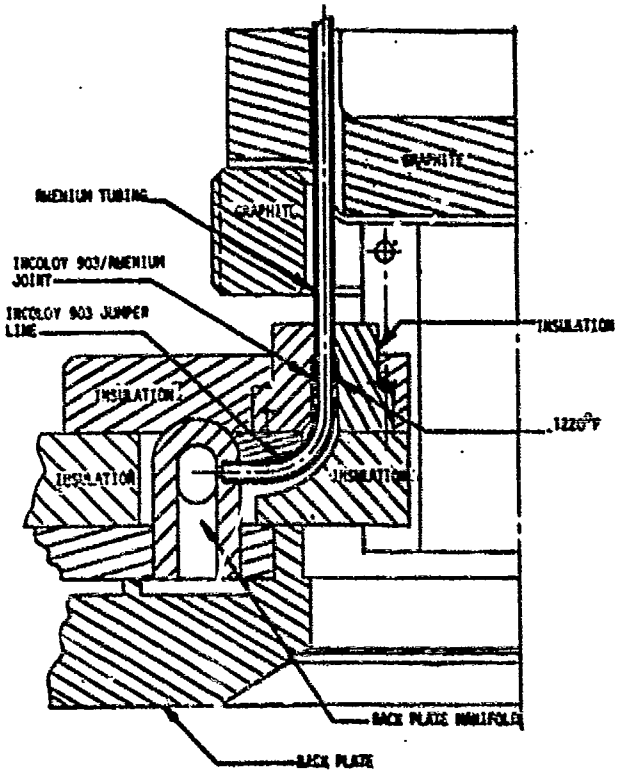

Figure 164. Absorber/Backplate Jumper Line Assembly

The assembly of the thruster to the vacuum chamber backplate involved EB welding of the adapter ring to the backplate (Incoloy 903 to Incoloy 903) and EB welding of the thruster to the absorber tube coil.

The depth of the adapter ring-to-back plate EB weld was of concern and was re-evaluated. A reduction of the weld depth would improve the chances of not encountering disbonding from welding and also of minimizing any braze alloy migration. Based on a stress review, the final weld depth was set at 0.889 cm ±0.0635 cm (0.350 inch ±0.025 inch). Weld samples verified the weldment was satisfactory.

The hardware was taken to EB welding vendor where the thruster was welded to the absorber coil. The chamber pressure tube was then formed to its final configuration, and the thruster adapter ring was inserted into the backplate and welded, completing the assembly. The rhenium tube coiled absorber and the vacuum chamber backplate assembly is shown in Fig. 165. A close-up of the coiled absorber inlet and the top of the rhenium thruster are shown in Fig. 166. A view of the back of the backplate is shown in Fig. 167. The nozzle exit is shown in this photograph.

Figure 165. Coiled Absorber/Backplate Assembly

Figure. 166. Coiled Absorber/Backplate Assembly
Absorber Inlet and Thruster

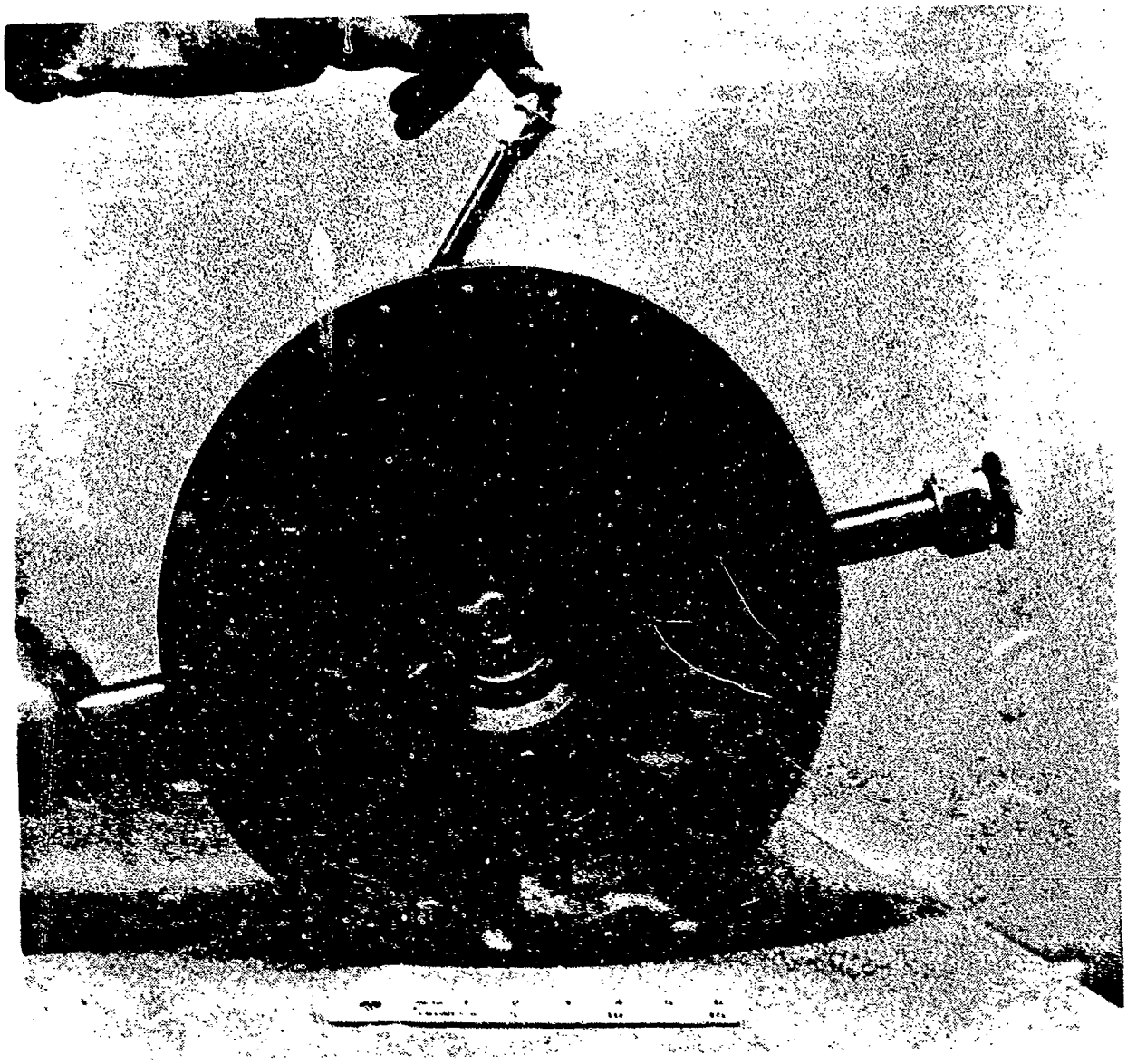

Figure 167. Backplate Assembly - View Looking Forward

FINAL ASSEMBLY

The final assembly was initiated by installing the graphite base, the thruster heat shield, and the graphite nut on the absorber/thruster/vacuum chamber backplate subassembly. As part of this same operation, the primary and secondary rigidized zirconium oxide insulation were also installed. The thruster thermocouples were also installed during this period. The actual procedure required some fitting, assembly, and reassembly until all of the items were compatible. The absorber thermocouples were then installed, starting from the thruster end and working toward the absorber inlet end. Rhenium foil was used to hold the thermocouples to the rhenium tubes.

After the thermocouples were installed, the graphite case was lowered over the assembly and the split graphite nut was screwed into the graphite case. The vacuum chamber was then installed on the final assembly fixture cradle (Fig. 168). The radiation heat shields were then installed into the vacuum chamber. The backplate subassembly (with thermocouples and graphite case) was then bolted to the final assembly fixture while the graphite case was supported. After the backplate assembly was supported on the assembly fixture, the vacuum chamber was moved forward so that the graphite case could be inserted into the radiation shield. The backplate assembly was then bolted to the vacuum chamber.

At this point the inlet insulation was installed with the retaining ring using silver plated screws. The Plexiglas cover was then installed for the vacuum leak checks. The propellant jumper line and the various plugs were also installed. The propellant jumper line, the plugs, and the thermocouple seals, were only tightened for leak-testing. All of these joints will have to be torqued for hot firing after the solar rocket assembly is installed into its test stand. This approach was selected on the basis that these items will be moved/opened/attached/etc., during stand installation. The final assembly is shown in Fig. 169.

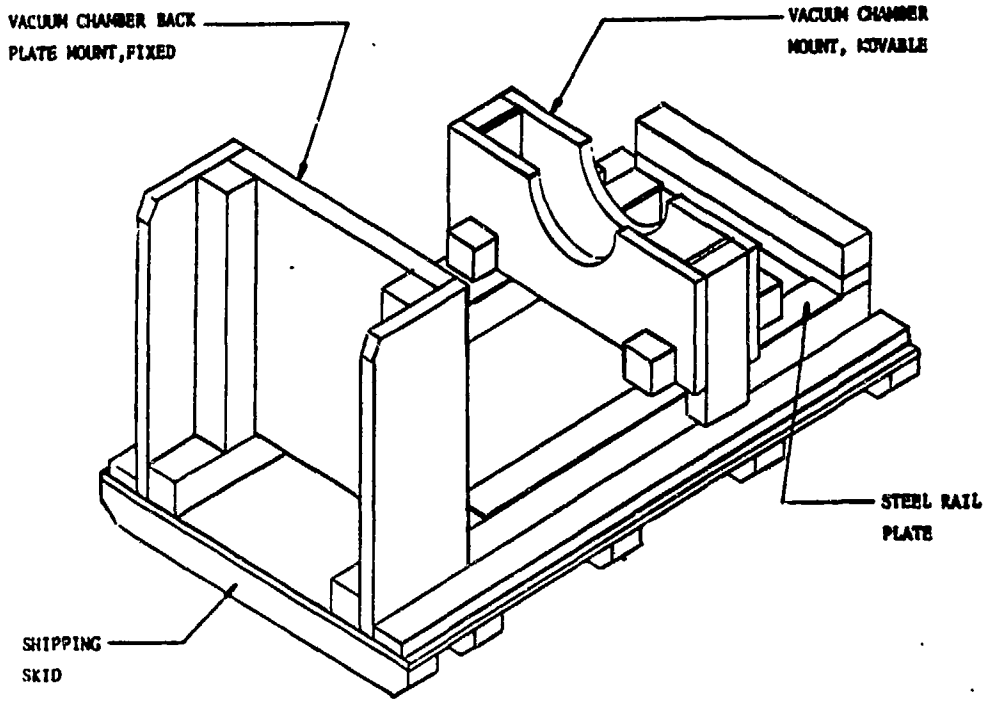

Figure 168. Solar Rocket Assembly Fixture

The vacuum chamber was then evacuated for a leak-check. The objective was to leak-check the metal seal between the vacuum chamber and the backplate. All of the other joints were temporarily sealed. The hardware was vacuum pumped for several days to outgas the assembly as much as practical. The final pumping achieved a vacuum of 10^{-3} torrs. A minor helium leak was observed in the metal seal joint. A slightly larger vacuum pump should have no problem overcoming such a leak for pump down at the test site. It is believed that over a sufficient amount of time 10^{-5} torrs can be achieved; however, since the hardware will not be installed for several months, and since it really has to be outgased at temperature 5000 R (4540 F), the pumping and testing of the hardware was terminated. The process will be resumed on the test stand.

The assembly was then packaged for shipment, using a vibration damping container system. Finally, the assembly was shipped to AFRPL for future installation into the test bed.

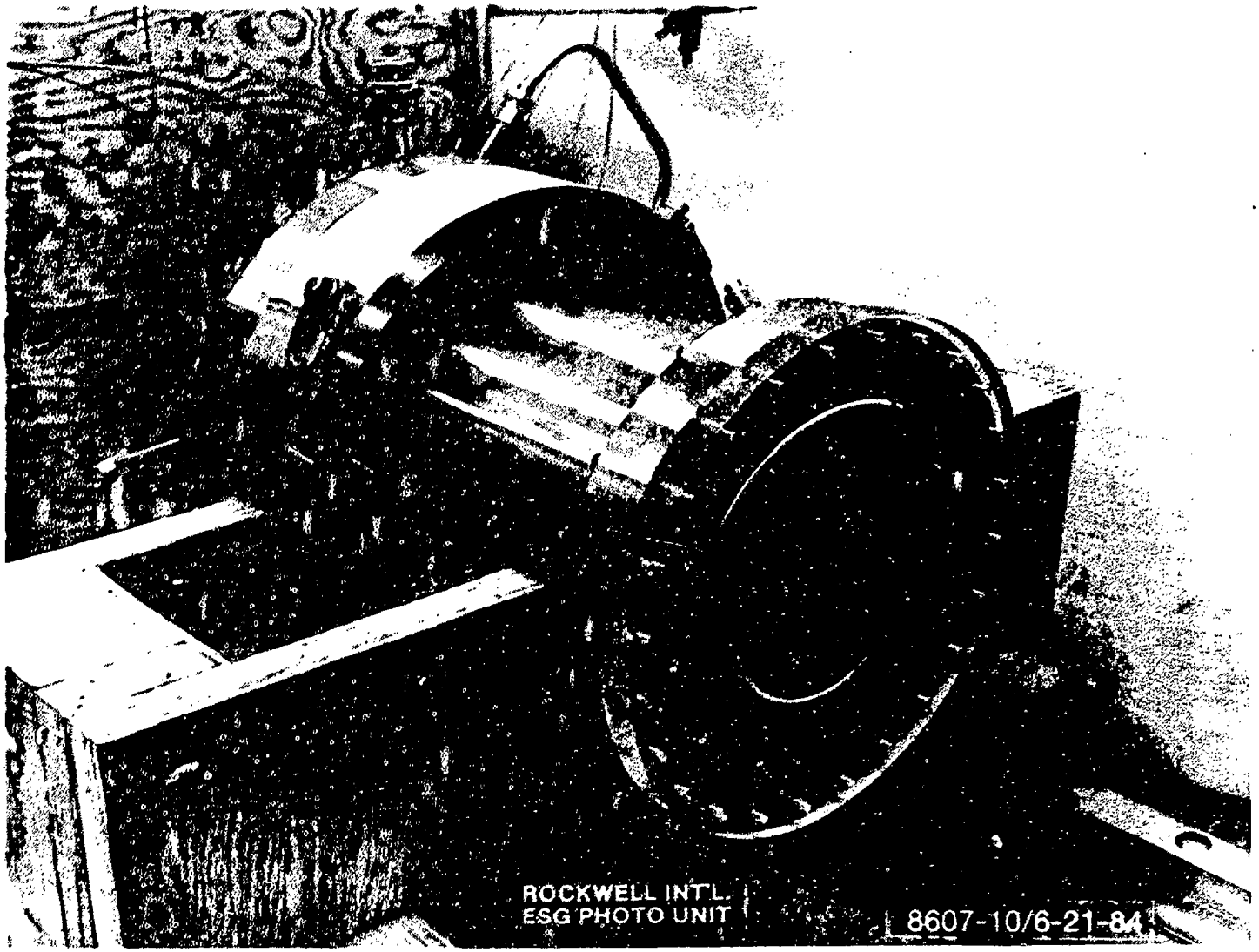

Figure 169. Solar Thermal Rocket Assembly (Viewed From Absorber Cavity End)

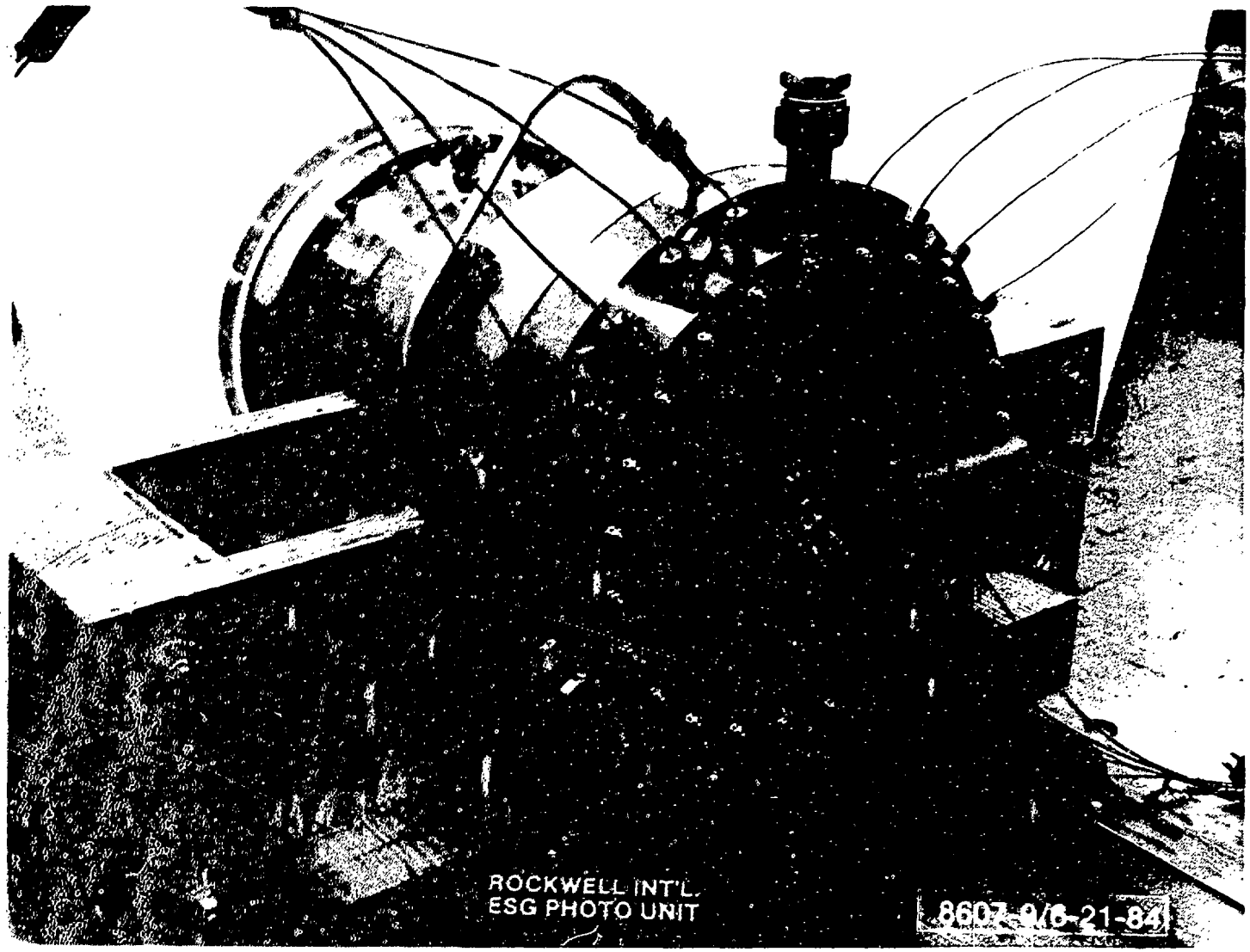

Figure 170. Solar Thermal Rocket Assembly (Viewed From Thruster End)

PHASE IV, SYSTEM SAFETY

A system safety evaluation of the grounded test hardware was completed with the objective of protection of personnel, facilities and hardware in the event of a failure. This objective has been accomplished by identifying safety hazards through a Preliminary Hazard Analysis (PHA), conducted per MIL-STD-882A. The PHA identifies safety critical areas, evaluates hazards and recommends/identifies safety, design and operational criteria for controlling or eliminating identified hazards.

ANALYSIS

In preparation for accomplishing the PHA, a Preliminary Hazard List (PHL) was generated. The PHL listed potential hazards of concern and design criteria recommendations for elimination/control of the hazard. The PHL aids the designer in designing when possible, to eliminate the potential hazard. The PHL is presented in Table 20.

A PHA was accomplished using MIL-STD-822A, Section 5.5.1.1. Initiation of the analysis was concurrent with the design effort to ensure that safety concerns were systematically evaluated and appropriately integrated into the decision making process for the system design.

The PHA (Table 21) includes the following information:

1. Hazard Source identifies potentially hazardous conditions associated with the proposed system which have been evaluated. These include hazardous components, safety related interface considerations among system elements such as material compatibilities, environmental constraints, and other sources of potentially hazardous conditions.

2. Operation Phase defines the activities when the hazard could accur.

3. Hazard describes the possible effects of the hazard source, including any jeopardy to the test hardware, personnel, and interfacing facility and equipment.

TABLE 20. PRELIMINARY HAZARD LIST (PHL)

HAZARD	HAZARD CONTROLS AND RECOMMENDATIONS
• CONTAMINATION • PERFORMANCE DEGRADATION ADVERSE LOCAL HEATING OF WINDOW • PLUGGING OF LINES	• WINDOW COOLING PURGE • TEMPERATURE MONITORING OF ABSORBER • PREOPERATION VERIFICATION OF WINDOW CLEANLINESS
• STRUCTURAL FAILURE • CONTAMINATION • COMPONENT FAILURE • INADEQUATE MATERIALS • HIGH TEMPERATURE OXIDATION • UNPROVEN MANUFACTURING TECHNIQUES	• MATERIALS SELECTION • COOLING OF HEAT SHIELD BY LH_2 • WINDOW COOLANT AND EJECTOR GN_2 PURGES • SAFETY DESIGN MARGINS • DETECTION OF WINDOW COOLANT OR LH_2 FLOW FAILURE • VACUUM ENCLOSURE AROUND ABSORBER • TEMPERATURE MONITORING OF ABSORBER • SYSTEM COOL DOWN PRIOR TO EXPOSURE TO AIR • SELECTION OF PROVEN MANUFACTURING TECHNIQUES USED PREVIOUSLY
• INSUFFICIENT SHIELDING, PROTECTION AND/OR ISOLATION OF ADJACENT EQUIPMENT FROM INTENSE HEAT RADIATED FROM ABSORBER	• ADJACENT EQUIPMENT PROTECTION FROM THRUSTER EXHAUST PLUME • ABSORBER SURROUNDED BY CARBON SHELL AND ENCLOSED IN COOLED HEAT SHIELD • VERIFICATION OF SYSTEM COOLDOWN PRIOR TO STOPPING LH_2 FLOW AND WINDOW COOLANT
• EXCESSIVELY HIGH GAS PRESSURE IN ABSORBER/THRUSTER WITH RESTRICTED EXHAUST PASSAGE	• SAFETY DESIGN MARGINS • PREOPERATION INSPECTION-VERIFY NO OBSTRUCTION
• FIRE/EXPLOSION/RUPTURE • IGNITION OF H_2 • AIR ENTRY INTO THRUST/ABSORBER • H_2 LEAKAGE • OVERHEATING OF PROPELLANT SUPPLY LINES AND STORAGE TANK	• DISPERSION OF H_2 BY EJECTOR GN_2 FLOW • PRESTART AND POST SHUTDOWN PROPELLANT SYSTEM PURGE • SYSTEM COOLDOWN PRIOR TO EXPOSURE TO AIR • POSITIVE PROPELLANT SHUTOFF • IMPLEMENTATION OF REGULARLY SCHEDULED LEAK TESTS • PROTECTION AGAINST ABSORBER CONVECTION/RADIATION HEATING PROVIDED BY CARBON SHELL AND HEAT SHIELD

TABLE 21. PRELIMINARY HAZARD ANALYSIS

SYSTEM: SOLAR ROCKET COMPONENT

DATE: 7/81

HAZARD SOURCE	OPERATIONAL PHASE	HAZARD	HAZARD CLASSIFICATION	HAZARD CONTROL	REMARKS
CONTAMINATION	OPERATION	PERFORMANCE DEGRADATION RESULTING FROM REDUCED SOLAR HEAT FLUX TRANSMISSION INTO ABSORBER.	IV	WINDOW COOLING PURGE WILL MAINTAIN WINDOW CLEANLINESS.	PRE-OPERATION MAINTENANCE SHOULD INCLUDE VERIFICATION OF WINDOW CLEANLINESS.
		ADVERSE LOCAL HEATING OF WINDOW DUE TO CONTAMINATION.	II	SEE ABOVE	SEE ABOVE
		INTRODUCTION OF CONTAMINATION DURING MANUFACTURING RESULTS IN PLUGGING OF LINES.	II	THERMOCOUPLES WILL MONITOR TEMPERATURE OF ABSORBER DURING OPERATION.	OPERATIONAL CONSTRAINT: 1. H_2 FLOW MUST BE VERIFIED PRIOR TO INTRODUCTION OF SOLAR FLUX. 2. TEMPERATURE OF ABSORBER SHOULD BE MONITORED PRESTART AS AN INDICATION OF LH_2 FLOW.
CORROSION	STANDBY	REDUCTION IN STRENGTH. LOW CYCLE FATIGUE OR H_2 EMBRITTLEMENT	II	MATERIALS SELECTED FOR NON-SUSCEPTIBILITY TO MOISTURE, AIRBORNE SALTS, AND HYDROGEN EMBRITTLEMENT CRES AND RHENIUM COMPONENTS ARE THE ONLY COMPONENTS IN CONTACT WITH H_2. RHENIUM AND CRES HAVE LOW SUSCEPTIBILITY TO HYDROGEN EMBRITTLEMENT.	INCORPORATE A REFACTORY CARBIDE LINING OF CARBON SHELL TO PREVENT CARBON INFILTRATION OF THE RHENIUM.

TABLE 21. (Continued)

SYSTEM: SOLAR ROCKET COMPONENT

DATE: 7/81

HAZARD SOURCE	OPERATIONAL PHASE	HAZARD	HAZARD CLASSIFICATION	HAZARD CONTROL	REMARKS
HIGH TEMPERATURE	OPERATION	STRUCTURAL FAILURE OF COMPONENT AS A RESULT OF EXCEEDING MATERIAL TEMPERATURE: ... INADEQUATE MATERIAL SELECTION ... COOLANT SYSTEM FAILURE	I	WINDOW COOLANT PURGE IS PROVIDED. LH_2 FLOW IS USED TO COOL CRES HEAT SHIELD. MATERIALS ARE SELECTED FOR HIGH TEMPERATURE SERVICE. STRUCTURAL INTEGRITY THROUGH SAFETY DESIGN MARGINS. EJECTOR GH_2 FLOW PROVIDES SOME COOLING OF THRUSTER.	PROVIDE MEANS OF DETECTING LOSS OF WINDOW COOLANT PURGE OR LH_2 FLOW. PROVIDE FOR IMMEDIATE SHUTDOWN FOR LOSS OF COOLANT OR LH_2 FLOW. INCORPORATION OF A SHUTTER COULD PROVIDE A QUICK MEANS OF BLOCKING SOLAR FLUX. FILTRATION OF LH_2 FLOW AND WINDOW COOLANT SHOULD BE PROVIDED TO PREVENT POSSIBILITY OF BLOCKED PROPELLANT AND COOLANT PASSAGES. OPERATIONAL CONSTRAINT: LH_2 AND WINDOW COOLANT FLOWS MUST BE INITIATED PRIOR TO INTRODUCING SOLAR FLUX.
	OPERATION POST SHUTDOWN	INSUFFICIENT SHIELDING, PROTECTION AND/OR ISOLATION OF ADJACENT EQUIPMENT FROM INTENSE HEAT RADIATED FROM ABSORBER RESULTING IN PERSONNEL INJURY AND/OR EQUIPMENT DAMAGE.	II	ABSORBER IS SURROUNDED BY A CARBON SHELL AND THEN ENCLOSED IN A LH_2 COOLED CRES HEAT SHIELD. THRUSTER EXHAUST PLUME IS AWAY FROM ADJACENT EQUIPMENT.	OPERATIONAL SEQUENCE SHALL INCLUDE COOL DOWN OF SYSTEM BEFORE LH_2 FLOW STOPPED. WINDOW COOLANT PURGE SHALL CONTINUE UNTIL SOLAR FLUX IS REDUCED.
	OPERATION	STRUCTURAL FAILURE DUE TO USE OF COMPONENTS WITH INCOMPATIBLE THERMAL EXPANSION RATES.	I	MATERIALS AND DESIGN REFLECT SELECTION OF COMPATIBLE MATERIALS. CARBON GRAPHITE AND RHENIUM HAVE LOW THERMAL EXPANSION RATES. DESIGN PROVIDES FOR EXPANSION OF ABSORBER AND FOR EXPANSION OF CARBON GRAPHITE SHELL. QUARTZ WINDOW COOLED TO PREVENT BUCKLING OF WINDOW DUE TO HEAT. SPACE PROVIDED IN DESIGN FOR EXPANSION OF WINDOW.	DESIGN ANALYSES SHOULD INCLUDE SPECIAL ATTENTION TO HEAT SHIELD SEAL SELECTION. VACUUM MUST BE MAINTAINED DESPITE THERMAL EXPANSION OF HEAT SHIELD.

TABLE 21. (Continued)

SYSTEM: SOLAR ROCKET COMPONENT

DATE: 7/81

HAZARD SOURCE	OPERATIONAL PHASE	HAZARD	HAZARD CLASSIFICATION	HAZARD CONTROL	REMARKS
HIGH TEMPERATURE (CONTINUED)	OPERATION	OXIDATION OF RHENIUM OCCURS RAPIDLY AT HIGH TEMPERATURES RESULTING IN REDUCED STRUCTURAL STRENGTH OF ABSORBER AND THRUSTER AND LOSS OF SYSTEM. ... STRUCTURAL FAILURE RESULTING IN LOSS OF VACUUM. ... SEAL LEAK ... VACUUM SYSTEM COMPONENT FAILURE	1	THE ABSORBER AND THRUSTER ARE ENCLOSED IN THE HEAT SHIELD. A VACUUM ATMOSPHERE WILL BE PROVIDED DURING OPERATION. VACUUM PRESSURE GAGE WILL BE PROVIDED. THERMOCOUPLES WILL MEASURE TEMPERATURE OF ABSORBER.	OPERATIONAL CONSTRAINTS: 1. ESTABLISH VACUUM WITHIN TEST CHAMBER PRIOR TO LH_2 FLOW INITIATION. 2. LH_2 FLOW MUST BE INITIATED BEFORE INTRODUCING SOLAR FLUX. PRESTART PURGE OF PROPELLANT SYSTEM SHOULD BE CONSIDERED. 3. MEANS MUST BE PROVIDED FOR DETERMINING WHEN SYSTEM IS COOLED ADEQUATELY TO PREVENT OXIDATION OF RHENIUM WHEN EXPOSED TO AIR (I.E., THERMOCOUPLE AT THRUSTER EXIT). 4. EJECTOR GH_2 FLOW AND LH_2 FLOW OR PROPELLANT PURGE FLOW MUST BE CONTINUED UNTIL SYSTEM IS ADEQUATELY COOLED. 5. PROVIDE CAPABILITY OF INERT GAS PURGE SHOULD VACUUM FAIL.

TABLE 21. (Continued)

SYSTEM: SOLAR ROCKET COMPONENT

DATE: 7/81

HAZARD SOURCE	OPERATIONAL PHASE	HAZARD	HAZARD CLASSIFICATION	HAZARD CONTROL	REMARKS
HIGH PRESSURE	OPERATION	EXCESSIVELY HIGH GAS PRESSURE IN ABSORBER/THRUSTER WITH RESTRICTED EXHAUST PASSAGE. HARDWARE RUPTURE.	II	STRUCTURAL INTEGRITY THROUGH DESIGN SAFETY MARGIN. RELATIVELY LOW CHAMBER PRESSURE.	OPERATIONAL CONSTRAINT: PRETEST INSPECTION REQUIRED TO VERIFY NO OBSTRUCTION AT THRUSTER EXIT.
FIRE/EXPLOSION/RUPTURE	OPERATION	DELAYED COMBUSTION/DETONATION OF EXHAUSTED H_2 WHEN MIXED WITH AIR.	III	COMBUSTION OF EXHAUSTED, HEATED H_2 COULD BE EXPECTED AT THE EXIT OF THE DIFFUSER. HOWEVER, THE EJECTOR GH_2 FLOW WILL PROBABLY DISPERSE THE H_2 WITHOUT IT IGNITING DUE TO THE LOW H_2 FLOW.	
	START	PRESENCE OF AIR IN ABSORBER PRIOR TO INTRODUCTION OF H_2 AND HIGH RADIANT HEAT.	I		OPERATIONAL CONSTRAINTS: 1. INCORPORATE PRESTART INERT GAS PURGE OF PROPELLANT SYSTEM PRIOR TO INTRODUCTION OF H_2. HELIUM SHOULD BE CONSIDERED FOR INERT GAS PURGES SINCE USE OF GN_2 IN A LH_2 SYSTEM RESULTS IN A POTENTIAL FREEZING PROBLEM. 2. H_2 FLOW MUST BE INITIATED PRIOR TO INTRODUCTION OF SOLAR FLUX.

TABLE 21. (Continued)

SYSTEM: SOLAR ROCKET COMPONENT

DATE: 7/81

HAZARD SOURCE	OPERATIONAL PHASE	HAZARD	HAZARD CLASSIFICATION	HAZARD CONTROL	REMARKS
FIRE/EXPLOSION/RUPTURE (CONTINUED)	POST SHUTDOWN	AIR ENTRY INTO THRUSTER/ABSORBER FOLLOWING SHUTDOWN WITH PRESENCE OF HOT RESIDUAL H_2.	I		OPERATIONAL CONSTRAINTS: 1. INCORPORATE INERT GAS PURGE OF PROPELLANT SYSTEM TO EXPEL ALL RESIDUAL H_2 AND AID IN COOLDOWN. HELIUM SHOULD BE CONSIDERED SINCE USE OF GN_2 IS A POTENTIAL FREEZING PROBLEM. PURGE SHOULD BE INITIATED AS CLOSE TO LH_2 TANK AS POSSIBLE TO CLEAR AS MUCH OF THE LINES AS POSSIBLE. 2. MAINTAIN EJECTOR GN_2 PURGE UNTIL SYSTEM COOLED DOWN. PROPELLANT SHUTOFF VALVE SHOULD BE AS CLOSE AS POSSIBLE TO SYSTEM TO REDUCE H_2 RESIDUALS FOLLOWING SHUTDOWN.
	STANDBY POST SHUTDOWN OPERATIONAL	UNCONTROLLED RELEASE OF LH_2/H_2 OR LEAKAGE OF H_2 IS IGNITED RESULTING IN FIRE/EXPLOSION.	I	SYSTEM PROOF AND LEAK TEST. HEAT SHIELD ENCLOSURE SHOULD PROVIDE PROTECTION FOR ADJACENT EQUIPMENT IN THE CASE OF AN ABSORBER/ THRUSTER EXPLOSION	TEST FACILITY RESPONSIBILITY FOR PROVIDING POSITIVE PROPELLANT SHUT-OFF VALVES AND PRESSURE RELIEF DEVICES. OPERATIONAL CONSTRAINT: PROVIDE FOR REGULARLY SCHEDULED EXAMINATION FOR EVIDENCE OF LEAKAGE.

TABLE 21. (Concluded)

SYSTEM: SOLAR ROCKET COMPONENT

DATE: 7/81

HAZARD SOURCE	OPERATIONAL PHASE	HAZARD	HAZARD CLASSIFICATION	HAZARD CONTROL	REMARKS
FIRE/EXPLOSION/RUPTURE (CONTINUED)	OPERATION POST SHUTDOWN	UNCONTROLLED HEATING OF PROPELLANT SUPPLY LINES AND STORAGE TANK: ... CONDUCTION ... CONVECTION ... RADIATION	I	DESIGN OF CARBON SHELL AND LH_2 COOLED CRES HEAT SHIELD PROVIDES PROTECTION AGAINST CONVECTION/ RATIATION HEATING OF ADJACENT EQUIPMENT.	A CHECK VALVE SHOULD BE PROVIDED IN THE LH_2 SUPPLY LINE TO PREVENT BACK-FLOW OF HOT H_2. OPERATION CONSTRAINTS: 1. LH_2 FLOW OR PROPELLANT PURGE FLOW SHOULD BE CONTINUED UNTIL SYSTEM IS ADEQUATELY COOLED.
MANUFACTURE OF COMPONENTS	OPERATION	STRUCTURAL FAILURE OF COMPONENTS DUE TO USE OF UNPROVEN MANUFACTURING TECHNIQUES.	I	RHENIUM TUBES ARE MANUFACTURED BY CHEMICAL VAPOR DEPOSITION IN AN INERT ATMOSPHERE. (CURRENT STATE OF THE ART). RHENIUM IS BRAZEABLE AND WELDABLE BY ELECTRON BEAM WELDING, WHICH ARE THE PROCESSES WHICH WILL BE USED FOR JOINING AND FOR REWORK OR REPAIR DURING FABRICATION. WELDING WILL BE PERFORMED IN AN INERT GAS ATMOSPHERE. MULTIPLE LEAK CHECKS AND PROOF TESTS ARE PERFORMED DURING THE MANUFACTURING PROCESS. RHENIUM IS READILY FORMABLE AT ROOM TEMPERATURE. SIMILAR TYPES OF HARDWARE HAVE BEEN FABRICATED FROM RHENIUM. REQUIRED FABRICATION TECHNIQUES FOR CRES AND CARBON GRAPHITE ARE WELL DEVELOPED AND UNDERSTOOD. A DESIGN AND FABRICATION SPECIFICATION WILL BE PREPARED WHICH WILL STATE ALL DESIGN AND OPERATING CHARACTERISTICS, DESIGN SAFETY FACTORS, LIMIT VALUES, PROOF TEST REQUIREMENTS, FABRICATION MATERIALS SPECIFICATIONS AND CRITICAL TEST PROCEDURES.	

4 Hazard Classification is per paragraph 5.4.3.1 of MIL-STD-882A, ranging from Category 1 catastrophic to Category IV negligible.

5. Hazard Control identifies design and operational features which have been incorporated into the system design and which provide controls to reduce or eliminate potential hazards.

6. Remarks flags out recommended design/operational criteria and safety critical areas where implemented design or operational controls are not adequate to eliminate or reduce potential hazards.

CONCLUSIONS

The major hazards of concern are structural failure, high temperature oxidation and fire/explosion. These hazards arise from the chemical pressure and thermal energies of the hydrogen gas and solar heat flux.

The features of the conceptual design are generally adequate for control of the critical and catastrophic hazards. The following design and operational criteria are recommended for additional hazard prevention.

1. Incorporation a refractory carbide lining within the carbon shell.

2. Investigate the incorporation of a shutter to control solar heat flux through window.

3. Incorporate instrumentation for monitoring of LH_2 propellant flows, and for determining that hardware is adequately cooled during post-shutdown.

4. Careful selection of heat shield seals.

5. Propellant shut-off valves should be located so as to minimize H_2 residuals following shutdown.

6. Provide check valve in LH_2 supply line.

7. Provide capability for inert gas purge should vacuum fail.

8. Operational test procedure recommendations:

   a. Pretest inspections - verify window cleanliness and no obstruction at thruster exit

   b. Prestart purge of propellant system

   c. Monitor absorber temperature prestart and during test

   d. Establish vacuum within test chamber prior to LH_2 flow initiation

   e. Postshutdown purge of propellant system to expel residual H_2

   f. Regularly scheduled examination for evidence of leakage

CONCLUSIONS AND RECOMMENDATIONS

The program which was conducted, selected a solar rocket thruster concept for design, fabrication and future test demonstration. The concept selected was the windowless heat exchanger cavity configuration and was chosen over other concepts evaluated based on its good performance potential and its superior rating in terms of minimum complexity, technical risk and cost. The test demonstration design provided a projected specific impulse of 7930 Nsec/kg (807 lbf sec/lbm) with a thrust of 3.69 N (0.83 lbf) and was the most viable near-term concept consistent with allocated funds and schedule.

CONTINUED TECHNOLOGY INVESTIGATIONS

To realize the full potential of the solar rocket concept, continued studies are recommended on the higher temperature, higher specific impulse approaches such as the windowless stationary porous cylinder, rotating bed and the aerodynamic window concept. To make these approaches practical, further component materials and component technology work is required as defined in the following.

Absorber and Thruster Wall Materials

The near-term recommended wall material was rhenium, which limits the hydrogen propellant temperature to 2777 K (5000 R). This limit in turn limits the specific impulse and life.

Improved materials, such as carbon-carbon composites with a high temperature carbide coating offer the potential for higher temperature operation with improved specific impulse and life. Many fabricability unknowns need to be investigated, including the candidate coatings of tantalum, niobium, tungsten, and rhenium.

Window

Based on analysis of the data available, a quartz window with a Iridium-Tin oxide IR coating was selected for the demonstrator design. Property data was

scarce for windows and coatings and the properties vary widely with thickness, polish and quality of material. Property data were generally presented at room temperature and extrapolation to elevated temperatures was necessary, which is a risky design practice.

Elevated temperature testing of window materials and IR coatings is recommended to establish data in transmitivity and reflectivity. Experimental testing to investigate coatings and particle deposition are also recommended, together with design analyses of the disc versus hemispherical configurations and mounting and sealing of these configurations.

Porous Cylinder

The porous cylinder concept offers improved specific impulse resulting from higher temperature operation. To realize this potential, further investigations are required on porous wall materials including erosion characteristics, possible surface treatment, and achieving uniform porosity. Design analysis is also recommended on methods for incorporating the porous cylinder, and on the hydrogen feed and flow dynamics.

Rotating Bed

The rotating bed concept also offers improved performance potential, however, additional technology work is required to investigate drive methods, including feasibility of the drive approach and high-temperature bearing operation. Investigation is also recommended on the rotating bed operation, including flow and particle uniformity, particle charging mechanism, start sequence feasibility and speed control.

Aerowindow

The aerowindow concept removes limitations due to window cooling and has potential application to extremely high propellant temperatures. To realize this potential, investigations into design and operation are recommended, including aerowindow leakage and diffuser operation. The secondary mirror design and coating also needs further investigation.

INITIAL TEST RECOMMENDATIONS

To reduce the uncertainties and increase the probability of success during the initial testing, several recommendations are highlighted below. Additional test recommendations are presented in the System Safety Analysis of Phase IV.

Window

A pretest durablity check of the window is recommended. The window would be exposed to the concentrator solar radiation without being installed into the vacuum chamber assembly. The window would be inspected after the exposure for signs of cracking or opaqueness.

Test Series

Conduct the initial tests starting with approximately five times the design flowrate and decrease to design value on subsequent tests. The data and hardware would be inspected after each test.

APPENDIX A

WINDOWLESS ABSORBER/THRUSTER EFFICIENCY CALCULATIONAL METHOD

The cavity absorber efficiency relationship for the windowless absorber/thruster was derived based on an extension of the work of Kreith (Ref. 5) and Stephens and Haire (Ref. 6). The cavity absorber efficiency was defined as:

$$\eta_{\substack{\text{Cavity}\\ \text{Absorber}}} = \frac{Q_s - (/Q_{r_1} + Q_{r_2})}{Q} \tag{A-1}$$

where

Q_s = the solar radiation absorbed by the cavity and working fluid

Q_{r_1} = the energy lost through reradiation through the opening

Q_{r_2} = the energy lost from the cavity external surface

Q = the incoming solar energy

The complete energy transfer mechanism is illustrated in Fig. A-1. Continuing with equation:

$$\eta_{\substack{\text{Cavity}\\ \text{Absorber}}} = \frac{1}{1-(1-F_{12})(1-e_1)} \left[e_1 - \frac{3.9860465 \times 10^{-12}}{C\ (A_2/A_1)} \left\{ \sigma_1 e_2 F_{12} T_1^{\ 4} + e_w T_w^{\ 4} \left(1-(1-F_{12})(1-e_1)\right) \right\} \right] \tag{A-2}$$

where

F_{12} = shape or view factor

e_1 = cavity internal surface emissivity

e_2 = cavity opening emissivity

e_w = cavity external surface emissitivity

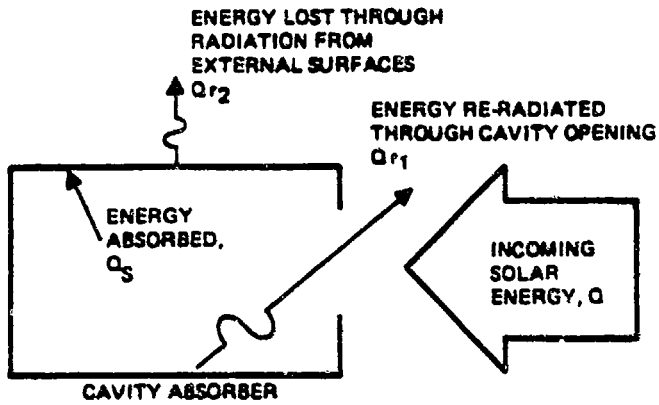

Figure A-1. Windowless Heat Exchanger Cavity Absorber Performance Parameters

C	=	concentration ratio of energy entering cavity absorber
A_2/A_1	=	ratio of cavity opening area to internal area
T_1	=	cavity absorber internal surface temperature, R
T_w	=	cavity absorber external surface temperature, R

For the heat exchanger-type cavity, e_2 is equal to 1.0. For the degenerate case of flat disk, the above expression becomes:

$$\eta_{\substack{\text{Flat}\\ \text{Disk}\\ \text{Absorber}}} = e_1 - \frac{3.9860465 \times 10^{-12}}{C}\left[e_1 T_1^{\,4} + e_w T_w^{\,4}\right] \qquad \text{(A-3)}$$

Equation (A-2) is applicable to analyzing to any shape absorber since the respective cavity view factor is the parameter which describes the absorber shape. The cavity view factors for the various absorber configurations analyzed were obtained from Fig. A-2 or analytically derived.

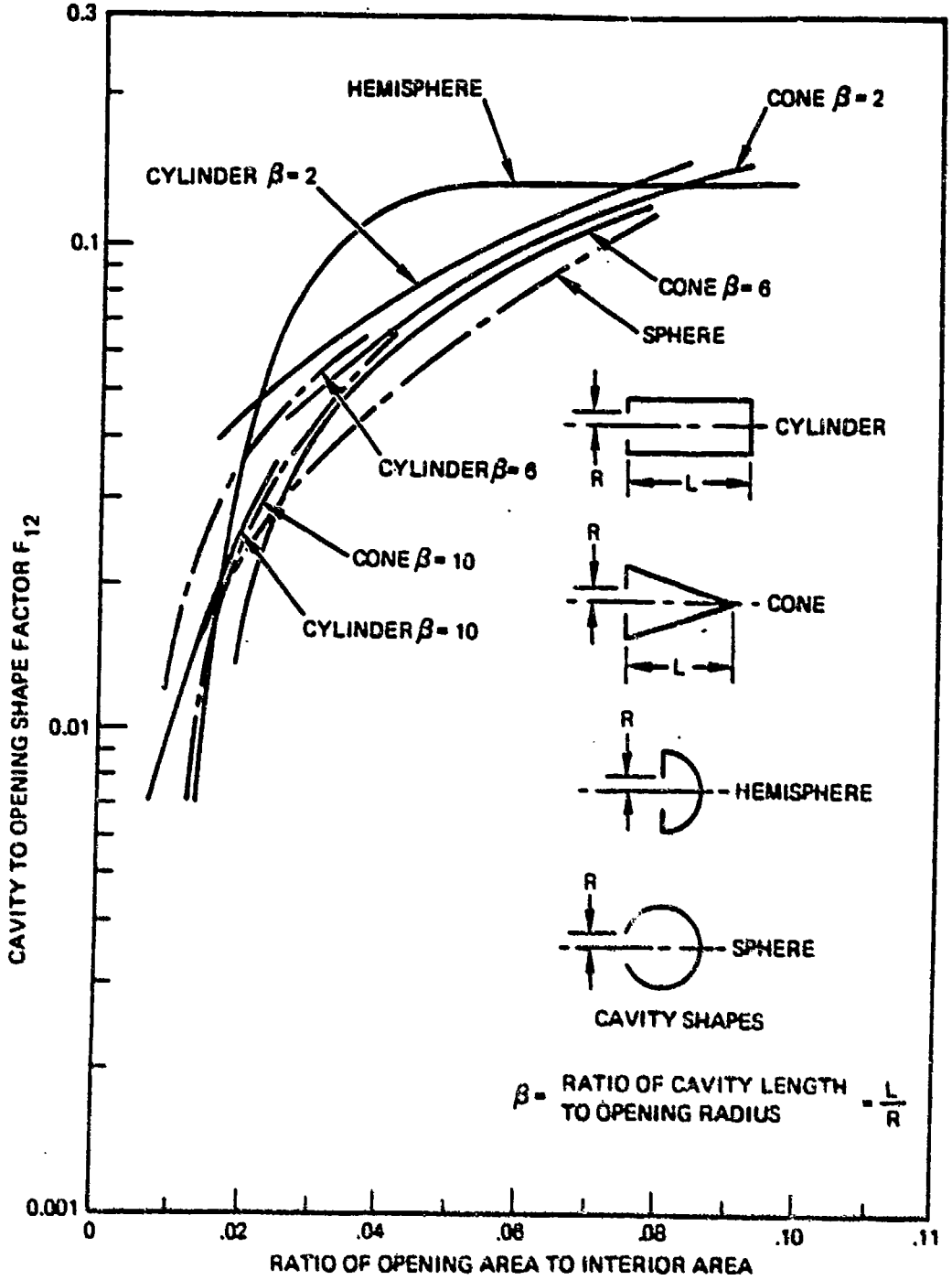

Figure A-2. Cavity to Opening Shape Factors

For the open-ended cylinder, the cavity view factor is given by the analytically derived relationship:

$$F_{12} = 1 + \left(\frac{R}{2L} - 1\right) \left[\frac{1}{2} \left(\frac{L}{R} \sqrt{4 + \left(\frac{L}{R}\right)^2} - \left(\frac{L}{R}\right)^2\right)\right] \tag{A-4}$$

where

R = radius of the cylinder

L = length of the cylinder

APPENDIX B

DELIVERED SPECIFIC IMPULSE AND THRUST ANALYSIS METHOD

In determining the delivered performance of the windowless absorber/thruster, the hydrogen flowrate, thruster throat radius, delivered specific impulse and thrust were computed using the following relationships:

Hydrogen Flowrate:

$$\dot{m}_{H_2} = \frac{Q_{absorber}}{\Delta H_{H_2}}$$

Thruster Throat Radius:

$$R_t = \sqrt{\frac{2C^*\dot{m}_{H_2}}{P_c \ v \ g}}$$ (Assuming two absorbers with one thruster)

Delivered Specific Impulse:

Simplified JANNAF procdure

Thrust:

$$F = 2 \ I_2 \ \dot{m}_{H_2}$$

where

$\dot{m}_{H_2}$ = hydrogen mass flowrate

$Q_{absorbed}$ = heat absorbed by absorber

ΔH_{H_2} = enthalphy difference from inlet to final H_2 temperature

R_t	=	thruster throat radius
C^*	=	theoretical characteristic velocity
P_c	=	thruster chamber pressure
g	=	gravitational constant
I_s	=	Delivered specific impulse
F	=	thrust

APPENDIX C

VACUUM CHAMBER WINDOW SPECIFICATIONS

Specifications for the quartz vacuum chamber window and the IR coating were prepared as shown in Table C-1 and C-2. A potential supplier for the quartz window was Corning Glass Works. The potential suppliers of the IR coating were:

Optical Coating Laboratory Inc. (OCLI), Santa Rosa, CA
Liberty Mirror, Brackenridge, PA
Midwest Coating Research Corporation, Chicago, IL
DYN, Optics,

In addition to meeting the window and coating specifications, the window assembly should be tested for high temperature durability prior to installation on the absorber/thruster. Window structural failure during the testing of the absorber/thruster could result in absorber overheating unless a vacuum chamber purge and a solar radiation shutter can be implemented quickly. The recommended window test was to focus the solar radiation onto the window assembly without the absorber/thruster assembly.

TABLE C-1. VACUUM CHAMBER WINDOW SPECIFICATIONS

MATERIAL: FUSED SILICA (QUARTZ)

DIMENSIONS: 30.48 CM (12-INCH) DIAMETER
1.905 CM (0.75-INCH) THICKNESS

INCLUSIONS: MAXIMUM NUMBER/CU CM = 0.061 (1/CU IN.)
MAXIMUM AVERAGE NUMBER/CU CM = 0.0122 (0.2/CU IN.)
MAXIMUM MEAN DIAMETER = 0.0203 CM (0.008 IN.)

WATER CONTENT: 0.1%

SURFACES: GROUND AND POLISHED
FLATNESS WITHIN 0.0127 CM (0.005 IN.)

OPTICAL PROPERTIES:

SPECTRAL TRANSMISSIVITY:

λ, MICRONS	MINIMUM TRANSMISSIVITY
0.16 - 0.18	0.35
0.18 - 0.20	0.82
0.20 - 0.24	0.90
0.24 - 2.2	0.92
2.2 - 2.25	0.60
2.25 - 2.30	0.72
2.3 - 2.75	0.40
2.75 - 3.2	0.40
3.2 - 3.4	0.75

SPECTRAL EMISSIVITY:

λ, MICRONS	MAXIMUM EMISSIVITY
0 - 2	0.01
2 - 2.5	0.54
2.5 - 3.5	0.75
3.5 - 7.3	0.97
7.3 - 8.0	0.90
8.0 - 8.8	0.60
8.8 - 9.0	0.42
9.0 - 10.0	0.65
10 - 14	0.92
14 - 19	0.97
19 - 20.5	0.79
20.5 - 21.0	0.60
21 - 23	0.67
23 - ∞	0.74

THERMAL PROPERTIES: THERMAL CONDUCTIVITY 0.0044 CAL CM/CM^2 SEC C AT 450 C
GOOD THERMAL SHOCK RESISTANCE
MAXIMUM OPERATING TEMPERATURE = 867 K (1100 F)
= FOR THE ABOVE OPTICAL PROPERTIES AND AN 85% REFLECTIVITY COATING.

TABLE C-2. VACUUM CHAMBER WINDOW IR COATING SPECIFICATIONS

COATING MATERIAL: INDIUM TIN OXIDE (ITO) OR ANOTHER COATING MATERIAL THAT CAN MEET THE OPTICAL AND THERMAL REQUIREMENTS.

OPTICAL PROPERTIES:

0.2 TO 2 MICRONS: HIGH TRANSMISSIVITY

λ, MICRONS	MINIMUM VALUE
0.16 - 0.18	0.35
0.18 - 0.20	0.82
0.20 - 0.24	0.90
0.24 - 2.0	0.92

BEYOND 2 MICRONS: REFLECTIVITY 85%

MAXIMUM OPERATING TEMPERATURE: 867 K (1100 F) FOR THE ABOVE OPTICAL PROPERTIES

APPENDIX D

THERMOCOUPLE ERROR

Thermocouples to be installed on the absorber/thruster assembly will provide a real time monitoring of test conditions and one of the parameters needed to evaluate the actual performance of the device. Therefore, errors in these measurements, in particular the thermocouples measuring the high temperatures on the thruster and near the absorber exit, are extremely important. These thermocouple errors can be the result of local radiation heat loss and conduction along the thermocouple wires. The tendency will be for the thermocouple to read lower than the actual value.

For the high temperature levels being measured, the thermocouples to be used will be tungsten-tungsten 20 percent rhenium. An installation sketch of the thruster thermocouple is shown in Fig. D-1. The thermocouple will be tacked to the thruster wall and the wires placed adjacent to the thruster to minimize the temperature gradient along the wires (heat loss). Since the temperature is being measured within a vacuum chamber, the heat transfer modes to be considered in evaluating the error are radiation and conduction.

To evaluate the heat loss from the thermocouple, a radiation and conduction heat balance was set up for the portion of the thermocouple within the thruster radiation heat shield. The thermocouple temperature error is represented by the equation:

$$\Delta T = \frac{\delta}{k_2 A_2} \left[\frac{T_2 - T_{31}}{\frac{L}{k_2 A_2} + \frac{L}{k_3 A_3}} + \alpha A_3 \left(T_{32}^{\ 4} - T_4^{\ 4} \right) \right]$$

where

L = wire length within the radiation sheild

k = thermal conductivity

A = area

Subscript

1 = thruster wall

2 = tungsten wire

3 = tungsten - 20% rhenium wire

4 = thruster radiation shield

T_{31} = wire-end temperature

T_{32} = average wire temperature

As shown in Fig. D-2, the temperature error due to radiation and conduction within the thruster radiation heat shield is dependent on the temperature difference between the thruster wall and the thruster radiation sheild. As this difference decreases, the thermocouple error decreases. Typically, this error would be approximately 2.8 K (5 F).

The heat conduction along the remainder of the thermocouple wire was calculated for 38.1 cm (15 inches) of wire with a 1667 K (3000 F) temperature differential. A thermocouple error of 3.3 K (6 F) resulted.

The radiation heat loss within the cavity outside the thruster radiation heat shield was assumed negligible due to the near isothermal environment.

Therefore, the thruster wall thermocouple temperature error would be less than 11.1 K (20 F) at the design absorber/thruster conditions which should not presented a problem. This result would also be a representative value for the thermocouples near the absorber exit.

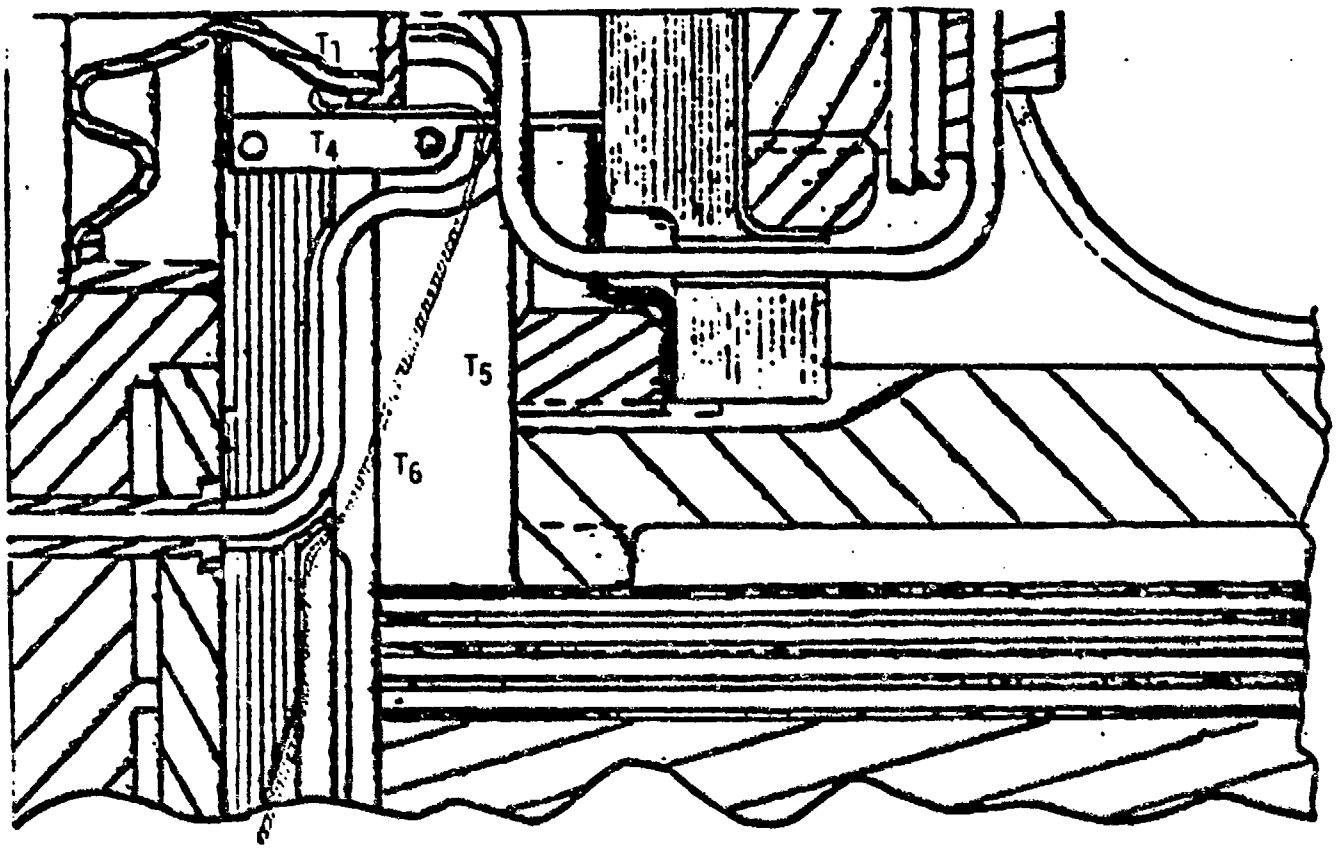

- T_4 = 2367 K (3800 F)
- T_5 = 2311 K (3700 F)
- T_6 = 2200 K (3500 F)

Figure D-1. Temperature Distribution at the End Enclosure Cavity

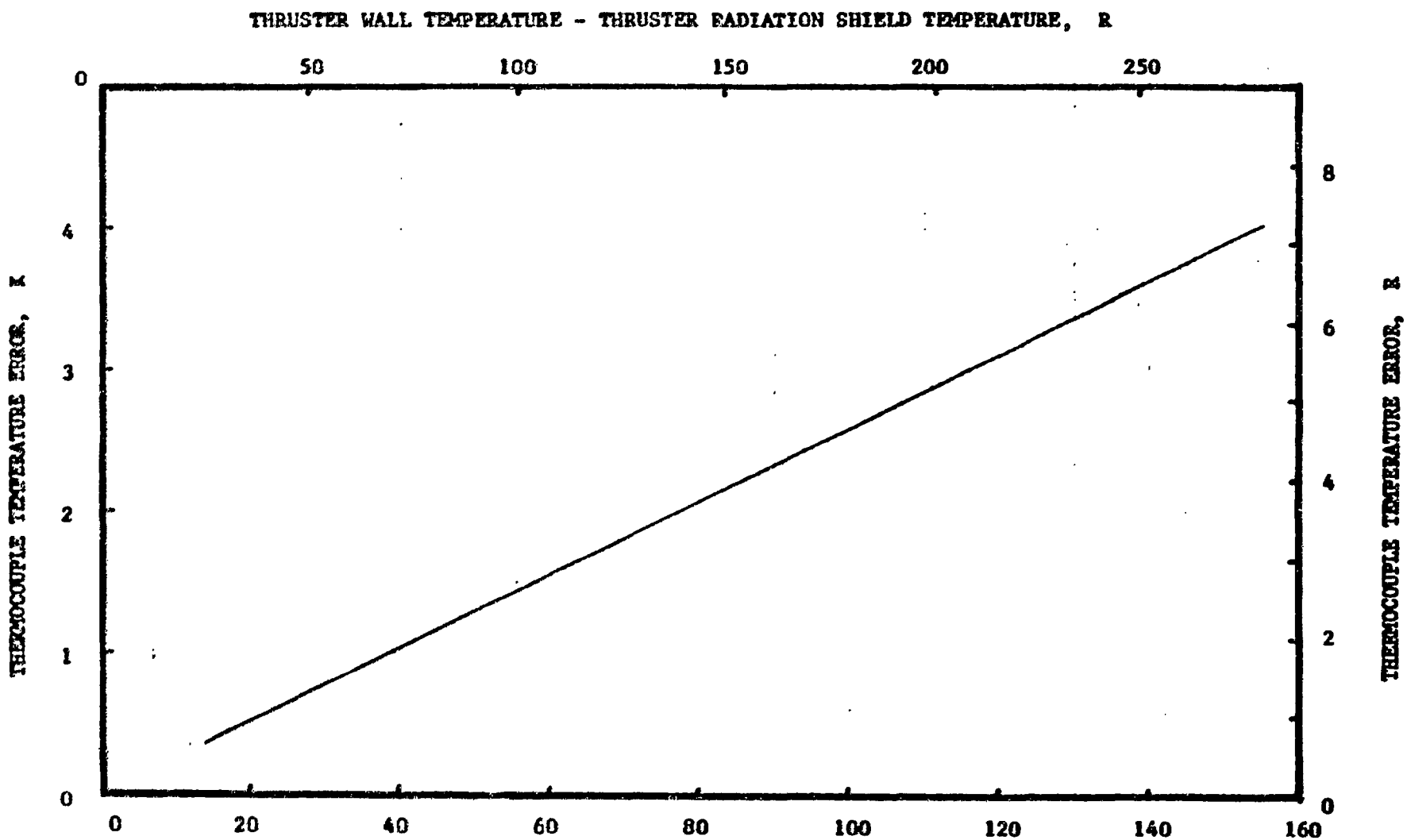

Figure D-2. Thrust Well Thermocouple Error with Thruster Radiation Shield

REFERENCES

1. AFRPL TR-79-79, "Solar Rocket System Concept Analysis," Final Technical Report, November 1979.
2. CPIA Publication 246, JANNAF Rocket Engine Performance Prediction and Evaluation Manual, April 1975.
3. Chemical Engineering Progress, Vol. 48, p. 98, 1962.
4. Davidson, J.F. and D. Harrison: Fluidization, Academic Press, 1971, p. 34.
5. Kreith, F.: Radiation Heat Transfer for Spacecraft and Solar Power Plant Design, International Textbook Company (1962).
6. Stephens, C. W., and A. M. Haire: "Internal Design Considerations for Cavity Type Solar Absorbers," Journal of American Rocket Society, 31, 896-901 (1961).